

PLASTIC CRYSTAL - GEL POLYMER ELECTROLYTES
FOR MAGNESIUM RECHARGEABLE BATTERIES

DIYANA HAMBALI

FACULTY OF SCIENCE
UNIVERSITI MALAYA
KUALA LUMPUR

2020

**PLASTIC CRYSTAL - GEL POLYMER
ELECTROLYTES FOR MAGNESIUM
RECHARGEABLE BATTERIES**

DIYANA HAMBALI

**THESIS SUBMITTED IN FULFILMENT OF THE
REQUIREMENTS FOR THE DEGREE OF
DOCTOR OF PHILOSOPHY**

**DEPARTMENT OF PHYSICS
FACULTY OF SCIENCE
UNIVERSITI MALAYA
KUALA LUMPUR**

2020

UNIVERSITI MALAYA
ORIGINAL LITERARY WORK DECLARATION

Name of Candidate: **DIYANA HAMBALI**

Matric No: **17020084/4**

Name of Degree: **DOCTOR OF PHILOSOPHY**

Title of Thesis (“this Work”):

**PLASTIC CRYSTAL - GEL POLYMER ELECTROLYTES FOR
MAGNESIUM RECHARGEABLE BATTERIES**

Field of Study: **EXPERIMENTAL PHYSICS**

I do solemnly and sincerely declare that:

- (1) I am the sole author/writer of this Work;
- (2) This Work is original;
- (3) Any use of any work in which copyright exists was done by way of fair dealing and for permitted purposes and any excerpt or extract from, or reference to or reproduction of any copyright work has been disclosed expressly and sufficiently and the title of the Work and its authorship have been acknowledged in this Work;
- (4) I do not have any actual knowledge nor do I ought reasonably to know that the making of this work constitutes an infringement of any copyright work;
- (5) I hereby assign all and every rights in the copyright to this Work to the University of Malaya (“UM”), who henceforth shall be owner of the copyright in this Work and that any reproduction or use in any form or by any means whatsoever is prohibited without the written consent of UM having been first had and obtained;
- (6) I am fully aware that if in the course of making this Work I have infringed any copyright whether intentionally or otherwise, I may be subject to legal action or any other action as may be determined by UM.

Candidate’s Signature

Date:

Subscribed and solemnly declared before,

Witness’s Signature

Date:

Name:

Designation

PLASTIC CRYSTAL - GEL POLYMER ELECTROLYTES FOR MAGNESIUM RECHARGEABLE BATTERIES

ABSTRACT

Polymer electrolytes are known to be the possible substitution for liquid electrolytes due to their excellent safe performance and good compatibility with electrodes compared to its liquid counterpart. Thus, in the present work, gel polymer electrolytes (GPEs) have been studied comprising plastic crystal succinonitrile (SN) to form plastic crystal - gel polymer electrolytes. The GPEs were prepared by using two types of magnesium salts which are magnesium trifluoromethanesulfonate (MgTf_2) and magnesium bis(trifluoromethanesulfonimide) ($\text{Mg}(\text{TFSI})_2$) varied from 5 to 30 wt.%. In the preparation of GPEs, four GPE systems were introduced which are single plasticized systems ($\text{PVdC-co-AN/SN/MgTf}_2$ and $\text{PVdC-co-AN/SN/Mg}(\text{TFSI})_2$) and double plasticized systems, i.e., combination of SN with ethylene carbonate (EC), ($\text{PVdC-co-AN/SN/EC/MgTf}_2$ and $\text{PVdC-co-AN/SN/EC/Mg}(\text{TFSI})_2$). The GPE samples were analyzed by means of alternating current (AC) impedance spectroscopy to determine the ionic conductivity at room temperature and at a temperature range of 303 K to 353 K. The conductivity temperature dependence studies of the GPEs were found to obey the Vogel-Tamman-Fulcher (VTF) relation. The ionic and cationic transference numbers were evaluated by direct current (DC) polarization method and the combination methods of AC impedance and DC polarization respectively to study the charge carrier species in the GPEs. To reveal the interactions among the constituents in the GPEs as well as to confirm the complexation between them, Fourier Transform Infrared Spectroscopy (FTIR) was carried out. The analysis of FTIR was extended by the deconvolution of the FTIR spectra to prove the dependability of ionic conductivity with the presence of free ions, ion pairs and ion aggregates in the GPEs. The amorphous nature of the GPEs was confirmed by X-ray diffraction (XRD) analysis while the surface morphology of GPEs

was analyzed by Field Emission Scanning Electron Microscopy (FESEM). On the other hand, differential scanning calorimetry (DSC) studies disclosed the relationship between the thermal stability of GPEs and ionic conductivity. The electrochemical stability of the GPEs was also determined by linear sweep voltammetry (LSV) and cyclic voltammetry (CV). The Mg/GPE/MgMn₂O₄ cells were assembled by using the most optimum GPE samples from all systems and their charge-discharge performances were studied. The best specific capacity of 90 mAh g⁻¹ was obtained from the cell that using PVdC-co-AN/SN/EC/15 wt.% Mg(TFSI)₂ based GPE as electrolyte.

Keywords: Gel polymer electrolytes, plastic crystal, PVdC-co-AN, magnesium salts, rechargeable batteries

KRISTAL PLASTIK - ELEKTROLIT POLIMER GEL UNTUK BATERI

MAGNESIUM BOLEH DICAS SEMULA

ABSTRAK

Elektrolit polimer dikenali sebagai pengganti untuk elektrolit cecair kerana ciri keselamatan yang sangat baik dan keserasian yang baik dengan elektrod berbanding dengan elektrolit cecair. Oleh itu, dalam kajian ini, elektrolit polimer jenis gel (GPE) telah dikaji yang terdiri daripada succinonitril kristal plastik untuk membentuk kristal plastik - elektrolit polimer gel. GPE disediakan dengan menggunakan dua jenis garam magnesium iaitu magnesium trifluoromethanesulfonat (MgTf_2) dan magnesium bis (trifluoromethanesulfonimide) ($\text{Mg}(\text{TFSI})_2$) bervariasi dari 5 hingga 30 wt.%. Dalam penyediaan GPE, empat sistem GPE telah disediakan iaitu sistem plastik tunggal (PVdC-co-AN/SN/ MgTf_2 dan PVdC-co-AN/SN/ $\text{Mg}(\text{TFSI})_2$) dan sistem dwiplastik, iaitu gabungan SN dengan etilena karbonat (EC), ($\text{PVdC-co-AN/SN/EC/MgTf}_2$ dan $\text{PVdC-co-AN/SN/EC/Mg}(\text{TFSI})_2$). Sampel GPE dianalisis dengan menggunakan spektroskopi impedans AC untuk menentukan kekonduksian ionik pada suhu bilik dan pada julat suhu 303 K hingga 353 K. Kajian kebergantungan suhu-konduktiviti GPE didapati mematuhi hubungan (Vogel-Tamman-Fulcher) VTF. Nombor-nombor pemindahan ionik dan kationik dikaji dengan menggunakan kaedah polarisasi arus terus (DC) dan kaedah gabungan arus ulang alik (AC) impedans dan polarisasi DC untuk mengkaji spesies-spesies pembawa caj dalam GPE. Untuk mengkaji interaksi antara bahan-bahan dalam GPE dan juga untuk mengesahkan pengkompleksan di antara mereka, Inframerah spektroskopi Fourier (FTIR) telah dijalankan. Analisis FTIR dilanjutkan dengan dekonvolusi spektrum FTIR untuk membuktikan kebergantungan kekonduksian ionik dengan kehadiran ion bebas, pasangan ion dan agregat ion dalam GPE. Sifat amorfus GPE disahkan oleh analisis pembelauan sinar-X (XRD) manakala morfologi permukaan GPE dianalisis oleh mikroskopi pengimbasan elektron pelepasan medan (FESEM). Selain itu,

kajian kalori pengimbasan yang berbeza (DSC) mendedahkan hubungan antara kestabilan terma GPE dan kekonduksian ionik. Kestabilan elektrokimia GPE juga dikaji dengan voltammetry menyapu linear (LSV) dan voltammetry kitaran (CV). Sel Mg/GPE/MgMn₂O₄ telah dibina dengan menggunakan sampel GPE yang paling optimum daripada semua sistem dan prestasi pelepasan caj mereka dipelajari. Kapasiti spesifik terbaik yang diperolehi ialah 90 mAh g⁻¹ iaitu daripada sel yang menggunakan GPE berasaskan PVdC-co-AN/SN/EC/15 wt.% Mg(TFSI)₂ sebagai elektrolit.

Kata kunci: Elektrolit polimer gel, kristal plastik, PVdC-co-AN, garam magnesium, bateri boleh dicas semula

Universiti Malaysia

ACKNOWLEDGEMENTS

First and foremost, praises and thanks to the God, the Almighty, for His shower of blessings and giving me strength and inspiration in completing my PhD study.

I would like to express my deep gratitude to my supervisor, Professor Dr. Zurina Osman, for giving me opportunity to do research works and providing invaluable guidance throughout the study. It was a great privilege and an honour to work and study under her supervision. I am extremely grateful for what she has taught and guided me.

My sincere thanks also go to my seniors, Dr. Lisani Othman and Dr. Khairul Bahiyah Md Isa, and to my labmates, Nurhidayu Harudin, Zaffan Zainuddin, Nurul Husna Zainol and Rosnadiya Rosli for assistance rendered and suggestions given during my research works. Without all of you, this research study might not be completed.

In addition, I would like to acknowledge the Ministry of Higher Education for the scholarship awarded and University of Malaya for the facilities provided.

My appreciation also extends to my family especially my beloved parents for their endless support and valuable prayers. Last but not least, to those who have directly or indirectly contributing towards the accomplishment of this research study, I would like to thank all of you.

TABLE OF CONTENTS

ABSTRACT	iii
ABSTRAK	v
ACKNOWLEDGEMENTS	vii
TABLE OF CONTENTS	vii
LIST OF FIGURES	xii
LIST OF TABLES	xviii
LIST OF SYMBOLS AND ABBREVIATIONS	xx
CHAPTER 1: INTRODUCTION	1
1.1 Background	1
1.2 Objectives of the Present Work.....	3
1.3 Organizing of the Thesis	4
CHAPTER 2: LITERATURE REVIEW	6
2.1 Polymer Electrolytes (PEs)	6
2.1.1 PVdC-co-AN copolymer -based electrolytes	8
2.1.2 Plasticizer/Plasticizing solvent	11
2.1.3 Plastic crystal succinonitrile (SN).....	14
2.1.4 Magnesium salt-based electrolytes	16
2.1.5 Rechargeable Batteries	18
2.1.5.1 Development of Magnesium Ion Rechargeable Batteries	21
CHAPTER 3: EXPERIMENTAL TECHNIQUES	24
3.1 Sample Preparation.....	24
3.2 Electrical and Electrochemical Properties	26

3.2.1	Impedance Spectroscopy	26
3.2.2	Transference Number	28
3.2.2.1	Ionic Transference Number, t_i	29
3.2.2.2	Cationic Transference Number, t_+	29
3.2.3	Linear Sweep Voltammetry (LSV)	30
3.2.4	Cyclic Voltammetry (CV)	31
3.3	Structural and Morphological Properties	32
3.3.1	Fourier Transform Infrared Spectroscopy (FTIR)	32
3.3.2	X-Ray Diffraction (XRD).....	33
3.4	Field Emission Scanning Electron Microscopy (FESEM)	35
3.5	Thermal Studies	36
3.5.1	Differential Scanning Calorimetry (DSC).....	36
3.6	Battery Fabrication	37
CHAPTER 4: ELECTRICAL AND TRANSPORT STUDIES		39
4.1	Ionic Conductivity Studies.....	39
4.1.1	Room Temperature Ionic Conductivity of Pure PVdC-co-AN and PVdC-co-AN with Varied Plasticizers.....	39
4.1.2	Room Temperature Ionic Conductivity of PVdC-co-AN/SN (single plasticized) and PVdC-co-AN/SN/EC (double plasticized) with Varied Magnesium Salts	43
4.1.2.1	PVdC-co-AN/SN/MgTf ₂ and PVdC-co-AN/SN/EC/MgTf ₂ systems.....	43
4.1.2.2	PVdC-co-AN/SN/Mg(TFSI) ₂ and PVdC-co- AN/SN/EC/Mg(TFSI) ₂ systems	46
4.1.3	Temperature-dependence Ionic Conductivity Studies	50

4.1.3.1	PVdC-co-AN/SN/MgTf ₂ and PVdC-co-AN/SN/EC/MgTf ₂ systems.....	50
4.1.3.2	PVdC-co-AN/SN/Mg(TFSI) ₂ and PVdC-co- AN/SN/EC/Mg(TFSI) ₂ systems	54
4.2	Transference Number.....	58
4.2.1	Ionic Transference Number, t_i	58
4.2.2	Cationic Transference Number, t_+	60
CHAPTER 5: STRUCTURAL AND MORPHOLOGICAL ANALYSIS		65
5.1	Fourier Transform Infrared Spectroscopy (FTIR) analysis	65
5.1.1	Pure PVdC-co-AN	65
5.1.2	PVdC-co-AN/SN/EC	67
5.1.3	PVdC-co-AN/SN/ MgTf ₂ and PVdC-co-AN/SN/EC/MgTf ₂ systems	72
5.1.4	PVdC-co-AN/SN/ Mg(TFSI) ₂ and PVdC-co-AN/SN/EC/Mg(TFSI) ₂ systems	80
5.1.5	Deconvolution of FTIR spectra	87
5.1.5.1	PVdC-co-AN/SN/MgTf ₂ and PVdC-co-AN/SN/EC/MgTf ₂ systems.....	87
5.1.5.2	PVdC-co-AN/SN/Mg(TFSI) ₂ and PVdC-co- AN/SN/EC/Mg(TFSI) ₂ systems	94
5.1.5.3	Determination of n , μ and D	101
5.2	X-Ray Diffraction.....	104
5.2.1	Pure PVdC-co-AN, SN and EC	104
5.2.2	PVdC-co-AN/SN/MgTf ₂ and PVdC-co-AN/SN/EC/MgTf ₂ systems ...	107
5.2.3	PVdC-co-AN/SN/Mg(TFSI) ₂ and PVdC-co-/SN/EC/Mg(TFSI) ₂ systems	110
5.3	Field Emission Scanning Electron Microscopy (FESEM)	113

CHAPTER 6: THERMAL ANALYSIS	116
6.1 Differential Scanning Calorimetry (DSC)	116
6.1.1 PVdC-co-AN/SN/MgTf ₂ and PVdC-co-AN/SN/EC/MgTf ₂	118
6.1.2 PVdC-co-AN/SN/Mg(TFSI) ₂ and PVdC-co-AN/SN/EC/Mg(TFSI) ₂ ...	121
CHAPTER 7: ELECTROCHEMICAL STUDIES AND BATTERY	
FABRICATION.....	125
7.1 Linear sweep voltammetry (LSV)	125
7.1.1 PVdC-co-AN/SN/MgTf ₂ and PVdC-co-AN/SN/EC/MgTf ₂	125
7.1.2 PVdC-co-AN/SN/Mg(TFSI) ₂ and PVdC-co-AN/SN/EC/Mg(TFSI) ₂ ..	127
7.2 Cyclic voltammetry.....	128
7.2.1 PVdC-co-AN/SN/MgTf ₂ and PVdC-co-AN/SN/EC/MgTf ₂	128
7.2.2 PVdC-co-AN/SN/Mg(TFSI) ₂ and PVdC-co-AN/SN/EC/Mg(TFSI) ₂ ..	132
7.3 Magnesium Rechargeable Batteries	135
7.3.1 Magnesium rechargeable battery containing PVdC-co-AN/SN/EC/30 wt.% MgTf ₂ based GPE	135
7.3.2 Magnesium rechargeable battery containing PVdC-co-AN/SN/EC/15 wt.% Mg(TFSI) ₂ based GPE.....	137
CHAPTER 8: CONCLUSIONS AND SUGGESTIONS FOR FUTURE WORK	140
8.1 Conclusions	140
8.2 Suggestions for Future Work	142
REFERENCES.....	144
LIST OF PUBLICATIONS AND PAPERS PRESENTED	159

LIST OF FIGURES

Figure 2.1	: Molecular structure of PVdC-co-AN (“Poly(vinylidene-chloride-co-acrylonitrile),” n.d.).....	9
Figure 2.2	: Molecular structure of Succinonitrile (SN) (“Succinonitrile,” n.d.).	15
Figure 2.3	: Schematic diagram of rechargeable battery during “charging” and “discharging” (“Li-ion Batteries in the Hot Seat (A Primer on the Science of Exploding Smartphones),” n.d.).....	19
Figure 2.4	: The growth of dendrites in rechargeable batteries (“Li-ion Batteries in the Hot Seat (A Primer on the Science of Exploding Smartphones),” n.d.).....	20
Figure 2.5	: Magnesium ion rechargeable battery diagram (Nguyen & Song, 2017).	22
Figure 3.1	: An example of impedance plot (Barsoukov & Macdonald, 2005).	27
Figure 3.2	: Schematic diagram of a three-electrode system (“Three electrode system,” n.d.).	31
Figure 3.3	: Block diagram of an FTIR Spectrometer (“How an FTIR Spectrometer Operates,” n.d.).	33
Figure 3.4	: X-Ray diffraction schematic diagram (“X-Ray Diffraction System,” n.d.).....	34
Figure 3.5	: Schematic diagram of FESEM (“Schematic-diagram-of-Field-Emission-Scanning-Electron-Microscope-FESEM,” n.d.).....	36
Figure 4.1	: Cole-Cole plot of pure PVdC-co-AN.....	41
Figure 4.2	: Cole-Cole plots of (a) PVdC-co-AN/SN, (b) PVdC-co-AN/SN/EC.	42
Figure 4.3	: Equivalent circuit in accordance of the impedance plots.	42
Figure 4.4	: Cole-Cole plots of (a) PVdC-co-AN/SN/30 wt.%MgTf ₂ and (b) PVdC-co-AN/SN/EC/30 wt.% MgTf ₂	45
Figure 4.5	: Ionic conductivity of GPE system of (a) PVdC-co-AN/SN/MgTf ₂ and (b) PVdC-co-AN/SN/EC/MgTf ₂	46
Figure 4.6	: Cole-Cole plots of (a) PVdC-co-AN/SN/20 wt.%Mg(TFSI) ₂ and (b) PVdC-co-AN/SN/EC/15 wt.% Mg(TFSI) ₂	48

Figure 4.7	: Ionic conductivity of GPE system of (a) PVdC-co-AN/SN/Mg(TFSI) ₂ and (b) PVdC-co-AN/SN/EC/Mg(TFSI) ₂	49
Figure 4.8	: Plot of log σ against 1000/T for PVdC-co-AN/SN samples containing 10 wt.%, 20 wt.% and 30 wt.% of MgTf ₂	52
Figure 4.9	: Plot of log σ against 1000/T for PVdC-co-AN/SN/EC samples containing 10 wt.%, 20 wt.% and 30 wt.% of MgTf ₂	52
Figure 4.10	: Plot of log $\sigma T^{1/2}$ against 1000/(T-T ₀) for PVdC-co-AN/SN samples containing 10 wt.%, 20 wt.% and 30 wt.% of MgTf ₂	53
Figure 4.11	: Plot of log $\sigma T^{1/2}$ against 1000/(T-T ₀) for PVdC-co-AN/SN/EC samples containing 10 wt.%, 20 wt.% and 30 wt.% of MgTf ₂	53
Figure 4.12	: Plot of log σ against 1000/T for PVdC-co-AN/SN samples containing 10 wt.%, 20 wt.% and 30 wt.% of Mg(TFSI) ₂	55
Figure 4.13	: Plot of log σ against 1000/T for PVdC-co-AN/SN/EC samples containing 10 wt.%, 15 wt.% and 30 wt.% of Mg(TFSI) ₂	56
Figure 4.14	: Plot of log $\sigma T^{1/2}$ against 1000/(T-T ₀) for PVdC-co-AN/SN samples containing 10 wt.%, 20 wt.% and 30 wt.% of Mg(TFSI) ₂	56
Figure 4.15	: Plot of log $\sigma T^{1/2}$ against 1000/(T-T ₀) for PVdC-co-AN/SN/EC samples containing 10 wt.%, 15 wt.% and 30 wt.% of Mg(TFSI) ₂	57
Figure 4.16	: Plot of normalized current against time for PVdC-co-AN/SN/30 wt.% MgTf ₂ and PVdC-co-AN/SN/EC/30 wt.% MgTf ₂	59
Figure 4.17	: Plot of normalized current against time for PVdC-co-AN/SN/20 wt.% Mg(TFSI) ₂ and PVdC-co-AN/SN/EC/15 wt.% Mg(TFSI) ₂	59
Figure 4.18	: DC polarization plots for GPE samples of (a) PVdC-co-AN/SN/30 wt.% MgTf ₂ and (b) PVdC-co-AN/SN/EC/30 wt.% MgTf ₂ . Inset graph shows the impedance plots (i) before and (ii) after DC polarization.	63
Figure 4.19	: DC polarization plots for GPE samples of (a) PVdC-co-AN/SN/20 wt.% Mg(TFSI) ₂ and (b) PVdC-co-AN/SN/EC/15 wt.% Mg(TFSI) ₂ . Inset graph shows the impedance plots (i) before and (ii) after DC polarization.	64
Figure 5.1	: FTIR spectra of pure PVdC-co-AN sample in the region of 800 cm ⁻¹ to 3200 cm ⁻¹	67
Figure 5.2	: FTIR spectra of pure SN in the region of 800 cm ⁻¹ to 3200 cm ⁻¹	69

Figure 5.3	: FTIR spectra of pure EC in the region of 800 cm ⁻¹ to 3200 cm ⁻¹	70
Figure 5.4	: FTIR spectra of (a) pure PVdC-co-AN, (b) PVdC-co-AN/SN and (c) PVdC-co-AN/SN/EC.	72
Figure 5.5	: FTIR spectrum of pure MgTf ₂	73
Figure 5.6	: FTIR spectra of PVdC-co-AN/SN containing (a) 5 wt.% MgTf ₂ , (b) 10 wt.% MgTf ₂ , (c) 15 wt.% MgTf ₂ , (d) 20 wt.% MgTf ₂ , (e) 25 wt.% MgTf ₂ and (f) 30 wt.% MgTf ₂	76
Figure 5.7	: The close up of nitrile band of PVdC-co-AN/SN containing (a) 5 wt.% MgTf ₂ , (b) 10 wt.% MgTf ₂ , (c) 15 wt.% MgTf ₂ , (d) 20 wt.% MgTf ₂ , (e) 25 wt.% MgTf ₂ and (f) 30 wt.% MgTf ₂	77
Figure 5.8	: FTIR spectra of PVdC-co-AN/SN/EC containing (a) 5 wt.% MgTf ₂ , (b) 10 wt.% MgTf ₂ , (c) 15 wt.% MgTf ₂ , (d) 20 wt.% MgTf ₂ , (e) 25 wt.% MgTf ₂ and (f) 30 wt.% MgTf ₂	78
Figure 5.9	: The close up of nitrile band of PVdC-co-AN/SN/EC containing (a) 5 wt.% MgTf ₂ , (b) 10 wt.% MgTf ₂ , (c) 15 wt.% MgTf ₂ , (d) 20 wt.% MgTf ₂ , (e) 25 wt.% MgTf ₂ and (f) 30 wt.% MgTf ₂	79
Figure 5.10	: FTIR spectrum of pure Mg(TFSI) ₂	81
Figure 5.11	: FTIR spectra of PVdC-co-AN/SN containing (a) 5 wt.% Mg(TFSI) ₂ , (b) 10 wt.% Mg(TFSI) ₂ , (c) 15 wt.% Mg(TFSI) ₂ , (d) 20 wt.% Mg(TFSI) ₂ , (e) 25 wt.% Mg(TFSI) ₂ and (f) 30 wt.% Mg(TFSI) ₂	83
Figure 5.12	: The close up of nitrile band of PVdC-co-AN/SN containing (a) 5 wt.% Mg(TFSI) ₂ , (b) 10 wt.% Mg(TFSI) ₂ , (c) 15 wt.% Mg(TFSI) ₂ , (d) 20 wt.% Mg(TFSI) ₂ , (e) 25 wt.% Mg(TFSI) ₂ and (f) 30 wt.% Mg(TFSI) ₂	84
Figure 5.13	: FTIR spectra of PVdC-co-AN/SN/EC containing (a) 5 wt.% Mg(TFSI) ₂ , (b) 10 wt.% Mg(TFSI) ₂ , (c) 15 wt.% Mg(TFSI) ₂ , (d) 20 wt.% Mg(TFSI) ₂ , (e) 25 wt.% Mg(TFSI) ₂ and (f) 30 wt.% Mg(TFSI) ₂	85
Figure 5.14	: The close up of nitrile band of PVdC-co-AN/SN/EC containing (a) 5 wt.% Mg(TFSI) ₂ , (b) 10 wt.% Mg(TFSI) ₂ , (c) 15 wt.% Mg(TFSI) ₂ , (d) 20 wt.% Mg(TFSI) ₂ , (e) 25 wt.% Mg(TFSI) ₂ and (f) 30 wt.% Mg(TFSI) ₂	86
Figure 5.15	: Deconvolution of FTIR spectra between 950 and 1150 cm ⁻¹ for PVdC-co-AN/SN with (a) 5 wt.% MgTf ₂ , (b) 10 wt.% MgTf ₂ ,	

(c) 15 wt.% MgTf ₂ , (d) 20 wt.% MgTf ₂ , (e) 25 wt.% MgTf ₂ and (f) 30 wt.% MgTf ₂	89
Figure 5.16 : Deconvolution of FTIR spectra between 950 and 1150 cm ⁻¹ for PVdC-co-AN/SN/EC with (a) 5 wt.% MgTf ₂ , (b) 10 wt.% MgTf ₂ , (c) 15 wt.% MgTf ₂ , (d) 20 wt.% MgTf ₂ , (e) 25 wt.% MgTf ₂ and (f) 30 wt.% MgTf ₂	90
Figure 5.17 : The relationship of (a) free ions, (b) ion pairs and (c) ion aggregates with ionic conductivity of PVdC-co-AN/SN/MgTf ₂ system.	92
Figure 5.18 : The relationship of (a) free ions, (b) ion pairs and (c) ion aggregates with ionic conductivity of PVdC-co-AN/SN/EC/MgTf ₂ system.	93
Figure 5.19 : Deconvoluted of FTIR spectra between 900 and 1500 cm ⁻¹ for PVdC-co-AN/SN with (a) 5 wt.% Mg(TFSI) ₂ , (b) 10 wt.% Mg(TFSI) ₂ , (c) 15 wt.% Mg(TFSI) ₂ , (d) 20 wt.% Mg(TFSI) ₂ , (e) 25 wt.% Mg(TFSI) ₂ and (f) 30 wt.% Mg(TFSI) ₂	96
Figure 5.20 : Deconvoluted of FTIR spectra between 900 and 1500 cm ⁻¹ for PVdC-co-AN/SN/EC with (a) 5 wt.% Mg(TFSI) ₂ , (b) 10 wt.% Mg(TFSI) ₂ , (c) 15 wt.% Mg(TFSI) ₂ , (d) 20 wt.% Mg(TFSI) ₂ , (e) 25 wt.% Mg(TFSI) ₂ and (f) 30 wt.% Mg(TFSI) ₂	97
Figure 5.21 : The relationship of (a) free ions, (b) ion pairs and (c) ion aggregates with ionic conductivity of PVdC-co-AN/SN/Mg(TFSI) ₂ system.	99
Figure 5.22 : The relationship of (a) free ions, (b) ion pairs and (c) ion aggregates with ionic conductivity of PVdC-co-AN/SN/EC/Mg(TFSI) ₂ system. ..	100
Figure 5.23 : X-Ray diffractogram of pure PVdC-co-AN.	105
Figure 5.24 : X-Ray diffractogram of (a) pure SN and (b) pure EC.....	106
Figure 5.25 : X-Ray diffractogram of (a) pure PVdC-co-AN, (b) PVdC-co-AN/SN, (c) PVdC-co-AN/EC and (d) PVdC-co-AN/SN/EC.	106
Figure 5.26 : X-Ray diffractogram of pure MgTf ₂	107
Figure 5.27 : X-Ray diffractograms of PVdC-co-AN/SN containing 10 wt.%, 20 wt.% and 30 wt.% MgTf ₂	108
Figure 5.28 : X-Ray diffractograms of PVdC-co-AN/SN/EC containing 10 wt.%, 20 wt.% and 30 wt.% MgTf ₂	109
Figure 5.29 : X-Ray diffractograms of PVdC-co-AN, PVdC-co-AN/SN and PVdC-co-AN/SN/EC containing 30 wt.% MgTf ₂	109

Figure 5.30 : X-Ray diffractogram of pure Mg(TFSI) ₂ salt.	110
Figure 5.31 : X-Ray diffractograms of PVdC-co-AN/SN containing 10 wt.%, 20 wt.% and 30 wt.% Mg(TFSI) ₂	111
Figure 5.32 : X-Ray diffractograms of PVdC-co-AN/SN/EC containing 10 wt.%, 15 wt.% and 30 wt.% Mg(TFSI) ₂	112
Figure 5.33 : PVdC-co-AN, PVdC-co-AN/SN and PVdC-co-AN/SN/EC containing 20 wt.% Mg(TFSI) ₂	112
Figure 5.34 : FESEM micrographs of (a) pure PVdC-co-AN (b) PVdC-co-AN/SN and (c) PVdC-co-AN/SN/EC samples.	114
Figure 5.35 : FESEM micrographs of (a) PVdC-co-AN/SN/30 wt.% MgTf ₂ and (b) PVdC-co-AN/SN/EC30 wt.% MgTf ₂	115
Figure 5.36 : FESEM micrographs of (a) PVdC-co-AN/SN/20 wt.% Mg(TFSI) ₂ and (b) PVdC-co-AN/SN/EC/15 wt.% Mg(TFSI) ₂	115
Figure 6.1 : DSC curves of pure PVdC-co-AN, PVdC-co-AN/SN and PVdC-co- AN/SN/EC samples.....	117
Figure 6.2 : DSC curves of PVdC-co-AN/SN/10 wt.% MgTf ₂ , PVdC-co-AN/SN/20 wt.% MgTf ₂ and PVdC-co-AN/SN/30 wt.% MgTf ₂ samples at a temperature range of -40 °C to 60 °C.	119
Figure 6.3 : DSC curves of PVdC-co-AN/SN/EC/10 wt.% MgTf ₂ , PVdC-co- AN/SN/EC/20 wt.% MgTf ₂ and PVdC-co-AN/SN/EC/30 wt.% MgTf ₂ samples at a temperature range of -40 °C to 60 °C.	120
Figure 6.4 : DSC curves of PVdC-co-AN/SN/10 wt.% Mg(TFSI) ₂ , PVdC-co- AN/SN/20 wt.% Mg(TFSI) ₂ and PVdC-co-AN/SN/30 wt.% Mg(TFSI) ₂ samples at a temperature range of -40 °C to 60 °C.	123
Figure 6.5 : DSC curves of PVdC-co-AN/SN/EC/10 wt.% Mg(TFSI) ₂ , PVdC-co- AN/SN/EC/20 wt.% Mg(TFSI) ₂ and PVdC-co-AN/SN/EC/30 wt.% Mg(TFSI) ₂ samples at a temperature range of -40 °C to 60 °C.	123
Figure 7.1 : The linear voltammogram of (a) PVdC-co-AN/SN/30 wt.% MgTf ₂ and (b) PVdC-co-AN/SN/EC/30 wt.% MgTf ₂	126
Figure 7.2 : The linear voltammogram of (a) PVdC-co-AN/SN/20 wt.% Mg(TFSI) ₂ and (b) PVdC-co-AN/SN/EC/15 wt.% Mg(TFSI) ₂	127
Figure 7.3 : The cyclic voltammograms of (a) Cell-I: SS/GPE/SS and (b) Cell-II: Mg/GPE/Mg for PVdC-co-AN/SN/30 wt.% MgTf ₂ sample.....	130

Figure 7.4	: The cyclic voltammograms of (a) Cell-I: SS/GPE/SS and (b) Cell-II: Mg/GPE/Mg for PVdC-co-AN/SN/EC/30 wt.% MgTf ₂ sample.....	131
Figure 7.5	: The cyclic voltammograms of (a) Cell I: SS/GPE/SS and (b) Cell II: Mg/GPE/Mg for PVdC-co-AN/SN/20 wt.% Mg(TFSI) ₂ sample.	133
Figure 7.6	: The cyclic voltammograms of (a) Cell I: SS/GPE/SS and (b) Cell II: Mg/GPE/Mg for PVdC-co-AN/SN/EC/15 wt.% Mg(TFSI) ₂ sample. ...	134
Figure 7.7	: Discharge voltage against specific capacity for magnesium battery containing PVdC-co-AN/SN/EC/30 wt.% MgTf ₂	136
Figure 7.8	: Specific capacity against cycle number for magnesium battery containing PVdC-co-AN/SN/EC/30 wt.% MgTf ₂	136
Figure 7.9	: Discharge voltage against specific capacity for magnesium battery containing PVdC-co-AN/SN/EC/15 wt.% Mg(TFSI) ₂	138
Figure 7.10	: Specific capacity against cycle number for magnesium battery containing PVdC-co-AN/SN/EC/15 wt.% Mg(TFSI) ₂	139

LIST OF TABLES

Table 2.1	: Physical properties of some plasticizers commonly used in polymer matrices (Song et al., 2000; Stephan, 2006).	12
Table 3.1	: Compositions of the samples.	24
Table 3.2	: Compositions of GPE samples with magnesium salts.....	25
Table 4.1	: The ionic conductivity of samples with varied plasticizers.	42
Table 4.2	: Ionic conductivity of GPEs with MgTf ₂ salt.	45
Table 4.3	: Ionic conductivity of GPEs with Mg(TFSI) ₂ salt.	49
Table 4.4	: The VTF parameters for PVdC-co-AN/SN/MgTf ₂ and PVdC-co-AN/SN/EC/MgTf ₂ systems.	54
Table 4.5	: The VTF parameters for PVdC-co-AN/SN/Mg(TFSI) ₂ and PVdC-co-AN/SN/EC/Mg(TFSI) ₂ systems.	57
Table 4.6	: Ionic transference number of GPE samples for MgTf ₂ and Mg(TFSI) ₂ systems.	60
Table 4.7	: Magnesium ion transference number of GPE samples for MgTf ₂ and Mg(TFSI) ₂ systems.....	62
Table 5.1	: The vibrational modes and corresponding wavenumbers of pure PVdC-co-AN.	66
Table 5.2	: The vibrational modes and corresponding wavenumbers of pure SN.....	68
Table 5.3	: The vibrational modes and corresponding wavenumbers of pure EC.....	70
Table 5.4	: The vibrational modes and corresponding wavenumbers of pure MgTf ₂	73
Table 5.5	: The vibrational modes and corresponding wavenumbers of pure Mg(TFSI) ₂	80
Table 5.6	: The integrated area of free ions, ion pairs and ion aggregates bands correspond to Tf ₂ ⁻ ions in PVdC-co-AN/SN/MgTf ₂ system.	91
Table 5.7	: The integrated area of free ions, ion pairs and ion aggregates bands correspond to Tf ₂ ⁻ ions in PVdC-co-AN/SN/EC/MgTf ₂ system.	91

Table 5.8	: The integrated area of free ions, ion pairs and ion aggregates bands correspond to TFSI ⁻ ions in PVdC-co-AN/SN/Mg(TFSI) ₂ system.	98
Table 5.9	: The integrated area of free ions, ion pairs and ion aggregates bands correspond to TFSI ⁻ ions in PVdC-co-AN/SN/EC/Mg(TFSI) ₂ system.	98
Table 5.10	: The values of n , μ and D for PVdC-co-AN/SN/MgTf ₂ system.....	102
Table 5.11	: The values of n , μ and D for PVdC-co-AN/SN/EC/MgTf ₂ system.....	103
Table 5.12	: The values of n , μ and D for PVdC-co-AN/SN/Mg(TFSI) ₂ system.....	103
Table 5.13	: The values of n , μ and D for PVdC-co-AN/SN/EC/Mg(TFSI) ₂ system.	104
Table 6.1	: Glass transition temperature and ionic conductivity of unsalted GPEs.....	117
Table 6.2	: T_g values for GPE samples in PVdC-co-AN/SN/MgTf ₂ and PVdC-co-AN/SN/EC/MgTf ₂ systems.	120
Table 6.3	: T_g values for GPE samples in PVdC-co-AN/SN/Mg(TFSI) ₂ and PVdC-co-AN/SN/EC/Mg(TFSI) ₂ systems.	124

LIST OF SYMBOLS AND ABBREVIATIONS

ARPA-E	:	Advanced Research Project Agency - Energy
AC	:	Alternating current
v_{as}	:	Asymmetrical stretching
R_b	:	Bulk resistance
t_+	:	Cationic transference number
R_s	:	Cell resistance after polarization
R_0	:	Cell resistance before polarization
q	:	Charge
CPEs	:	Composite polymer electrolytes
σ	:	Conductivity
I	:	Current
CV	:	Cyclic voltammetry
DEC	:	Diethyl carbonate
DSC	:	Differential scanning calorimetry
D	:	Diffusion coefficient
DMC	:	Dimethyl carbonate
DMP	:	Dimethyl phthalate
DC	:	Direct current
i_e	:	Electronic current
t_e	:	Electronic transference number
EC	:	Ethylene carbonate
EV	:	Electric vehicles
FESEM	:	Field emission scanning electron microscopy
I_s	:	Final current

FTIR	:	Fourier transform infrared spectroscopy
HEV	:	Hybrid electric vehicles
T_{cp}	:	From normal crystal to plastic crystal temperature
GPEs	:	Gel polymer electrolytes
T_g	:	Glass transition temperature
Z_i	:	Imaginary impedance
I_0	:	Initial current
t_i	:	Ionic transference number
LSV	:	Linear sweep voltammetry
LIBs	:	Li-ion batteries
Li	:	Lithium
Li^+	:	Lithium ions
LiBETI	:	Lithium bis(pentafluoroethanesulfonyl) imide
LiTFSI	:	Lithium bis(trifluoromethanesulfonyl) imide
$LiPF_6$:	Lithium hexafluorophosphate
$LiClO_4$:	Lithium perchlorate
$LiBF_4$:	Lithium tetrafluoroborate
$LiCF_3SO_3$:	Lithium trifluoromethanesulfonate
Mg	:	Magnesium
$Mg(TFSI)_2$:	Magnesium bis(trifluoromethanesulfonimide)
$Mg(BH_4)_2$:	Magnesium borohydride
Mg^{2+}	:	Magnesium ions
MgO	:	Magnesium oxide
$Mg(ClO_4)_2$:	Magnesium perchlorate
$MgTf_2$:	Magnesium trifluoromethanesulfonate
MIT	:	Massachusetts Institute of Technology

T_m	:	Melting temperature
μ	:	Mobility
N	:	Number density
OCV	:	Open circuit voltage
PCE	:	Plastic crystal electrolyte
PAN	:	Polyacrylonitrile
PEO	:	Polyethylene oxide
PGMA	:	Poly glycidyl methacrylate
PEs	:	Polymer electrolytes
PMMA	:	Poly (methyl metacrylate)
PVC	:	Poly(vinyl chloride)
PVdC-co-AN	:	Polyvinylidene chloride co acrylonitrile
PVdF	:	Poly(vinylidene fluoride)
PVdF-HFP	:	Poly(vinylidene fluoride-co-hexafluoropropylene)
PC	:	Propylene carbonate
Z_r	:	Real impedance
SiO_2	:	Silicon dioxide
SEI	:	Solid electrolyte interface
SN	:	Succinonitrile
δ_s	:	Symmetrical bending
ν_s	:	Symmetrical stretching
Θ	:	Theta
TG/DTA	:	Thermogravimetry/Differential Thermal Analysis
TiO_2	:	Titanium dioxide
i_T	:	Total current
V	:	Voltage

V_2O_5	:	Vanadium(V) oxide
VTF	:	Vogel-Tamman-Fulcher
λ	:	Wavelength
XRD	:	X-Ray diffraction

Universiti Malaya

CHAPTER 1: INTRODUCTION

1.1 Background

At present, energy storage devices such as rechargeable batteries, supercapacitors, solar cells and electrochromic displays have been a great interest globally. Due to the fact that the increasing in demands of products like mobile phones, notebooks, personal computers, and digital cameras, many research efforts are focusing on the development of rechargeable batteries as they have many desirable features including light weight, high energy densities, high open-circuit potentials, fast charging and low self-discharge rates (Balasubramanian et al., 2001; Young et al., 2014). Moreover, they also exhibit excellent prospects for applications in electric vehicles (EV), hybrid electric vehicles (HEV), aviation technology and energy storage apparatus (Long et al., 2016). Currently, rechargeable Li-ion batteries (LIBs) have conquered the growth of the market of these popular devices and vehicles in view of its specific capacity and cycle stability (Pandey & Hashmi, 2009; Tarascon & Armand, 2001). However, while promising for several applications, these LIBs suffer from many drawbacks which are relatively expensive due to high demand of lithium and have some safety issues because of the use of flammable and reactive Li-ion conducting liquids as electrolyte. In this regard, magnesium ion rechargeable battery system has gained considerable popularity as an alternative way since they offer to provide the best economical solutions for electrical storage with performance capabilities closed to lithium (Asmara et al., 2011; Pandey & Hashmi, 2009). These are due to the abundance of magnesium in the earth's crust hence more affordable than lithium, low in atomic weight, environmentally benign (less reactive than lithium), electrochemically active (equivalent weight 12.15/Faraday) in nature and can also serve as a potential negative electrode (electrochemical potential -2.37 V vs. standard hydrogen electrode) (Kumar & Munichandraiah, 2000a; Oh et al., 2004; Saha et al., 2014).

Meanwhile, in order to improve more on safety issues, the conception of polymer electrolytes (PEs) is a highly specialized and multidisciplinary field that covers the disciplines of electrochemistry, polymer science, organic and inorganic chemistry (Aziz, 2013; Aziz et al., 2018). Polymer electrolytes are promising materials for electrochemical device applications, particularly rechargeable batteries. These dry solid polymer electrolytes (SPEs) have attracted great attention as safer alternatives to liquid electrolytes regarding some concerns on the leakage of liquid electrolyte in electronic devices and the resulting fire hazards (Li et al., 2016). Gel polymer electrolyte (GPE) on the other hand, is a hybrid electrolyte material, that combined both characteristics of solid electrolyte and liquid electrolyte to improve safety, less reactivity, high flexibility, leakage proof, good interface stability and better manufacturing integrity (Tang et al., 2016). Consequently, gel polymer electrolytes (GPEs) have received high consideration as they are found to be more attractive due to these characteristics. There are various research works have been made and examples of polymer host that successfully prepared into GPE are polyethylene oxide (PEO) (Cheng et al., 2007), poly (methyl metacrylate) (PMMA) (Othman et al., 2007) and poly(vinylidene fluoride-co-hexafluoropropylene) (PVdF-HFP) (Isa et al., 2014) and they showed promising properties of polymer electrolytes.

Nevertheless, despite the success of GPEs, most GPEs have low in mechanical properties due to the impregnation of large amount of liquid electrolytes into the polymer matrix (Fan et al., 2009; Yang et al., 2006). It is well known that the addition of plasticizer/plasticizing solvent decreased the mechanical strength of the polymer electrolyte; i.e. free standing film is hardly to achieve, although produced high in ionic conductivity (Ahmad et al., 2006; Deka & Kumar, 2011; Patel et al., 2008; Stephan & Nahm, 2006). Thus, a new material has been introduced which is succinonitrile (SN), a typical plastic crystal material. This material possesses high dielectric constant (~ 55), low melting temperature (~ 54 °C), and has plasticizing property whereby the trans-

isomers act as impurities that create mono-vacancies in the lattice and hence lead to high molecular diffusivity (Gupta & Rhee, 2012). The incorporation of SN also proposed a balance between their mechanical properties and electrochemical performance (Lu et al., 2013). This argument might be the reason for the introducing of SN which it has high dissociating ability, coupled with producing stable mechanical properties of the polymer electrolyte film.

In this work, SN is used as a plasticizer in the polymer electrolytes system. The plastic crystal-gel polymer electrolytes (GPEs) have been prepared which composed of poly(vinylidene chloride-co-acrylonitrile) (PVdC-co-AN) as the polymer host. This work also involves the incorporation of plasticizer ethylene carbonate (EC) into the plasticized PVdC-co-AN system; the use of double plasticizers gave significant improvement in ionic conductivity as our previous work (Chong & Osman, 2014). On preparing the GPEs, two types of magnesium salts are used which are magnesium trifluoromethanesulfonate (MgTf_2) and magnesium bis(trifluoromethanesulfonimide) ($\text{Mg}(\text{TFSI})_2$) and the concentration of each salt is varied in the GPE system. The effects of the salts on ionic conductivity, transport properties, electrochemical, structural and thermal properties will be analyzed and discussed. The GPEs with the optimum conductivity will then being utilized in the fabrication of magnesium rechargeable batteries and the performance will be investigated.

1.2 Objectives of the Present Work

In general, the purpose of this work is to explore new types of gel polymer electrolytes (GPEs) consist of PVdC-co-AN as the polymer host with plastic crystal succinonitrile (SN) (single plasticized system) and a combination of SN with ethylene carbonate (EC) (double plasticized system). Four systems are eventually prepared in this study by using

two types of magnesium salts which are magnesium trifluoromethanesulfonate (MgTf_2) and magnesium bis(trifluoromethanesulfonimide) ($\text{Mg}(\text{TFSI})_2$). The objectives of this study are specifically as follows:

- i. To determine the relationship between ionic conductivity, structural, thermal and electrochemical properties of the magnesium based plastic crystal-GPEs.
- ii. To investigate the effects of various magnesium salts concentrations on the conduction mechanisms of the GPEs.
- iii. To compare the transport properties of GPEs containing MgTf_2 and $\text{Mg}(\text{TFSI})_2$ salts.
- iv. To evaluate the performance of magnesium batteries that use the optimized GPEs as electrolytes.

1.3 Organizing of the Thesis

This thesis comprised the study of electrical, transport, electrochemical, structural, thermal and surface morphological properties of PVdC-co-AN based gel polymer electrolytes (GPEs). It is organized into eight chapters. The first chapter describes on the general introduction of the research work. The background of the research, the objectives of this work and the organization of the thesis are also included here.

Chapter two discusses briefly about polymer electrolytes and other works that have been done by other research groups. The properties and chemical structures of materials used for this present work are also described. The application of the prepared GPEs is further designated in the last part of this chapter.

Chapter three illustrates the sample preparation method and various experimental techniques that have been employed to prepare and study the properties of GPEs. The

techniques are Impedance Spectroscopy (IS), Transference Number Measurements, Linear Sweep Voltammetry (LSV), Cyclic Voltammetry (CV), Fourier Transform Infrared Spectroscopy (FTIR), X-Ray Diffraction (XRD), Field Emission Scanning Electron Microscopy (FESEM) and Differential Scanning Calorimetry (DSC). The working principle of the experiment used in the techniques are also been reviewed.

The results and analysis are presented in chapter four to seven and discussed according to their characterization techniques and properties of GPEs. In chapter four, the results of impedance spectroscopy and transference number measurements are studied to investigate the electrical and transport properties of GPEs. Chapter five explored on structural and morphological properties of prepared GPEs through FTIR, XRD, and FESEM. For chapter six, DSC profiles are examined to determine the thermal properties of GPEs. Meanwhile, the electrochemical properties of GPEs are discussed in chapter seven via LSV and CV experiments. The performances of the batteries fabricated using the most optimum GPEs are also discussed at the end of this chapter.

Finally, chapter eight concludes the findings throughout the study with some suggestions for future work.

CHAPTER 2: LITERATURE REVIEW

2.1 Polymer Electrolytes (PEs)

Polymer electrolyte (PE) generally defined as a membrane that possesses transport properties comparable with that of common liquid ionic solutions (Hallinan & Balsara, 2013; Stephan, 2006). Basically, polymer electrolyte is a solvent-free system whereby the ionically conducting pathway is generated by dissolving the low lattice energy metal salts in a high molecular weight polymer matrix. In 1973, Fenton et al. (Fenton et al., 1973) was the first research group to discover that alkali salts could be dissolved in poly(ethylene oxide) (PEO), thereby opening up the field of dry polymer electrolytes.

The idea of polymer electrolyte is actually to replace the conventional liquid electrolyte/electrolyte solvent that has many disadvantages especially in rechargeable batteries application. Liquid electrolytes relatively have poor physical and chemical stability, have to rely on the formation of “solid electrolyte interface” (SEI) layer, may have both ions and electrons conduction and have high possibility of leakage and explosion and these become the drawbacks in electrolytes field. Furthermore, an ideal and safe electrolyte solvent should be inert to all cell components especially positive and negative electrode materials and the current collectors which it is hardly to be achieved when using liquid electrolytes (Marcinek et al., 2015). Polymer based electrolytes on the other hand, offer few advantages over its counterpart – liquid electrolytes, such as no internal short circuit, no electrolyte leakage, and the absence of any combustible reaction products that often exist at the electrode/electrolyte interfaces (Saha et al., 2014). Hence, polymer electrolytes are more preferable than liquid electrolytes and other advantages of polymer electrolytes are listed as below (Marcinek et al., 2015):

- shape flexibility
- non-volatility

- lowering the cell weight
- improved shock resistance
- viability of metallic lithium as a negative electrode in secondary cells (lithium dendrites growing on the electrode surface would be stopped by the polymer electrolyte)
- fabrication of cell would be easier hence cheaper

The pre-requisite criteria for the membrane material of polymer electrolytes are (i) adequate ionic conductivity for practical purposes, (ii) decent mechanical strength/integrity of polymer or gel, (iii) high transference number, and (iv) high electrochemical stability and compatibility with electrodes (Stephan, 2006). Since 1978, when Michel Armand first introduced poly(ethylene oxide) (PEO)–alkali–metal salt complexes to the solid state community as a potential material for electrochemical devices, there are tremendous amount of research carried out after that on these (particularly poly(ethylene oxide)–lithium salt systems), to obtain a better understanding of their fundamental properties (Armand, 1983; Armand et al., 1979). Researches also want to develop new generations of polymer electrolyte materials that are commercially more attractive as well as to achieve the required properties as efficient electrolytes in devices. Therefore, many types of polymer have been studied which are poly(ethylene oxide) (PEO) (Andreev & Bruce, 2000; Appetecchi et al., 2000; Bruce, 1995; Bruce et al., 1995; Communication et al., 1995), poly (methyl methacrylate) (PMMA) (Frاند et al., 1993; Osman et al., 2012; Othman et al., 2013; Rajendran et al., 1999), poly(vinyl chloride) (PVC) (Alamgir & Abraham, 1993; Rajendran & Uma, 2000; Ramesh et al., 2002), poly(vinylidene fluoride) (PVdF) (Muniyandi et al., 2001; Tsuchida & Ohno, 1983) and polyacrylonitrile (PAN) (Abraham & Alamgir, 1989; Chong & Osman, 2014; Reich & Michaeli, 1975; Watanabe et al., 1983).

In polymer electrolytes field, there are actually three types of polymer electrolytes which are solid polymer electrolytes (SPEs), gel polymer electrolytes (GPEs) and composite polymer electrolyte (CPEs). The preparation of polymer electrolytes started with solid polymer electrolytes but inadequate values of conductivity of SPEs developed the introduction of gel polymer electrolytes and these GPEs became greatly preferable since then (Osman et al., 2014; Othman et al., 2017; Pandey et al., 2009; Saikia & Kumar, 2004). GPEs possess both cohesive properties of solids and the diffusive property of liquids and the unique characteristics of GPEs are usually obtained by incorporating a large quantity of liquid plasticizer and or solvents to a polymer matrix that is capable of forming a stable gel with polymer host structure (Song et al., 1999). However, GPEs are said to lose their mechanical strength when they were plasticized (Angulakshmi et al., 2013). Thus, the third type of polymer electrolytes which is composite polymer electrolytes (CPEs) was introduced with an idea of incorporating electrochemically inert fillers such as silicon dioxide (SiO_2) and titanium dioxide (TiO_2) into polymer matrices (Cao et al., 2013; Kumar & Hashmi, 2010) to improve the mechanical stability of the free standing films (Boaretto et al., 2020).

2.1.1 PVdC-co-AN copolymer -based electrolytes

The requirements of the polymer electrolytes to give their best performance in electrochemical devices are strictly hard to achieve. Therefore, there are several methods have been introduced due to this matter. One of that is the use of copolymer as polymer matrix in polymer-based electrolytes system. The difference between co-polymer and common polymer is that it is made between two or more different types of monomers while polymer is formed from the joining together of the same type of monomers. The process involves a process called copolymerization which is the polymerizing between

two different monomers simultaneously, resulting in the incorporating both of the structures into a single polymer chain. This significantly increases the range and diversity of properties of copolymer molecules, and allows for the integration of desirable properties from differing monomer units (which can be useful for many applications) (Scott & Penlidis, 2017). Poly(vinylidene fluoride–hexafluoropropylene) (P VdF–HFP) is a well known copolymer that has been used in these past few years as an electrolyte (Saikia & Kumar, 2004; Stephan et al., 2006). They obtained high in ionic conductivity as well as improved in mechanical and electrochemical stability. In 2013, there is a new copolymer introduced which is Poly(vinylidene-chloride-co-acrylonitrile) (PVdC-co-AN) (Shanthi et al., 2013a). It is a type of copolymer made by the process of copolymerization between the monomers of vinylidene chloride with acrylonitrile. The molecular structure of PVdC-co-AN is as shown in Figure 2.1.

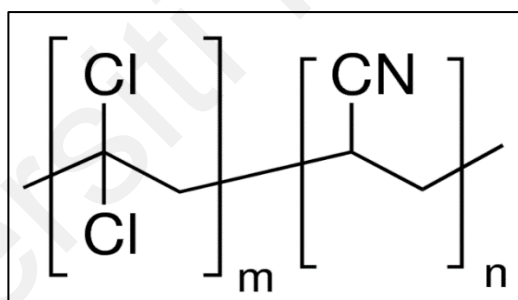


Figure 2.1: Molecular structure of PVdC-co-AN (“Poly(vinylidene-chloride-co-acrylonitrile),” n.d.).

The characteristics of PVdC-co-AN are (“Poly(vinylidene-chloride-co-acrylonitrile),” n.d.):

- has glass transition temperature, T_g of 50 °C
- has amorphous density of 1.6 g cm⁻³ at 25 °C
- has molecular weight of 150000 g mol⁻¹

Several works on preparing PVdC-co-AN based electrolytes have been reported since the work by Shanthi et al. (Shanthi et al., 2013a). In this pioneer work, solid polymer electrolytes composed of PVdC-co-AN dissolved with LiBF₄ have been prepared. The structural properties of the SPEs have been studied whereby the interaction of nitrile groups C≡N of PVdC-co-AN with Li⁺ ions and the complexation of the polymer with the salt were analyzed by FTIR analysis. Building of the amorphous phase in the complex matrix was also studied and confirmed by XRD studies. The change of T_g with respect to the LiBF₄ concentration and its major effect on the ionic conductivity were also studied using DSC analysis. It has been found that the maximum room temperature ionic conductivity is in the order of 10^{-4} S cm⁻¹ while the temperature dependent ionic conductivity of the sample indicates that the sample obtained is desirable for using as electrolyte in the electrochemical applications.

Whereas, in 2015, there is a work on preparation of PVdC-co-AN blended with PMMA based gel polymer electrolytes (Mathew et al., 2015). This new GPE system obtained maximum ionic conductivity value of 0.398×10^{-6} S cm⁻¹ with the addition of 60 wt.% of EC to PVdC-AN/PMMA blend. The increase of temperature on the other hand, non-linearly increases the ionic conductivity of polymer complex over the studied temperature range.

In addition, the preparation of PVdC-co-AN/PEO blend doped with different lithium salts which are LiBF₄, LiClO₄ and LiCF₃SO₃ (Shanthi et al., 2017) has also been carried out. They obtained maximum conductivity up to 10^{-3} S cm⁻¹ at room temperature with good mechanical stability has been observed from PVdC-co-AN(92)-EC-(80) - LiClO₄(8) system. The thermal stability of this polymer electrolyte system is up to 268 °C which is being confirmed by TG/DTA analysis.

Other works on PVdC-co-AN are the preparation of PVdC-co-AN/PEO-LiClO₄ based gel polymer electrolytes with different plasticizers (Subbu et al., 2016) and preparation of system of PVdC-co-AN/PMMA-LiClO₄-ZrO₂ composite polymer electrolytes (Shanthi et al., 2017). As a whole, to date, all the prepared electrolytes with PVdC-co-AN as the host polymer were only dissolved with lithium salts, neither in magnesium salt nor other alkali/alkaline earth metals based-salt.

2.1.2 Plasticizer/Plasticizing solvent

Crystallinity and segmental motion were identified as main parameters that decide the ionic conductivity of polymer electrolyte systems and therefore, it was tempting to use additives. The additive is the plasticizer or plasticizing solvent usually an organic solvent that will be added directly into the polymer matrix. Addition of plasticizer resulted in the lowering of the glass transition temperature, effective dissociation of the salt, and enhancement in the electrical conductivity (Hambali et al., 2016; M. Kumar & Sekhon, 2002; Pradhan et al., 2011). The increase in conductivity was mainly attributed to the reduction of crystallinity and increasing of free volume of the system. The degree of amorphousness which predominantly controls the ion conduction in the polymer complex can also be greatly enhanced (Hambali et al., 2016).

Therefore, the use of plasticizer in improving the ionic conductivity of polymer electrolytes is in the following ways (Kumar & Sekhon, 2002):

- by increasing the amorphous content of polymer electrolytes—at all salt concentrations;
- by dissociating ion aggregates present in polymer electrolytes—dominant at higher salt concentrations;
- by lowering the glass transition temperature T_g .

Due to this, the plasticizer used should have the following properties (Kumar & Sekhon, 2002):

- dielectric constant should be higher than that of the polymer used
- good miscibility with polymer electrolytes
- low volatility
- stability towards electrode materials
- low freezing temperature
- high boiling temperature

There are many types of plasticizers that have been used in polymer electrolytes system. Table 2.1 shows the physical properties of some plasticizers commonly used.

Table 2.1: Physical properties of some plasticizers commonly used in polymer matrices (Song et al., 2000; Stephan, 2006).

	Melting point, MP (°C)	Boiling point, BP (°C)	Density (g cm ⁻³)	Dielectric constant, ε	Molecular weight	Solubility parameter (J cm ⁻³) ^{1/2}
Dimethyl carbonate (DMC)	2.4	90	1.06	3.12	90.08	20.3
Diethyl carbonate (DEC)	43.0	126	0.9752	2.82	118.13	18.0
Propylene carbonate (PC)	48.8	242	1.2047	66.14	102.09	27.2
Ethylene carbonate (EC)	36.4	248	1.3214	89.78	88.06	30.1

In polymer electrolyte system, the most commonly used plasticizer is ethylene carbonate (EC). The incorporation of EC into the polymer electrolytes system has been

worked effectively with many types of polymers such as the research done by Imperiyka et al. (Imperiyka et al., 2014). They proved that the conductivity of the system increased with EC concentration and reached a maximum value of $2.0 \times 10^{-4} \text{ S cm}^{-1}$ when 80 wt.% of EC concentration was added into the poly glycidyl methacrylate (PGMA) system. This is due to the high value of dielectric constant of EC which reduces the inter-ion coulomb interactions and cohesive forces between the polymer chains and therefore increase the chain segmental mobility. Consequently, the lithium ions contribution to the conductivity will be increased. Other research work is done by Shanti et al. (Shanthi, Ramachandran, et al., 2017) by using PVdC-co-AN as the polymer host and obtained highest conductivity of $6.726 \times 10^{-3} \text{ S cm}^{-1}$ at room temperature with good mechanical stability observed for PVdC-co-AN (92)-EC (80)-LiClO₄(8) system.

Other than that, propylene carbonate (PC) is another plasticizer that is also widely used as the additive in polymer electrolyte system. For example, fast ion transport has been found in PMMA-LiClO₄-PC gel polymer electrolytes, i.e. from 10^{-4} to $10^{-3} \text{ S cm}^{-1}$ at room temperature (Frاند et al., 1993). Meanwhile, research done by Das & Ghosh shows that the addition of PC in the PEO-LiClO₄ polymer electrolyte decreases the crystallinity in the PEO polymer matrix. They found out that the content of free ions increases up to 40 wt.% of PC, thus increasing the ionic conductivity, while for the higher content of PC which is beyond 40 wt. %, the contribution of ion-pairs and ion-aggregates dominates leading to a decrease in the conductivity. The dielectric constants also increase with the addition of PC in the polymer electrolyte system (Das & Ghosh, 2015).

In addition, there is also other plasticizer that works on polymer which is dimethyl phthalate (DMP). Research done by Rajendran et al. (Rajendran et al., 2002) shows that by adding DMP into the PMMA/PVDF-LiClO₄ system, the conductivity increases with the increase in the concentration of DMP. They claimed that, the purpose of adding

plasticizers is to increase the free volume of the polymer electrolytes and hence increase the overall ionic mobility which enhances the ionic conductivity (Hambali et al., 2016).

However, the most well known research on addition of plasticizers in the polymer matrices is actually the use of two different types of plasticizers in a single polymer electrolyte system. The use of double plasticizers is mainly because of the argument by Pistoia et al. (Pistoia et al., 1970) who discovered the advantages of binary plasticizers and the good combination of plasticizers will not only improve the ion dissociation but also balancing their unique characteristics and at the same time improve the interfacial properties (Hambali et al., 2018). For examples, the used of both EC and PC in polymer electrolytes system (Ericson et al., 2000; Kumar & Munichandraiah, 2000b; Osman et al., 2014; Othman et al., 2017; Pandey et al., 2009; Saikia et al., 2011; Zainol et al., 2013) EC and DMP (Chong & Osman, 2014), PC and DEC (Saikia & Kumar, 2004), and EC and DEC (Asmara et al., 2011; Zugmann et al., 2011).

2.1.3 Plastic crystal succinonitrile (SN)

Apart from various attractive properties, the use of plasticizers in polymer electrolytes system actually suffer from few drawbacks such as (i) poor dimensional and mechanical stability, (ii) interfacial instability towards cathode materials and (iii) lower liquid retention capacity (Kumar & Hashmi, 2010). Recently, a plastic crystal electrolyte (PCE) (Liu et al., 2016), which is composed of lithium salts and plastic crystals with solvation capability, have been received considerable attentions due to their unique characteristics of soft matters (Singh et al., 2015; Taib & Hayati, 2014). Plastic crystal is a kind of mesophase formed predominantly by quasi-spherical or disk-like molecules demonstrating rotational and/or orientational disorder while preserving a long-range translational order (Alarco et al., 2004a). One representative example is the succinonitrile

($\text{N}\equiv\text{C}-\text{CH}_2-\text{CH}_2-\text{C}\equiv\text{N}$), (Figure 2.2) which is a solid organic non-ionic plastic material, where the impurity ‘trans’ isomer imparts a plastic character in the material before its melting temperature is reached (Fan et al., 2008). It shows a phase transition at about -30 °C, above which the material exhibits a stable plastic crystal phase until it melts at 54 °C which keeps plastic crystalline phase in a temperature range between approximately -40 °C and 60 °C (Alarco et al., 2004a; Liu et al., 2016). Due to the presence of non-ionic plastic crystalline phase, SN can be employed as a solid solvent to dissolve lithium salts.

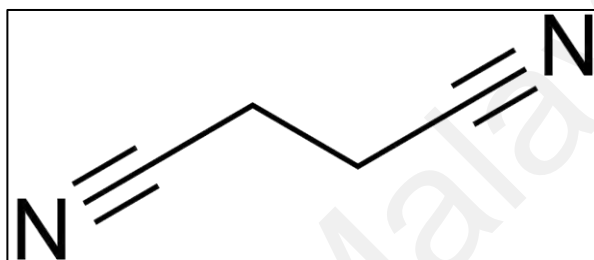


Figure 2.2: Molecular structure of Succinonitrile (SN) (“Succinonitrile,” n.d.).

SN has the properties of (Alarco et al., 2004a; Gupta & Rhee, 2012):

- high dielectric constant (~ 55)
- has low melting temperature (54°C)
- has plasticizing property
- high polarity and diffusivity

These good properties show that SN can help in dissociating ion aggregates in the polymer electrolytes system as well as help in increasing the amorphous content which shows that SN can also act as plasticizer. However, this kind of material possesses not only high ionic conductivity but also favorite mechanical strength which is the main drawback of organic solvent (common plasticizer).

For example, the research done on P(VdF- HFP)-SN complexed with four different types of lithium salts which are LiCl, LiPF₆, LiCF₃SO₃, and LiBETI and the addition of SN greatly enhances ionic conductivities of the polymer electrolytes due to the high polarity and diffusivity of SN (Fan et al., 2009). Lu et al. have prepared a polymer electrolytes system which consists of PEO-PSF-SN-LiTFSI; the optimum ionic conductivity obtained is $1.6 \times 10^{-4} \text{ Scm}^{-1}$, and the electrolyte shows excellent mechanical properties and high thermal stability in a wide temperature range (Lu et al., 2013). Meanwhile, research done by Taib et al. (Taib & Hayati, 2014) has proved that the use of SN can improve the electrochemical properties of chitosan-SN-LiTFSI-based SPEs. They obtained higher value of lithium ion transport number of 0.598 compared to the sample without SN, i.e., 0.119. The sample with SN also showed high electrochemical stability of 4.7 V.

In addition, there are also other research works on SN prepared with various lithium salts (Das & Bhattacharyya, 2010; Gupta & Rhee, 2012; X. Li et al., 2016; Liu et al., 2016; Long et al., 2004; Mohapatra, 2018; Voigt & Wüllen, 2014). However, recently, there is a work has been reported by Sharma and Hashmi by preparing gel polymer electrolytes consist of SN incorporated with magnesium triflate salt (MgTf₂). The gel electrolyte film is found to be flexible, free-standing and transparent with excellent mechanical stability. The GPE offers high ionic conductivity of $\sim 4 \times 10^{-3} \text{ S cm}^{-1}$ at room temperature with a wider electrochemical stability window of $\sim 4.1 \text{ V}$.

2.1.4 Magnesium salt-based electrolytes

Since the introduction of polymer electrolytes field by Fenton et al. (Fenton et al., 1973), research have been focused more on the doping of lithium salts in the polymer electrolytes system rather than other alkali/alkaline earth metal-based salts. The

exploration on magnesium based electrolytes especially in rechargeable batteries is actually interesting in comparison with lithium rechargeable batteries on account of the following advantages (Kumar & Munichandraiah, 2000b, 2002):

- natural resources of the magnesium are abundant and thus, it is much cheaper than lithium;
- magnesium metal is more stable than lithium, hence, it can be handled safely in oxygen and humid atmospheres unlike lithium, which requires a high purity argon or helium atmosphere. Therefore, safety problems associated with Mg metal are minimal;
- the ionic radii of Li^+ and Mg^{2+} are comparable in magnitude. Hence, Li^+ ions in insertion compounds can easily be replaced by Mg^{2+} ions.

There are several works have been reported on magnesium-based polymer electrolytes. Examples of magnesium salts that have been widely used are magnesium trifluoromethanesulfonate (MgTf_2) (Asmara et al., 2011; Hambali et al., 2016; Kumar & Munichandraiah, 2000b; Lee & Allcock, 2010; Osman et al., 2014; Pandey & Hashmi, 2009; Ramesh et al., 2012), magnesium perchlorate ($\text{Mg}(\text{ClO}_4)_2$) (Osman et al., 2014; Pandey et al., 2009), magnesium nitrate ($\text{Mg}(\text{NO}_3)_2 \cdot 6\text{H}_2\text{O}$) (Mahalakshmi et al., 2020) and magnesium bis(trifluoromethanesulfonimide) ($\text{Mg}(\text{TFSI})_2$) (Ha et al., 2014; Lee & Allcock, 2010).

In addition, a comparative study between MgTf_2 and $\text{Mg}(\text{ClO}_4)_2$ has been studied by our research group (Osman et al., 2014). The highest room temperature conductivity value obtained from the PMMA-EC-PC based gel polymer electrolyte containing 15 wt. % of $\text{Mg}(\text{ClO}_4)_2$ is higher than that containing 20 wt. % of MgTf_2 salt and the values are $3.31 \times 10^{-3} \text{ S cm}^{-1}$ and $1.27 \times 10^{-3} \text{ S cm}^{-1}$ respectively. The Mg^{2+} ions transport number of the highest conducting film from both systems is also higher for $\text{Mg}(\text{ClO}_4)_2$ system which

is 0.39 than MgTf_2 system which is 0.38. This shows that salt with a polarizing cation and larger anion with a well delocalized charge has a lower lattice energy, thus is more preferable to be used in polymer electrolytes. Salts with low lattice energies are easier to dissociate into cations and anions and therefore, increase the conductivity.

2.1.5 Rechargeable Batteries

Polymer electrolytes are well known to operate in various electrochemical devices especially in rechargeable batteries. A battery is a device that converts the chemical energy contained in its active materials directly into electric energy by electrochemical oxidation-reduction (redox) reaction. In rechargeable battery system, the battery is recharged by a reversal of the process. This type of reaction involves the transfer of electrons from one material to another through an electric circuit. While the term “battery” is often used, the basic electrochemical unit being referred to is the “cell.” A battery consists of one or more of these cells, connected in series or parallel, or both, depending on the desired output voltage and capacity (Liden & Reddy, 2004).

The cell consists of three major components:

- i. The anode or negative electrode i.e.; the reducing or fuel electrode: gives up electrons to the external circuit and is oxidized during the electrochemical reaction.
- ii. The cathode or positive electrode i.e.; the oxidizing electrode: accepts electrons from the external circuit and is reduced during the electrochemical reaction.
- iii. The electrolyte i.e.; the ionic conductor: provides the medium for transfer of charge, as ions, inside the cell between the anode and cathode.

Figure 2.3 shows a schematic diagram of a Li-ion battery during discharging and charging processes. In a charged Li-ion battery, the Li atoms are initially located in the ‘anode’ (graphite in this case). During the discharge process (Figure 2.3 (a)), the Li atoms inside the graphite anode release electrons, which are collected by the external circuit, passing through an electrical load (whether a motor or the circuitry of a cell phone). The produced free electrons end up at the opposite side of the battery (the ‘cathode’). Meanwhile, the resulting Li-ions are now in search of the lost electrons. The only pathway that Li-ions can take is through the electrolyte, which provides a conductive path for Li-ions (but not electrons) to cross from the anode to the cathode of the battery. However, there are only limited number of places where the Li-ions can fit within the cathode, and once all the vacancy sites are filled, the battery must be recharged. During the recharging process shown in Figure 2.3(b), an external power supply pulls electron from the cathode and pushes them into the anode. The Li-ions within the cathode again migrate in search of electrons, and those electrons are obtained in the anode.

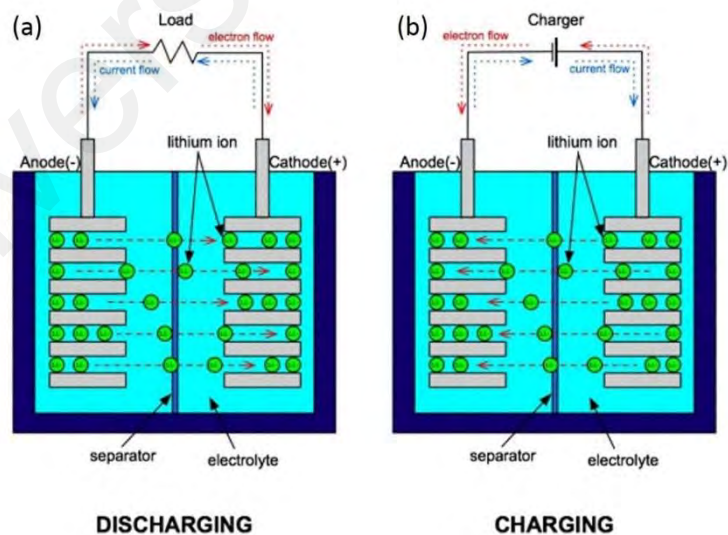


Figure 2.3: Schematic diagram of rechargeable battery during “charging” and “discharging” (“Li-ion Batteries in the Hot Seat (A Primer on the Science of Exploding Smartphones),” n.d.).

However, it is during charging that most of the problems occur within Li-ion batteries. A metallic Li deposit will be formed if the charging process is too fast as Li-ions will take the available electrons on the outside of the anode. Once a metallic Li deposit formed outside of the anode, it becomes a favourable site for other Li-ions to deposit, and eventually a dendrite of metallic Li will be formed, as shown in Figure 2.4. The continuous growth of Li dendrite can eventually break through the battery separator and cause a short circuit within the cell between the anode and cathode consequently, can cause overheating and in some cases combustion of the battery.

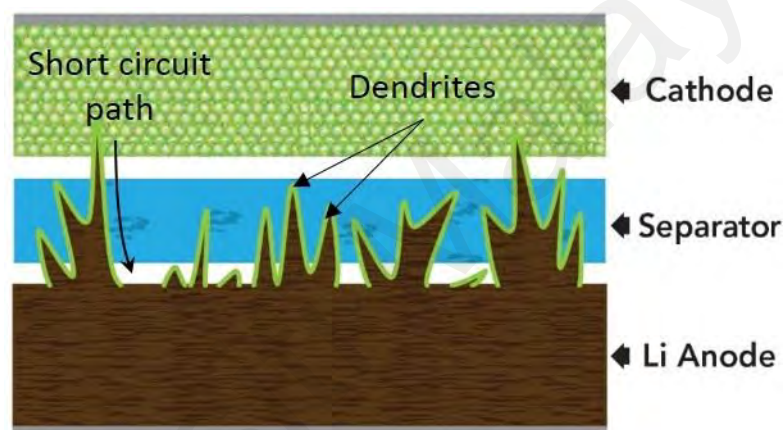


Figure 2.4: The growth of dendrites in rechargeable batteries (“Li-ion Batteries in the Hot Seat (A Primer on the Science of Exploding Smartphones),” n.d.).

Therefore, the rechargeable lithium batteries which used solid polymer electrolytes are considered to have a safety advantage over the organic liquid electrolytes because of their lower reactivity with lithium and the absence of volatile, flammable organic solvent. The field of lithium ion polymer rechargeable battery was opened up by Armand et al. (Armand et al., 1979). Since then, several works have been reported on this (Hofmann et al., 2013; Kim et al., 1999; Li et al., 2011; Masoud et al., 2013; Sumathipala et al., 2007)

Nevertheless, as lithium is a reactive alkaline metal (will combust spontaneously if it comes in contact with water), the electrolyte that fills the battery must be made of an inflammable non-aqueous organic liquid. This is because, if a Li-ion battery ruptures due to overheating, the exposed liquid electrolyte can also cause fire, and the highly reactive lithium will contribute to the severity of the fire.

2.1.5.1 Development of Magnesium Ion Rechargeable Batteries

The disadvantages of lithium ion polymer batteries including the fabrication of the batteries due to the highly reactive of lithium salt has triggered the development of other alternative material such as the introduction of magnesium ion-based batteries. Compared with lithium ion batteries, magnesium ion batteries offer a higher volumetric capacity (3833 mA h/cc for Mg vs. 2046 mA h/cc for Li) for stationary EES applications (Saha et al., 2014) and originate from bivalent Mg^{2+} and thus less reactive than lithium; hence, can be fabricated safely without protection (Muldoon et al., 2012; Wang et al., 2017). An example of magnesium rechargeable battery diagram is as shown in Figure 2.5. In this diagram, the rechargeable battery mechanism is actually similar to that of lithium ion battery but in this battery, the anode material is being replaced by magnesium metal while metal oxide is worked as the cathode. The charge and discharge process are also through the electrolyte which provides a conductive pathway for magnesium ions (but not electrons) to cross from the anode to the cathode of the battery.

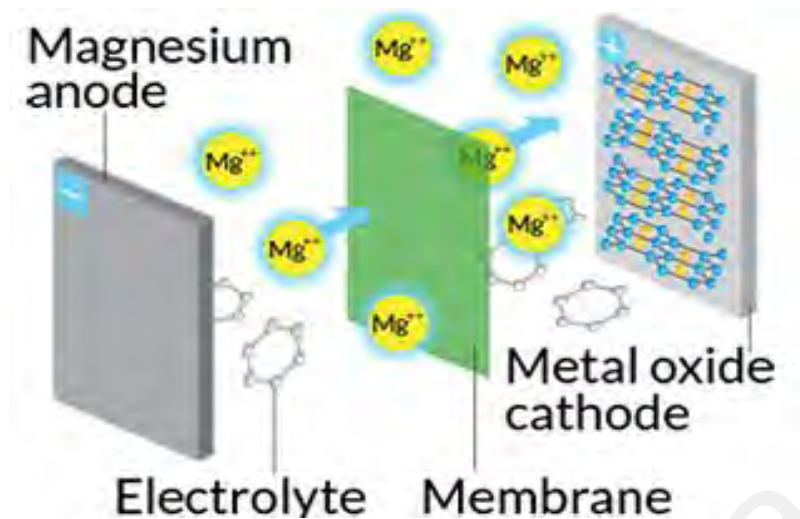


Figure 2.5: Magnesium ion rechargeable battery diagram (Nguyen & Song, 2017).

Examples on works in magnesium batteries including the work by Pellion Technologies founded by Khosla Ventures and the Advanced Research Project Agency - Energy (ARPA-E) (researchers from Massachusetts Institute of Technology (MIT)). They initiated the development of high energy density rechargeable magnesium ion batteries and found its use for applications ranging from portable electronic devices to electric vehicle (EV) (Saha et al., 2014).

Other example on the preparation of Mg ion battery is from the work by Oh et al. by fabricating Mg/GPE/V₂O₅ cell which showed initial discharge capacity of 58 mAh/g based on active V₂O₅ material (Oh et al., 2004). Apart from that, research on nanocomposite polymer electrolyte consists of PEO, Mg(BH₄)₂ and MgO nanoparticles has also been developed for rechargeable Mg batteries. It results in a high coulombic efficiency of 98% for Mg plating/stripping, high cycling stability and highly efficient Mg intercalation/deintercalation in MO₆S₈ (Shao et al., 2015).

Furthermore, a solid-state magnesium battery has been constructed with a novel polymeric electrolyte that conducts Mg²⁺ ion at ambient temperature. The polymeric

electrolyte consisting of oligoethylene oxide-grafted polymethacrylate and a linear polyether dissolving a Mg salt which showed high ionic conductivity of 0.4 mS cm^{-1} at 60°C . A test cell made of a V_2O_5 cathode and an Mg metal anode ($\text{Mg}/\text{V}_2\text{O}_5$) with the Mg^{2+} -conducting polymeric electrolyte showed the first discharge capacity of about 100 mAh g^{-1} (Morita et al., 2001).

In short, all of these research outcomes show that magnesium can be a promising substitution over lithium in rechargeable batteries field.

Universiti Malaysia

CHAPTER 3: EXPERIMENTAL TECHNIQUES

3.1 Sample Preparation

In this study, gel polymer electrolytes (GPEs) based on polyvinylidene (chloride-co-acrylonitrile) (PVdC-co-AN) were prepared with magnesium trifluoromethanesulfonate (MgTf_2) and magnesium bis(trifluoromethanesulfonimide) ($\text{Mg}(\text{TFSI})_2$) as dopant salts. The GPEs were categorized into four systems namely as single plasticized- MgTf_2 salt, double plasticized- MgTf_2 salt, single plasticized- $\text{Mg}(\text{TFSI})_2$ salt and double plasticized- $\text{Mg}(\text{TFSI})_2$ salt. The single plasticized system contained plastic crystal succinonitrile (SN) with varied weight percentages of magnesium salts while double plasticized system contained both plastic crystal SN and plasticizer ethylene carbonate (EC) with varied weight percentages of magnesium salts.

Before the preparation of the four GPE systems, the optimum weight ratio of SN and EC was determined first by varying their weight ratio where this method has been reported by our research group (Chong & Osman, 2014). The compositions of the samples are as shown in Table 3.1. Pure PVdC-co-AN sample was also prepared as reference.

Table 3.1: Compositions of the samples.

Sample	Composition (wt.%)		
	PVdC-co-AN	SN	EC
Pure PVdC-co-AN	100	0	0
PVdC-co-AN-SN	70	30	0
PVdC-co-AN-EC	70	0	30
PVdC-co-AN-SN-EC	56	22	22
PVdC-co-AN-2 SN-1 EC	46	36	18
PVdC-co-AN-1 SN-2 EC	46	18	36

The method of solution casting technique was used in preparing the GPEs. Polyvinylidene (chloride-co-acrylonitrile) PVdC-co-AN, ($M_w \sim 150000$ g/mol), was

dissolved in tetrahydrofuran (THF) (Sigma Aldrich) and the solution was stirred and heated at 40°C until became clear and homogeneous. Succinonitrile (SN) obtained from Sigma Aldrich was added to the polymer solution for single plasticized system while for double plasticized system, both SN and ethylene carbonate (EC) (Merck) were added into the solution. The mixtures were stirred for another 2 hours at 40°C until completely dissolved. The solutions were then cast on petri dishes and left to dry at 40°C overnight until the GPEs were obtained. Then, the conductivity measurements were performed on the prepared samples. The samples that exhibited the highest conductivity value from single and double-plasticized systems were used to prepare the GPEs with magnesium salts.

The same method was used to prepare the GPEs with magnesium salts. The varied concentrations of MgTf₂ salt from 5 to 30 wt.% was added to the optimized composition of single and plasticized system and the solution was stirred until homogeneous. The GPEs obtained were then characterized to study in terms of their electrical, thermal, structural and electrochemical properties. These steps were repeated by replacing the MgTf₂ with Mg(TFSI)₂ salt. Table 3.2 shows the compositions of all prepared GPE samples with magnesium salts.

Table 3.2: Compositions of GPE samples with magnesium salts.

Sample	Composition (wt.%)				
	PVdC-co-AN	SN	EC	MgTf ₂	Mg(TFSI) ₂
PVdC-co-AN/SN	70	30	0	Varied (5 to 30 wt.%)	
PVdC-co-AN-SN/EC	56	22	22	Varied (5 to 30 wt.%)	
PVdC-co-AN/SN	70	30	0		Varied (5 to 30 wt.%)
PVdC-co-AN/SN/EC	56	22	22		Varied (5 to 30 wt.%)

3.2 Electrical and Electrochemical Properties

3.2.1 Impedance Spectroscopy

Impedance spectroscopy (IS) is one of the techniques used to determine the conductivity of polymer electrolytes by evaluating the electrochemical behavior of electrode and/or electrolyte materials which are usually made with cells having two identical electrodes. The general approach is to apply an electrical stimulus (a known voltage or current) to the electrodes and the resulting response is observed (the resulting current or voltage). The properties of the electrode–material system is assumed to be time-invariant and it is one of the basic purposes of IS to determine their interrelations and dependences on controllable variables such as temperature, oxygen partial pressure, applied hydrostatic pressure and applied static voltage or current bias.

In addition, impedance is a more general concept than resistance because it takes phase differences into account and it has become a fundamental and essential concept in electrical engineering. Impedance spectroscopy is thus just a specific branch of the tree of electrical measurements. The instrument will measure the impedance as a function of frequency automatically in a specific frequency ranges which is easily interfaced to laboratory microcomputers. The advantages of this approach are the availability of these instruments and the ease of their use, as well as the fact that a better signal-to-noise ratio can be achieved.

For the theoretical part of this impedance technique, consider the magnitude and direction of a planar vector in a right-hand orthogonal system of axes which can be expressed by the vector sum of the component a and b along the axes, that is, by the complex number:

$$Z = a + jb \tag{3.1}$$

The imaginary number $j\exp(jp/2)$ indicates an anticlockwise rotation by $p/2$ relative to the x axis. Thus, the real part of Z , a , is in the direction of the real axis x , and the imaginary part b is along the y axis. An impedance;

$$Z(w) = Z + jZ \quad (3.2)$$

is such a vector quantity and may be plotted in the plane with either rectangular or polar coordinates, as shown in Figure 3.1.

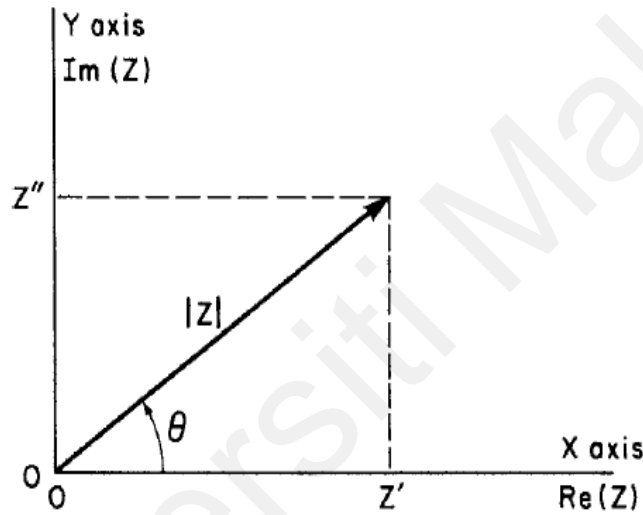


Figure 3.1: An example of impedance plot (Barsoukov & Macdonald, 2005).

From the impedance plot i.e.; Cole-Cole plot obtained, the conductivity value, σ can be calculated from the value of bulk electrolyte resistance, R_b (obtained from the x -intercept of the real axis) according to the following equation

$$\sigma = \frac{t}{R_b A} \quad (3.3)$$

where t is the thickness of the GPE sample (cm) and A is the effective contact area between the electrode and the sample. In this research study, the room temperature ionic

conductivity of GPEs were determined using a HIOKI 3533 LCR bridge over the frequency range of 10 Hz to 200 kHz. The GPE sample was placed between the stainless steel electrodes of the cell holder to perform the impedance measurements. The conductivity temperature dependence studies were also carried out for the GPEs by varying the temperature from 303 K to 353 K.

3.2.2 Transference Number

Transference number is defined as the net number of faradays of charge carried across the reference plane by the cation constituent in the direction of the cathode, during the passage of one faraday of charge across the plane (Evans et al., 1987). Transference number of charge carriers gives the ratio of the conductivity due to itself and the total conductivity, σ_T .

$$\text{The total } \sigma_T = \sigma_i + \sigma_e \quad (3.4)$$

where σ_i is the conductivity contributed by ions (cations/anions) and σ_e is the conductivity contributed by electrons/holes.

The fraction of conductivity will deduce equation for transference number which are:

$$\text{Ionic transference number: } t_i = \frac{\sigma_i}{\sigma_T} \quad (3.5)$$

$$\text{Electronic transference number: } t_e = \frac{\sigma_e}{\sigma_T} \quad (3.6)$$

In other words, transference number measurement is carried out to confirm the type of charge carrier species in polymer electrolytes either ions (cation or anion) or electrons that will take part in the conduction process. There are two processes involved in measuring the transference number of the gel polymer electrolytes. First is to determine

the value of ionic transference number, t_i to confirm the type of charge carrier and secondly, is to calculate the values of cationic transference number, t_+ after the type of carrier species has been confirmed.

3.2.2.1 Ionic Transference Number, t_i

To determine the ionic transference number of GPEs, direct current (DC) polarization method also called as Wagner's polarization method (Wagner & Wagner, 1957) is being used which utilizes a blocking electrode aimed at suppressing the current of one type of charge carrier. From this technique, voltage of 0.1 V was applied across the GPE sample that is sandwiched between the two blocking electrodes with cell configuration of SS/GPE/SS and the resulting current is measured as a function of time. If the electrical conductivity of the GPE is ionic, the current will decrease with time. From the plot, the ionic transference number can be determined by using equation:

$$t_e = \frac{\sigma_e}{\sigma_T} = \frac{i_e}{i_t} \quad (3.7)$$

and

$$t_i = 1 - \frac{i_e}{i_t} = 1 - t_e \quad (3.8)$$

where i_e is electronic current and i_t is the total current

3.2.2.2 Cationic Transference Number, t_+

Cationic transference number is then determined after the confirmation of charge species in the polymer electrolyte system by using the combination of AC impedance and D. C. polarization techniques as proposed by Evans (Evans et al., 1987). In this technique,

magnesium foils were being used as the electrodes with cell configuration of Mg/GPE/Mg. The cell was polarized by applying voltage of 0.1 V for about 5 hours and the value of initial and final currents were recorded. AC impedance was being measured before and after polarization to get the values of electrode-electrolyte resistances from the impedance plots obtained. Thus, the cationic transference number can be determined by using equation:

$$t_+ = \frac{I_s}{I_0} \left[\frac{\Delta V - I_0 R_0}{\Delta V - I_s R_s} \right] \quad (3.9)$$

where I_0 is the initial current and I_s is the final current, while R_0 and R_s are the cell resistance before and after polarization, respectively.

3.2.3 Linear Sweep Voltammetry (LSV)

Electrochemical stability is one of the important properties of the polymer electrolyte in the application of rechargeable batteries. Gel polymer electrolytes need to have a high electrochemical stability in order to operate at a higher voltage over a longer period of time. Linear sweep voltammetry is thus an electrochemical technique that is carried out to estimate the electrochemical stability window (ESW) or the working voltage limit of GPEs where the cell current of the working electrode is measured as a function of time and as a function of potential while the potential between the working electrode and reference electrodes is swept linearly with time. The experimental setup used the combination of three-electrode system (Figure 3.2) with stainless steel as working electrode while magnesium foils will act as reference and counter electrodes with the cell configuration of SS/GPE/Mg. In this technique, voltage is being scanned from lower limit to an upper limit and the current response is plotted as a function of voltage.

In this research work, LSV experiments were performed using WonATech system at a sweep rate of 5 mV s^{-1} in the voltage range of -5.0 V to 5.0 V (vs. Mg^{2+}/Mg) at room temperature for the GPEs from each system.

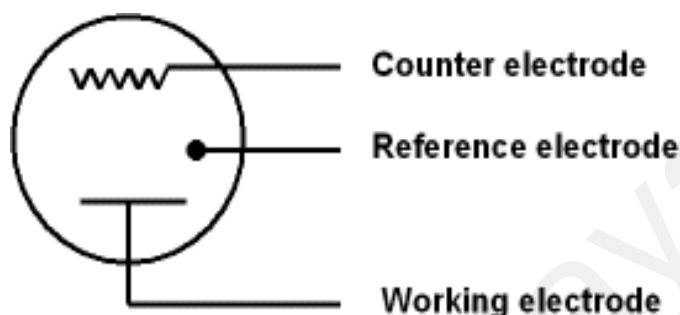


Figure 3.2: Schematic diagram of a three-electrode system (“Three electrode system,” n.d.).

3.2.4 Cyclic Voltammetry (CV)

Cyclic voltammetry (CV) is another technique on analyzing the electrochemical stability of polymer electrolytes. Cyclic voltammetry can be used to study the qualitative information about processes under various conditions, such as the presence of intermediates in oxidation-reduction reactions electrochemical and the reversibility of a reaction. Thus, it is a useful technique for detection and characterization of coupled chemical reaction and cycling process that involved in the mechanism of rechargeable batteries.

Cyclic voltammetry also used three electrode system as described from Section 3.2.3. The working electrode’s potential is varied linearly with time, while the reference electrode maintains a constant potential and the counter electrode conducts electricity from the signal source to the working electrode. Here, the purpose of the electrolyte is to provide ions to the electrodes during oxidation and reduction. The current-to-voltage

converter measures the resulting current and the data acquisition system produces the resulting voltammogram.

In this experiment, cyclic voltammetry has been carried out to confirm the Mg^{2+} ion conduction in the gel polymer electrolytes. The experiment has been performed on symmetrical cells SS/GPE/SS and Mg/GPE/Mg on GPE samples at room temperature with a scan rate of 5 mV s^{-1} from -5.0 V to 5.0 V .

3.3 Structural and Morphological Properties

3.3.1 Fourier Transform Infrared Spectroscopy (FTIR)

Fourier Transform Infrared Spectroscopy (FTIR) is one among the techniques that are used nowadays for measuring the intensity of infrared radiation as a function of frequency or wavelength. It is also a useful technique that provides information on the molecular structure and chemical bonding of materials either organic materials or the inorganic one. It can be performed to analyze solids, liquids, and gases and involves interaction between infrared radiations with various vibration modes of the molecules in the materials.

The essential piece of hardware in a FTIR spectrometer is a modified Michelson interferometer which is shown in Figure 3.3. The Michelson interferometer comprises a beam splitter, moving mirror, and fixed mirror. In this technique, an infrared light from the light source passes through a Michelson interferometer along the optical path. The light beam from the source splits into two by the beam splitter and reflected from the moving mirror and fixed mirror, before being recombined by the beam splitter. As the moving mirror makes reciprocating movements, the optical path difference to the fixed mirror changes, such that the phase difference changes with time. The light beams are recombined in the Michelson interferometer to produce interference light. The intensity

of the interference light is recorded in an interferogram as FTIR spectrum, with the optical path difference recorded along the horizontal axis.

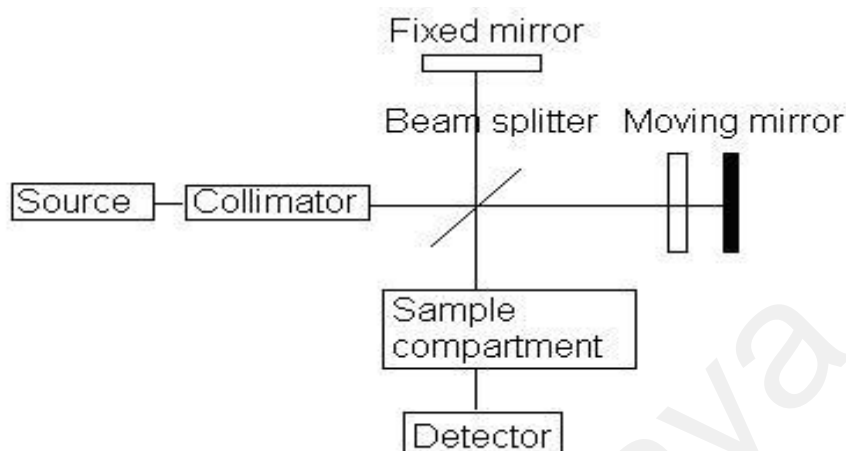


Figure 3.3: Block diagram of an FTIR Spectrometer (“How an FTIR Spectrometer Operates,” n.d.).

In this work, we were using Nicolet is10 (Thermo Scientific) spectrophotometer in the wavenumber region between 650 and 4000 cm^{-1} with a resolution of 1 cm^{-1} to carry out FTIR analysis on the GPE samples. FTIR spectra of pure PVdC-co-AN, pure SN, pure EC pure MgTf_2 and pure $\text{Mg}(\text{TFSI})_2$ salt were also analyzed for references.

3.3.2 X-Ray Diffraction (XRD)

X-ray diffraction (XRD) is a scattering of X-rays by the atoms of a crystal which produces an interference effect that will give information on the structure of the crystal or the identity of a crystalline substance. This microstructural analysis method is used for the identification of crystallinity of polymers, acknowledgment of crystalline stages (polymorphism), and orientation of polymers based on their diffraction pattern obtained.

The X-ray diffraction schematic diagram is as shown in Figure 3.4. An incident beam of monochromatic X-rays interacts with a target material (sample) and the X-rays from atoms will be scattered within the target material. In materials with regular structure (i.e. crystalline), the scattered X-rays undergo constructive and destructive interference. This is the process of diffraction. The diffraction of X-rays by crystals is described by Bragg's Law,

$$n\lambda = 2d \sin\theta \quad (3.10)$$

The directions of possible diffractions depend on the size and shape of the unit cell of the material while the intensities of the diffracted waves depend on the type and the arrangement of atoms in the crystal structure.

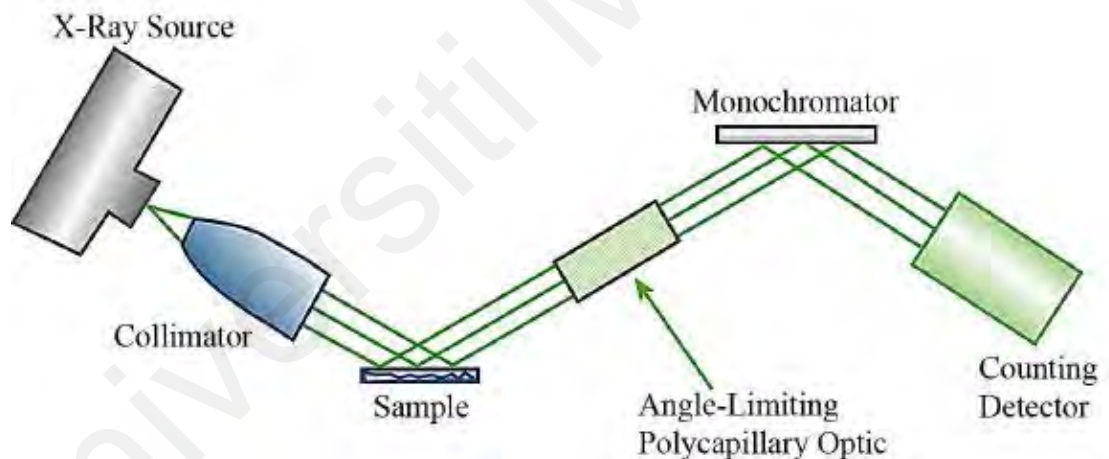


Figure 3.4: X-Ray diffraction schematic diagram (Gibson, n.d.).

In this study, XRD was carried out to study the structural and crystallinity of the GPEs by using X'Pert PRO PANalytical diffractometer of Cu K α radiation ($\lambda = 1.5406 \text{ \AA}$).

3.4 Field Emission Scanning Electron Microscopy (FESEM)

Field Emission Scanning Electron Microscope (FESEM) is a microscope that works with electrons (particles with a negative charge) instead of light. These electrons are liberated by a field emission source while the object or film or material that being scanned by electrons is according to a zig-zag pattern.

The main purpose of FESEM is actually to visualize very small topographic details on the surface or entire or fractioned objects. The observed structures might be as small as 1 nanometer. An example of FESEM microscope schematic diagram is as shown in Figure 3.5. From the diagram, the electrons are liberated from a field emission source (electron beam) and accelerated in a high electrical field gradient. Within the high vacuum column, these primary electrons are focused and deflected by magnetic lenses to produce a narrow scan beam that bombards the object. As a result, secondary electrons are emitted from each spot of the specimen and a detector will catch the secondary electrons and produced an electronic signal. This signal is amplified and transformed to a video scan-image that can be seen on a monitor or to a digital image and will be further analyzed.

In this work, the morphological properties of the GPE samples were analyzed by FESEM by using FEI Quanta 200 system and the FESEM images obtained were studied.

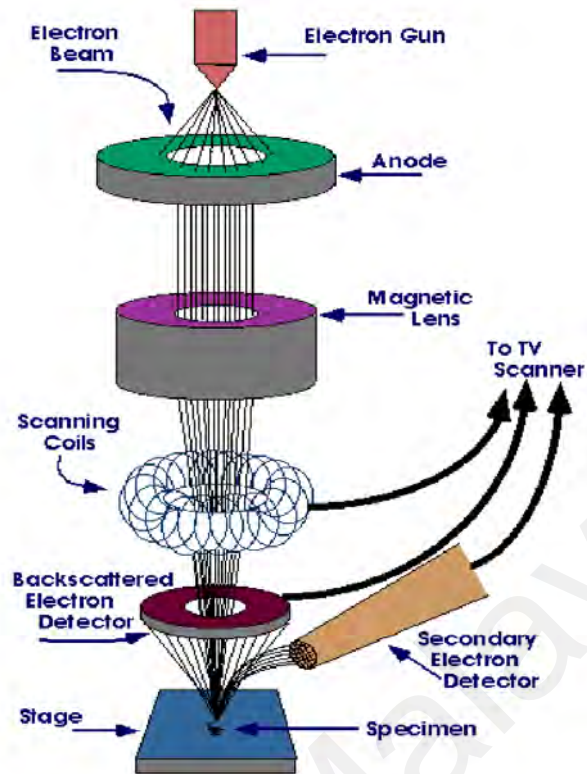


Figure 3.5: Schematic diagram of FESEM (Billah, n.d.).

3.5 Thermal Studies

3.5.1 Differential Scanning Calorimetry (DSC)

A calorimeter, measures the heat into or out of a sample. A differential calorimeter, measures the heat of a sample relative to a reference. Differential scanning calorimetry (DSC) is used widely for examining polymeric materials to determine their thermal transitions. Determination of the thermal behaviour is also an important part of physical characterization of polymer electrolyte.

DSC is highly relevant in order to:

- i. Determine melting point of polymer electrolyte.
- ii. Examine the stability of polymer electrolyte, as transitions or melting at low temperature is not desirable.

- iii. Evaluate the relative stability of different crystalline forms in order to avoid transitions between forms.
- iv. Evaluate crystallisation behaviour after heating – which might for instance lead to new polymorphic forms.
- v. Compare batches: Differences in energies upon melting might be due to impurities or content of amorphous material and the results might be used for regulatory purposes.

DSC measures the temperatures and heat flows associated with transitions in materials as a function of time and temperature in a controlled atmosphere. These measurements provide quantitative and qualitative information about physical and chemical changes that involve endothermic or exothermic processes or changes in heat capacity. When a small amount of sample is heated and any kind of transition takes place during the process, it will lead to a slight difference between the sample and a reference sample temperature, i.e. differential scanning calorimetry measures the amount of energy (heat) absorbed (endothermic) or released (exothermic) by a sample.

In this study, DSC was carried out for GPE samples by using Pelkin Elmer DSC instrument in the temperature range of -100 °C to 150 °C at heating rate of 10 °C/min under nitrogen atmosphere.

3.6 Battery Fabrication

The highest conducting GPE sample at room temperature from each system was used as an electrolyte for battery fabrication. Magnesium manganese oxide (MgMn_2O_4) was used as the cathode and magnesium metal as anode. The MgMn_2O_4 cathode was prepared by using a mixture of MgMn_2O_4 powder (80 wt.%), super-P carbon (10 wt.%) and PTFE

(10 wt.%) as the binder. The mixture of the cathode materials was thoroughly ground and applied to a stainless steel mesh with few drops of acetone. The mesh with cathode material was weighted and heated at 100 °C overnight.

The battery was assembled by sandwiching the GPE sample between the positive and negative electrodes in a sealed cell holder with cell configuration of $\text{MgMn}_2\text{O}_4/\text{GPE}/\text{Mg}$. The charge-discharge cycling was then carried out by using Neware Battery Analyzer at a constant current of 0.4 mA in the voltage range of 1.5 V – 3.0 V and the performance of the battery will be analyzed.

Universiti Malaysia

CHAPTER 4: ELECTRICAL AND TRANSPORT STUDIES

4.1 Ionic Conductivity Studies

In the characterization of the electrical properties of polymer electrolytes, the most important parameter is the ionic conductivity, σ which has been used as the basis for possible application in electrochemical devices. The ionic conductivity is caused by the diffusion of ions, as a result of concentration fluctuation in different regions of the electrolytes. It can be divided into a product of three terms: the carrier charge (q), the concentration (number of particles per unit volume, n) and the mobility (the average velocity of a carrier due to an applied electric field of unit strength, μ). Thus, an expression for the ionic conductivity, σ can be written as:

$$\sigma = nq\mu \quad (4.1)$$

In general, the ionic conductivity of polymer electrolyte is measured as a function of salt composition and temperature. The objective of this characterization is to identify the most optimum conductivity of GPE samples from each system to be used as electrolytes in the rechargeable batteries.

In this technique, AC impedance spectroscopy (IS) was used to determine the value of ionic conductivity for all GPE samples at room temperature as well as at varied temperature from 303 K to 353 K. The impedance measurements were carried out from 10 Hz to 200 kHz for single and double-plasticized MgTf_2 and $\text{Mg}(\text{TFSI})_2$ systems.

4.1.1 Room Temperature Ionic Conductivity of Pure PVdC-co-AN and PVdC-co-AN with Varied Plasticizers

From the IS technique, the Cole-Cole plots of unsalted GPE samples with varied plasticizers which are pure PVdC-co-AN, PVdC-co-AN/SN and PVdC-co-AN/SN/EC

were obtained and are depicted as shown in Figure 4.1 and 4.2 (a) and (b) respectively. The impedance plots comprise of a distorted semicircular arc and the depressed semicircle can be explained by incorporating a constant phase element (CPE) in equivalent circuit as shown in Figure 4.3 which is best described by a circuit composed of a resistor in parallel with a CPE that is connected in series with a resistor. The CPE is another generic distributed circuit element, arises from the fact that the electrode surface is normally rough and/or the bulk properties of the electrode material are inhomogeneous (Fernández-Sánchez et al., 2005; Osman et al., 2012). This CPE replacing the capacitors in the circuit is a leaky capacitor, which has an intermediate characteristic between a resistor and a capacitor (Hambali et al., 2018; Pradhan et al., 2007). The analysis and fitting of the impedance data according to the equivalent circuit was performed by a ZIVE ZMAN 2.3 EIS analysis software. The intercept of the semicircle with the real axis (Z_r) in the low frequencies region is the bulk resistance (R_b). Hence, from equation 3.3, the ionic conductivity values of each sample can be calculated.

Table 4.1 lists the compositions and the calculated ionic conductivity values of the unsalted GPE samples with varied SN and plasticizer EC. The ionic conductivity for pure PVdC-co-AN sample is $7.35 \times 10^{-10} \text{ S cm}^{-1}$ while for the PVdC-co-AN sample with SN, the conductivity is $1.82 \times 10^{-9} \text{ S cm}^{-1}$, increased up to one order of magnitude compared to that of pure PVdC-co-AN. Meanwhile, the conductivity of PVdC-co-AN/EC sample was also calculated and the value is $6.67 \times 10^{-9} \text{ S cm}^{-1}$. In optimizing the plasticizer, the sample of PVdC-co-AN/EC exhibits higher in conductivity than the sample of PVdC-co-AN/SN. Nevertheless, the GPE sample with SN is chosen due to the low mechanical stability of the PVdC-co-AN/EC sample i.e., the free standing film is hardly to be achieved. It is well known that the addition of plasticizer/plasticizing solvent decreased the mechanical strength of the polymer electrolyte, despite produced high in ionic

conductivity (Ahmad et al., 2006; Deka & Kumar, 2011; Patel et al., 2008; Stephan & Nahm, 2006).

On the other hand, the PVdC-co-AN/SN sample with EC plasticizer with ratio (1:1) shows an increment in conductivity up to $1.54 \times 10^{-8} \text{ S cm}^{-1}$. This shows that the combination of SN and EC gives a great influence on increasing the conductivity up to one order of magnitude. The combination of these two types of plasticizer/plasticizing material are chosen due to the argument claimed by Pistoia et al. that the advantages of binary plasticizers can improve the ion dissociation and also balancing their unique characteristics while at the same time improve the interfacial properties (Pistoia et al., 1970). Furthermore, a mixture of solvent is more effective for increasing the ionic conductivity compared with a single solvent, which reflects the combined action of the viscosity and dielectric permittivity (Bandara et al., 1998; Long et al., 2016). Therefore, GPEs formed blended with these two plasticizers are expected to perform better in devices than GPEs with single plasticizer.

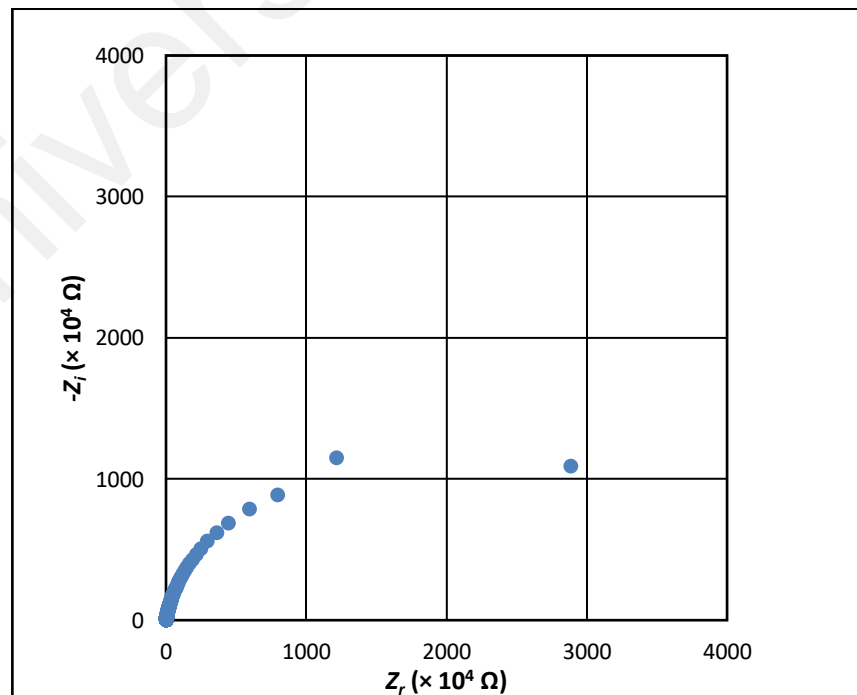


Figure 4.1: Cole-Cole plot of pure PVdC-co-AN.

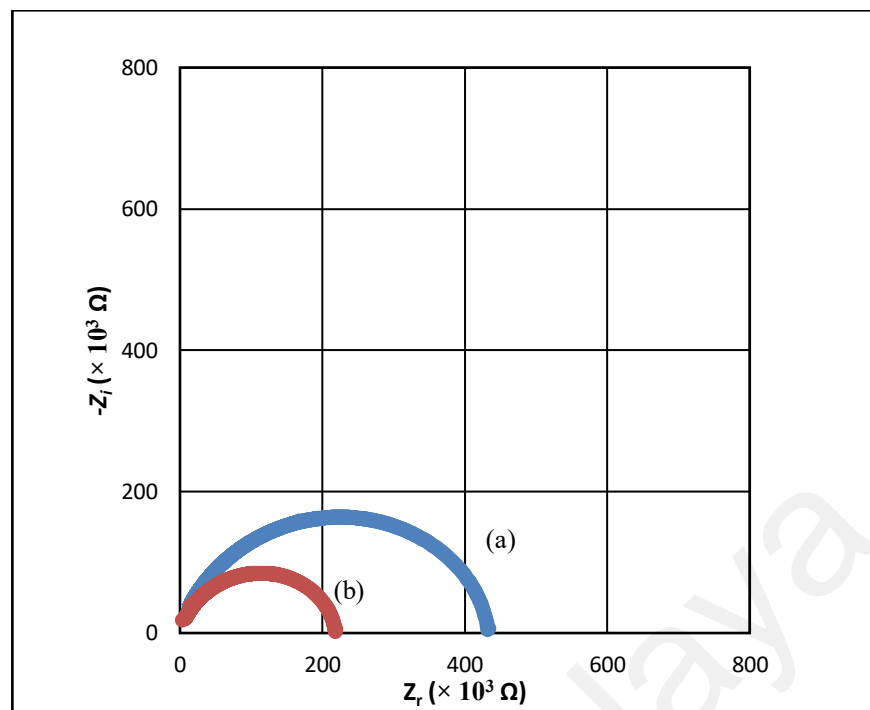


Figure 4.2: Cole-Cole plots of (a) PVdC-co-AN/SN, (b) PVdC-co-AN/SN/EC.

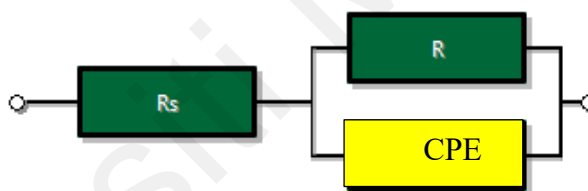


Figure 4.3: Equivalent circuit in accordance of the impedance plots.

Table 4.1: The ionic conductivity of samples with varied plasticizers.

Sample	Composition in weight ratio					Conductivity, σ (S cm ⁻¹)
	PVdC-co-AN	SN	EC	MgTf ₂	Mg(TFSI) ₂	
Pure PVdC-co-AN	100	0	0	0	0	7.35×10^{-10}
PVdC-co-AN-SN	70	30	0	0	0	1.82×10^{-9}
PVdC-co-AN-EC	70	30	0	0	0	6.67×10^{-9}
PVdC-co-AN-SN-EC	56	22	22	0	0	1.54×10^{-8}

4.1.2 Room Temperature Ionic Conductivity of PVdC-co-AN/SN (single plasticized) and PVdC-co-AN/SN/EC (double plasticized) with Varied Magnesium Salts

In this section, both single and double plasticized GPEs that prepared before were then mixed with two types of magnesium salts separately as their dopant which are magnesium trifluoromethanesulfonate (MgTf_2) and magnesium bis(trifluoromethanesulfonimide) ($\text{Mg}(\text{TFSI})_2$) salts. The magnesium salts were varied from 5 wt.% to 30 wt.% for each system and the values of ionic conductivity were calculated for all GPE samples and the results will be discussed below.

4.1.2.1 PVdC-co-AN/SN/ MgTf_2 and PVdC-co-AN/SN/EC/ MgTf_2 systems

Figure 4.4 shows the Cole-Cole plots of the GPE samples of PVdC-co-AN/SN/ MgTf_2 and PVdC-co-AN/SN/EC/ MgTf_2 systems. The plot for PVdC-co-AN/SN/EC/ MgTf_2 sample shows lower in R_b value than PVdC-co-AN/SN/ MgTf_2 . Table 4.2 shows the ionic conductivity of GPEs with MgTf_2 for both single and double plasticized systems while Figure 4.5 revealed the relationship between the ionic conductivity with varied concentrations of MgTf_2 salt from 5 wt.% to 30 wt.% for both systems. It can be observed that the conductivity of the GPE samples continued to increase until 30 wt.% of MgTf_2 with maximum conductivity of $2.26 \times 10^{-7} \text{ S cm}^{-1}$ and $2.82 \times 10^{-7} \text{ S cm}^{-1}$ for PVdC-co-AN/SN/ MgTf_2 and PVdC-co-AN/SN/EC/ MgTf_2 systems respectively. The increase in conductivity from 5 wt.% to 30 wt.% of MgTf_2 salt is attributed to the increase of the number of charge carrier, n and ionic mobility, μ as stated by equation 4.1. The enhancement of conductivity with salt also suggest that there is an increase in concentration of free Mg^{2+} ions in the polymer electrolyte matrix (not forming ion pair with bulkier anions) (Jayaraman et al., 2016). Nevertheless, further increasing on the

concentration of MgTf_2 salt formed a GPE sample with precipitate which shows that the amount of salt is already saturated and thus, 30 wt.% of MgTf_2 salt is the maximum concentration can be used.

Meanwhile, the maximum conductivity value of GPE from double plasticized system shows higher than that of single plasticized system. This confirms that the presence of EC helps in improving the conductivity of polymer electrolytes as well as the effect of double plasticizers in the polymer electrolyte system by assisting in dissociating the ion aggregates in polymer electrolytes as stated by Ali et al. (Ali et al., 2007). Furthermore, the addition of the EC plasticizer also decreases the ion pairing due to the high dielectric constant of EC which effectively reduces the inter-ion Coulomb interactions; hence, more Mg^{2+} contributed to the conductivity of the complexes.

However, there is only a slight difference in conductivity between the highest conducting sample of both systems, which both samples displayed the value of same order of magnitude. This indicates that the plastic crystal SN also plays an important role in enhancing the conductivity because of its capability to act as a solvent to dissociate MgTf_2 salt due to the high polarity and diffusivity properties (Chen et al., 2007; Wang et al., 2004). The high value of dielectric constant of SN and low melting temperature properties also promotes the dissociation of ion aggregates and increasing the amorphous content of the polymer electrolytes system respectively (Alarco et al., 2004b). Therefore, as the concentration of Mg salt increases, these effects of SN assisted in obtaining high in ionic conductivity (Long et al., 2003) and proved that it can also act as a plasticizer in polymer electrolytes system. Further, the role of SN and EC as plasticizers can also be seen here as the GPE containing 30 wt.% MgTf_2 without SN and EC (PVdC-co-AN/30 wt.% MgTf_2) was also prepared and it has lower conductivity of $1.02 \times 10^{-8} \text{ S cm}^{-1}$ compared to GPE with SN and EC.

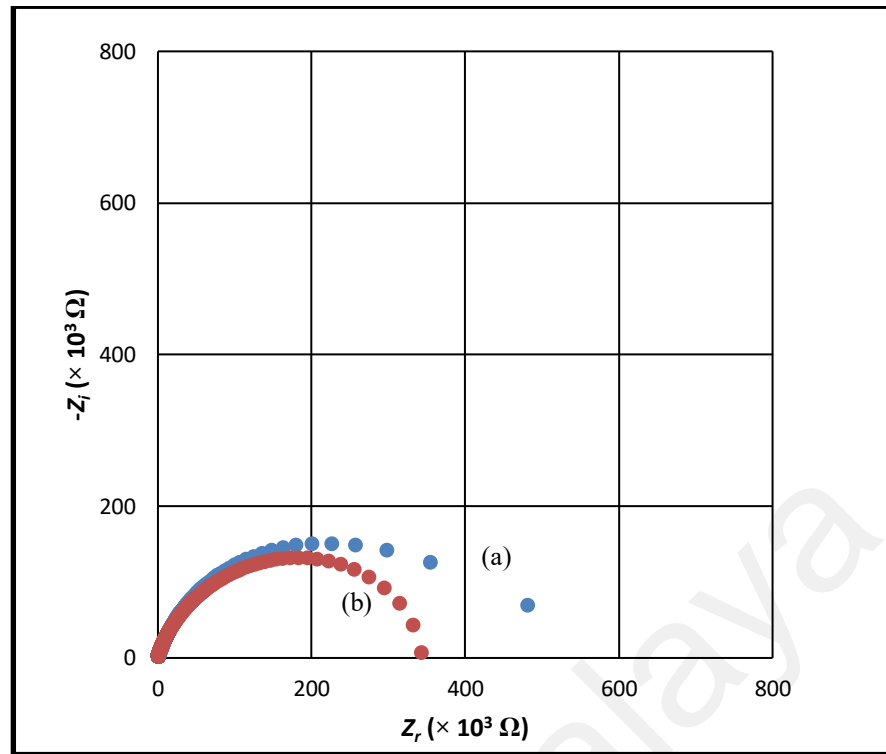


Figure 4.4: Cole-Cole plots of (a) PVdC-co-AN/SN/30 wt.%MgTf₂ and (b) PVdC-co-AN/SN/EC/30 wt.% MgTf₂.

Table 4.2: Ionic conductivity of GPEs with MgTf₂ salt.

System	Salt content (wt.%)	Average Bulk Resistance, R_b (Ω)	Average Conductivity, $(\sigma \pm \Delta\sigma)$ ($S\ cm^{-1}$)
PVdC-co-AN/SN/MgTf ₂	5	1.22×10^6	$(1.42 \pm 0.34) \times 10^{-8}$
	10	1.15×10^6	$(2.34 \pm 0.01) \times 10^{-8}$
	15	9.61×10^5	$(3.12 \pm 0.32) \times 10^{-8}$
	20	8.17×10^5	$(3.81 \pm 0.05) \times 10^{-8}$
	25	3.65×10^5	$(1.16 \pm 0.01) \times 10^{-7}$
	30	1.40×10^5	$(2.26 \pm 0.13) \times 10^{-7}$
PVdC-co-AN/SN/EC/MgTf ₂	5	1.01×10^6	$(2.82 \pm 0.04) \times 10^{-8}$
	10	2.57×10^5	$(6.54 \pm 0.52) \times 10^{-8}$
	15	2.35×10^5	$(1.14 \pm 0.10) \times 10^{-7}$
	20	1.54×10^5	$(2.13 \pm 0.16) \times 10^{-7}$
	25	1.53×10^5	$(2.48 \pm 0.08) \times 10^{-7}$
	30	1.15×10^5	$(2.82 \pm 0.01) \times 10^{-7}$

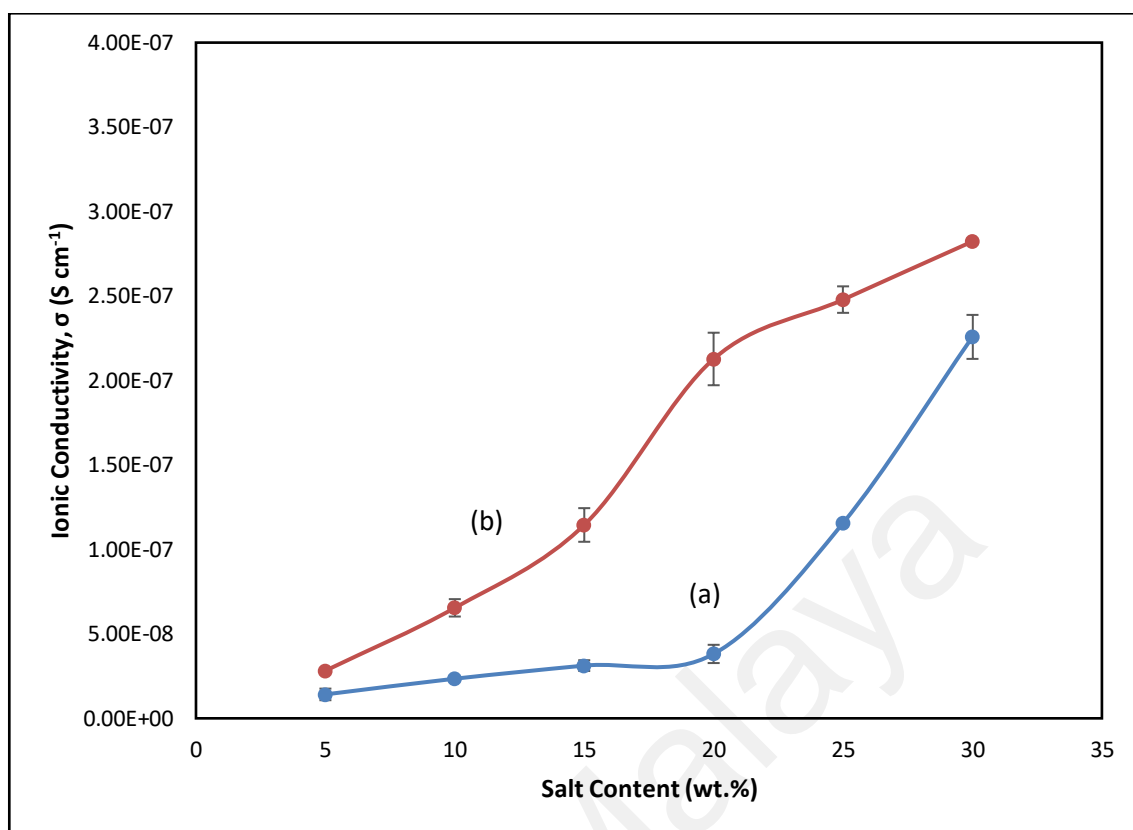


Figure 4.5: Ionic conductivity of GPE system of (a) PVdC-co-AN/SN/MgTf₂ and (b) PVdC-co-AN/SN/EC/MgTf₂.

4.1.2.2 PVdC-co-AN/SN/Mg(TFSI)₂ and PVdC-co-AN/SN/EC/Mg(TFSI)₂ systems

Figure 4.6 shows the Cole-Cole plots of the GPE samples from PVdC-co-AN/SN/Mg(TFSI)₂ and PVdC-co-AN/SN/EC/Mg(TFSI)₂ systems. The plot for PVdC-co-AN/SN/EC/Mg(TFSI)₂ sample shows lower in bulk resistance, R_b value than PVdC-co-AN/SN/Mg(TFSI)₂.

Table 4.3 shows the ionic conductivity of GPEs with Mg(TFSI)₂ for both single and double plasticized systems while Figure 4.7 revealed the relationship between the ionic conductivity with varied concentrations of Mg(TFSI)₂ salt from 5 wt.% to 30 wt.% for both systems. From the plot, it can be observed that the maximum conductivity obtained from PVdC-co-AN/SN/Mg(TFSI)₂ is 1.61×10^{-6} S cm⁻¹ that is when 20 wt.% of Mg(TFSI)₂ added into the GPE. Whereas, for PVdC-co-AN/SN/EC/Mg(TFSI)₂ system,

the maximum conductivity is achieved from PVdC-co-AN/SN/EC/15 wt.% Mg(TFSI)₂ sample which is $1.93 \times 10^{-6} \text{ S cm}^{-1}$. The increase of conductivity at this point is due to the increase of the number of charge carrier and ionic mobility in the GPEs as the concentration of Mg(TFSI)₂ increases. Beyond this point, i.e. the maximum conductivity of both systems, the conductivity decreases considerably until 30 wt.% of Mg(TFSI)₂ added attributed to the increase in the formation of ion pairs and ion aggregates which then decreasing in the number of mobile ions and mobility of the ions which is Mg²⁺ ions, in this case. This observation also suggests that the ionic conductivity is not a simple linear function of concentration as there is a concentration window for optimising the conductivity (Echeverri et al., 2012). The reduce in conductivity is also related to a greater cation-anion interactions competing for coordination of Mg²⁺ ions on the PVdC-co-AN nitrile group and also the drastic increase in viscosity of the mixture (Lascaud et al., 1994).

Further, the ionic conductivity results also show that the maximum conductivity value of GPE from PVdC-co-AN/SN/EC/Mg(TFSI)₂ system is higher than that obtained from PVdC-co-AN/SN/Mg(TFSI)₂ system due to the presence of EC that helps in improving the conductivity of polymer electrolytes as well as the effect of double plasticizers in the polymer electrolyte system (Ali et al., 2007). The concentration of Mg(TFSI)₂ required to achieve maximum conductivity is also less for the double plasticized GPE compared to the single plasticized GPE. Nevertheless, GPE containing 20 wt.% Mg(TFSI)₂ without SN and EC was also prepared and the ionic conductivity obtained is $1.87 \times 10^{-8} \text{ S cm}^{-1}$ which is lower than the GPEs containing SN (single plasticized) and SN and EC (double plasticized) and thus the role of SN and EC as plasticizers can also be seen here.

In contrast, from the conductivity results of single and double plasticized- MgTf₂ and single and double plasticized- Mg(TFSI)₂ systems, the conductivity values are observed

to be higher for GPEs containing $\text{Mg}(\text{TFSI})_2$ salt than GPEs containing MgTf_2 salt. This is because of the characteristics of the anion, $-(\text{TFSI})_2$ group. This type of anion was reported to have a highly delocalized anionic charge and a flexible structure and a larger ionic radius may result in the easier ionic dissociation of $\text{Mg}(\text{TFSI})_2$ with the nitrile group of the polymer (Hambali et al., 2017) compared with MgTf_2 salt (He et al., 2013; Marzantowicz et al., 2009).

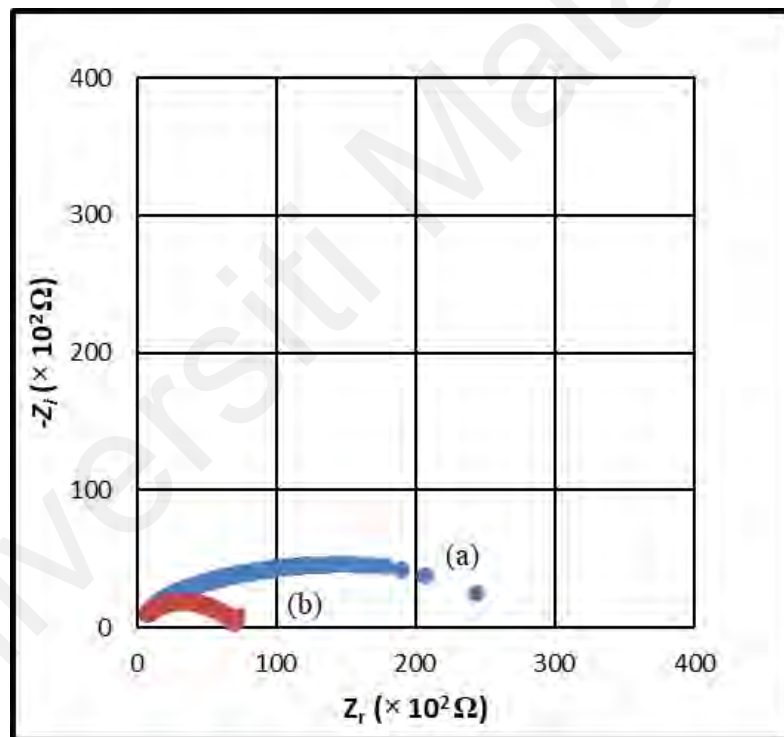


Figure 4.6: Cole-Cole plots of (a) PVdC-co-AN/SN/20 wt.% $\text{Mg}(\text{TFSI})_2$ and (b) PVdC-co-AN/SN/EC/15 wt.% $\text{Mg}(\text{TFSI})_2$.

Table 4.3: Ionic conductivity of GPEs with Mg(TFSI)₂ salt.

System	Salt content (wt.%)	Average Bulk Resistance, R_b (Ω)	Average Conductivity, ($\sigma \pm \Delta\sigma$) ($S\ cm^{-1}$)
PVdC-co-AN/SN/Mg(TFSI) ₂	5	3.43×10^5	$(1.54 \pm 0.04) \times 10^{-7}$
	10	2.03×10^5	$(2.12 \pm 0.51) \times 10^{-7}$
	15	1.16×10^5	$(3.29 \pm 0.20) \times 10^{-7}$
	20	3.05×10^4	$(1.61 \pm 0.03) \times 10^{-6}$
	25	3.42×10^4	$(1.06 \pm 0.03) \times 10^{-6}$
	30	1.07×10^5	$(4.57 \pm 0.23) \times 10^{-7}$
PVdC-co-AN/SN/EC/Mg(TFSI) ₂	5	2.13×10^4	$(8.69 \pm 0.01) \times 10^{-7}$
	10	1.11×10^4	$(1.54 \pm 0.02) \times 10^{-7}$
	15	1.41×10^4	$(1.93 \pm 0.04) \times 10^{-7}$
	20	2.39×10^5	$(3.01 \pm 0.05) \times 10^{-7}$
	25	1.23×10^5	$(2.12 \pm 0.08) \times 10^{-7}$
	30	3.10×10^5	$(1.00 \pm 0.02) \times 10^{-7}$

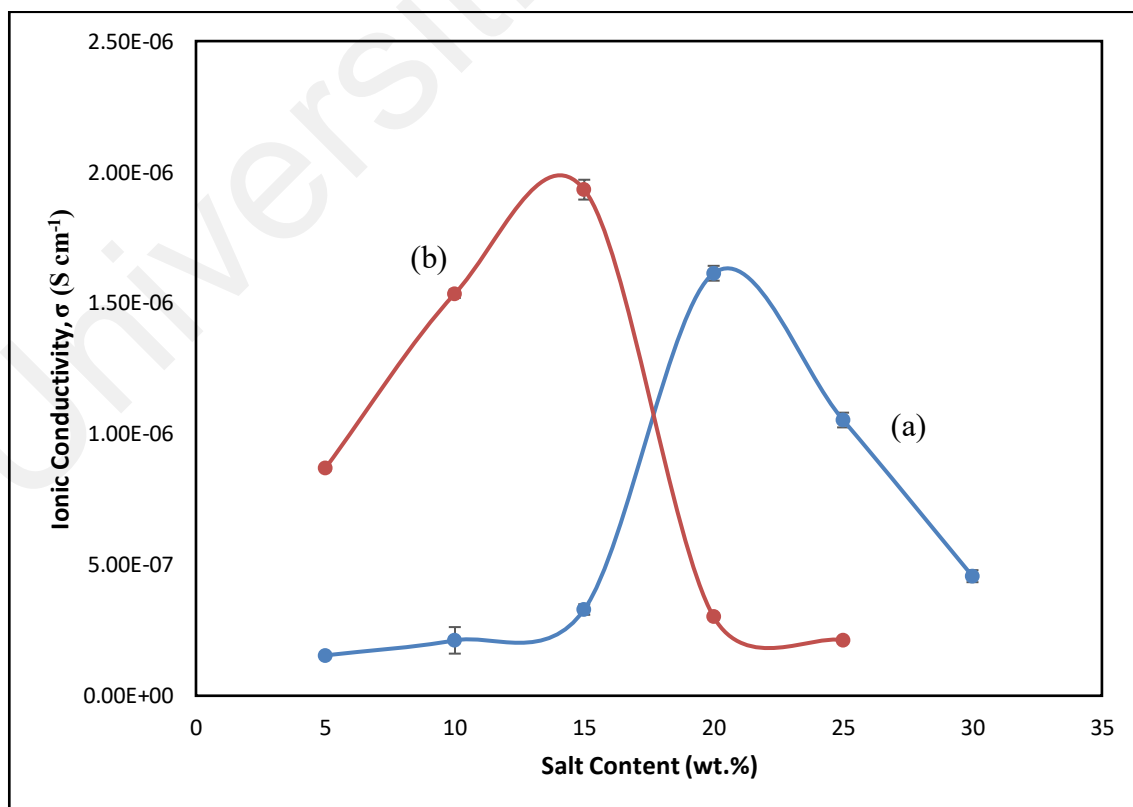


Figure 4.7: Ionic conductivity of GPE system of (a) PVdC-co-AN/SN/Mg(TFSI)₂ and (b) PVdC-co-AN/SN/EC/Mg(TFSI)₂.

4.1.3 Temperature-dependence Ionic Conductivity Studies

The relationship between ionic conductivity with temperature on the ion transport mechanism of GPEs were also evaluated by operating temperature-dependence ionic conductivity studies. The study was conducted for the selected samples from all GPE systems at a temperature range of 303 K to 353 K.

4.1.3.1 PVdC-co-AN/SN/MgTf₂ and PVdC-co-AN/SN/EC/MgTf₂ systems

Figure 4.8 and 4.9 display the plot of $\log \sigma$ against $1000/T$ for PVdC-co-AN/SN and PVdC-co-AN/SN/EC containing 10 wt.%, 20 wt.% and 30 wt.% of MgTf₂. For each system, the plot shows increment in conductivity with temperature. However, the plots of both systems are non-linear and suggest that they did not follow the typical Arrhenius relation and such non-Arrhenius temperature dependence of conductivity originates from the coupling of the ionic motion to the polymer segmental dynamics (Pradhan et al., 2014). This temperature dependence ionic conductivity behaviour can also be explained on the basis of free volume theory (Ali et al., 2007; Ulaganathan et al., 2012). The concept is that the ionic diffusion process is not an activated process but is controlled by the redistribution of free volume within the material (Premila et al., 2018) and can be quantitatively described by the empirical Vogel-Tamman-Fulcher (Ratner & Shriver, 1988) in equation 4.2:

$$\sigma(T) = A_0 T^{-1/2} \exp(-B/k(T - T_0)) \quad (4.2)$$

Here, T is the absolute temperature; A , B and T_0 are the fitting constants and k is Boltzmann constant. The constant A_0 is a pre-exponential factor related to the number of charge carriers and is assumed to be independent of temperature. B is pseudo-activation associated with the rate at which viscosity changes with temperature (Pandey & Hashmi,

2009). T_0 is the critical (ideal glass transition) temperature, which is generally 30 to 50 K below T_g . It is also the temperature at which configuration entropy or free volume disappears (Aziz et al., 2012). Figure 4.10 and 4.11 show linear variation between $\log \sigma T^{1/2}$ against $1000/(T-T_0)$ for PVdC-co-AN/SN/MgTf₂ and PVdC-co-AN/SN/EC MgTf₂ respectively and the parameters A_0 , B and T_0 obtained are shown in Table 4.4. The linearity of plot for all GPE samples of both systems suggests that the σ - T relationship obeys the VTF rule as their regression values are close to unity. The B values for GPE samples is very low which is in the range of 0.092 to 0.104. These values are related to the critical volume for displacement in free volume model and to the energy barrier for rotational motion of polymer segment in configuration entropy model (Pandey & Hashmi, 2009). For A_0 values which related to the number of charge carriers, the value is the highest for PVdC-co-AN/SN/30 wt.% MgTf₂ for single plasticized system which is 4.127 S cm⁻¹ K^{1/2} and PVdC-co-AN/SN/EC/30 wt.% MgTf₂ for double plasticized system which is 4.443 S cm⁻¹ K^{1/2}. From these values also, double plasticized system exhibits higher in A_0 than single plasticized one and the values are in accordance with the room temperature ionic conductivity where the conductivity value for the samples in double plasticized system are higher than the single plasticized system.

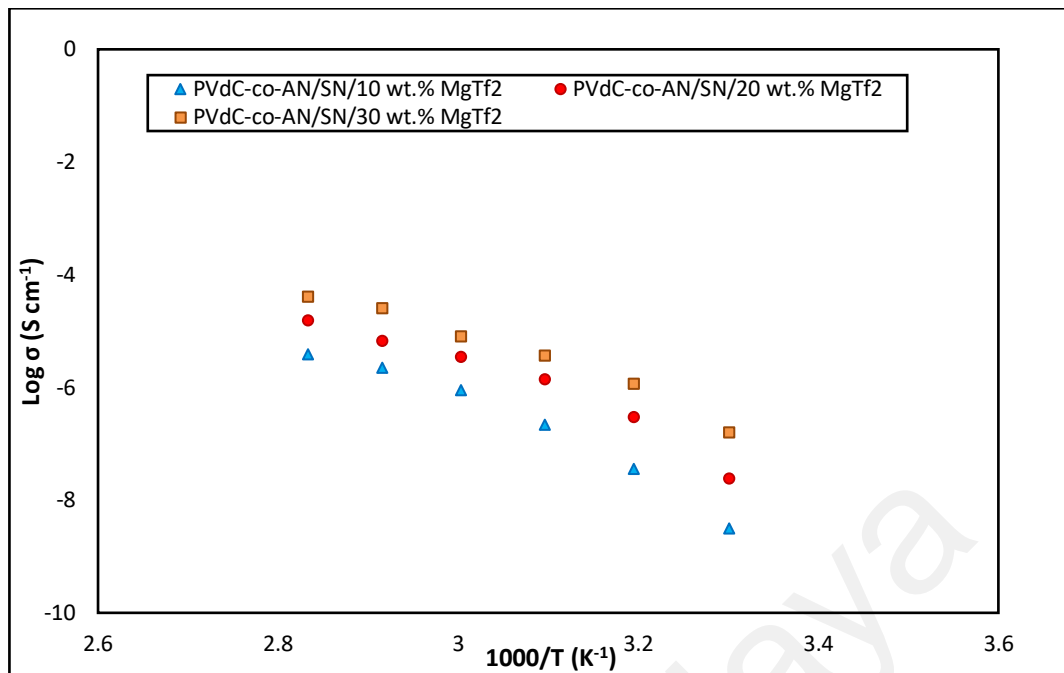


Figure 4.8: Plot of $\log \sigma$ against $1000/T$ for PVdC-co-AN/SN samples containing 10 wt.%, 20 wt.% and 30 wt.% of MgTf₂.

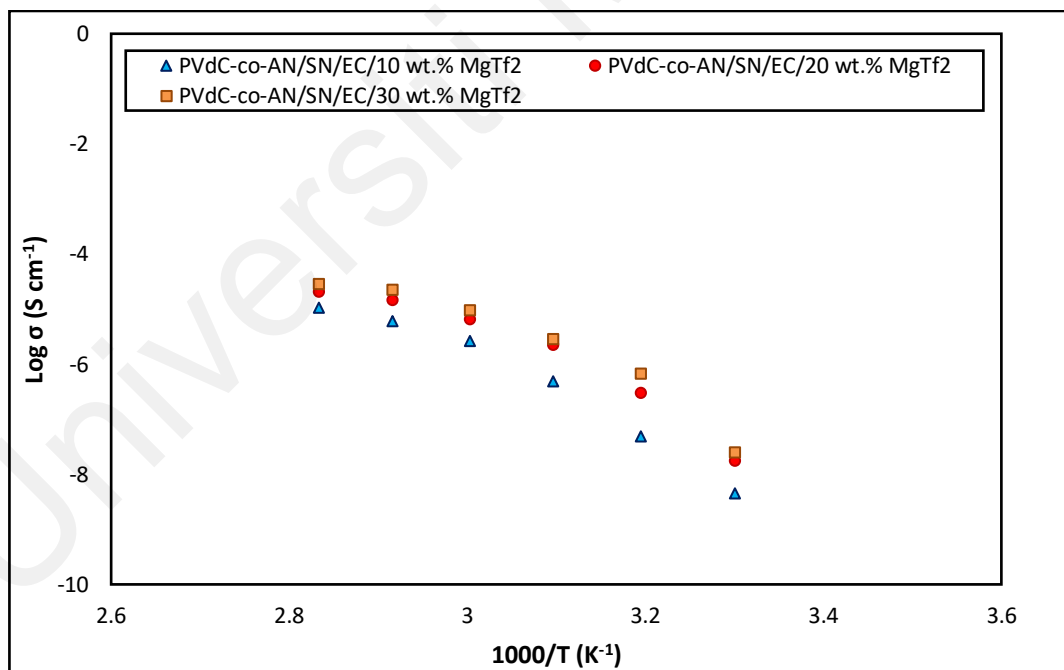


Figure 4.9: Plot of $\log \sigma$ against $1000/T$ for PVdC-co-AN/SN/EC samples containing 10 wt.%, 20 wt.% and 30 wt.% of MgTf₂.

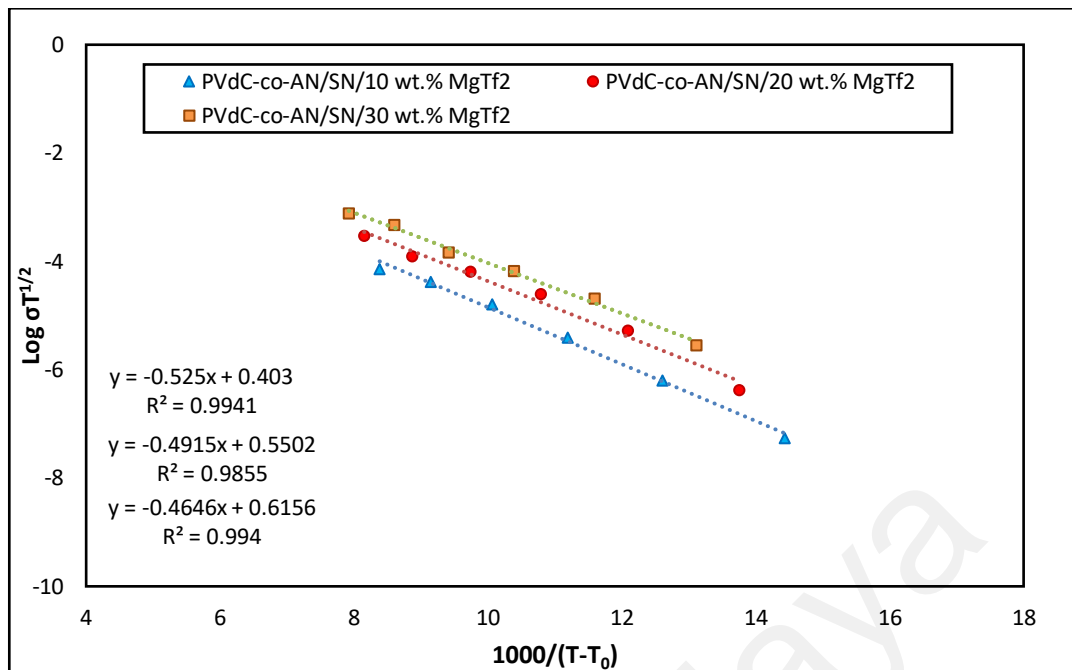


Figure 4.10: Plot of $\log \sigma T^{1/2}$ against $1000/(T-T_0)$ for PVdC-co-AN/SN samples containing 10 wt.%, 20 wt.% and 30 wt.% of MgTf₂.

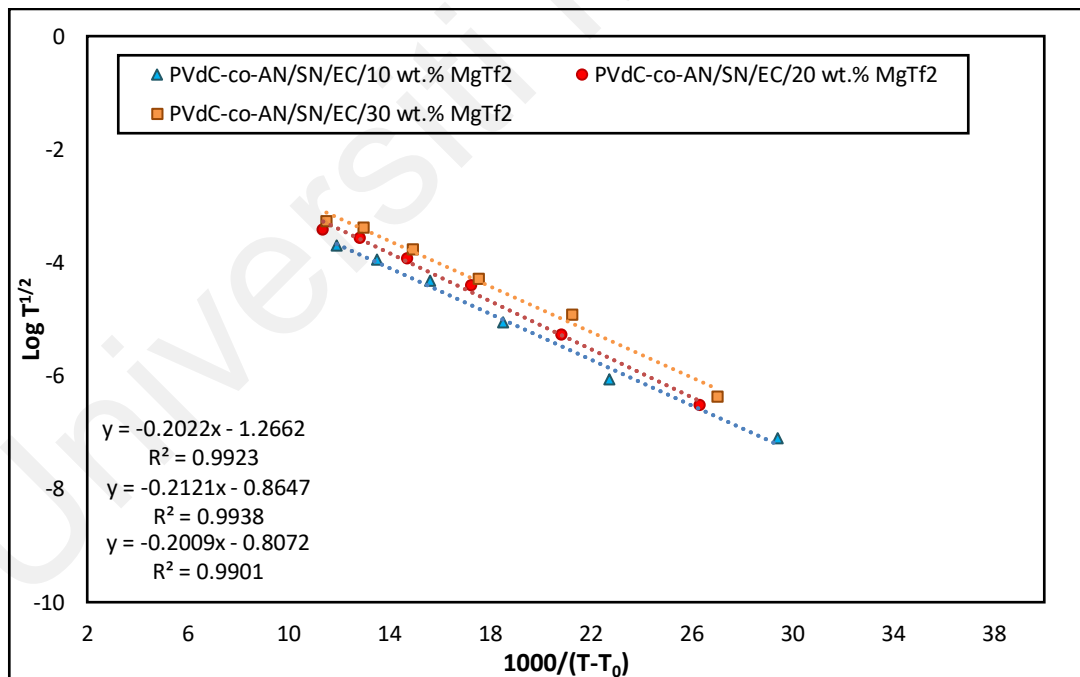


Figure 4.11: Plot of $\log \sigma T^{1/2}$ against $1000/(T-T_0)$ for PVdC-co-AN/SN/EC samples containing 10 wt.%, 20 wt.% and 30 wt.% of MgTf₂.

Table 4.4: The VTF parameters for PVdC-co-AN/SN/MgTf₂ and PVdC-co-AN/SN/EC/MgTf₂ systems.

System	Content of MgTf ₂ (wt. %)	<i>B</i> (eV)	<i>A</i> ₀ (S cm ⁻¹ K ^{1/2})	<i>T</i> ₀ (K)
PVdC-co-AN/SN	10	0.104	2.529	233.71
	20	0.097	3.550	230.42
	30	0.092	4.127	226.73
PVdC-co-AN/SN/EC	10	0.102	3.415	235.28
	20	0.097	3.623	227.52
	30	0.095	4.443	225.01

4.1.3.2 PVdC-co-AN/SN/Mg(TFSI)₂ and PVdC-co-AN/SN/EC/Mg(TFSI)₂ systems

For GPEs containing Mg(TFSI)₂ salt, the plot of $\log \sigma$ against $1000/T$ for PVdC-co-AN/SN and PVdC-co-AN/SN/EC containing 10 wt.%, 20 wt.% and 30 wt.% of Mg(TFSI)₂ are shown in Figure 4.12 and 4.13 respectively. From the figures, the plots show increment in conductivity with temperature for all GPE samples in both systems. However, the plots are non-linear and suggest that they did not follow the typical Arrhenius relation and such non-Arrhenius temperature dependence of conductivity originates from the coupling of the ionic motion to the polymer segmental dynamics (Pradhan et al., 2014). The role of temperature is significant here in enhancing the free volume. As temperature increases, the polymer chain undergoes faster internal modes, facilitating the segmental motion due to bond rotation and the increase in the flexibility and mobility of polymer chains providing more free volume whereby ions can move into the free volume, causing the increase in conductivity (Isa et al., 2014). This behavior is again quantitatively described by the empirical Vogel-Tamman-Fulcher (VTF) behaviour (Ratner & Shriver, 1988) (equation 4.2). Figure 4.14 and 4.15 show linear variation between $\log \sigma T^{1/2}$ against $1000/(T-T_0)$ for PVdC-co-AN/SN/MgTf₂ and PVdC-co-AN/SN/EC MgTf₂ respectively and the parameters *A*₀, *B* and *T*₀ obtained are shown in

Table 4.5. The linearity of plot for all GPE samples of both systems suggests that the σ - T relationship obeys the VTF rule as their regression values are close to unity. The B values for GPE samples is also low here which is in the range of 0.086 to 0.108. For A_0 values, the values follow the room temperature ionic conductivity values which is the highest A_0 value comes from PVdC-co-AN/SN/20 wt.% Mg(TFSI)₂ for single plasticized system which is 1.512 S cm⁻¹ K^{1/2} and PVdC-co-AN/SN/EC/15 wt.% Mg(TFSI)₂ sample for double plasticized system which is 21.712 S cm⁻¹ K^{1/2}. The A_0 values also higher in double plasticized system compared to the single one, which proved the dependence of the number of charge carriers with ionic conductivity.

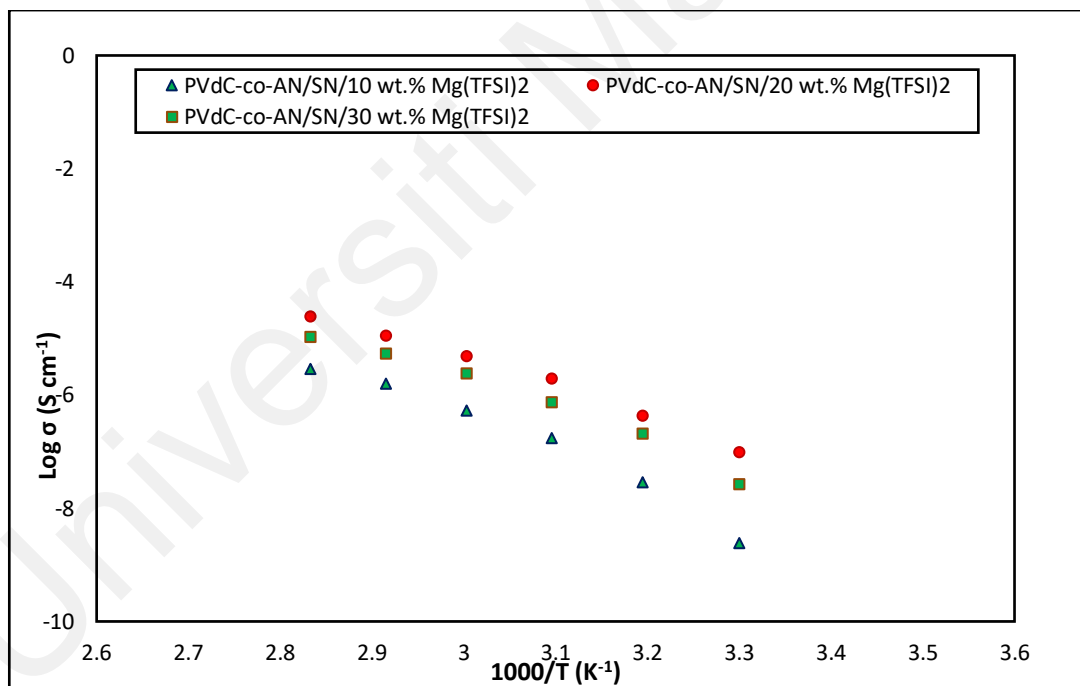


Figure 4.12: Plot of $\log \sigma$ against $1000/T$ for PVdC-co-AN/SN samples containing 10 wt.%, 20 wt.% and 30 wt.% of Mg(TFSI)₂.

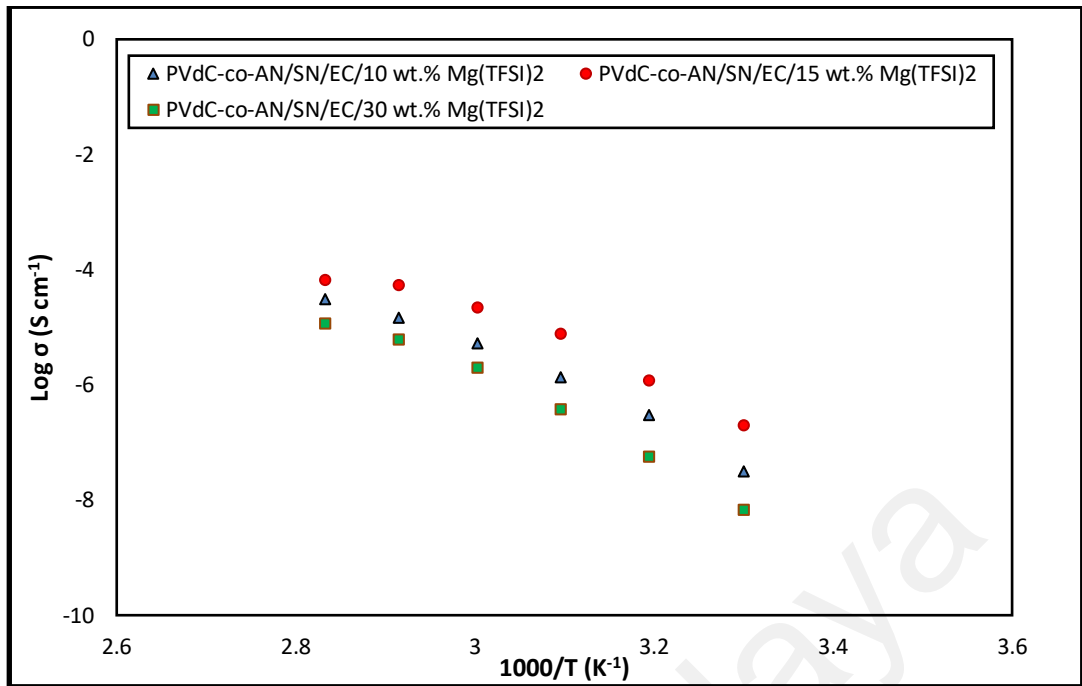


Figure 4.13: Plot of $\log \sigma$ against $1000/T$ for PVdC-co-AN/SN/EC samples containing 10 wt.%, 15 wt.% and 30 wt.% of $\text{Mg}(\text{TFSI})_2$.

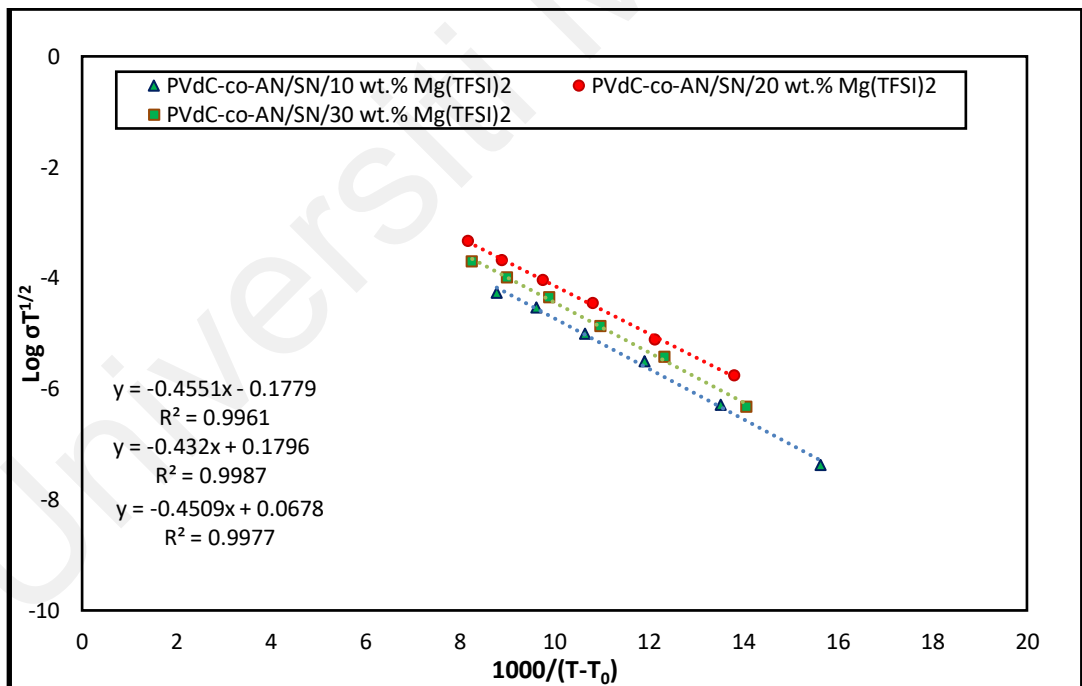


Figure 4.14: Plot of $\log \sigma T^{1/2}$ against $1000/(T-T_0)$ for PVdC-co-AN/SN samples containing 10 wt.%, 20 wt.% and 30 wt.% of $\text{Mg}(\text{TFSI})_2$.

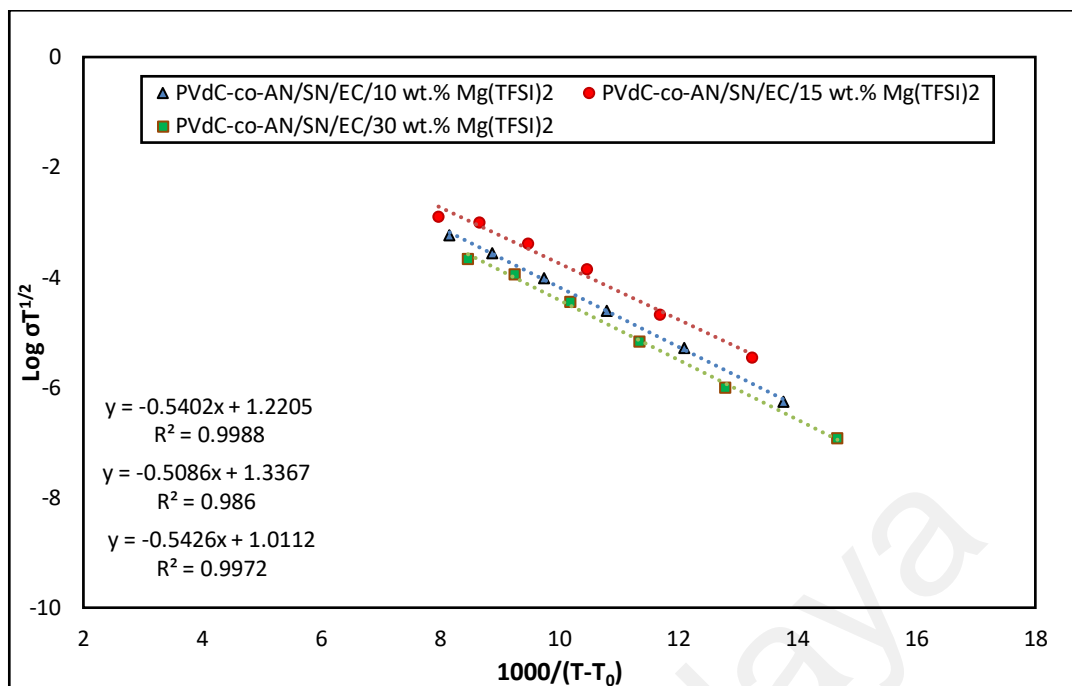


Figure 4.15: Plot of $\log \sigma T^{1/2}$ against $1000/(T-T_0)$ for PVdC-co-AN/SN/EC samples containing 10 wt.%, 15 wt.% and 30 wt.% of Mg(TFSI)₂.

Table 4.5: The VTF parameters for PVdC-co-AN/SN/Mg(TFSI)₂ and PVdC-co-AN/SN/EC/Mg(TFSI)₂ systems.

System	Content of Mg(TFSI) ₂ (wt. %)	B (eV)	A_0 (S cm ⁻¹ K ^{1/2})	T_0 (K)
PVdC-co-AN/SN	10	0.090	0.664	239.07
	20	0.086	1.512	230.56
	30	0.089	1.169	231.89
PVdC-co-AN/SN/EC	10	0.107	16.615	230.39
	20	0.101	21.712	227.51
	30	0.108	10.261	234.85

4.2 Transference Number

The application of an external electric field will cause cations and anions to move in opposite directions. According to Kohlrausch's law, the conductivity measures the sum of the conductivities from migration of both the positive and negative ions. The transference number is therefore defined as the different fractions of current carried by the cation or the anion. In this study, ionic transference number, t_i is determined to confirm the type of charge carrier species exists in the GPEs by using DC or Wagner's polarization method (Wagner & Wagner, 1957) for the highest conducting sample from each system. After the confirmation of the type of charge carrier, cationic transference number is carried out by using a combined method of DC polarization and AC impedance spectroscopy as proposed by Evans (Evans et al., 1987).

4.2.1 Ionic Transference Number, t_i

In Wagner's polarization technique (Wagner & Wagner, 1957), the DC current is monitored as a function of time by applying a fixed voltage of 0.1 V across the GPE sample with blocking electrodes SS/GPE/SS. Plots of normalized current against time are shown in Figure 4.16 and 4.17 for the highest conducting samples from MgTf₂ and Mg(TFSI)₂ systems respectively. The values of ionic transference number, t_i were then calculated by using equation 3.8 and tabulated in Table 4.6. From the table, the t_i values obtained for PVdC-co-AN/SN/30 wt.% MgTf₂, PVdC-co-AN/SN/EC/30 wt.% MgTf₂, PVdC-co-AN/SN/20 wt.% Mg(TFSI)₂ and PVdC-co-AN/SN/EC/15 wt.% Mg(TFSI)₂ samples are greater than 0.9 and shows that the charge carriers exist in the GPE systems are predominantly ions and the samples are ionic conductors. The results agreed with the argument that no electronic conductivity is expected in the gel-like electrolytes where

liquid electrolytes are entrapped in the almost inert network of polymer hosts and liquid-like charge transport takes place in such systems (Pandey & Hashmi, 2009).

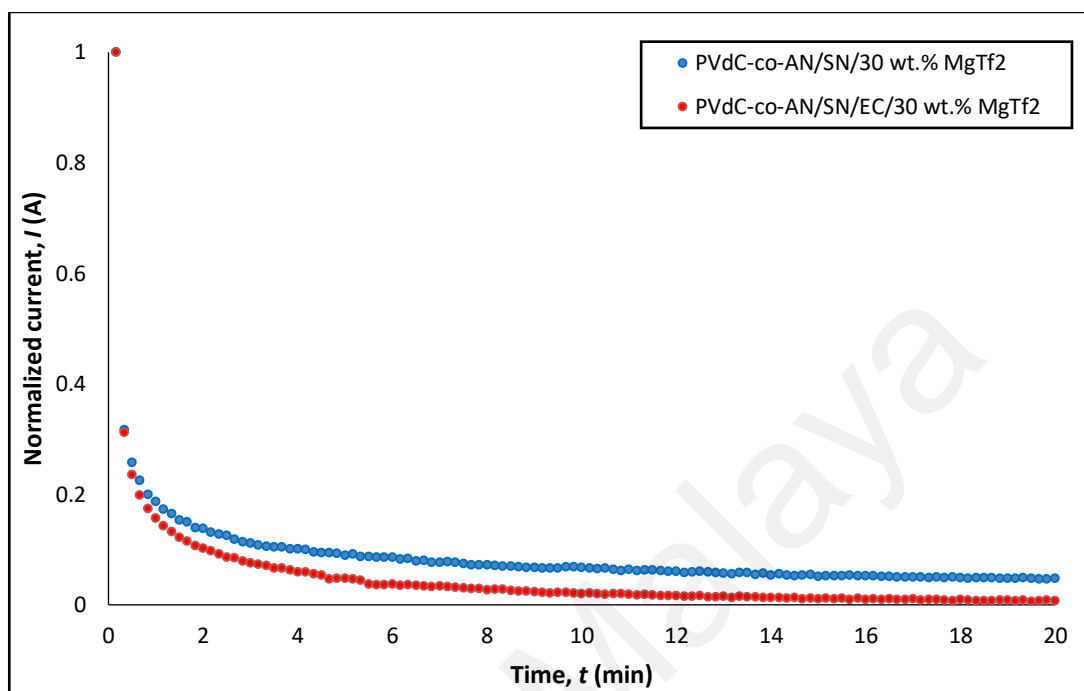


Figure 4.16: Plot of normalized current against time for PVdC-co-AN/SN/30 wt.% MgTf₂ and PVdC-co-AN/SN/EC/30 wt.% MgTf₂.

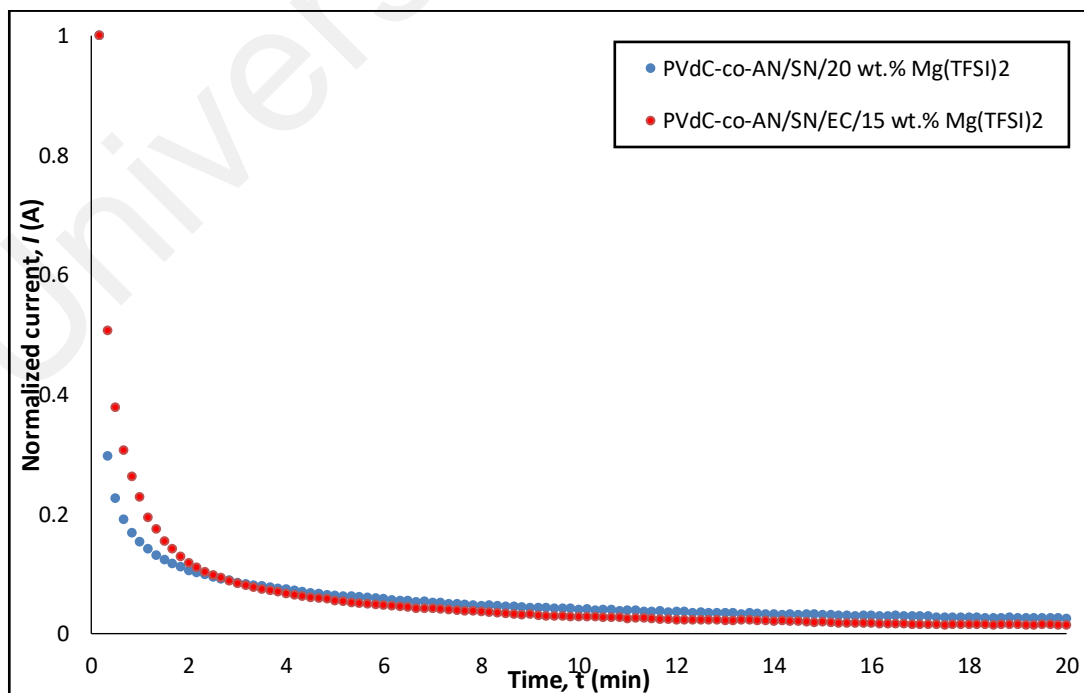


Figure 4.17: Plot of normalized current against time for PVdC-co-AN/SN/20 wt.% Mg(TFSI)₂ and PVdC-co-AN/SN/EC/15 wt.% Mg(TFSI)₂.

Table 4.6: Ionic transference number of GPE samples for MgTf₂ and Mg(TFSI)₂ systems.

Sample	Ionic Transference Number, t_i
PVdC-co-AN/SN/30 wt.% MgTf ₂	0.97
PVdC-co-AN/SN/EC/30 wt.% MgTf ₂	0.99
PVdC-co-AN/SN/20 wt.% Mg(TFSI) ₂	0.98
PVdC-co-AN/SN/EC/15 wt.% Mg(TFSI) ₂	0.99

4.2.2 Cationic Transference Number, t_+

The cationic transference number was then carried out after the confirmation of the charge carriers in the GPEs which are predominantly ions and the contribution from electrons are relatively negligible. In GPE system, due to the difference in mobility of cations and anions, they will have different in transference number, i.e. they contribute differently to the total conductivity. The sum of the transference numbers of cations and anions equals to unity. A method that has been proposed by Evans et. al (Evans et al., 1987) using the combination of AC impedance and DC polarization techniques has been used to evaluate the Mg²⁺ ions transference number, $t_{Mg^{2+}}$ in the polymer electrolytes. In this technique, magnesium foil was used with cell configuration of Mg/GPE/Mg and the cell has been polarized by applying a constant voltage of 0.1 V for 5 hours and the values of initial and final currents, I_0 and I_s were recorded. AC impedance was measured before and after polarization to obtain the values of electrode-electrolyte resistances. The $t_{Mg^{2+}}$ were therefore can be calculated by using equation 3.9. The plot of DC polarization for the highest conducting samples for both MgTF₂ and Mg(TFSI)₂ systems are shown in Figure 4.18 and 4.19 respectively. From all the figures, there is an initial current I_0

observed at the very beginning and the current is then drop continuously. The fall in current from $t = 0$ until the steady-state current I_s was reached is considered to result from two processes (Pandey & Hashmi, 2009):

- (i) the growth at the electrodes of passivating layers to a limiting thickness (which occurs whether or not a current is flowing), and
- (ii) the establishment of a concentration gradient in the electrolyte which affects the motion of the ions.

Meanwhile, the inset graphs of Figure 4.18 and 4.19 show the impedance plots from AC measurements before and after polarization to determine the values of cell resistances. The cell resistances here also increase after polarization due to the resistive characteristic of passivation layer formed at the electrolyte-electrode interfaces. The magnesium ion transference number, $t_{Mg^{2+}}$ for PVdC-co-AN/SN/30 wt.% MgTf₂, PVdC-co-AN/SN/EC/30 wt.% MgTf₂, PVdC-co-AN/SN/20 wt.% Mg(TFSI)₂ and PVdC-co-AN/SN/EC/15 wt.% Mg(TFSI)₂ samples were then calculated and the values obtained are tabulated in Table 4.7. From the table, it can be observed that higher value in cationic transference numbers obtained from double plasticized system for both MgTf₂ and Mg(TFSI)₂ than single plasticized which shows that EC can help in dissociating magnesium salt thus increase the number of Mg²⁺ ions in the system. The GPEs containing Mg(TFSI)₂ also show higher in $t_{Mg^{2+}}$ than that of containing MgTf₂ for both single and double plasticized systems which relates to the easier in ion dissociation of Mg(TFSI)₂ salt than MgTf₂ salt. However, the highest $t_{Mg^{2+}}$ value obtained is from the double plasticized-Mg(TFSI)₂ sample which is 0.59 and thus suggests substantial contributions of Mg²⁺ ions to the total conduction in the electrolyte system. The $t_{Mg^{2+}}$ values obtained are also higher than that calculated by other researchers such as by Choe

et al. (Choe et al., 1997) and also by Mahalakshmi et al. (Mahalakshmi et al., 2020) which they obtained values of 0.38 and 0.35 respectively. A large transference number can reduce concentration polarization of electrolytes during charge–discharge steps, and thus produce higher power density. It is highly desirable that the transference number of lithium ions (in general) approaches value of one in an electrolyte system. However, many existing electrolyte systems, either liquid or polymeric have transference numbers less than 0.5 (Bruce et al., 1989; Evans et al., 1987; Song et al., 1999).

Table 4.7: Magnesium ion transference number of GPE samples for MgTf₂ and Mg(TFSI)₂ systems.

Sample	Magnesium ion transference number, $t_{Mg^{2+}}$
PVdC-co-AN/SN/30 wt.% MgTf ₂	0.33
PVdC-co-AN/SN/EC/30 wt.% MgTf ₂	0.56
PVdC-co-AN/SN/20 wt.% Mg(TFSI) ₂	0.36
PVdC-co-AN/SN/EC/15 wt.% Mg(TFSI) ₂	0.59

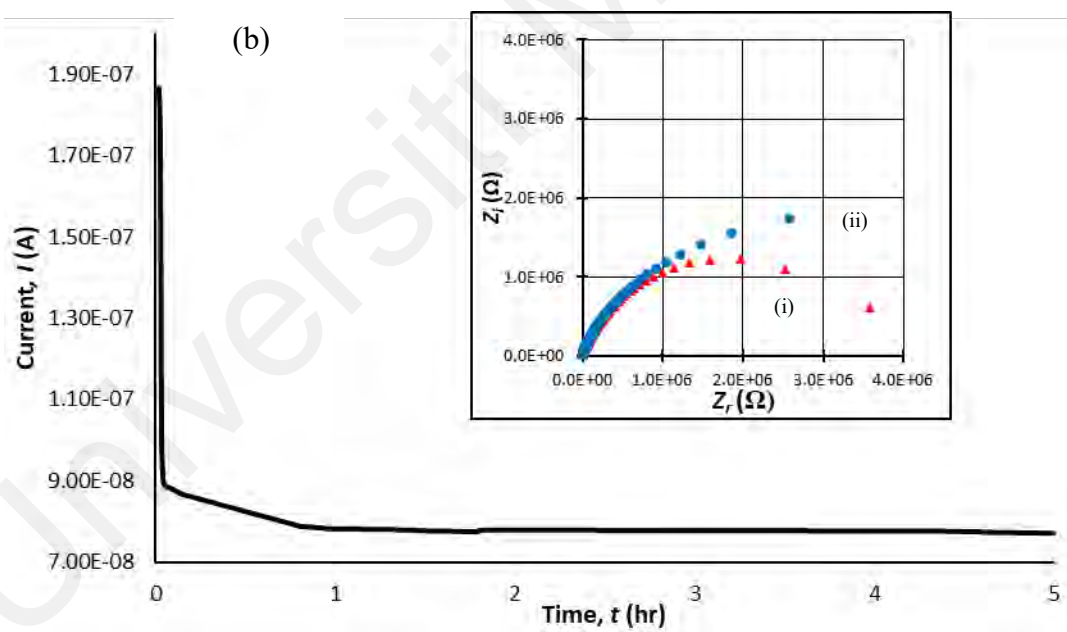
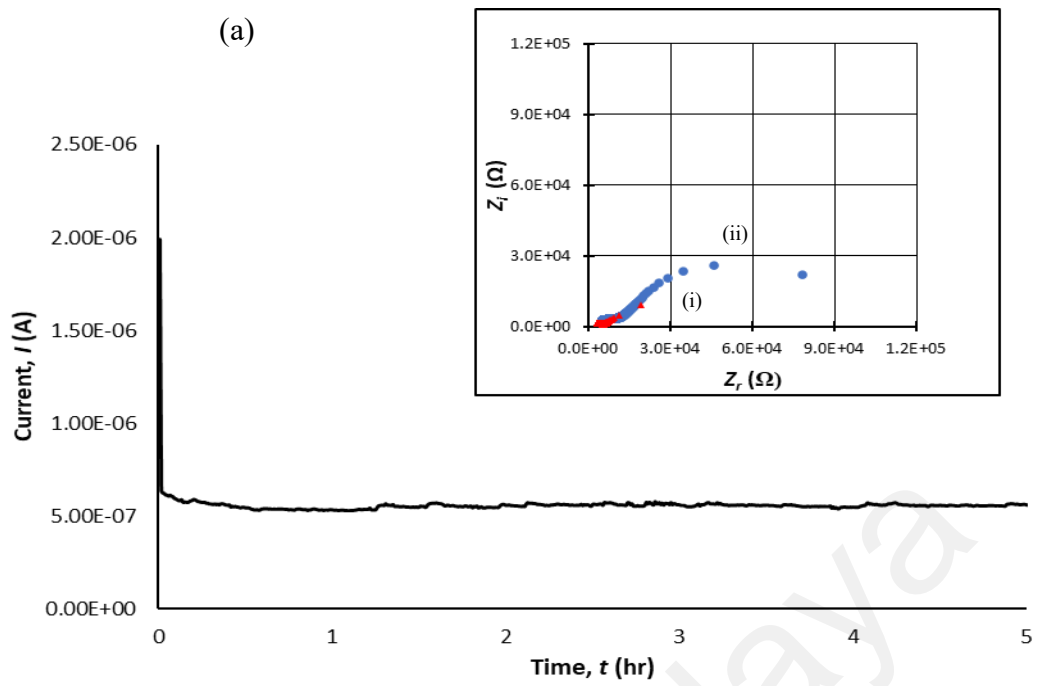


Figure 4.18: DC polarization plots for GPE samples of (a) PVdC-co-AN/SN/30 wt.% MgTf₂ and (b) PVdC-co-AN/SN/EC/30 wt.% MgTf₂. Inset graph shows the impedance plots (i) before and (ii) after DC polarization.

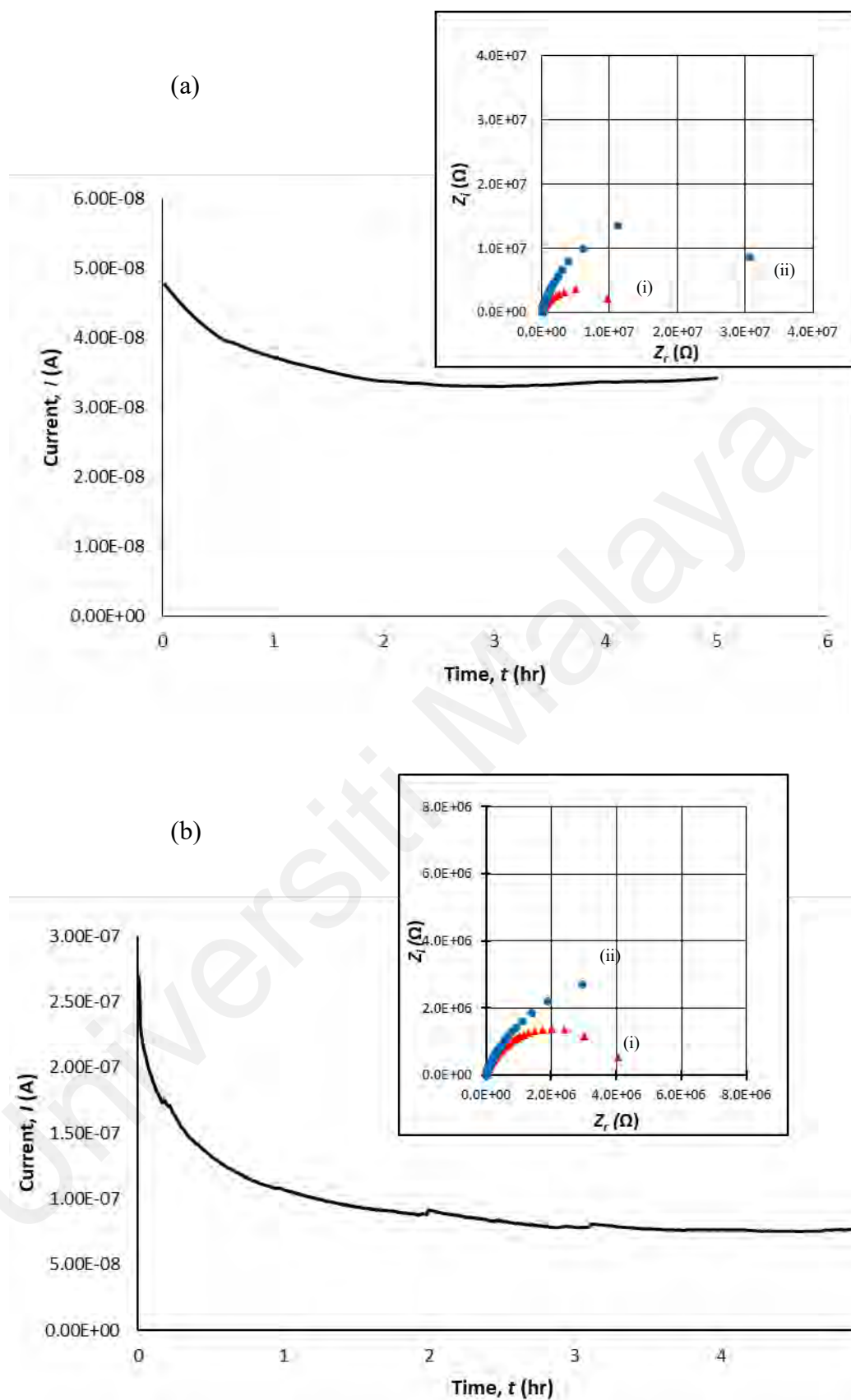


Figure 4.19: DC polarization plots for GPE samples of (a) PVdC-co-AN/SN/20 wt.% Mg(TFSI)₂ and (b) PVdC-co-AN/SN/EC/15 wt.% Mg(TFSI)₂. Inset graph shows the impedance plots (i) before and (ii) after DC polarization.

CHAPTER 5: STRUCTURAL AND MORPHOLOGICAL ANALYSIS

5.1 Fourier Transform Infrared Spectroscopy (FTIR) analysis

Fourier Transform Infrared Spectroscopy (FTIR) is used to study the structure of polymer PVdC-co-AN, plastic crystal SN, plasticizer EC, MgTf₂ and Mg(TFSI)₂ salts as well as the interaction between them. In this FTIR analysis, since the interaction between the constituents were influenced by the vibrational modes of their atoms or molecules, the changes of the vibrational bands such as the bands' intensity and shifting of bands observed in the FTIR spectra were investigated. If the interactions exist, complexation of the GPE samples were verified.

5.1.1 Pure PVdC-co-AN

Table 5.1 lists the vibrational modes and their corresponding wavenumbers of pure PVdC-co-AN sample while the FTIR spectrum of the sample is as shown in Figure 5.1. It can be observed that the vibrational band detected at 2245 cm⁻¹ is the C≡N stretching (nitrile group) which in PVdC-co-AN, it is the most important band as it representing the functional group of the polymer. Any changes of this vibrational band will be related to the interaction of magnesium salts with nitrogen atoms in the polymer since nitrile band is a strong electron withdrawing group. An intense band was also appeared at 1059 cm⁻¹ which assigned as CH₂ asymmetric stretching of the pure polymer whereas a weak vibrational band at 1358 cm⁻¹ is referred to CH₂ wagging. Meanwhile, the vibrational bands at 1433 cm⁻¹, (1775 and 1803 cm⁻¹) and 2976 cm⁻¹ are denoted as CH₂ symmetric bending, C=O stretching, and C=CH₂ symmetric stretching, respectively.

Table 5.1: The vibrational modes and corresponding wavenumbers of pure PVdC-co-AN.

Assignment of bands	Wavenumbers (cm ⁻¹)	References	Wavenumbers obtained from this work (cm ⁻¹)
CH ₂ asymmetric stretching (w)	1038-1073	(Mathew et al., 2015; Shanthi et al., 2013a)	1059
CH ₂ wagging	1357	(Shanthi, Ramachandran, et al., 2017)	1358
CH ₂ symmetric bending	1425	(Shanthi et al., 2013a)	1433
C=O stretching	1775	(Shanthi et al., 2013a; Shanthi, Ramachandran, et al., 2017)	1775, 1803
C≡N stretching	2245	(Shanthi, Ramachandran, et al., 2017; Shanthi, Subadevi, et al., 2017; Subbu et al., 2015)	2245
C=CH ₂ symmetric stretching	2975	(Shanthi, Ramachandran, et al., 2017)	2976

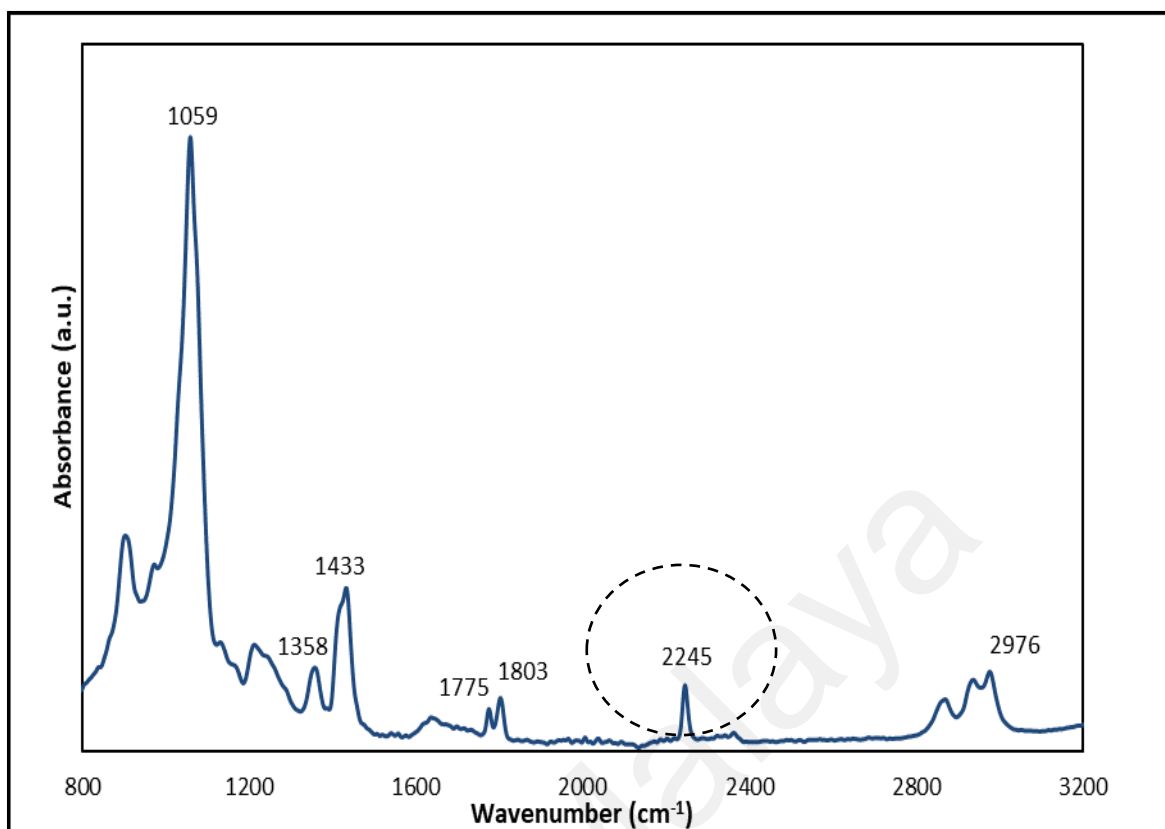


Figure 5.1: FTIR spectra of pure PVdC-co-AN sample in the region of 800 cm^{-1} to 3200 cm^{-1} .

5.1.2 PVdC-co-AN/SN/EC

In this section, FTIR spectra of pure SN and EC will be discussed along with the FTIR spectra of GPE samples containing SN (single plasticized) and both SN and EC (double plasticized).

Table 5.2 shows the vibrational modes exist in SN and their corresponding wavenumbers. Several vibrational bands are observed on the FTIR spectrum of SN as in Figure 5.2 with wavenumber at 1336 cm^{-1} denoted as CH_2 bending and gauche whereas an intense peak observed at 1424 cm^{-1} is associated with CH_2 bending, gauche and trans of SN. In SN, its functional group is also the nitrile group ($\text{C}\equiv\text{N}$ stretching), same as the pure PVdC-co-AN which detected at 2253 cm^{-1} . On the other hand, vibrational bands at 2951 cm^{-1} and (2987 and 1001) cm^{-1} are denoted as CH_2 bending and CH_2 gauche

respectively. For wavenumbers below 1000 cm^{-1} , the vibrational band at 917 cm^{-1} is referred as C-CN stretch and trans while at 963 cm^{-1} represents C-CN gauche, CH_2 rock and CH_2 twist of SN.

Table 5.2: The vibrational modes and corresponding wavenumbers of pure SN.

Assignment of bands	Wavenumbers (cm^{-1})	References	Wavenumbers obtained from this work (cm^{-1})
C-CN stretch, trans	917	(Das et al., 2009; Das & Bhattacharyya, 2010; Gupta & Rhee, 2012)	917
C-CN, gauche, CH_2 rock, CH_2 twist	963	(Das et al., 2009; Das & Bhattacharyya, 2010; Gupta & Rhee, 2012; Taib & Hayati, 2014)	962
CH_2 gauche	1004, 2990	(Das et al., 2009; Das & Bhattacharyya, 2010; Gupta & Rhee, 2012)	1001, 2987
CH_2 bending, gauche	1335	(Das et al., 2009; Gupta & Rhee, 2012)	1336
CH_2 bending, gauche and trans	1424	(Das et al., 2009; Gupta & Rhee, 2012; Taib & Hayati, 2014)	1424
$\text{C}\equiv\text{N}$ stretching	2254	(Das et al., 2009; Gupta & Rhee, 2012; Taib & Hayati, 2014)	2253
CH_2 bending	2953	(Das et al., 2009; Gupta & Rhee, 2012)	2951

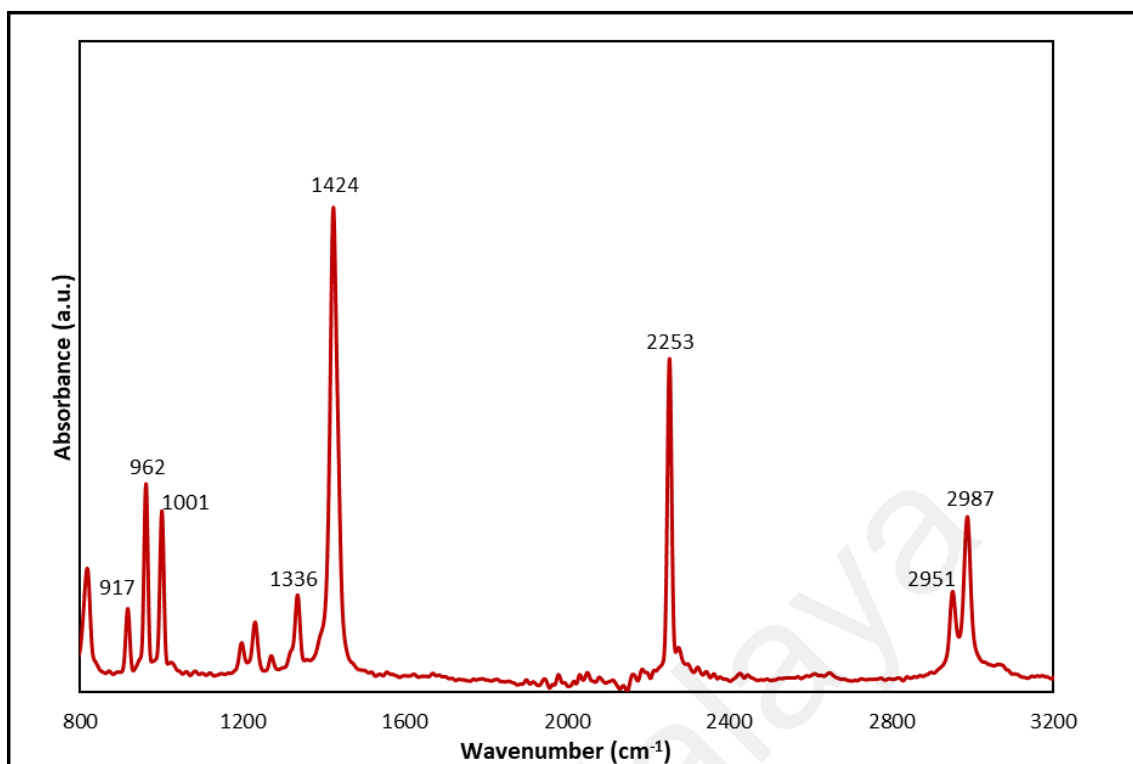


Figure 5.2: FTIR spectra of pure SN in the region of 800 cm⁻¹ to 3200 cm⁻¹.

Meanwhile, the list of vibrational modes and the corresponding wavenumbers of pure EC is displayed as in Table 5.3. From the FTIR spectrum plotted in Figure 5.3, the ring breathing are observed at 893 and 1070 cm⁻¹. The vibrational bands at 973 and 1170 cm⁻¹ are denoted as the skeletal stretching of EC while the bands at (1400 and 1420) cm⁻¹ and 1470 cm⁻¹ are designated for CH₂ wagging and CH₂ bending respectively. The C=O stretching of EC which is the carbonyl group is depicted at 1780 and 1810 cm⁻¹ (doublet characteristic peaks) and act as the functional group of EC.

Table 5.3: The vibrational modes and corresponding wavenumbers of pure EC.

Assignment of bands	Wavenumbers (cm ⁻¹)	References	Wavenumbers obtained from this work (cm ⁻¹)
Ring breathing	891,1060, 1224,1059	(Huang, 1996; Johan et al., 2011; Z. Wang et al., 1996)	893, 1070
Skeletal stretching	975,1160	(Chintapalli & Frech, 1996; Johan et al., 2011)	973, 1170
CH ₂ wagging	1390,1420	(Chintapalli & Frech, 1996; Johan et al., 2011)	1400, 1420
CH ₂ bending	1470	(Chintapalli & Frech, 1996; Johan et al., 2011)	1470
C=O stretching	1773 & 1898, 1786, 1730, 1751, 1775, 1806	(Chintapalli & Frech, 1996; Huang, 1996; Johan et al., 2011; Kim et al., 1998; Z. Wang et al., 1996)	1780, 1810

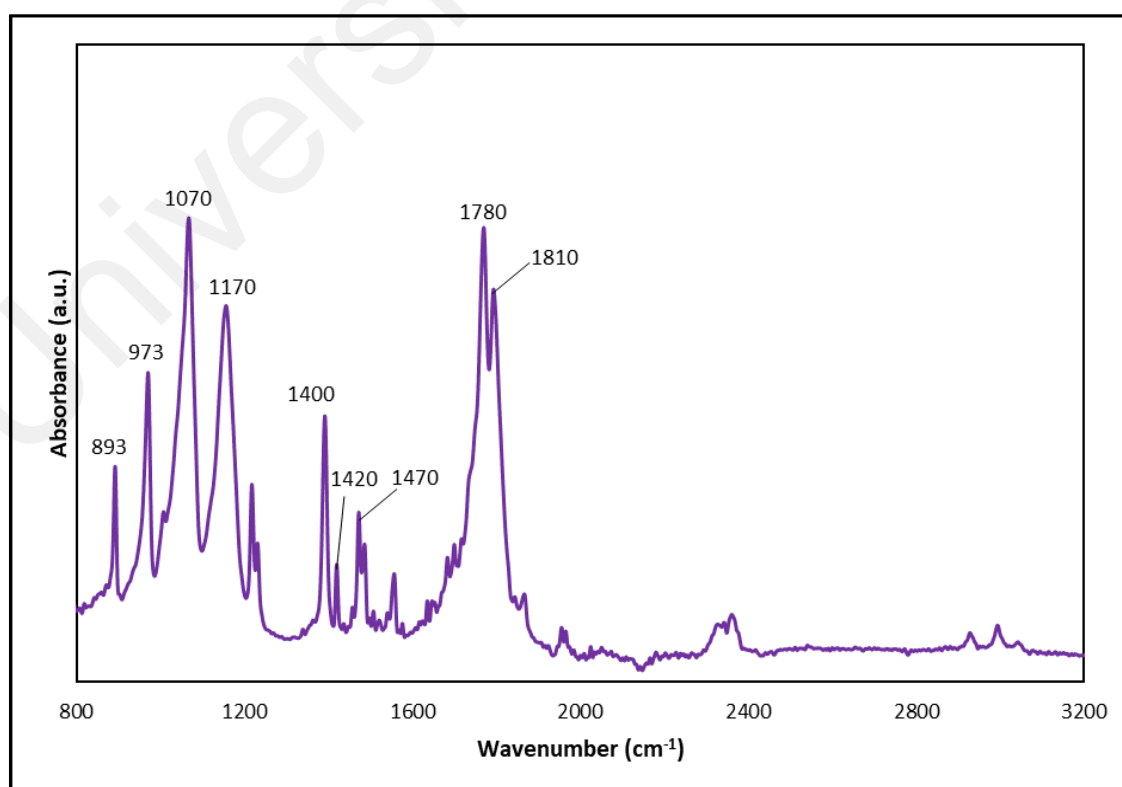


Figure 5.3: FTIR spectra of pure EC in the region of 800 cm⁻¹ to 3200 cm⁻¹.

Figure 5.4 shows the FTIR spectra of pure PVdC-co-AN, PVdC-co-AN/SN and PVdC-co-AN/SN/EC. From the spectra, the changes of the vibrational bands of the PVdC-co-AN were observed. Upon the addition of SN, the band at 1059 cm^{-1} associated to CH_2 asymmetric stretching of PVdC-co-AN is shifted to 1065 cm^{-1} and the intensity decreased. Whereas, the bands at 1775 cm^{-1} and 1803 cm^{-1} assigned as $\text{C}=\text{O}$ stretching of PVdC-co-AN disappeared affected from SN. For other vibrational bands, the overlapping of the bands of both PVdC-co-AN and SN were detected which are the band at 2976 cm^{-1} of $\text{C}=\text{CH}_2$ symmetric stretching (shifted to 2987 cm^{-1}) and 1433 cm^{-1} and 1358 cm^{-1} (CH_2 bending of SN) (shifted to 1424 cm^{-1} and 1336 cm^{-1} respectively). While for the band at 2253 cm^{-1} associates with both $\text{C}\equiv\text{N}$ stretching of PVdC-co-AN and SN, the band retained at 2253 cm^{-1} and increase in intensity which shows strong combination of the functional group from both PVdC-co-AN and SN.

From the spectrum of PVdC-co-AN/SN/EC in Figure 5.4, the addition of EC drastically changed the spectrum of PVdC-co-AN/SN by reappearing of the $\text{C}=\text{O}$ stretching at 1774 cm^{-1} and 1799 cm^{-1} results from the overlapping of the doublet characteristics peaks of EC with the vibrational band of polymer. There are also huge increases observed on the intensity of these bands compared to pure PVdC-co-AN. These bands which are disappeared in PVdC-co-AN/SN system as stated before proved the presence of EC in PVdC-co-AN/SN/EC system. On the other hand, the bands at 1358 cm^{-1} and 1058 cm^{-1} denoted as CH_2 wagging and CH_2 asymmetric stretching of PVdC-co-AN are both shifted to 1391 cm^{-1} and 1072 cm^{-1} respectively also with the overlapping of the characteristics band of EC with the polymer. The band at 2253 cm^{-1} associates with $\text{C}\equiv\text{N}$ stretching of PVdC-co-AN and SN) shifted back to 2252 cm^{-1} with a decrease in intensity. This shows the presence of EC has affected the combined nitrile group of PVdC-co-AN and SN. Meanwhile, the band at 1424 cm^{-1} referred as CH_2 symmetric bending shows an

intense decrease in peak which also indicates some interactions between PVdC-co-AN, SN and EC.

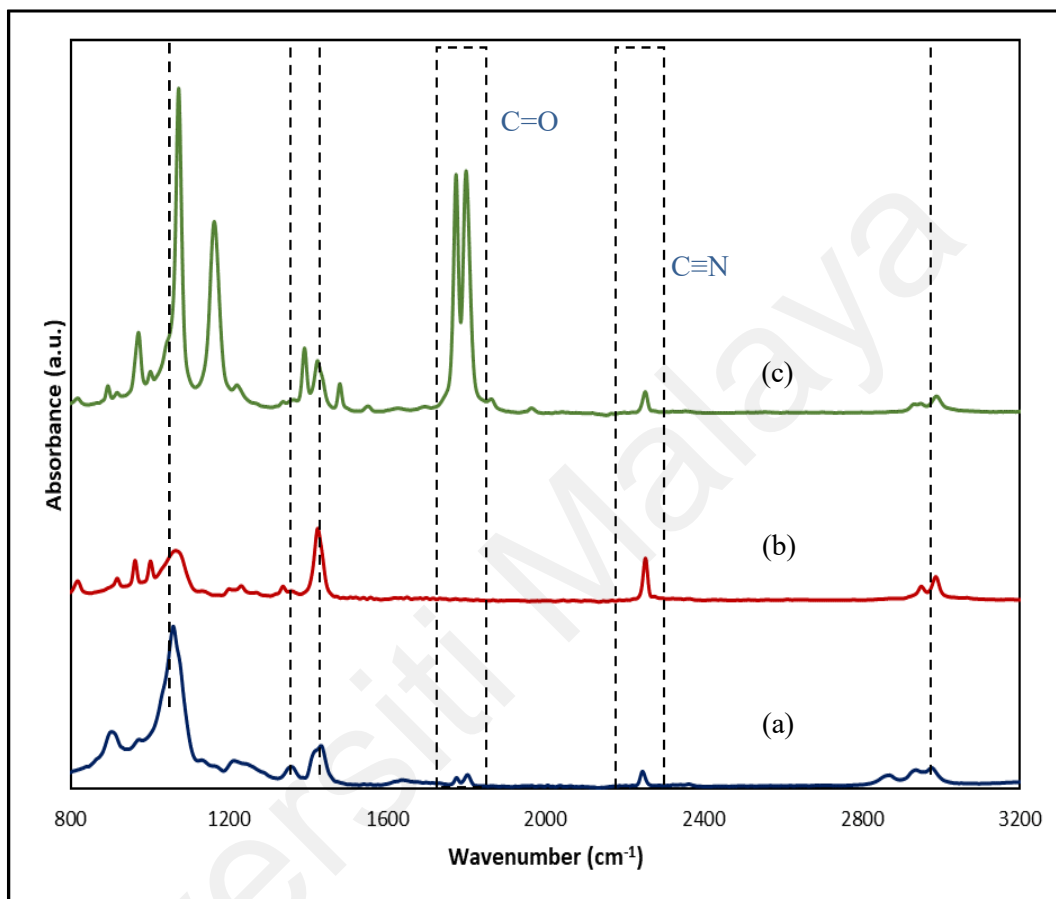


Figure 5.4: FTIR spectra of (a) pure PVdC-co-AN, (b) PVdC-co-AN/SN and (c) PVdC-co-AN/SN/EC.

5.1.3 PVdC-co-AN/SN/MgTf₂ and PVdC-co-AN/SN/EC/MgTf₂ systems

The vibrational modes and corresponding wavenumbers of pure MgTf₂ is as shown in Table 5.4 where the FTIR spectrum of pure MgTf₂ is shown in Figure 5.5. The changes of the vibrational bands of the spectra of PVdC-co-AN/SN and PVdC-co-AN/SN/EC after the addition of MgTf₂ were analyzed.

Table 5.4: The vibrational modes and corresponding wavenumbers of pure MgTf₂.

Assignment of bands	Wavenumbers (cm ⁻¹)	References	Wavenumbers obtained from this work (cm ⁻¹)
SO ₃ symmetrical stretching, $\nu_s(\text{SO}_3)$	1032	(Isa et al., 2014; Jeong et al., 2006; Pandey & Hashmi, 2009)	1035, 1056
SO ₃ asymmetrical stretching, $\nu_{as}(\text{SO}_3)$	1157	(Isa et al., 2014; Jeong et al., 2006; Pandey & Hashmi, 2009)	1190
CF ₃ symmetrical bending, $\delta_s(\text{CF}_3)$	756	(Isa et al., 2014; Pandey & Hashmi, 2009)	760

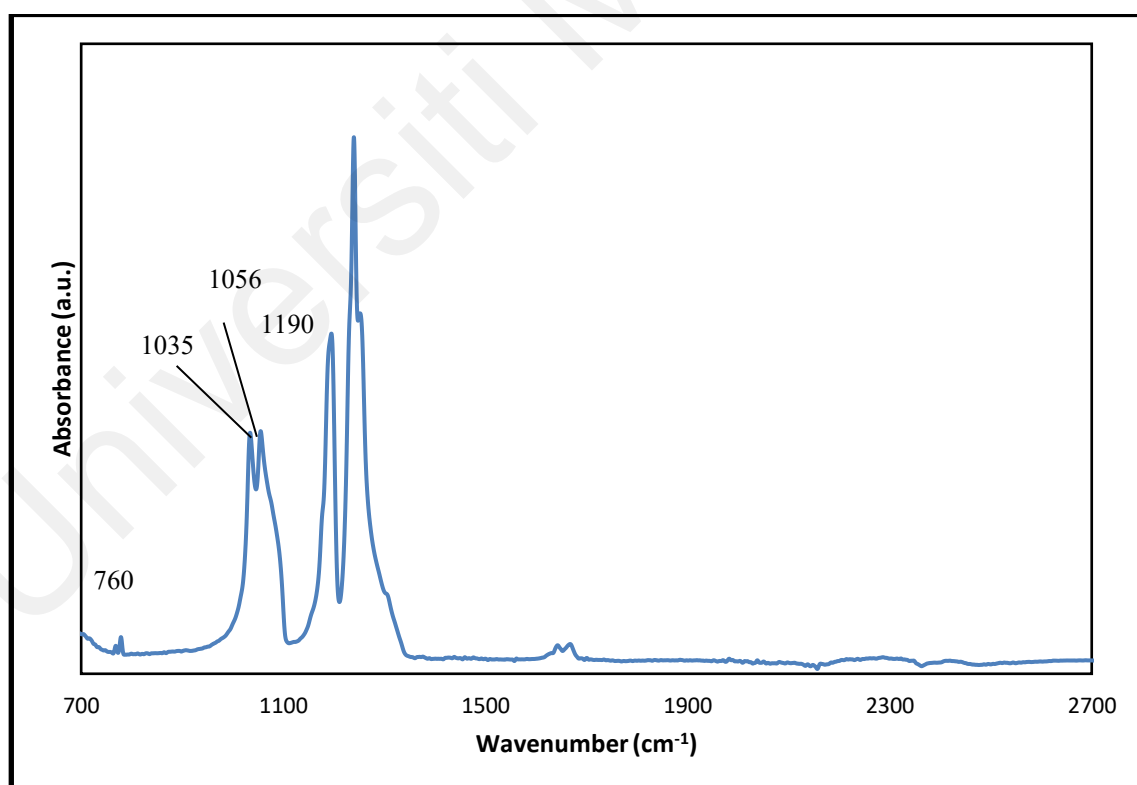


Figure 5.5: FTIR spectrum of pure MgTf₂.

Figure 5.6 depicts the FTIR spectra of PVdC-co-AN/SN system with 5 to 30 wt.% MgTf₂. These spectra are analyzed in reference to the spectrum of PVdC-co-AN/SN sample in Figure 5.4. Upon the addition of MgTf₂ salt, the band at 1065 cm⁻¹ associated with CH₂ asymmetric stretching of PVdC-co-AN is shifted to 1071 cm⁻¹ for PVdC-co-AN/SN sample containing 5 to 15 wt.% MgTf₂. However, the vibrational band is then shifted back to 1059 cm⁻¹ after the addition of 20 wt.% MgTf₂ into the sample and then disappeared when the salt increases up to 25 wt.% and 30 wt.%. This shows the interaction between PVdC-co-AN, SN and MgTf₂ since the peak at 1059 cm⁻¹ also originate from pure MgTf₂. Whereas, the band at 2987 cm⁻¹ of C=CH₂ symmetric stretching of the polymer is shifted in between 2986 to 2981 cm⁻¹ throughout the GPE system. For CH₂ symmetric bending, the band at 1424 cm⁻¹ is shifted between 1425 to 1426 cm⁻¹ as well as the intensity decreases as the salt increases. The functional group of the polymer which is the C≡N stretching, this band is shifted from 2253 cm⁻¹ to between 2250 and 2248 cm⁻¹ throughout the PVdC-co-AN/SN/MgTf₂ system. In order to obtain a better clarity on the interaction occur in the nitrile group of the polymer, the FTIR spectra is then expanded at the range of the wavenumber where the nitrile group of the PVdC-co-AN located as shown in Figure 5.7. From the spectra, as the concentration of MgTf₂ salt increases, the peaks at (2200 cm⁻¹ to 2300 cm⁻¹) decreases. This is because of the two arguments, i.e; firstly, as SN also has the nitrile functional group, the GPE with less amount of MgTf₂ salt exhibits more intense peak as SN might be dominant in the system, while secondly, the weaker peak indicated an amorphous nature of GPE system. These arguments show the interaction between the nitrile group, C≡N and Mg²⁺ ions from MgTf₂ salt (Hambali et al., 2016; Yoshihara et al., 1964).

Figure 5.8 shows the FTIR spectra of PVdC-co-AN/SN/EC/MgTf₂ system. From the spectra, it is observed that the doublet characteristics of EC at 1799 cm⁻¹ and 1774 cm⁻¹ are shifted to between 1800 to 1802 cm⁻¹ and almost remains at 1774 cm⁻¹ respectively.

This shows the strong characteristic of functional group of EC which is not highly affected by the presence of MgTf_2 salt. Meanwhile, the band at 1391 cm^{-1} of CH_2 wagging (overlapped band of PVdC-co-AN and EC) shifted to between 1392 and 1393 cm^{-1} when 5 to 15 wt.% of MgTf_2 added and then disappeared beyond 15 wt.% of MgTf_2 . For the next overlapping band of PVdC-co-AN with EC which is CH_2 asymmetric stretching, this band shifted to between 1072 to 1074 cm^{-1} throughout the system. Whereas, the band of CH_2 symmetric bending of PVdC-co-AN at 1424 cm^{-1} also shifted to between 1423 to 1424 cm^{-1} . In addition, there also exists new vibrational band due to the addition of MgTf_2 salt which can be observed at 1030 to 1031 cm^{-1} associates with the SO_3 symmetrical stretching of the salt. For the functional group of the polymer which is the nitrile band, this band shifted to between 2248 cm^{-1} and 2250 cm^{-1} and the intensities decrease upon the addition of MgTf_2 which shows the interaction between the nitrile group, $\text{C}\equiv\text{N}$ with Mg^{2+} ion. For more clarifying on the interaction of these Mg^{2+} ions, the close up of the nitrile band is also plotted in the wavenumber region between 2200 and 2300 cm^{-1} as shown in Figure 5.9.

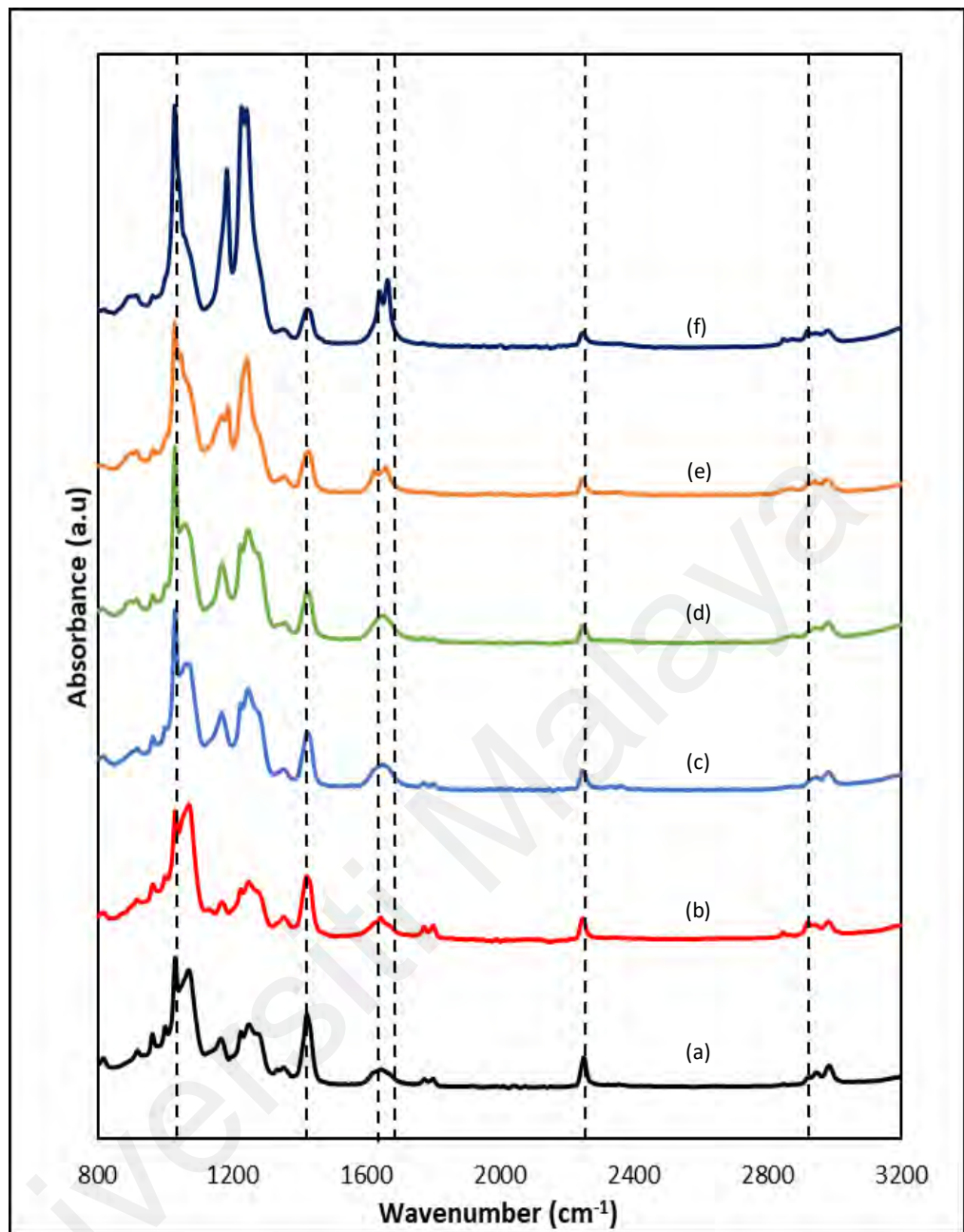


Figure 5.6: FTIR spectra of PVdC-co-AN/SN containing (a) 5 wt.% MgTf₂ , (b) 10 wt.% MgTf₂, (c) 15 wt.% MgTf₂, (d) 20 wt.% MgTf₂, (e) 25 wt.% MgTf₂ and (f) 30 wt.% MgTf₂.

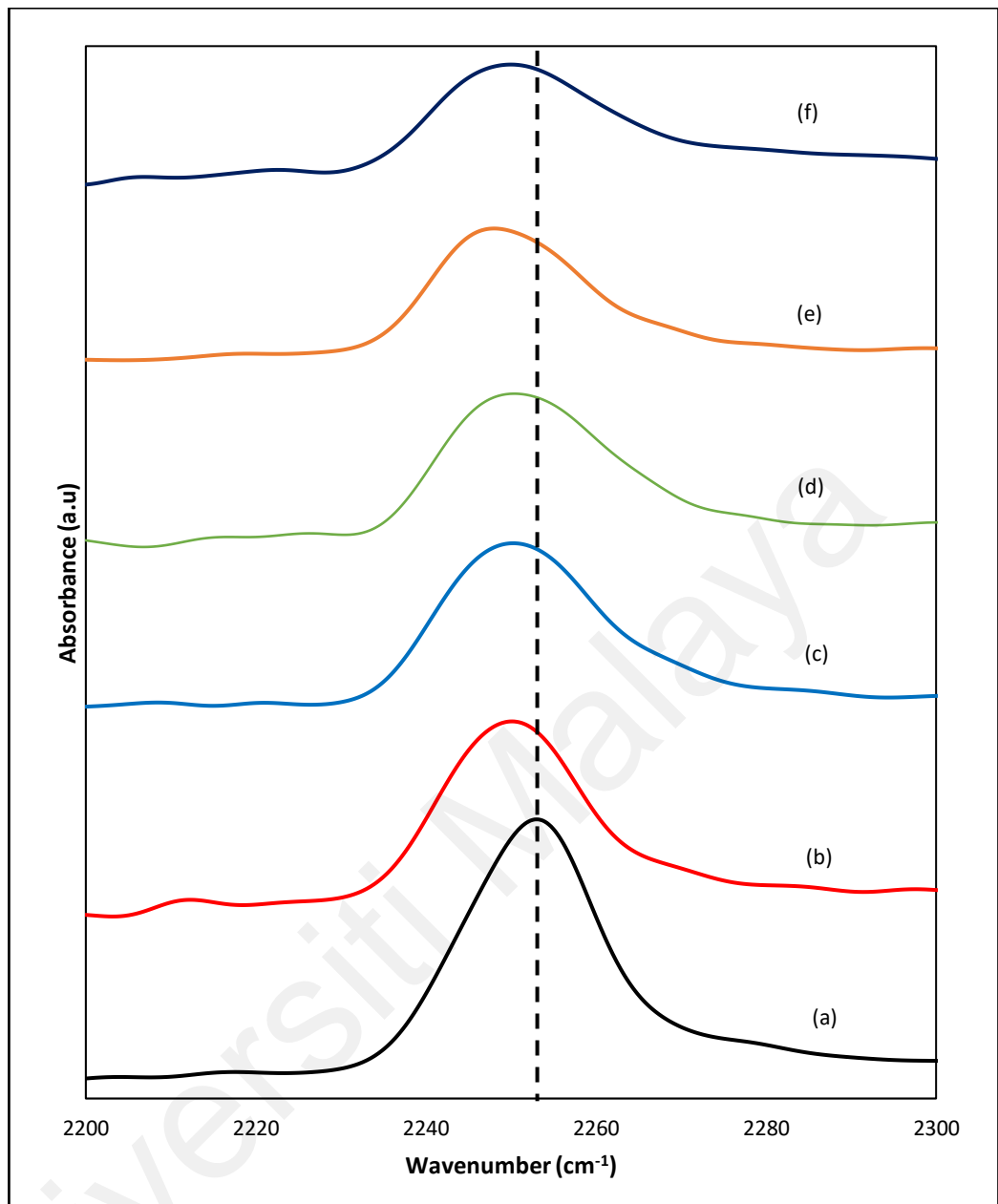


Figure 5.7: The close up of nitrile band of PVdC-co-AN/SN containing (a) 5 wt.% MgTf₂, (b) 10 wt.% MgTf₂, (c) 15 wt.% MgTf₂, (d) 20 wt.% MgTf₂, (e) 25 wt.% MgTf₂ and (f) 30 wt.% MgTf₂.

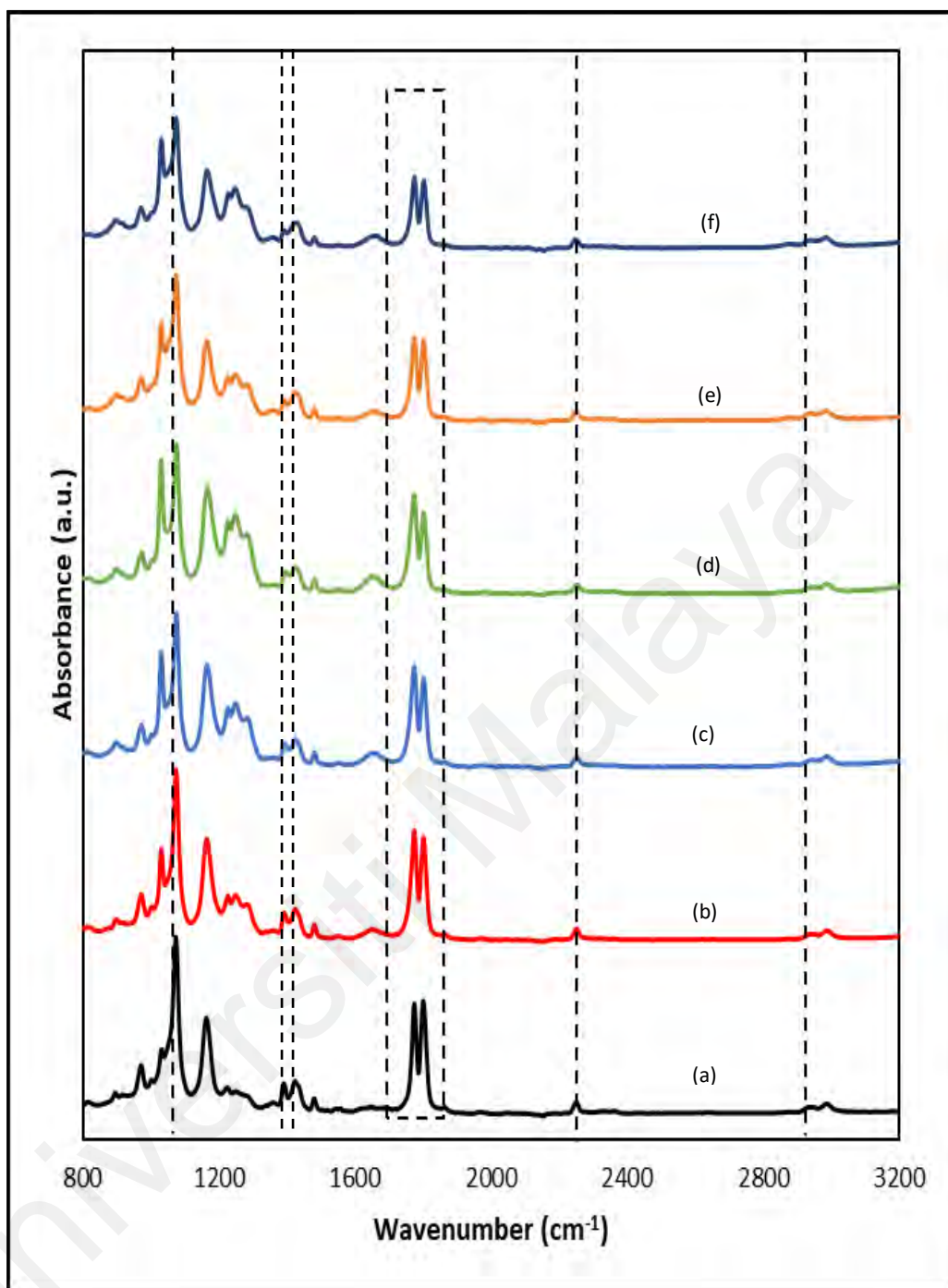


Figure 5.8: FTIR spectra of PVdC-co-AN/SN/EC containing (a) 5 wt.% MgTf₂, (b) 10 wt.% MgTf₂, (c) 15 wt.% MgTf₂, (d) 20 wt.% MgTf₂, (e) 25 wt.% MgTf₂ and (f) 30 wt.% MgTf₂.

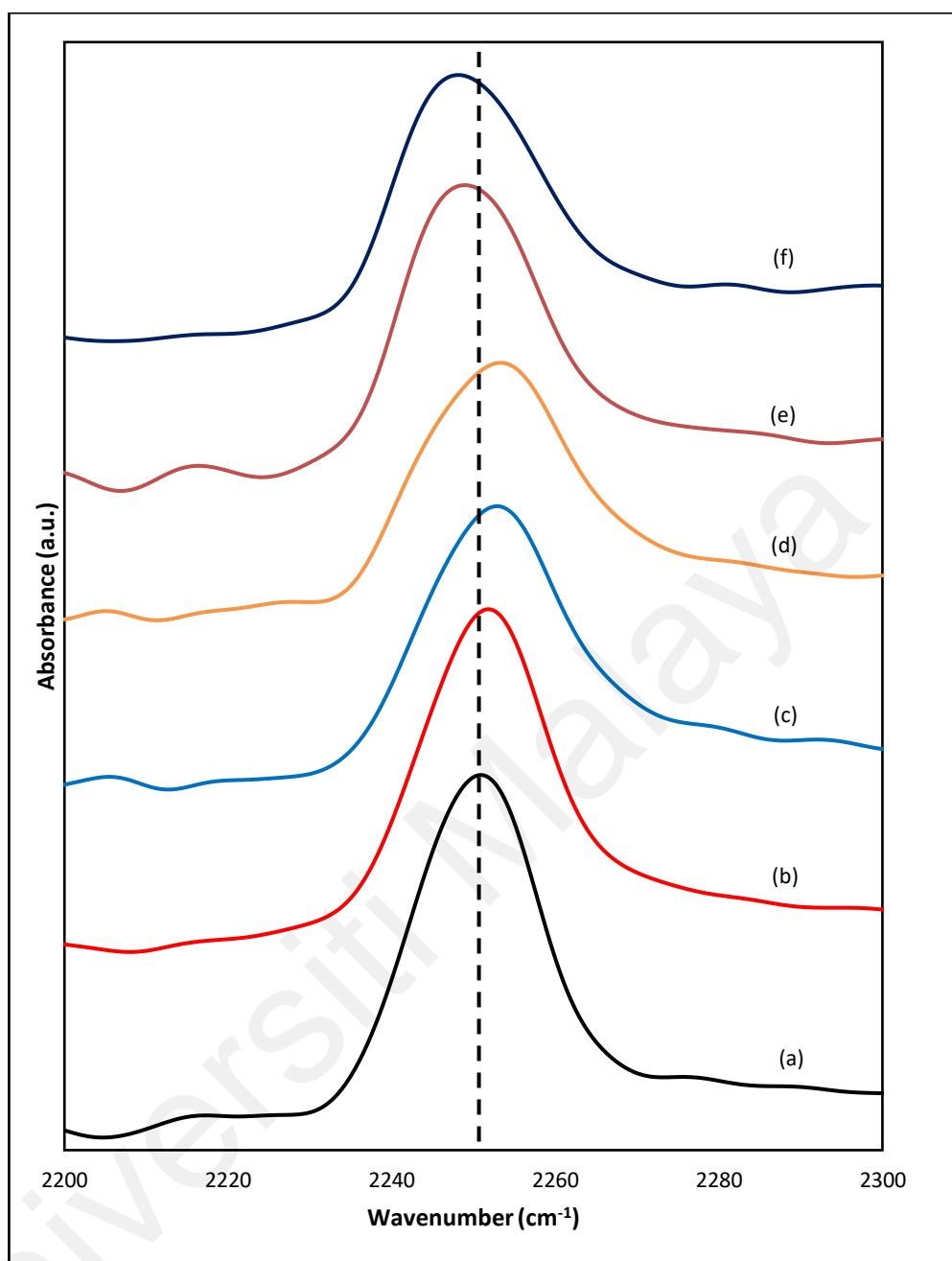


Figure 5.9: The close up of nitrile band of PVdC-co-AN/SN/EC containing (a) 5 wt.% MgTf₂, (b) 10 wt.% MgTf₂, (c) 15 wt.% MgTf₂, (d) 20 wt.% MgTf₂, (e) 25 wt.% MgTf₂ and (f) 30 wt.% MgTf₂.

5.1.4 PVdC-co-AN/SN/ Mg(TFSI)₂ and PVdC-co-AN/SN/EC/ Mg(TFSI)₂ systems

The vibrational modes and their corresponding wavenumbers of pure Mg(TFSI)₂ is as shown in Table 5.5 while the FTIR spectrum of pure Mg(TFSI)₂ is shown in Figure 5.10. The changes of the vibrational bands of the spectra of PVdC-co-AN/SN and PVdC-co-AN/SN/EC after the addition of Mg(TFSI)₂ were analyzed.

Table 5.5: The vibrational modes and corresponding wavenumbers of pure Mg(TFSI)₂.

Assignment of bands	Wavenumbers (cm ⁻¹)	References	Wavenumbers obtained from this work (cm ⁻¹)
SO ₂ symmetrical stretching, $\nu_s(\text{SO}_2)$	1065	(Ramesh & Lu, 2008; Sim et al., 2016)	1043
SO ₂ asymmetrical stretching, $\nu_{as}(\text{SO}_2)$	1142, 1333, 1356	(Ramesh & Lu, 2008; Sim et al., 2016)	1132, 1345
CF ₃ symmetrical stretching, $\nu_s(\text{CF}_3)$	1193	(Ramesh & Lu, 2008; Sim et al., 2016)	1190
S-N stretching	740	(Ramesh & Lu, 2008; Sim et al., 2016)	743
C-S and S-N stretching	787	(Ramesh & Lu, 2008)	795

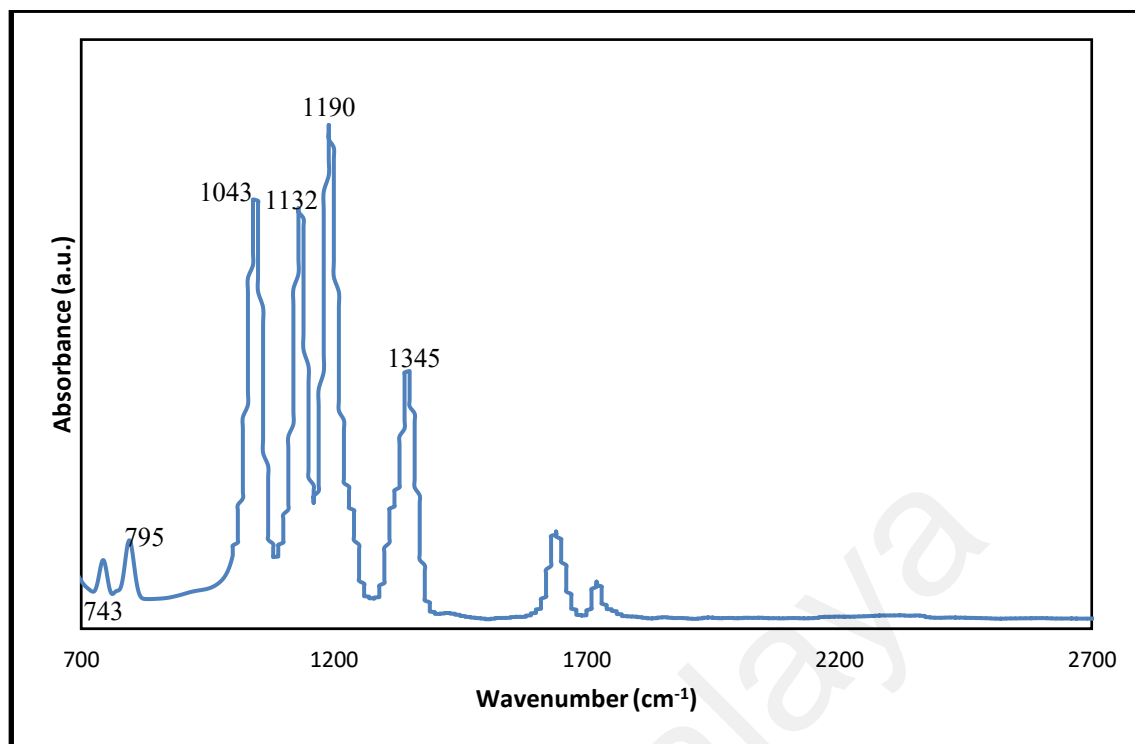


Figure 5.10: FTIR spectrum of pure Mg(TFSI)₂.

Figure 5.11 depicts the FTIR spectra of PVdC-co-AN/SN system with 5 to 30 wt.% Mg(TFSI)₂. The change of vibrational bands of PVdC-co-AN/SN after the addition of Mg(TFSI)₂ are observed. The band at 1065 cm⁻¹ associated with CH₂ asymmetric stretching of PVdC-co-AN is shifted back to between 1055 and 1059 cm⁻¹. Meanwhile, for the vibrational band of CH₂ symmetric bending, the band at 1424 cm⁻¹ is shifted between 1423 to 1425 cm⁻¹ while for the band at 1336 cm⁻¹, the band is shifted from 1350 to 1352 cm⁻¹ throughout the system. There are also new peaks detected due to the addition of Mg(TFSI)₂ into the PVdC-co-AN/SN system which are peaks at (1336 to 1137 cm⁻¹) due to SO₂ asymmetrical stretching and peaks of CF₃ symmetrical stretching (1189 to 1198 cm⁻¹). The band at 2987 cm⁻¹ of C=CH₂ symmetric stretching of the polymer is shifted in between 2984 to 2986 cm⁻¹ throughout the GPE system. For the most important band which is the nitrile band at 2253 cm⁻¹, this band shifted to between 2248 to 2255 cm⁻¹. The close up of the nitrile band is plotted in the Figure 5.12. From the figure, the

shifting of the nitrile band can be clearly observed as well as the change in intensity of the vibrational band and prove the interaction of $\text{Mg}(\text{TFSI})_2$ with the pure polymer.

Figure 5.13 shows the FTIR spectra of PVdC-co-AN/SN/EC/ $\text{Mg}(\text{TFSI})_2$ system. From the spectra, it is observed that the doublet characteristics of EC in 1799 and 1774 cm^{-1} are shifted to (1880 to 1802 cm^{-1}) and almost remains at 1774 cm^{-1} with decreased in intensity respectively. Meanwhile, the band at 1391 cm^{-1} of CH_2 wagging (overlapped band of PVdC-co-AN and EC) shifted to 1392 cm^{-1} when 5 wt.% of $\text{Mg}(\text{TFSI})_2$ added and then shifted to 1393 cm^{-1} when 10 wt.% of $\text{Mg}(\text{TFSI})_2$ added to the samples. The band then disappeared when higher salt content added. This shows the presence of salt has affected the vibrational band origins from both the pure polymer and EC which shows the interaction between them. Whereas, for the next overlapping band of PVdC-co-AN with EC which is CH_2 asymmetric stretching, this band shifted to between 1073 to 1075 cm^{-1} throughout the system. The band at 1424 cm^{-1} referred as CH_2 symmetric bending also shifted to between 1423 to 1424 cm^{-1} . In addition, there also exists new vibrational band due to the addition of $\text{Mg}(\text{TFSI})_2$ salt which can be observed at 1350 to 1352 (comes from SO_2 asymmetrical stretching at 1345 cm^{-1}) throughout the system. This confirms the interaction of all the constituents in the system and complexation between them has occurred. For the FTIR spectra of PVdC-co-AN/SN/EC/ $\text{Mg}(\text{TFSI})_2$, the close up of nitrile band of the PVdC-co-AN are also plotted in the wavenumber region between 2200 and 2300 cm^{-1} as shown in Figure 5.14 to give more clarity on the shifting of the band. The band also shown a decrease in intensity when adding $\text{Mg}(\text{TFSI})_2$ salt with the lowest intensity detected at 15 wt.% $\text{Mg}(\text{TFSI})_2$ salt; this shows at this point, the interaction of Mg^{2+} with the nitrile group might be the highest as the sample also shows the highest in conductivity compared to the other samples.

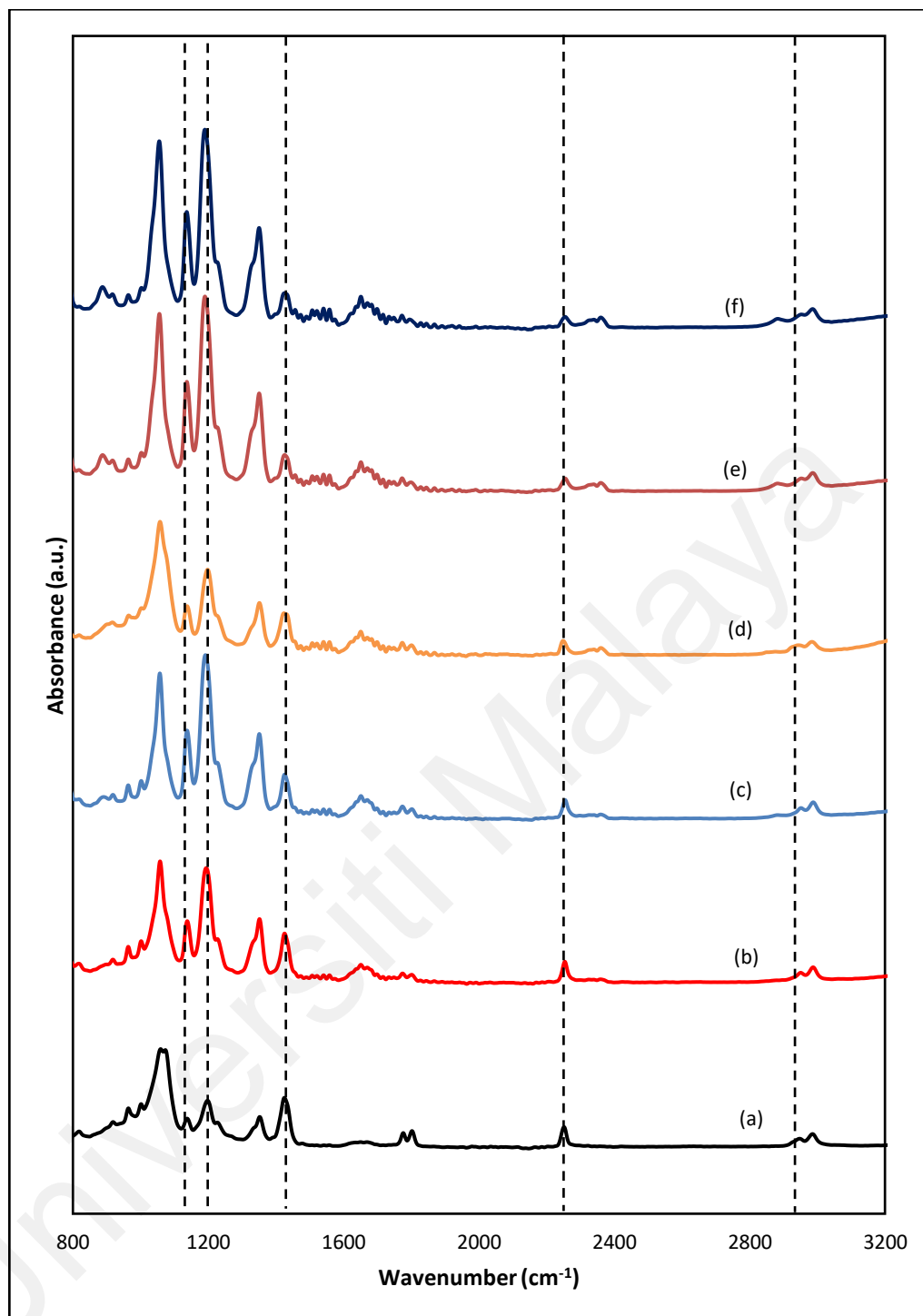


Figure 5.11: FTIR spectra of PVdC-co-AN/SN containing (a) 5 wt.% Mg(TFSI)₂, (b) 10 wt.% Mg(TFSI)₂, (c) 15 wt.% Mg(TFSI)₂, (d) 20 wt.% Mg(TFSI)₂, (e) 25 wt.% Mg(TFSI)₂ and (f) 30 wt.% Mg(TFSI)₂.

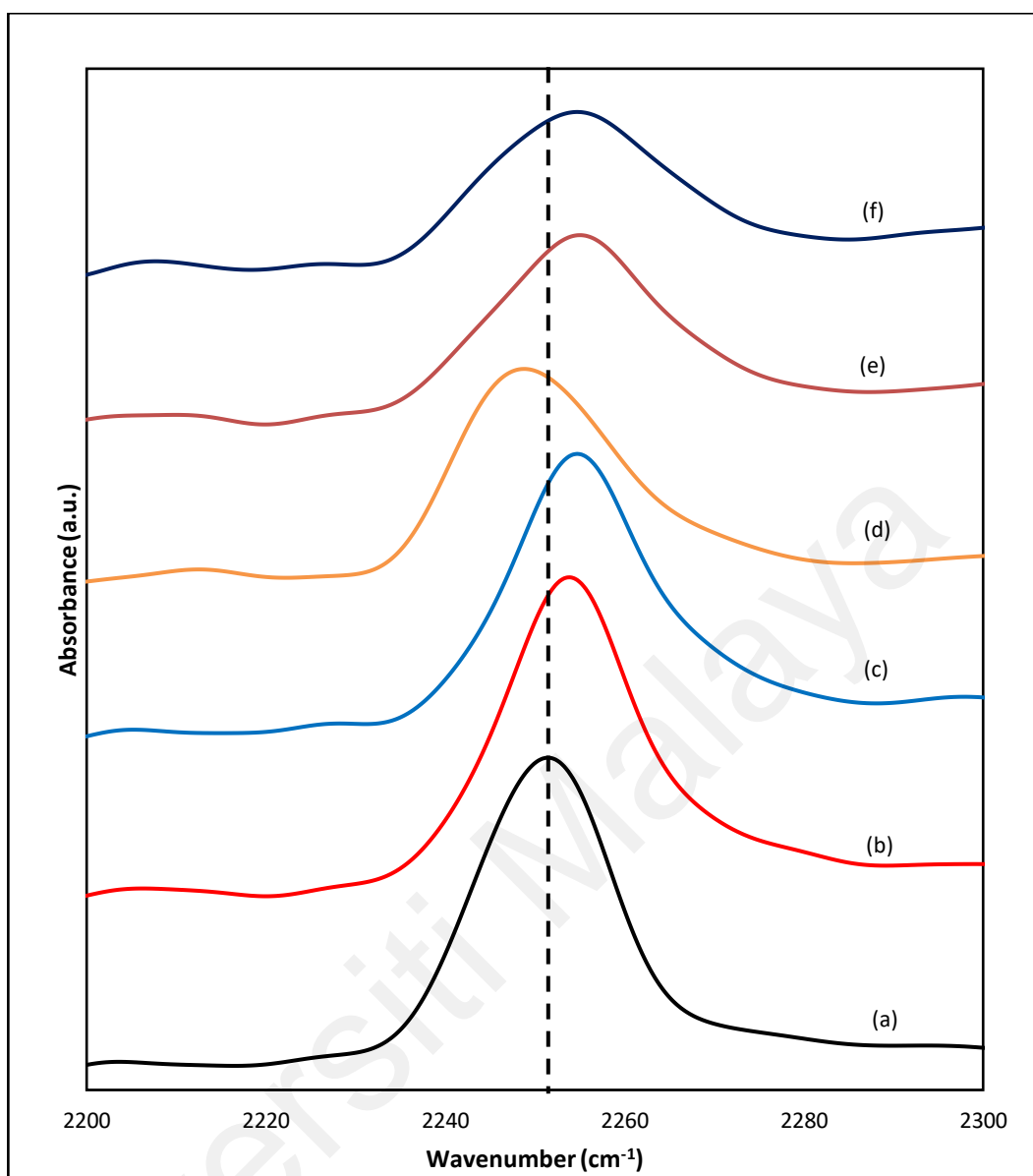


Figure 5.12: The close up of nitrile band of PVdC-co-AN/SN containing (a) 5 wt.% Mg(TFSI)₂, (b) 10 wt.% Mg(TFSI)₂, (c) 15 wt.% Mg(TFSI)₂, (d) 20 wt.% Mg(TFSI)₂, (e) 25 wt.% Mg(TFSI)₂ and (f) 30 wt.% Mg(TFSI)₂.

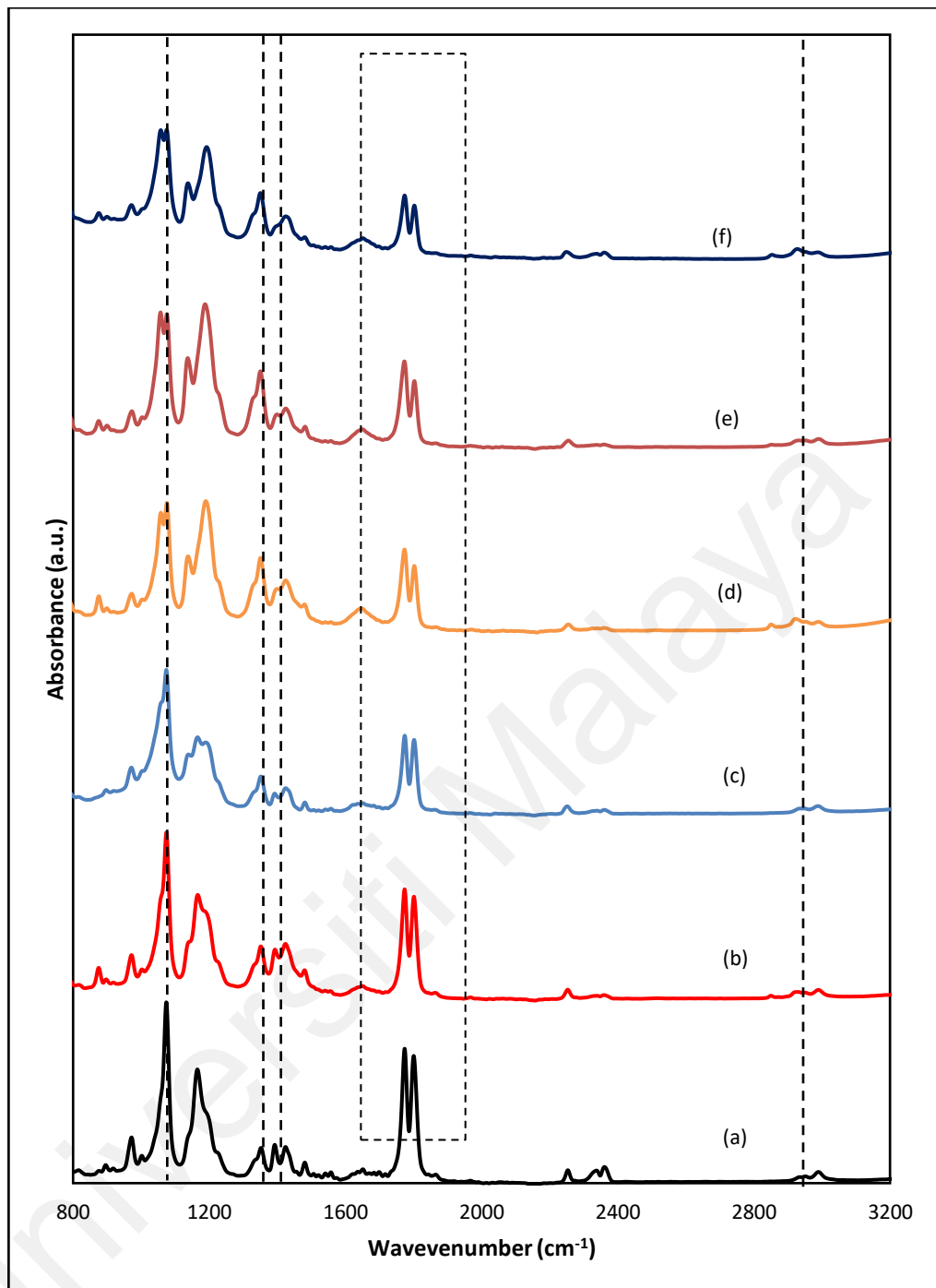


Figure 5.13: FTIR spectra of PVdC-co-AN/SN/EC containing (a) 5 wt.% Mg(TFSI)₂, (b) 10 wt.% Mg(TFSI)₂, (c) 15 wt.% Mg(TFSI)₂, (d) 20 wt.% Mg(TFSI)₂, (e) 25 wt.% Mg(TFSI)₂ and (f) 30 wt.% Mg(TFSI)₂.

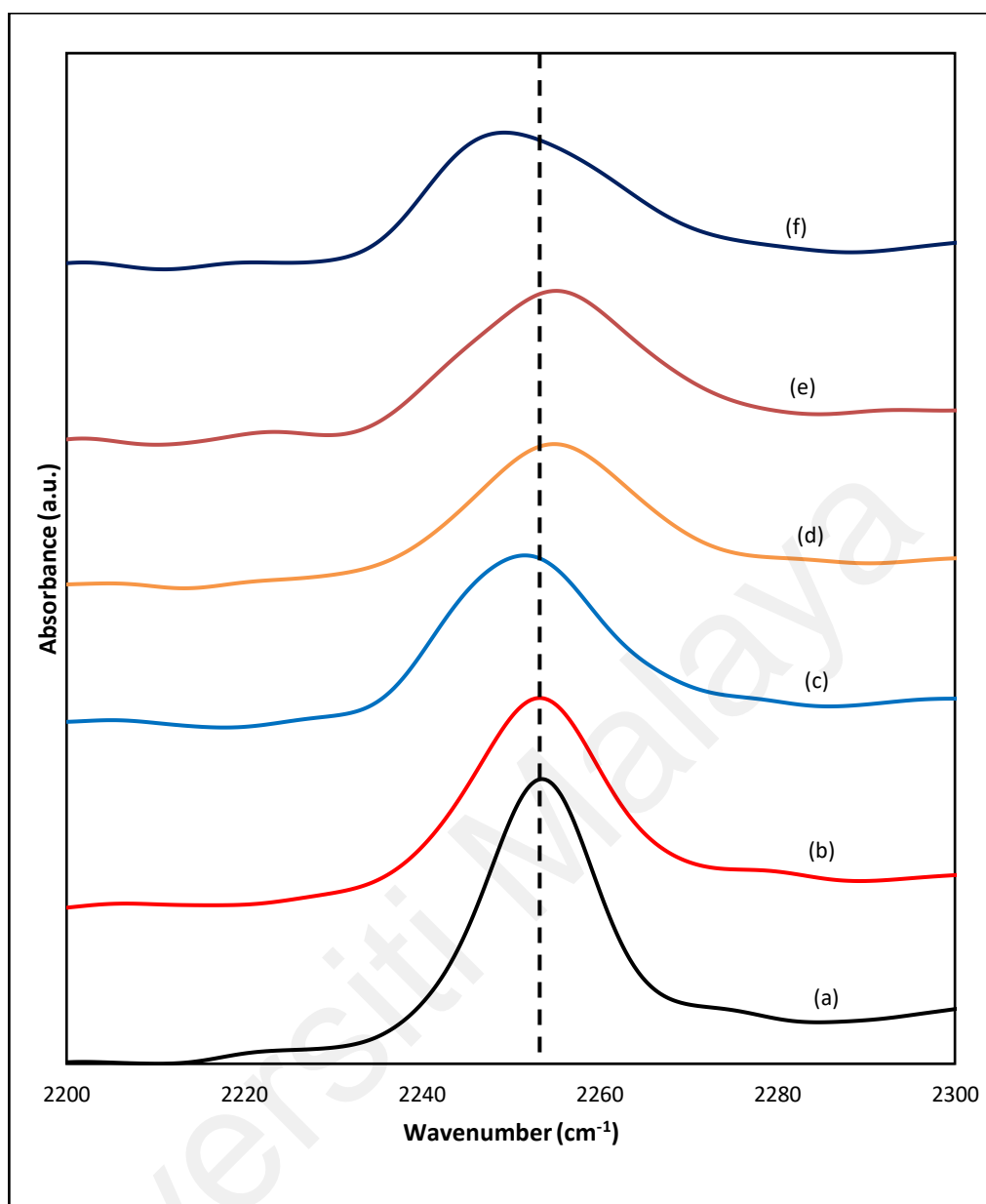


Figure 5.14: The close up of nitrile band of PVdC-co-AN/SN/EC containing (a) 5 wt.% Mg(TFSI)₂, (b) 10 wt.% Mg(TFSI)₂, (c) 15 wt.% Mg(TFSI)₂, (d) 20 wt.% Mg(TFSI)₂, (e) 25 wt.% Mg(TFSI)₂ and (f) 30 wt.% Mg(TFSI)₂.

In summary, FTIR interaction studies show ion-polymer interaction occurs between PVdC-co-AN and MgTf₂ and PVdC-co-AN and Mg(TFSI)₂ due to the formation of polymer-salt complex. This interaction can be observed at the functional group of the pure PVdC-co-AN which is the nitrile group (C≡N). For the interaction between plasticizer and salt, they occurred at the C≡N band of SN (overlapped with the pure

polymer) and C=O band of EC. Meanwhile, studies on polymer-plasticizer spectra suggest that there is no polymer-solvent (THF) interaction (Saidi et al., 2014; Shurvell & Southby, 1997). FTIR results also show some shifting of bands, change in intensity of bands, disappearance of bands and appearance of new vibrational bands which show good evidence for the compatibility between polymer, plasticizer and salts. Thus, the interaction between PVdC-co-AN, SN, EC, MgTf₂ and Mg(TFSI)₂ are prove to be exist and complexation has occurred between them.

5.1.5 Deconvolution of FTIR spectra

FTIR deconvolution is the process of rectifying the intrinsic line widths of bands in order to resolve possible overlapping bands (Aniskari & Mohd Isa, 2017; Kauppinen et al., 1981). This technique allows the determination of significant peaks come from MgTf₂ and Mg(TFSI)₂ salts which may then be distinguished into the bands of free ions, contact ion pairs and ion aggregates of the salt. The deconvolution was based on the Gaussian-Lorentzian function by using Omnic fitting software.

5.1.5.1 PVdC-co-AN/SN/MgTf₂ and PVdC-co-AN/SN/EC/MgTf₂ systems

In MgTf₂ systems, ion association occurs at the end of the SO₃ of the anion. Therefore, the symmetric SO₃ stretching modes ($\nu_s(\text{SO}_3)$) will be highly sensitive to the changes in the coordination state of the anion (Jeong et al., 2006). The deconvolution of symmetric SO₃ stretching was used to investigate the effect of salt in ion association/dissociation in the polymer electrolyte. Figure 5.15 and 5.16 show the deconvoluted of FTIR spectra that fitted to the function Gaussian-Lorentzian of SO₃⁻ absorbance region for PVdC-co-AN/SN/MgTf₂ and PVdC-co-AN/SN/EC/MgTf₂ systems respectively. Throughout both systems, the $\nu_s(\text{SO}_3)$ envelope can be resolved into three separate vibrational bands which are the bands within the range of 1029 to 1032 cm⁻¹ assigned to the free Tf₂ ions, between

1049 and 1053 cm^{-1} for contact ion pairs of (MgTf_2) , MgTf_4^{2-} MgTf_6^{4-} and as well as at the range of 1071 to 1076 cm^{-1} which represents ion aggregates of $\text{Mg}_2\text{Tf}_2^{2+}$ and $\text{Mg}_4\text{Tf}_2^{6+}$ (Jeong et al., 2006; Shanthi et al., 2013b). The fraction of area for each band was then calculated using the following formula below (Arof et al., 2014; Arya & Sharma, 2018):

$$\text{Fraction of free ions} = \frac{\text{Area of free ions}}{\text{Total peak Area}} \quad (5.1)$$

$$\text{Fraction of ion pairs} = \frac{\text{Area of ion pairs}}{\text{Total peak Area}} \quad (5.2)$$

$$\text{Fraction of ion aggregates} = \frac{\text{Area of ion aggregates}}{\text{Total peak Area}} \quad (5.3)$$

The calculated fraction of free ions, ion pairs and ion aggregates are as shown in Table 5.6 and 5.7 for PVdC-co-AN/SN/ MgTf_2 and PVdC-co-AN/SN/EC/ MgTf_2 systems respectively. The free ions peak area gives a direct measure of the free mobile ions contribute to the ionic conduction (Arya & Sharma, 2018). It can be observed that the fraction of free ions increases when the concentration of MgTf_2 increases for both systems. Meanwhile, for the fraction of ion pairs and ion aggregates, the peak areas decrease with the increase of the concentration of MgTf_2 salt. This shows high dissociation of free ions occurred and low ion associations and aggregations taken place in the system with higher concentration of MgTf_2 salt. As a consequence, the maximum conductivity obtained from both GPE systems came from the maximum concentration of MgTf_2 and prove the relationship between the ion conduction of the GPEs with the fraction of free ions, ion pairs and ion aggregates. For a clearer understanding, the relationship between free ions, ion pairs and ion aggregates with ionic conductivity are presented in Figure 5.17 and 5.18 for PVdC-co-AN/SN/ MgTf_2 and PVdC-co-AN/SN/EC/ MgTf_2 systems respectively.

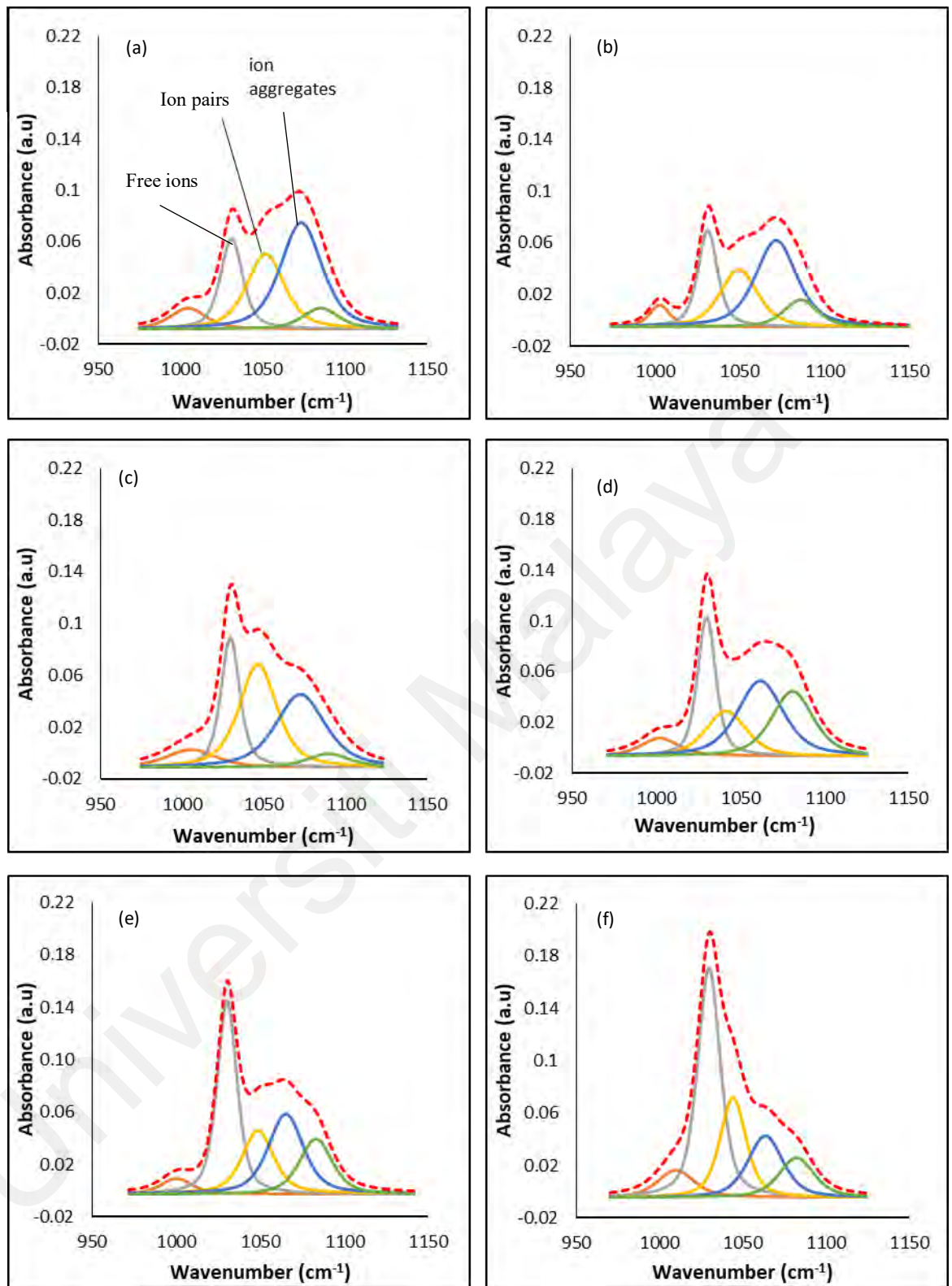


Figure 5.15: Deconvolution of FTIR spectra between 950 and 1150 cm⁻¹ for PVdC-co-AN/SN with (a) 5 wt.% MgTf₂, (b) 10 wt.% MgTf₂, (c) 15 wt.% MgTf₂, (d) 20 wt.% MgTf₂, (e) 25 wt.% MgTf₂ and (f) 30 wt.% MgTf₂.

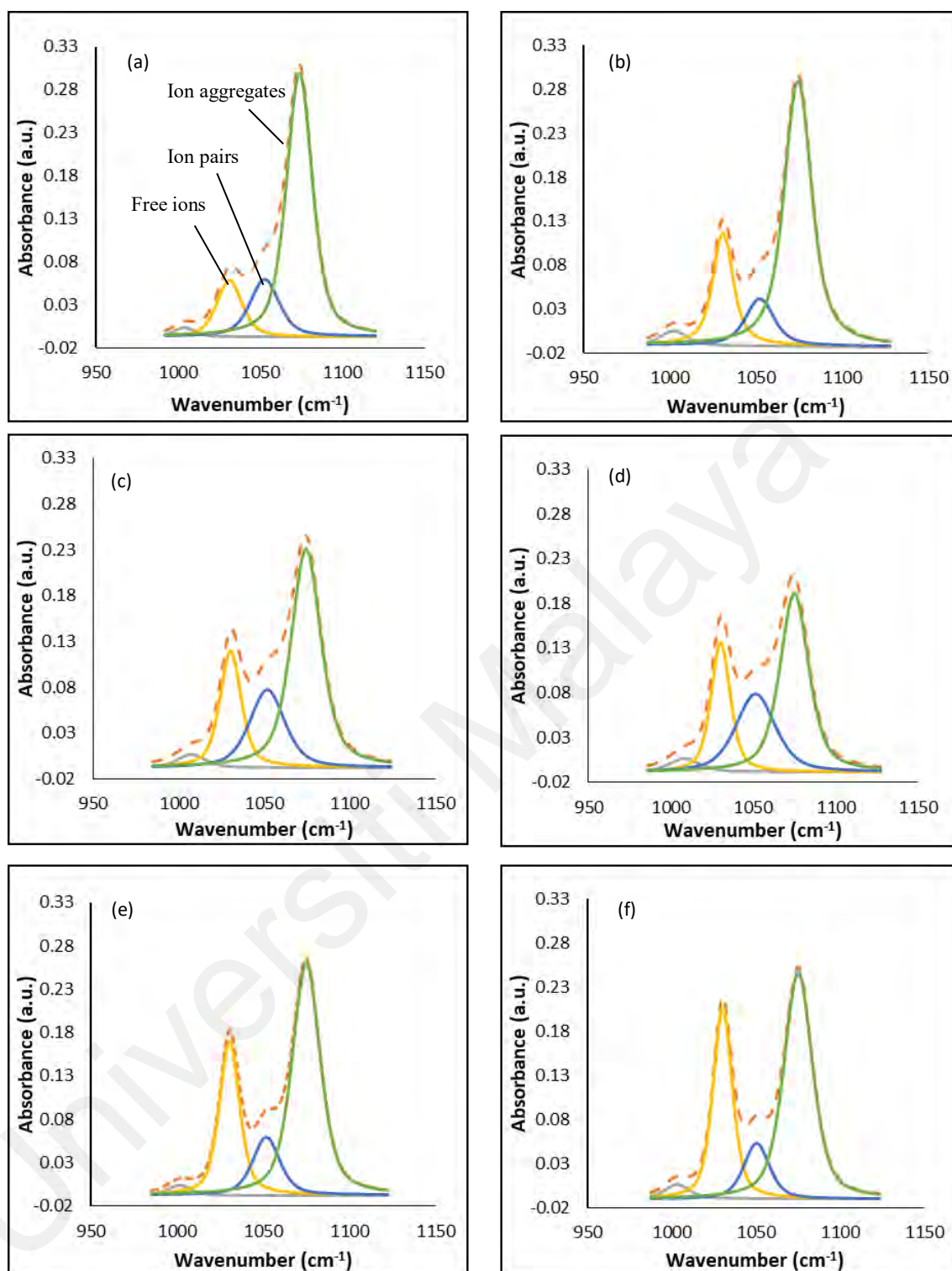


Figure 5.16: Deconvolution of FTIR spectra between 950 and 1150 cm^{-1} for PVdC-co-AN/SN/EC with (a) 5 wt.% MgTf_2 , (b) 10 wt.% MgTf_2 , (c) 15 wt.% MgTf_2 , (d) 20 wt.% MgTf_2 , (e) 25 wt.% MgTf_2 and (f) 30 wt.% MgTf_2 .

Table 5.6: The integrated area of free ions, ion pairs and ion aggregates bands correspond to Tf_2^- ions in PVdC-co-AN/SN/MgTf₂ system.

Salt content (wt.%)	Integrated Area (%)		
	Free ions	Ion pairs	Ion aggregates
5	21.9	30.7	47.4
10	25.1	28.4	46.5
15	31.3	25.9	42.8
20	39.1	24.7	36.2
25	44.8	23.0	32.3
30	52.5	21.5	26.0

Table 5.7: The integrated area of free ions, ion pairs and ion aggregates bands correspond to Tf_2^- ions in PVdC-co-AN/SN/EC/MgTf₂ system.

Salt content (wt.%)	Integrated Area (%)		
	Free ions	Ion pairs	Ion aggregates
5	14.3	21.4	64.8
10	17.1	20.4	63.4
15	21.5	17.9	60.8
20	26.2	15.6	58.8
25	31.4	13.1	55.5
30	37.6	12.8	50.4

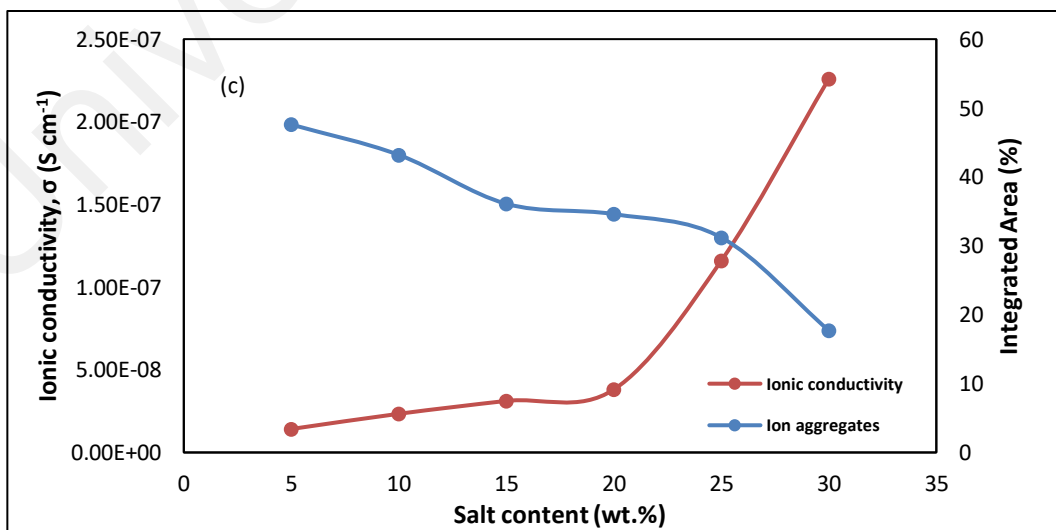
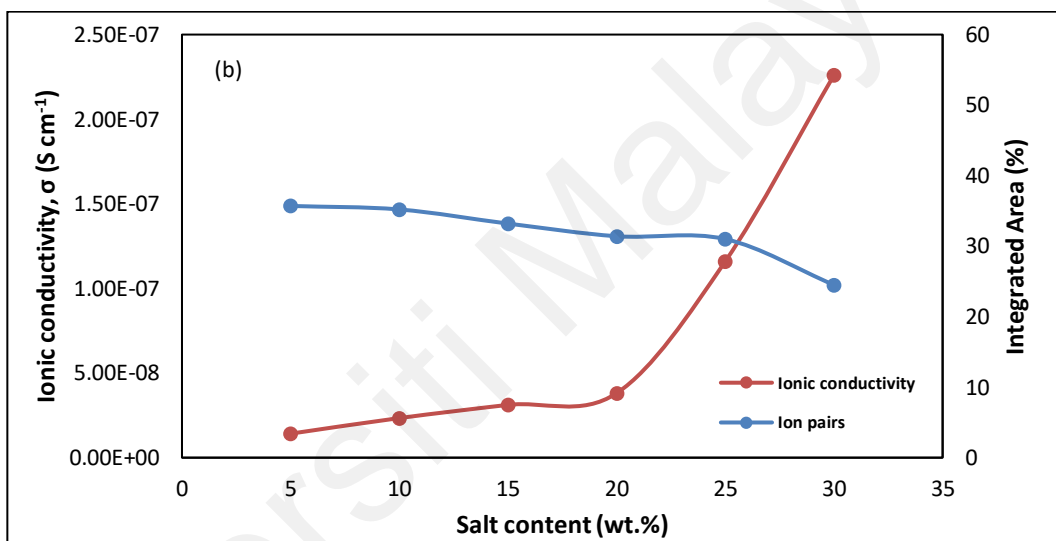
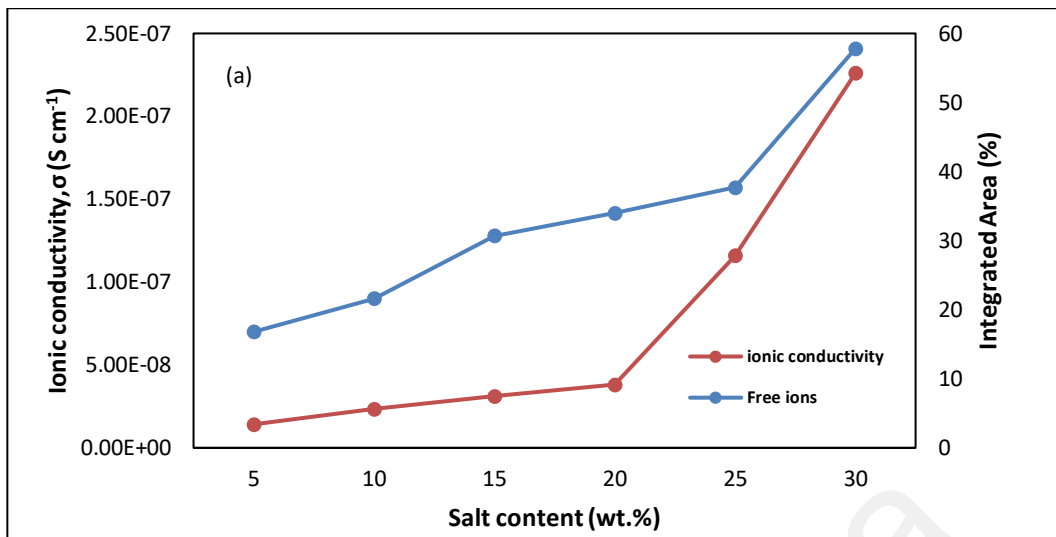


Figure 5.17: The relationship of (a) free ions, (b) ion pairs and (c) ion aggregates with ionic conductivity of PVdC-co-AN/SN/MgTf₂ system.

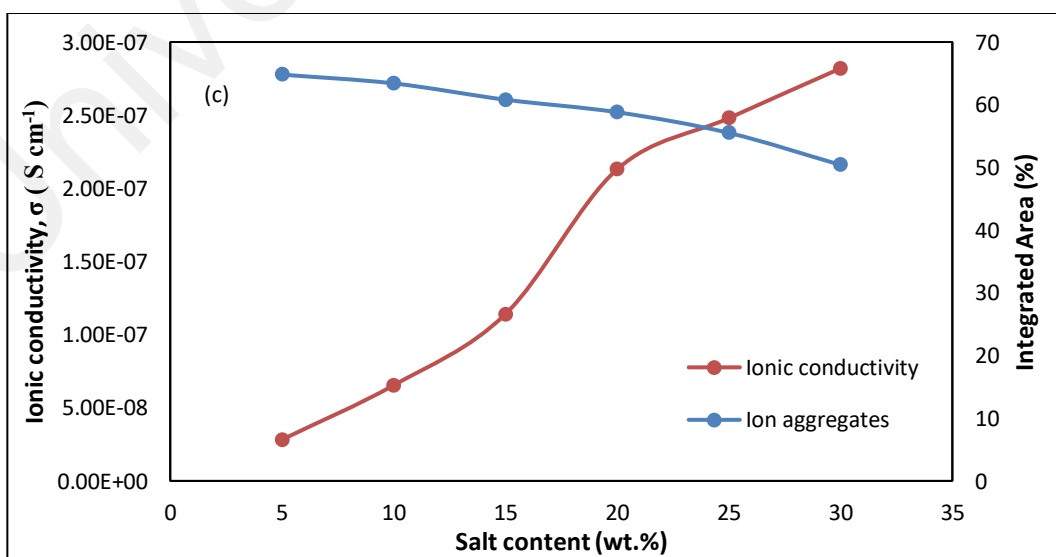
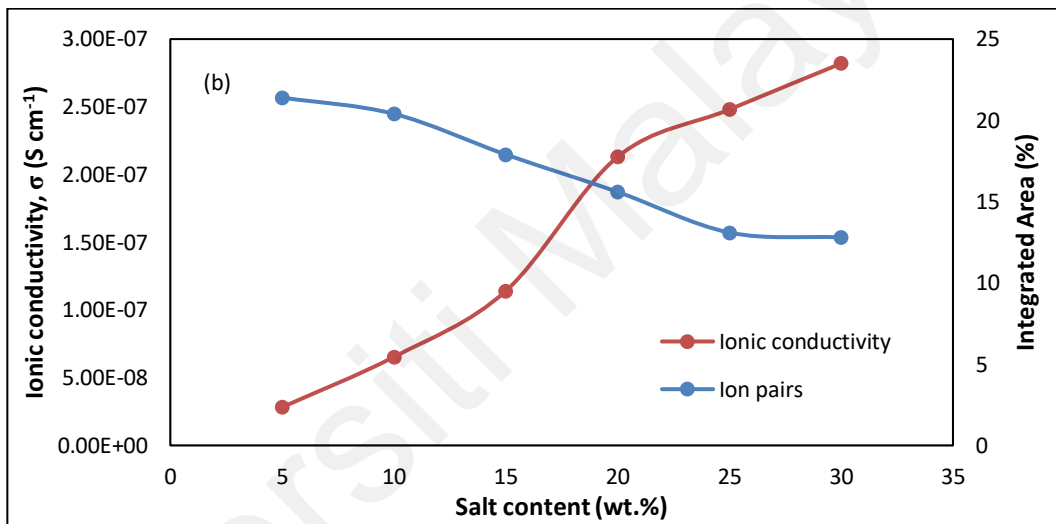
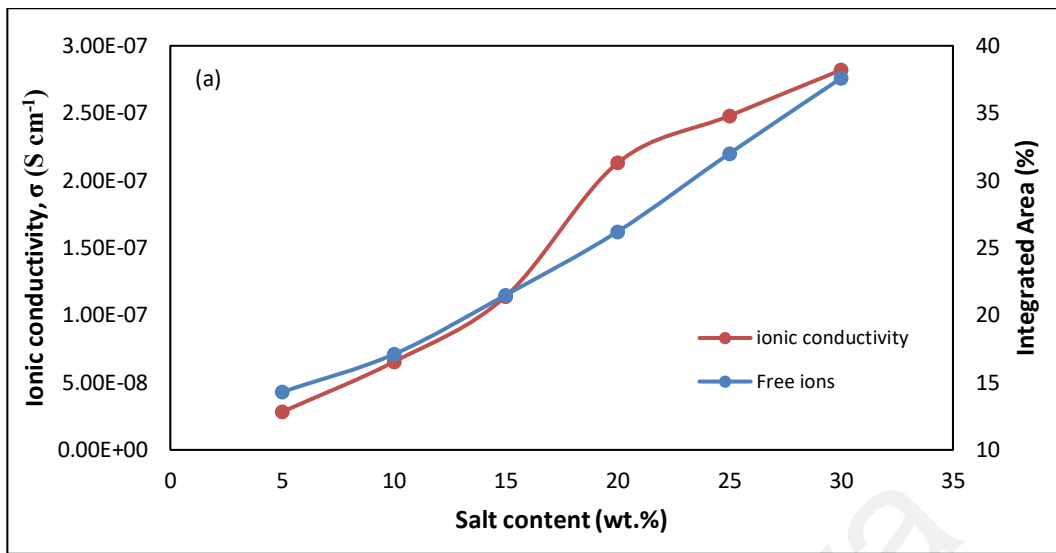


Figure 5.18: The relationship of (a) free ions, (b) ion pairs and (c) ion aggregates with ionic conductivity of PVdC-co-AN/SN/EC/MgTf₂ system.

5.1.5.2 PVdC-co-AN/SN/Mg(TFSI)₂ and PVdC-co-AN/SN/EC/Mg(TFSI)₂ systems

For Mg(TFSI)₂ systems, the TFSI envelope can also be resolved into the band of free ions, ion pairs and ion aggregates where the ion dissociation/association occurs at the end of the NSO₂ ions. The specific deconvoluted spectra of the GPE complexes for PVdC-co-AN/SN/Mg(TFSI)₂ and PVdC-co-AN/SN/EC/Mg(TFSI)₂ systems in the region of 900-1500 cm⁻¹ are presented in Figure 5.19 and Figure 5.20 respectively. For PVdC-co-AN/SN/Mg(TFSI)₂, the band of free ions are in the range of 1056 to 1061 cm⁻¹, while the band of 1137 to 1143 cm⁻¹ and 1191 to 1194 cm⁻¹ are specified for ion aggregates and 1227 to 1236 cm⁻¹, 1313 to 1327 cm⁻¹ and 1349 to 1357 cm⁻¹ represent ion pairs. Meanwhile, for PVdC-co-AN/SN/EC/Mg(TFSI)₂ system, the band of free ions are in the range of 1060 to 1076 cm⁻¹, ion aggregates are within 1164 to 1167 cm⁻¹ and 1195 to 1205 cm⁻¹ and ion pairs endorsed at 1342 to 1359 cm⁻¹ throughout the system. The percentage area of fraction of free ions, ion aggregates and ion pairs were calculated by comparing with the total area of TFSI envelope denoted by equation 5.1 to 5.3 and were tabulated in Table 5.8 and 5.9. From the table, it can be observed that the percentage area of free ions increases from 5 wt% until 20 wt.% of Mg(TFSI)₂ added for PVdC-co-AN/SN/Mg(TFSI)₂ system and from 5 wt% until 15 wt.% of Mg(TFSI)₂ added for PVdC-co-AN/SN/EC/Mg(TFSI)₂ where the PVdC-co-AN/SN/20 wt.% Mg(TFSI)₂ and PVdC-co-AN/SN/EC/15 wt.% Mg(TFSI)₂ samples recorded as the highest percentage area of free ions compared to other samples. This is consistent with the results of ionic conductivity whereby for these two samples, their conductivities are the highest from each system. Beyond the maximum conductivity, the percentage area of free ions decreased upon further addition of Mg(TFSI)₂ salt for both systems while for ion pairs and ion aggregates, their percentage areas increase. The high percentage areas of ion pairs and ion aggregates show ion association has occurred to form neutral ion pairs and larger ion aggregates and thus, reduced the dissociation of ions (Zulkepeli et al., 2017). As a

consequence, the ionic conductivity of the GPEs decreased after 20 wt.% of $\text{Mg}(\text{TFSI})_2$ added for PVdC-co-AN/SN/ $\text{Mg}(\text{TFSI})_2$ system and after 15 wt.% of $\text{Mg}(\text{TFSI})_2$ added for PVdC-co-AN/SN/EC/ $\text{Mg}(\text{TFSI})_2$ system.

For a clearer understanding, the relationship between free ions, ion pairs and ion aggregates with ionic conductivity are presented in Figure 5.21 and 5.22 for PVdC-co-AN/SN/ $\text{Mg}(\text{TFSI})_2$ and PVdC-co-AN/SN/EC/ $\text{Mg}(\text{TFSI})_2$ systems respectively.

Universiti Malaya

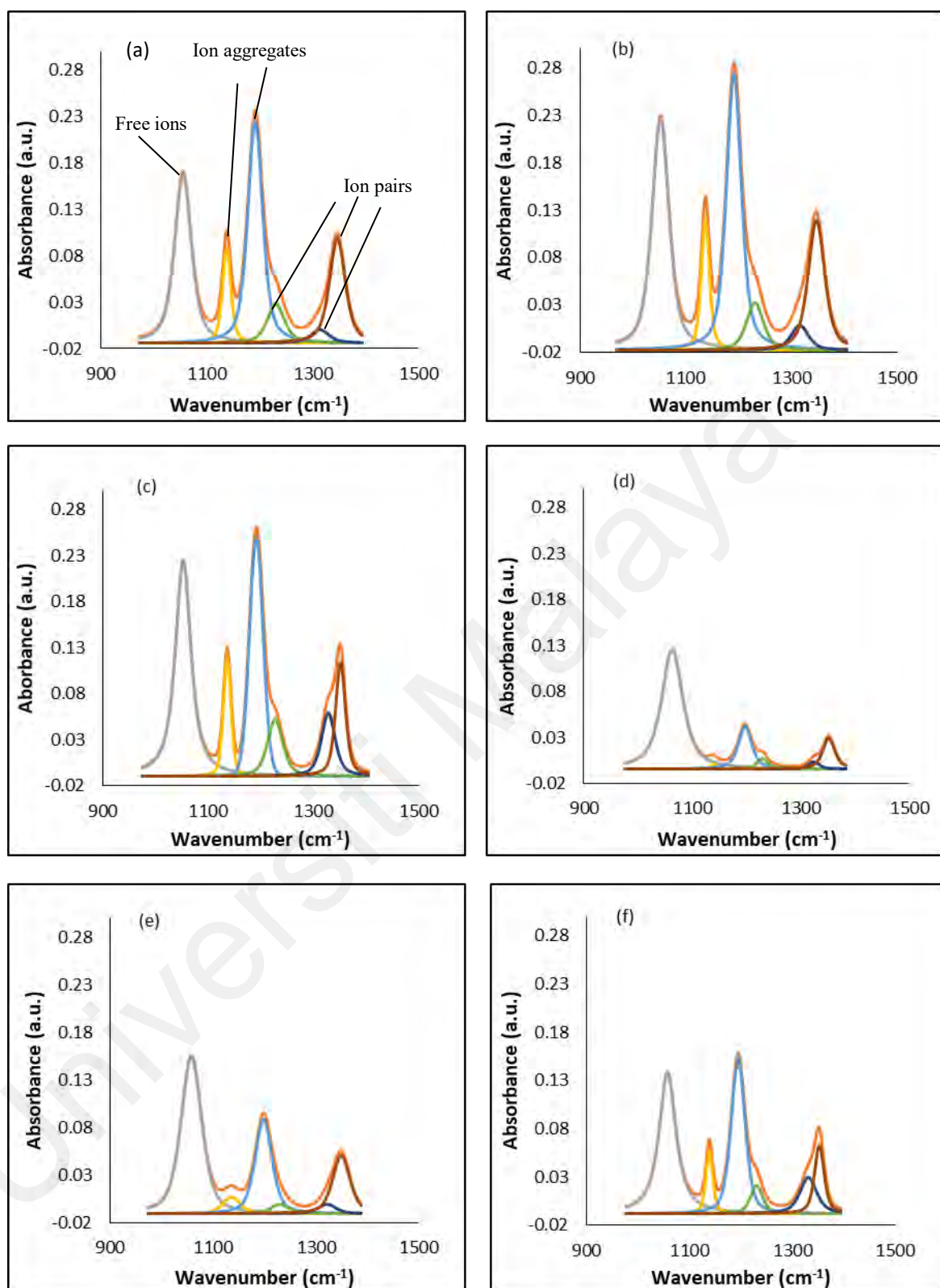


Figure 5.19: Deconvoluted of FTIR spectra between 900 and 1500 cm^{-1} for PVdC-co-AN/SN with (a) 5 wt.% $\text{Mg}(\text{TFSI})_2$, (b) 10 wt.% $\text{Mg}(\text{TFSI})_2$, (c) 15 wt.% $\text{Mg}(\text{TFSI})_2$, (d) 20 wt.% $\text{Mg}(\text{TFSI})_2$, (e) 25 wt.% $\text{Mg}(\text{TFSI})_2$ and (f) 30 wt.% $\text{Mg}(\text{TFSI})_2$.

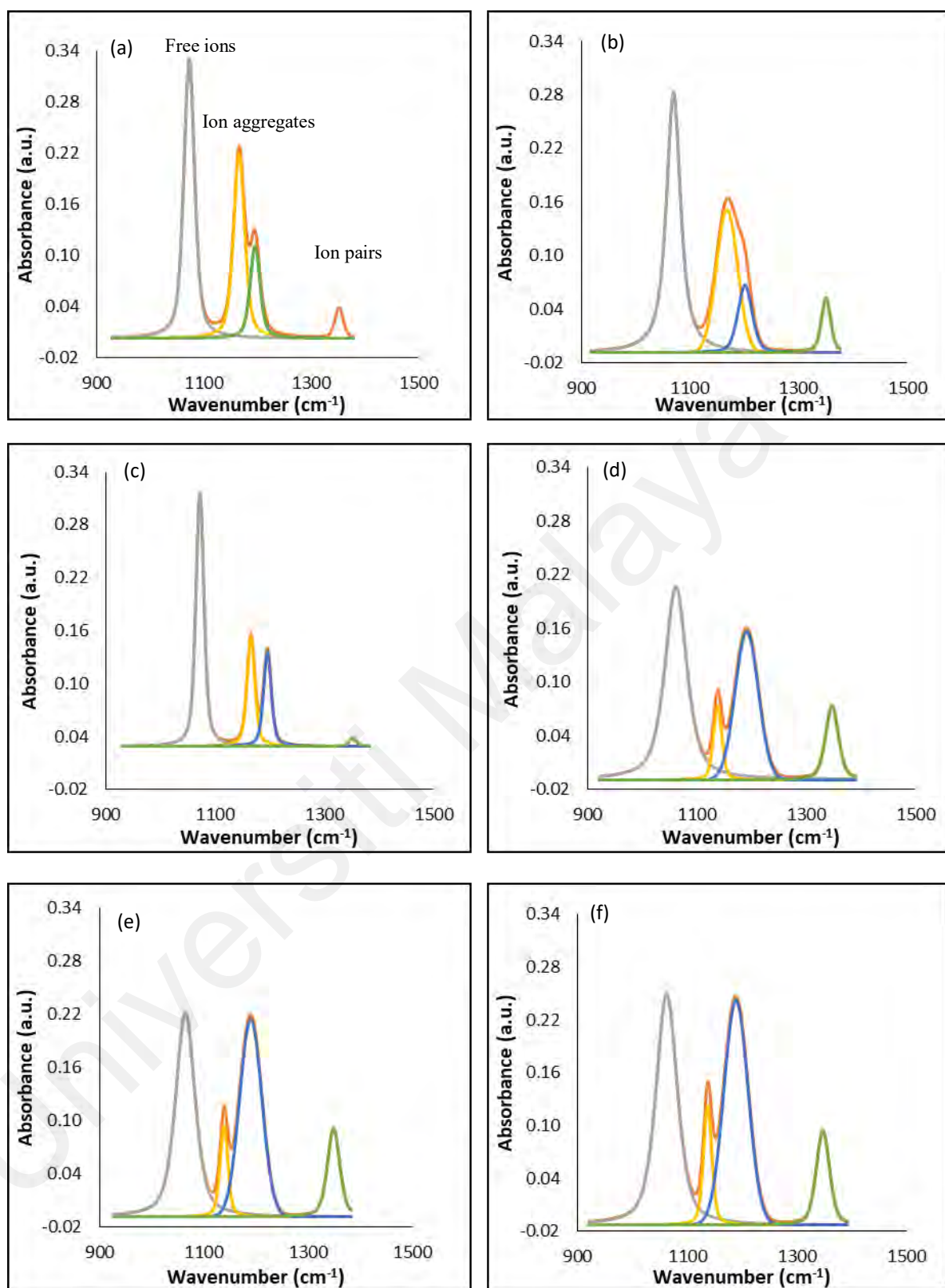


Figure 5.20: Deconvoluted of FTIR spectra between 900 and 1500 cm^{-1} for PVdC-co-AN/SN/EC with (a) 5 wt.% $\text{Mg}(\text{TFSI})_2$, (b) 10 wt.% $\text{Mg}(\text{TFSI})_2$, (c) 15 wt.% $\text{Mg}(\text{TFSI})_2$, (d) 20 wt.% $\text{Mg}(\text{TFSI})_2$, (e) 25 wt.% $\text{Mg}(\text{TFSI})_2$ and (f) 30 wt.% $\text{Mg}(\text{TFSI})_2$.

Table 5.8: The integrated area of free ions, ion pairs and ion aggregates bands correspond to TFSI⁻ ions in PVdC-co-AN/SN/Mg(TFSI)₂ system.

Salt content (wt.%)	Integrated Area (%)		
	Free ions	Ion pairs	Ion aggregates
5	29.0	42.7	28.3
10	31.6	41.2	27.2
15	36.6	37.7	25.7
20	68.9	15.7	15.4
25	49.9	29.0	21.1
30	41.2	34.5	24.3

Table 5.9: The integrated area of free ions, ion pairs and ion aggregates bands correspond to TFSI⁻ ions in PVdC-co-AN/SN/EC/Mg(TFSI)₂ system.

Salt content (wt.%)	Integrated Area (%)		
	Free ions	Ion pairs	Ion aggregates
5	47.4	6.2	44.7
10	52.0	8.0	41.8
15	57.5	3.6	38.9
20	43.6	9.7	46.7
25	40.9	11.5	47.6
30	38.2	13.3	48.5

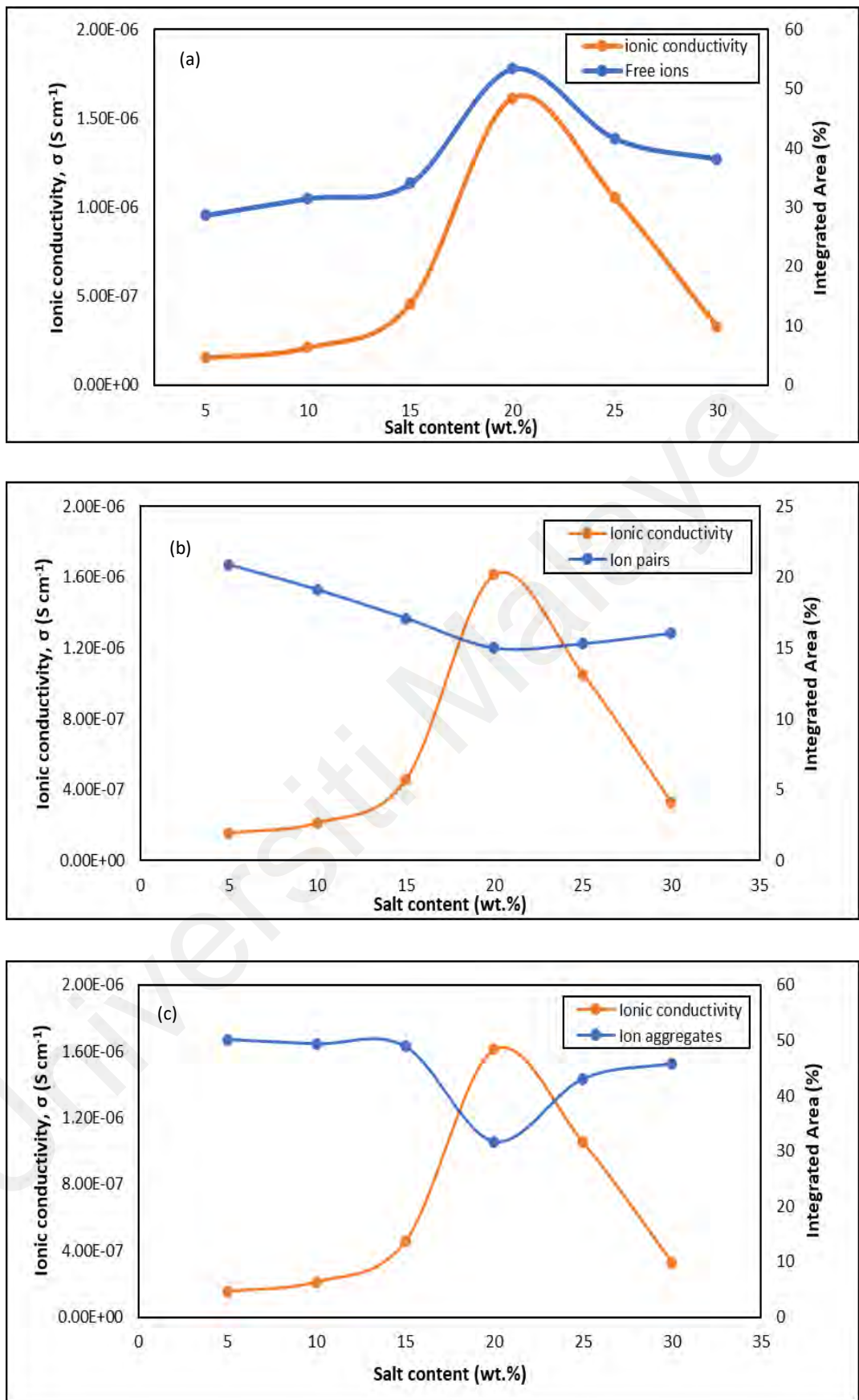


Figure 5.21: The relationship of (a) free ions, (b) ion pairs and (c) ion aggregates with ionic conductivity of PVdC-co-AN/SN/Mg(TFSI)₂ system.

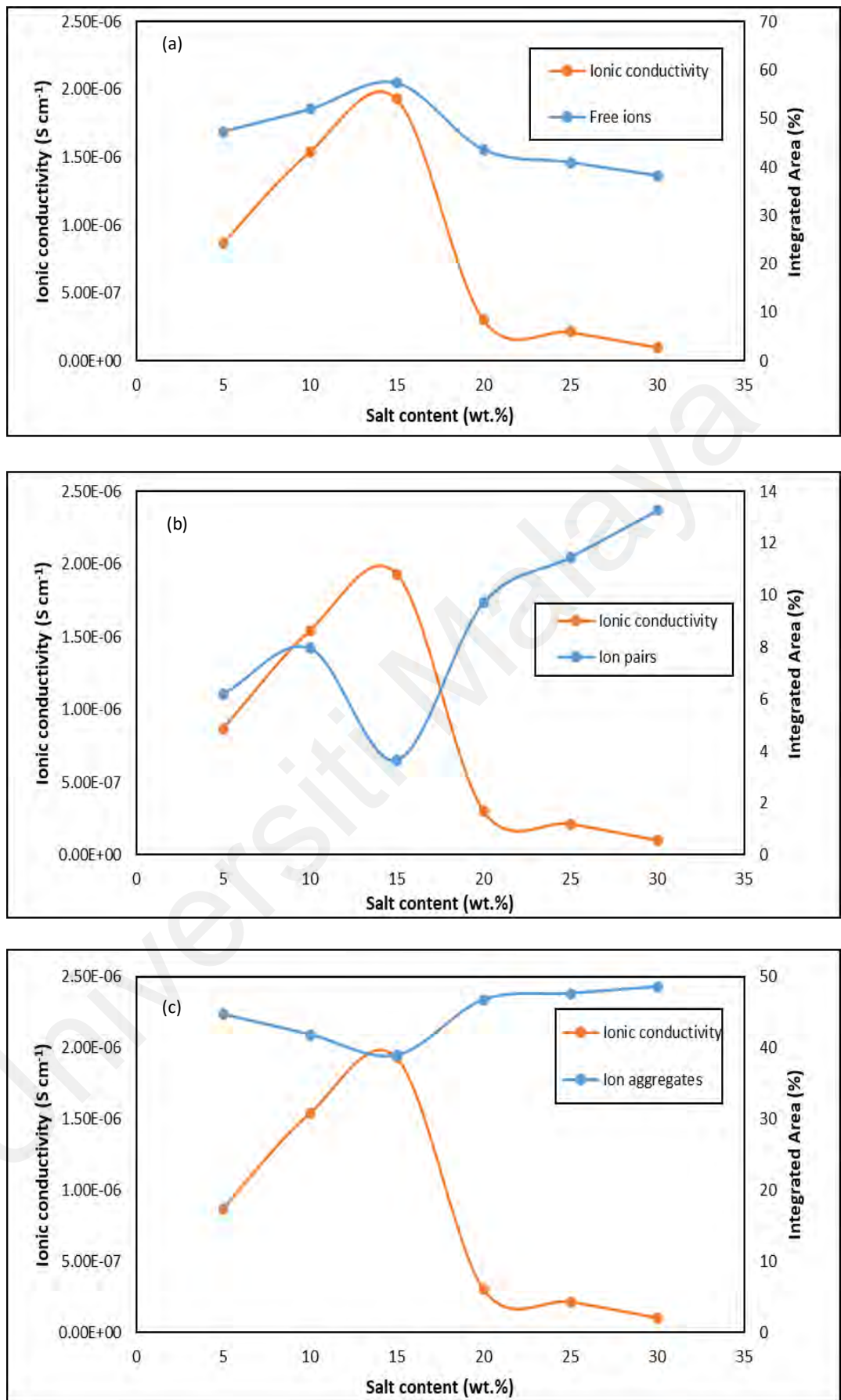


Figure 5.22: The relationship of (a) free ions, (b) ion pairs and (c) ion aggregates with ionic conductivity of PVdC-co-AN/SN/EC/Mg(TFSI)₂ system.

5.1.5.3 Determination of n , μ and D

From equation 4.1, the ionic conductivity of polymer electrolytes is related to the number density (number of charge carrier), n and ionic mobility, μ . Thus, in this section, the values of n , μ and diffusion coefficient, D are calculated by using FTIR spectroscopy results proposed by Petrowsky and Frech (Petrowsky & Frech, 2008) for liquid electrolytes while Ericson et al. (Ericson et al., 2000) have used it for a gel polymer electrolyte (Arof et al., 2014).

From FTIR deconvolution analysis, the values of percentage area of free ions have been determined for each sample from all systems. Thus, by using these values, the values of number density, n , ionic mobility, μ and diffusion coefficient, D can be calculated from equations 5.4 to 5.6 respectively;

$$n = \frac{M \times N_A}{V_{Total}} \times \text{free ions (\%)} \quad (5.4)$$

$$\mu = \frac{\sigma}{ne} \quad (5.5)$$

$$D = \frac{\mu kT}{e} \quad (5.6)$$

where M is the number of moles of salt used in each electrolyte, N_A is Avogadro's number ($6.02 \times 10^{23} \text{ mol}^{-1}$), V_{Total} is the total volume of the gel polymer electrolyte and σ is ionic conductivity. The constant e is the electron charge ($1.602 \times 10^{-19} \text{ C}$), k is the Boltzmann constant ($1.38 \times 10^{-23} \text{ J K}^{-1}$) and T is the absolute temperature (Arof et al., 2014). The calculated values of n , μ and D for all systems were tabulated in Table 5.10 to 5.13. From the tables, it can be observed that the conductivity variation of the GPEs is strongly dependent by the values of n , μ and D where, the conductivity increases with the values of n , μ and D and vice versa. This shows that as conductivity increases, more dissociated

ions occurred in the GPE system, resulting in an increase in the number density of mobile ions which is also influenced by the increase in ionic mobility and the diffusion coefficient of the system. Whereas, decreasing in ionic conductivity values leads to a decrease in the number density of mobile ions attributed to the formation of ion clouds where most of free ions present in the sample are blocked by the overcrowding phenomenon which in turn causes a decrement in mobility and diffusivity of charges carriers (Aniskari & Mohd Isa, 2017). To sum up, analyzing of n , μ and D parameters brought in a deep understanding of ionic conduction behavior of polymer electrolytes (Arof et al., 2014) and the dependence of ionic conductivity with the number of charge carrier and ionic mobility as discussed earlier in Section 4.1 (ionic conductivity studies) has been proven.

Table 5.10: The values of n , μ and D for PVdC-co-AN/SN/MgTf₂ system.

Salt content (wt.%)	n ($\times 10^{21} \text{ cm}^{-3}$)	μ ($\times 10^{-11}$ $\text{cm}^2 \text{ V}^{-1} \text{ s}$)	D ($\times 10^{-13}$ $\text{cm}^2 \text{ s}^{-1}$)
5	8.87	1.00	2.61
10	14.20	1.03	2.68
15	18.69	1.04	2.72
20	21.30	1.12	2.91
25	26.01	2.78	7.27
30	30.03	4.66	12.17

Table 5.11: The values of n , μ and D for PVdC-co-AN/SN/EC/MgTf₂ system.

Salt content (wt.%)	n ($\times 10^{21}$ cm ⁻³)	μ ($\times 10^{-11}$ cm ² V ⁻¹ s)	D ($\times 10^{-13}$ cm ² s ⁻¹)
5	9.65	1.82	4.76
10	17.65	2.31	6.04
15	24.03	2.96	7.73
20	30.55	4.35	11.36
25	34.54	4.48	11.70
30	35.84	4.91	12.82

Table 5.12: The values of n , μ and D for PVdC-co-AN/SN/Mg(TFSI)₂ system.

Salt content (wt.%)	n ($\times 10^{21}$ cm ⁻³)	μ ($\times 10^{-11}$ cm ² V ⁻¹ s)	D ($\times 10^{-13}$ cm ² s ⁻¹)
5	5.01	1.92	5.01
10	6.78	1.95	5.09
15	9.25	2.22	5.79
20	12.03	8.36	21.81
25	11.85	5.58	14.57
30	10.95	2.60	6.80

Table 5.13: The values of n , μ and D for PVdC-co-AN/SN/EC/Mg(TFSI)₂ system.

Salt content (wt.%)	n ($\times 10^{21}$ cm ⁻³)	μ ($\times 10^{-11}$ cm ² V ⁻¹ s)	D ($\times 10^{-13}$ cm ² s ⁻¹)
5	10.02	5.29	13.82
10	10.06	9.02	23.55
15	12.21	9.88	25.79
20	10.03	1.93	4.78
25	10.00	1.32	3.46
30	9.39	0.67	1.74

5.2 X-Ray Diffraction

X-ray diffraction (XRD) is one of the microstructural analysis and a powerful nondestructive technique used for the identification of crystallinity and amorphous nature of polymer electrolytes. The analysis was carried out for the GPE samples of all systems. The x-ray diffractograms of pure PVdC-co-AN, SN, EC, MgTf₂ and Mg(TFSI)₂ were also presented and the effects of plasticizers and salts on the structure of polymer were studied.

5.2.1 Pure PVdC-co-AN, SN and EC

The X-Ray diffractogram of pure PVdC-co-AN is as shown in Figure 5.23. The graph shows only a diffraction hump in the range of $2\theta = 2.8^\circ$ to 9.7° with no intense peaks indicates that it is amorphous in nature. Meanwhile, Figure 5.24 (a) and (b) illustrate the XRD patterns of pure SN and EC respectively. Both plots generally show crystalline

characteristics with several sharp peaks at $2\theta = 19.9^\circ$ and 28.1° for SN and at $2\theta = 17.4^\circ$, 20.1° , 22.5° , 46.2° , and 50.2° for EC. Thus, they are suggested as crystalline in nature.

The XRD patterns of PVdC-co-AN samples with SN and EC are depicted as shown in Figure 5.25. It can be seen that the crystalline peaks found from SN and EC were disappeared when the polymer, plastic crystal SN and plasticizer EC were mixed together. The broad peak of the pure polymer also becomes broaden after the addition of SN, EC and SN combined with EC. This is due to the interaction between the polymer atoms and plasticizers which disturbed the polymer network, leads to the decrease in crystallinity (Mathew et al., 2015). Thus, the XRD patterns in the Figure 5.25 confirmed the amorphous nature which is essential for a polymer electrolyte.

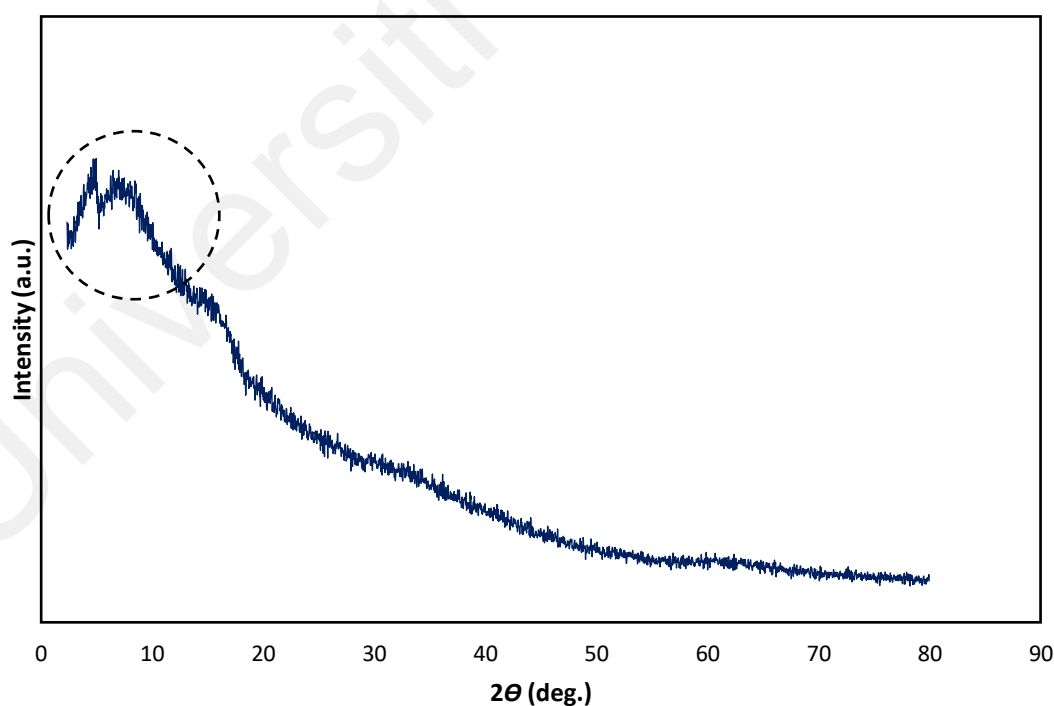


Figure 5.23: X-Ray diffractogram of pure PVdC-co-AN.

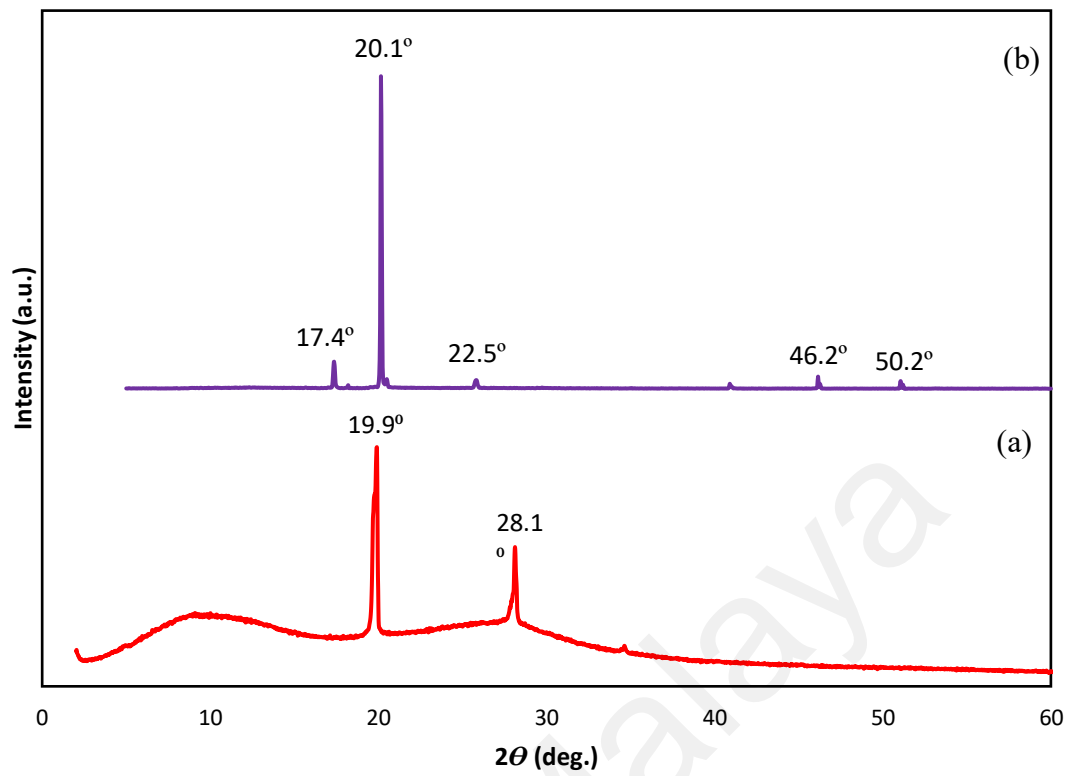


Figure 5.24: X-Ray diffractogram of (a) pure SN and (b) pure EC.

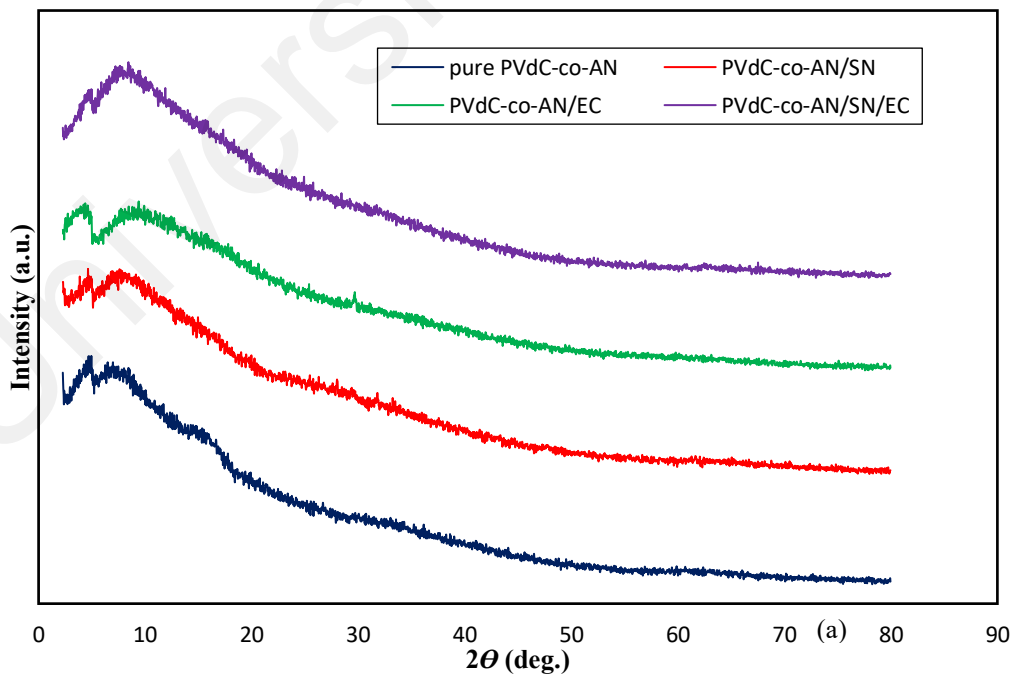


Figure 5.25: X-Ray diffractogram of (a) pure PVdC-co-AN, (b) PVdC-co-AN/SN, (c) PVdC-co-AN/EC and (d) PVdC-co-AN/SN/EC.

5.2.2 PVdC-co-AN/SN/MgTf₂ and PVdC-co-AN/SN/EC/MgTf₂ systems

Figure 5.26 depicts the X-Ray diffractogram of pure MgTf₂ salt. The strong crystalline peaks can be observed clearly at 13.9°, 17.3°, 24.1°, 29.7°, 30.8°, 33.9°, 34.7°, 42.5°, 52.4° and 76.6°.

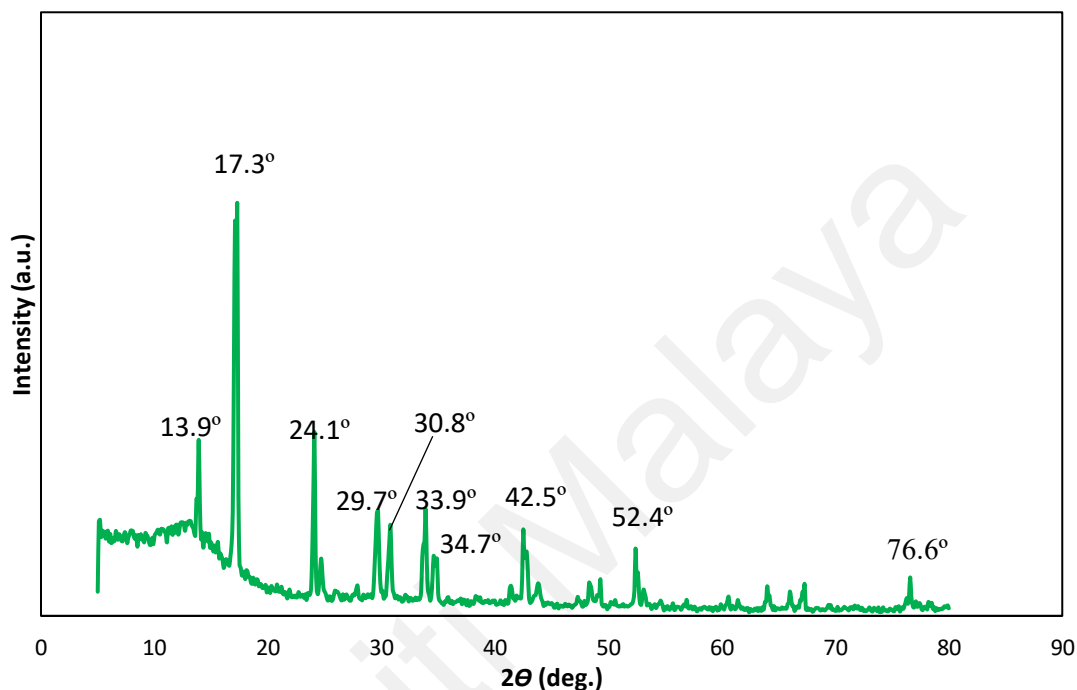


Figure 5.26: X-Ray diffractogram of pure MgTf₂.

The XRD patterns of PVdC-co-AN/SN and PVdC-co-AN/SN/EC samples containing 10 wt.%, 20 wt.% and 30 wt.% of MgTf₂ salt are presented in Figure 5.27 and 5.28 respectively. From the figures, all the GPEs show amorphous characteristic with only one broad peak. This shows that, the addition of MgTf₂ salt into the PVdC-co-AN/SN and PVdC-co-AN/SN/EC systems form the prepared GPEs into amorphous material as they did not exhibit any of the SN, EC and MgTf₂ characteristic peaks. Further, the absence of MgTf₂ peaks in the XRD patterns of these GPEs infers that the complete amount of salt has been dissociated owing to the formation of ion-dipolar coordination (Choudhary & Sengwa, 2017).

Meanwhile, the X-Ray diffractograms of PVdC-co-AN, PVdC-co-AN/SN and PVdC-co-AN/SN/EC containing 30 wt.% MgTf₂ are also plotted as shown in Figure 5.29 to explore the effects of SN and EC on the prepared GPE samples. From the XRD pattern, it can be observed the PVdC-co-AN/30 wt.% MgTf₂ exhibits several sharp peaks due to MgTf₂ characteristic peaks at 30.1° and 40.4°. Whereas, for PVdC-co-AN/SN/30 wt.% MgTf₂ and PVdC-co-AN/SN/EC/30 wt.% MgTf₂, no intense peaks observed on the XRD patterns. This suggested that the presence of SN and EC can improve the amorphousity of the GPE and confirmed the dependence of ionic conductivity with the degree of crystallinity as PVdC-co-AN/SN/30 wt.% MgTf₂ and PVdC-co-AN/SN/EC/30 wt.% MgTf₂ samples exhibit higher in conductivity compared to PVdC-co-AN/30 wt.% MgTf₂ without SN and EC.

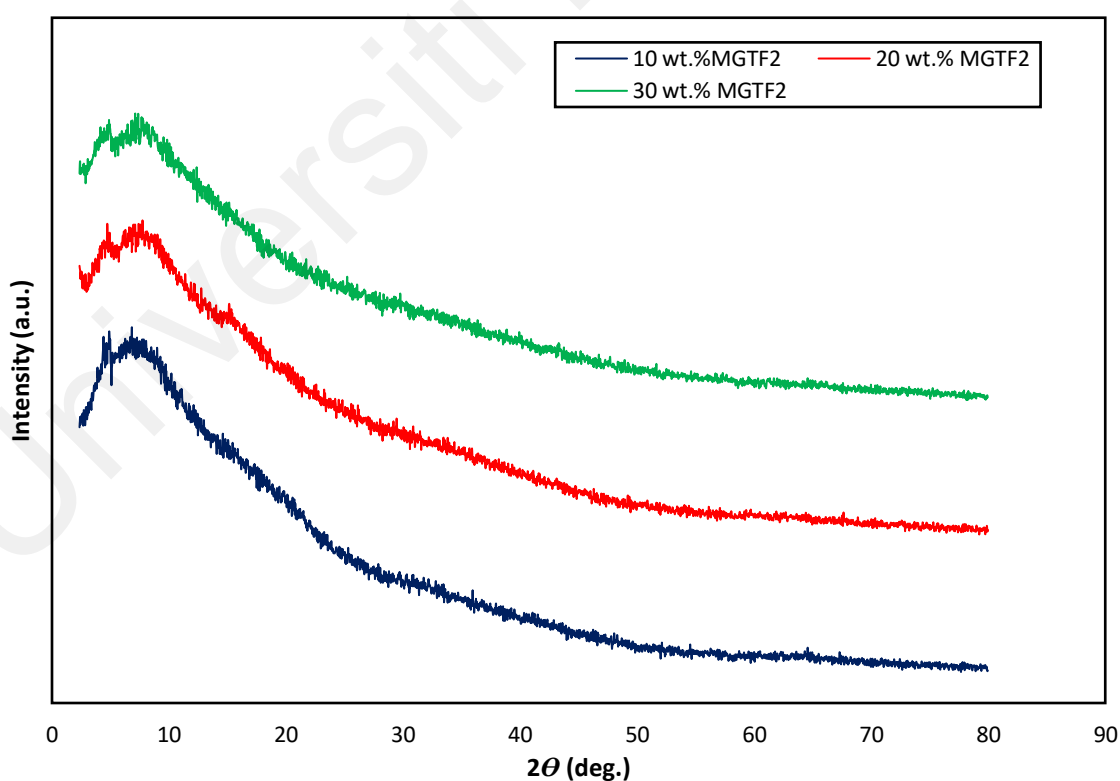


Figure 5.27: X-Ray diffractograms of PVdC-co-AN/SN containing 10 wt.%, 20 wt.% and 30 wt.% MgTf₂.

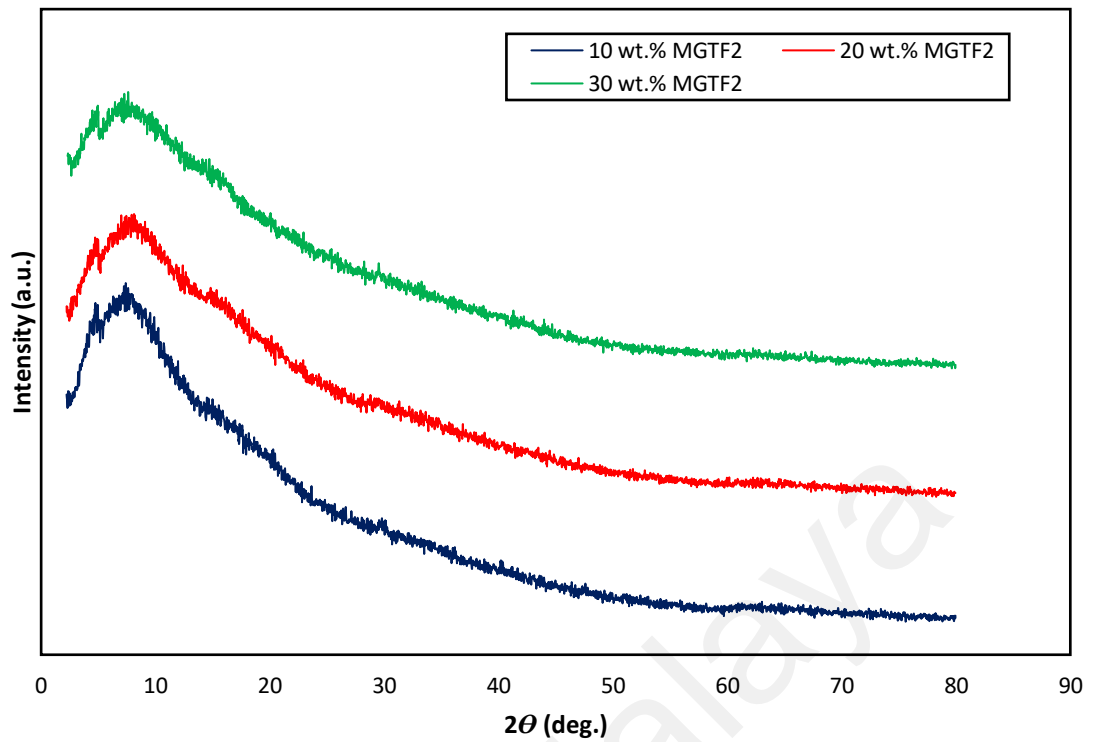


Figure 5.28: X-Ray diffractograms of PVdC-co-AN/SN/EC containing 10 wt.%, 20 wt.% and 30 wt.% MgTf₂.

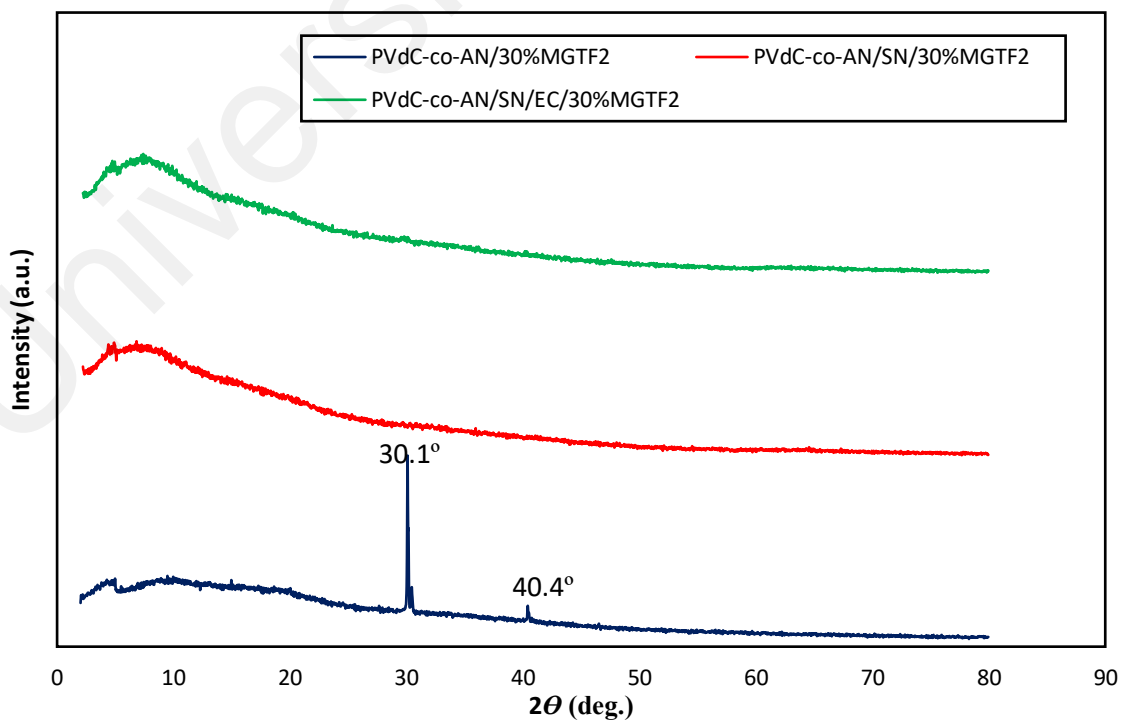


Figure 5.29: X-Ray diffractograms of PVdC-co-AN, PVdC-co-AN/SN and PVdC-co-AN/SN/EC containing 30 wt.% MgTf₂.

5.2.3 PVdC-co-AN/SN/Mg(TFSI)₂ and PVdC-co-/SN/EC/Mg(TFSI)₂ systems

Figure 5.30 depicts the X-Ray diffractogram of pure Mg(TFSI)₂ salt. The strong peaks reveal the crystalline nature of the ionic salt at 12.6°, 14.1°, 16.1°, 17.4°, 19.9°, 22.7°, 23.8°, 29.1°, 30.1° and 37.8°.

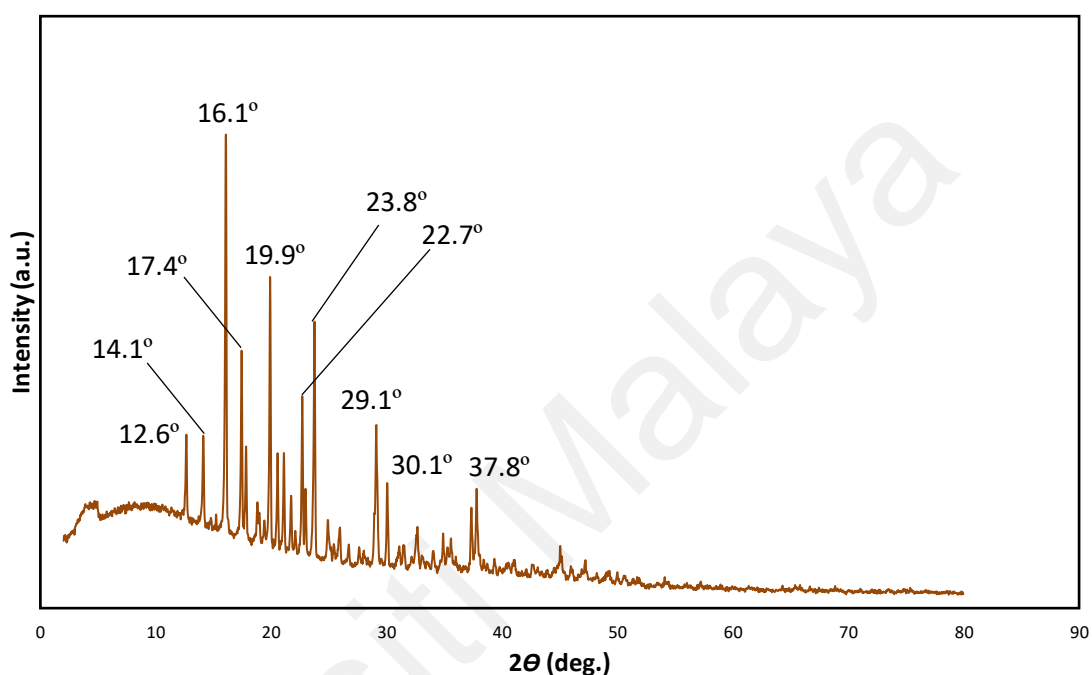


Figure 5.30: X-Ray diffractogram of pure Mg(TFSI)₂ salt.

Figure 5.31 and 5.32 show the XRD patterns of PVdC-co-AN/SN containing 10 wt.%, 20 wt.% and 30 wt.% of Mg(TFSI)₂ and PVdC-co-AN/SN/EC samples containing 10 wt.%, 15 wt.% and 30 wt.% of Mg(TFSI)₂ salt respectively. It can be observed that the addition of Mg(TFSI)₂ salt into the PVdC-co-AN/SN and PVdC-co-AN/SN/EC systems produced GPE with amorphous characteristic as there are no intense peaks associate to the characteristic peaks of SN, EC and Mg(TFSI)₂ detected. Hence, the absence of peaks pertaining to Mg(TFSI)₂ salt in the complexes indicates the complete dissolution of the salt in the polymer matrix (Subbu et al., 2016).

The X-Ray diffractograms of PVdC-co-AN, PVdC-co-AN/SN and PVdC-co-AN/SN/EC containing 20 wt.% Mg(TFSI)₂ are also plotted as shown in Figure 5.33 to investigate the role of SN and EC on the prepared GPE samples. From the plot, it can be observed that there is a small peak at 4.2° detected on the PVdC-co-AN/20 wt.% Mg(TFSI)₂ sample. However, the peak broadens after the addition of SN and disappeared after the addition of EC and shows the improvement of the amorphousity of the GPE.

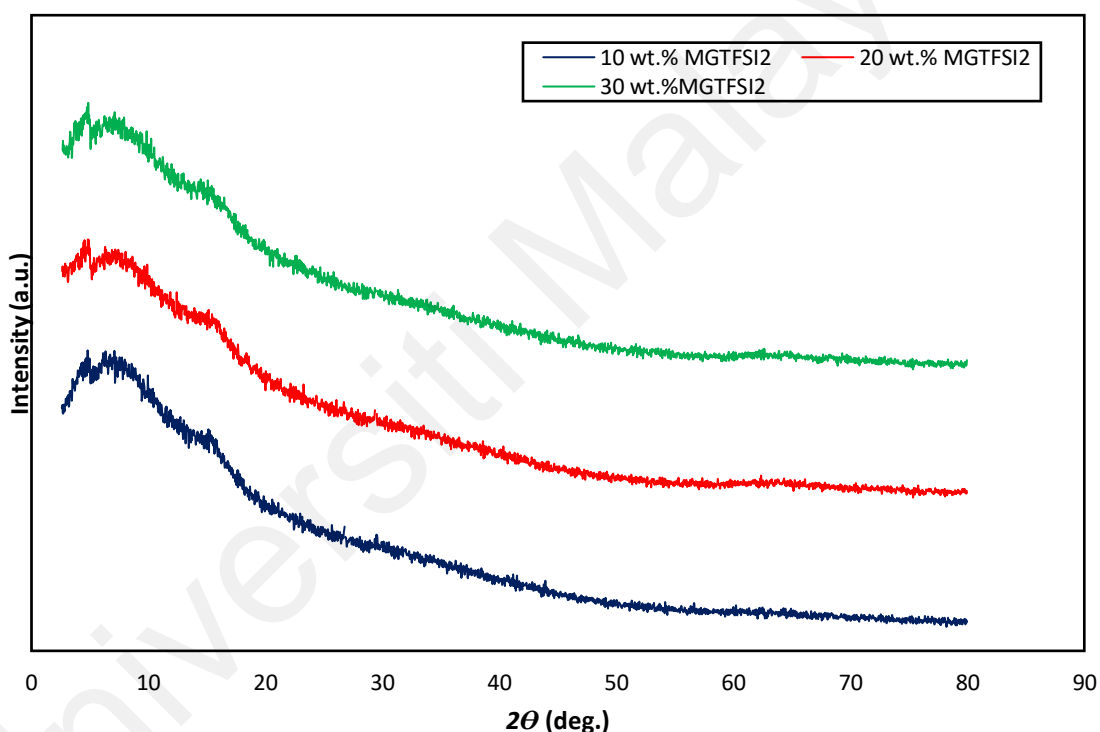


Figure 5.31: X-Ray diffractograms of PVdC-co-AN/SN containing 10 wt.%, 20 wt.% and 30 wt.% Mg(TFSI)₂.

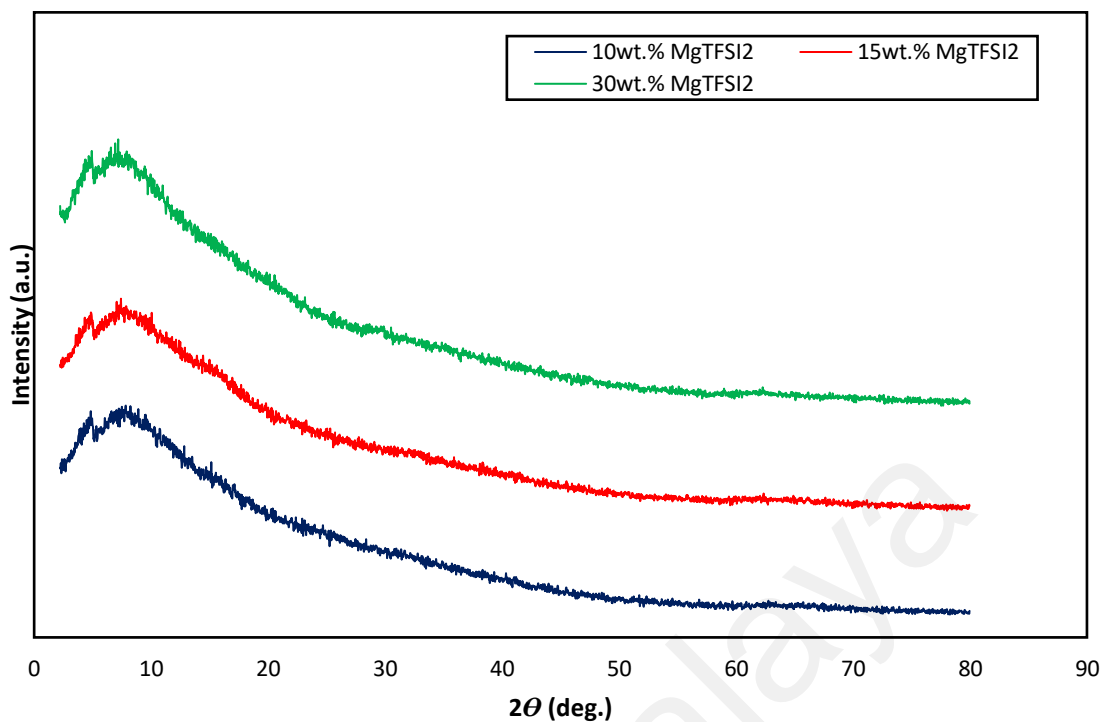


Figure 5.32: X-Ray diffractograms of PVdC-co-AN/SN/EC containing 10 wt.%, 15 wt.% and 30 wt.% Mg(TFSI)₂.

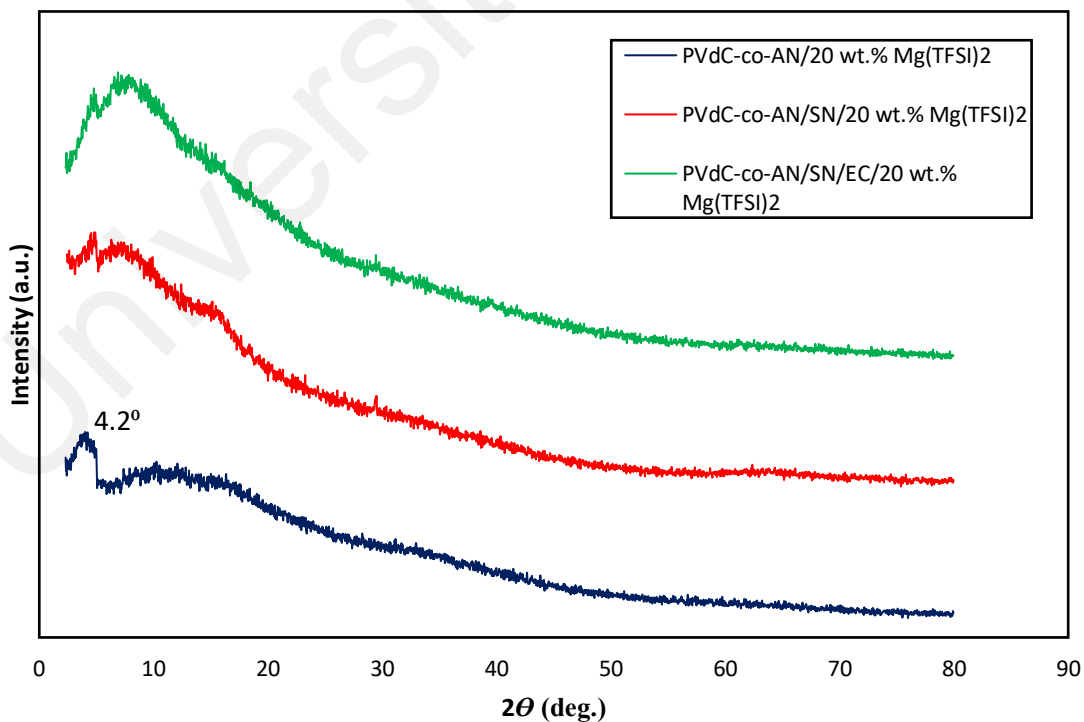


Figure 5.33: PVdC-co-AN, PVdC-co-AN/SN and PVdC-co-AN/SN/EC containing 20 wt.% Mg(TFSI)₂.

In short, XRD result in Figure 5.19 shows the pure PVdC-co-AN is originally amorphous in nature. It is observed that with the addition of crystalline SN, EC, MgTf₂ and Mg(TFSI)₂, the amorphousness of the polymer remains with only one broad peak exist throughout the GPE systems. In addition, the absence of intense diffraction peaks of both polymer, plasticizer and salt complexes reveal the good miscibility of polymer and salt, with plasticizer at the molecular level. However, it was found that the type of salt added to the polymer influences the amorphousness of the GPE. In the case of the PVdC-co-AN/30 wt.% MgTf₂ and PVdC-co-AN/20 wt.% Mg(TFSI)₂ samples; both without SN and EC, the sample with MgTf₂ salt produce several sharp peaks on the XRD pattern, while for the sample with Mg(TFSI)₂, only one small peak detected. This shows that Mg(TFSI)₂ gives better amorphousity to the prepared GPEs. In addition, the role of SN as plasticizer can also be seen here as the addition of SN helps in reducing the existing peaks of the GPEs as shown in Figure 5.29 and 5.33.

5.3 Field Emission Scanning Electron Microscopy (FESEM)

In this work, Field Emission Scanning Electron Microscopy (FESEM) is carried out to study the morphological surface of GPEs and visualize very small topographic details on the surface of GPEs. The FESEM images for pure PVdC-co-AN, PVdC-co-AN/SN and PVdC-co-AN/SN/EC samples are shown in Figure 5.34 (a) to (c) respectively. For pure PVdC-co-AN, it displayed a waving smooth and uniform structure without any phase separation at room temperature. This indicates of the high affinity of the polymer host (Carquigny et al., 2008; Johan et al., 2011). Meanwhile, the micrograph of PVdC-co-AN/SN sample illustrates a fibrous texture at microscopic level which shows plastic crystal SN appears to be uniformly distributed in the form of fine fibres, entrapped in the polymeric network (Sharma & Hashmi, 2018). When plasticizer EC is added into the

PVdC-co-AN/SN sample, the fibres of SN are distinctly disappeared might be due to the presence of EC and the possibility of the compatibility of the combination of both SN and EC which resulting to a smoother and clearer surface of GPE.

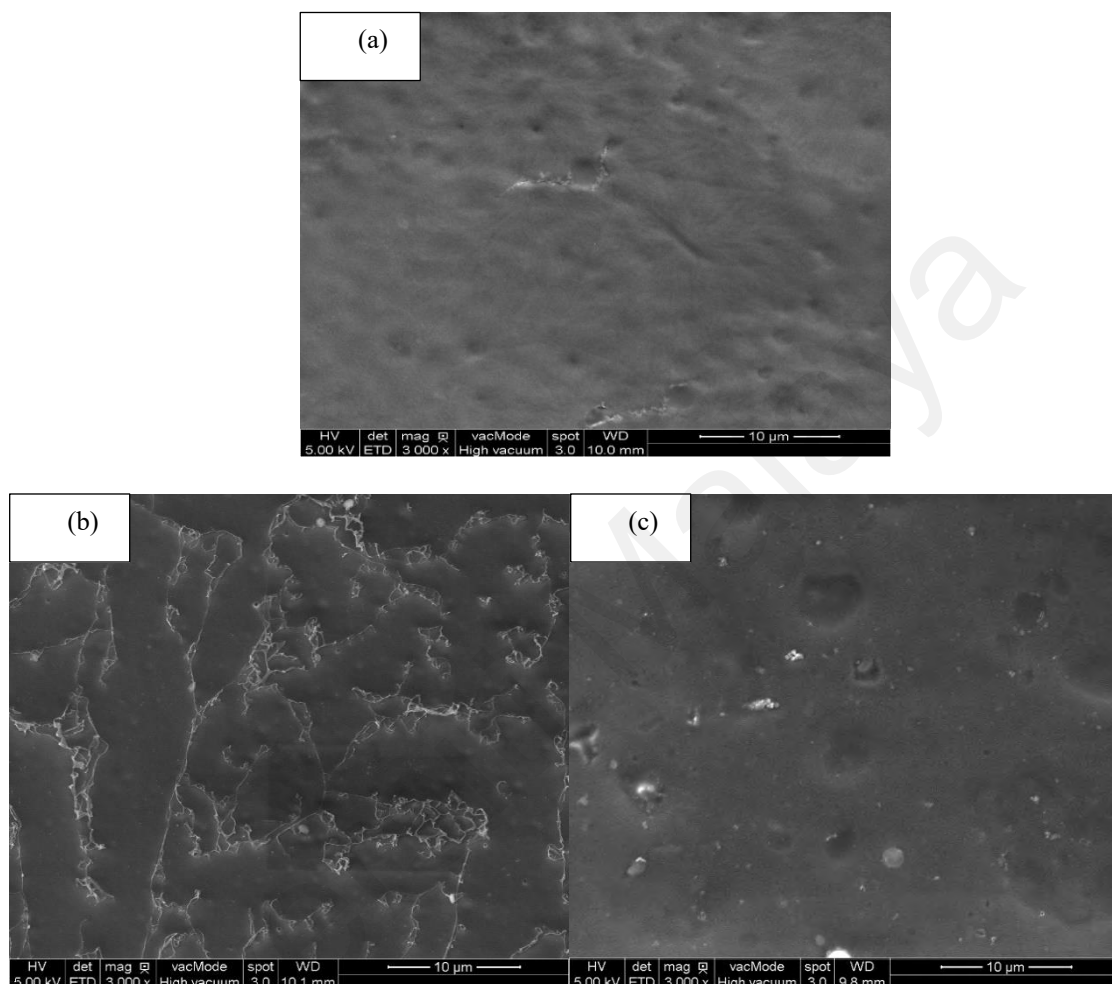


Figure 5.34: FESEM micrographs of (a) pure PVdC-co-AN (b) PVdC-co-AN/SN and (c) PVdC-co-AN/SN/EC samples.

Figure 5.35 shows the FESEM images of PVdC-co-AN/SN/30 wt.% MgTf₂ and PVdC-co-AN/SN/EC/30 wt.% MgTf₂ samples. For PVdC-co-AN/SN/30 wt.% MgTf₂, the morphological surface of the sample shows the presence of pores which mainly due to the solvent removal (removal of THF solvent), increased amorphousity (proved by XRD), and solvent retention ability in the polymer electrolyte system (Flora et al., 2013). The pores become less visible and smoother after the addition of EC which is closely related

to the amorphous nature of the polymer electrolyte complex (Baskaran et al., 2007). The same results are also observed for GPE containing $\text{Mg}(\text{TFSI})_2$ in Figure 5.36. For PVdC-co-AN/SN/20 wt.% $\text{Mg}(\text{TFSI})_2$ sample, the presence of pores are quite distinct and comparing it with PVdC-co-AN/SN/EC/15 wt.% $\text{Mg}(\text{TFSI})_2$ sample, the surface is almost flat and uniform with less visible pores which is also related to the amorphous nature of the GPE that has been proven by XRD analysis. In short, from these FESEM results, it can be concluded that EC helps in obtaining smoother and clearer surface of GPE in microscopic level.

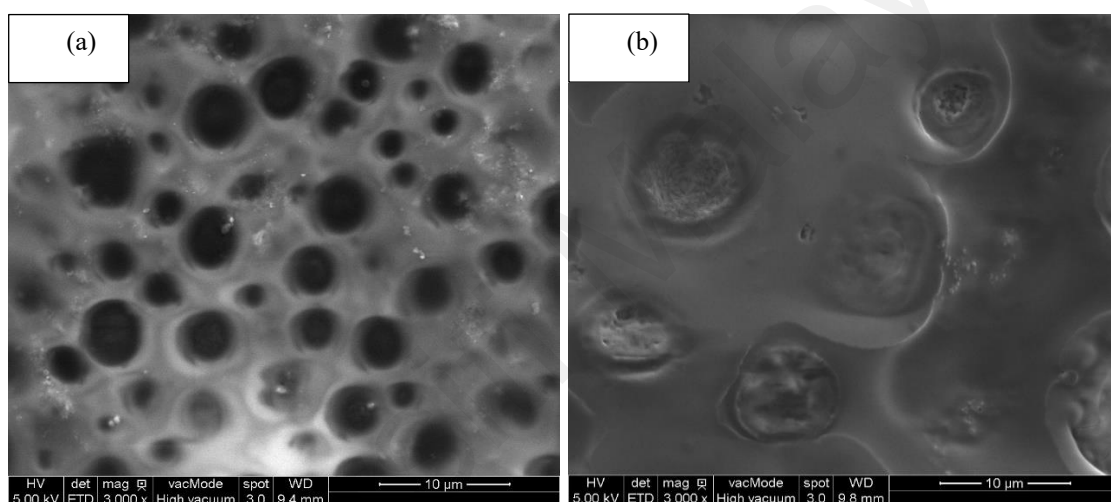


Figure 5.35: FESEM micrographs of (a) PVdC-co-AN/SN/30 wt.% MgTf_2 and (b) PVdC-co-AN/SN/EC30 wt.% MgTf_2 .

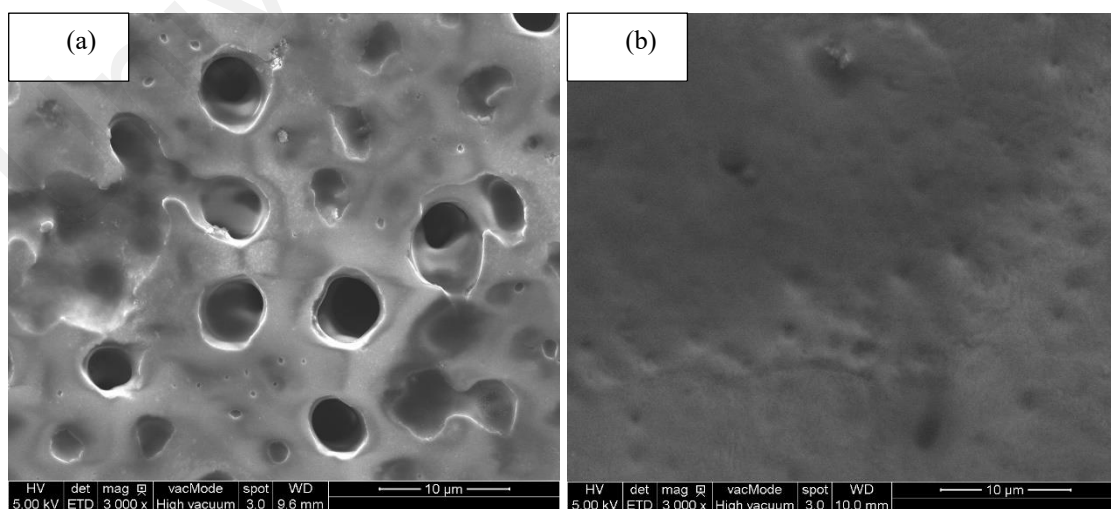


Figure 5.36: FESEM micrographs of (a) PVdC-co-AN/SN/20 wt.% $\text{Mg}(\text{TFSI})_2$ and (b) PVdC-co-AN/SN/EC/15 wt.% $\text{Mg}(\text{TFSI})_2$.

CHAPTER 6: THERMAL ANALYSIS

6.1 Differential Scanning Calorimetry (DSC)

In this study, differential scanning calorimetry (DSC) is chosen to analyse the thermal properties of prepared GPE samples by evaluating the changes in the heat capacities/physical transformation of the materials with temperature. The transitions such as glass transitions (T_g), melting point (T_m) and phase changes are identified during this process.

Figure 6.1 shows the DSC curves for pure PVdC-co-AN, PVdC-co-AN/SN and PVdC-co-AN/SN/EC samples. It can be observed that the pure PVdC-co-AN sample exhibits a glass transition temperature, T_g value of 51.42 °C and no endothermic/exothermic peaks detected which explains the existence of complete amorphous phase of the pure polymer. For PVdC-co-AN/SN, the DSC curve shows two endothermic peaks which are the characteristic transition temperature T_{cp} (from normal crystal to plastic crystal) at -38.90 °C and melting temperature, T_m at 56.78 °C. Both peaks indicate the plastic crystal behavior of SN (Alarco et al., 2004a; Li et al., 2016). The curve also recorded a lower value of T_g compared to pure PVdC-co-AN which is 24.78 °C. Since T_g is the temperature where the polymer transformed from rigid (glassy solid) to being soft and flexible (rubbery material), thus, a lower value of T_g indicates polymer with higher flexibility while high value of T_g increase the stiffness of the polymer. The chain flexibility on the other hand is defined as the ability of a chain to rotate about the chain bonds. Therefore, the decrease in the value of T_g will also helps in easy movement of the polymer chains resulting an increase in the conductivity. From the result outcomes, it is shown that SN can lower the T_g value and confirms its role as plasticizer.

In PVdC-co-AN/SN/EC sample, the T_g value is then lowered to 15.34 °C compared to PVdC-co-AN/SN which might be attributed to the increase in the mobility of the polymer

chain as EC is well known to help in soften the polymer backbone. The characteristic peaks of SN also disappeared after the addition of EC and shows that the amorphousness of the GPE sample increases after adding EC and thus, conductivity increases (Pradhan et al., 2007). The values of T_g with conductivity is tabulated in Table 6.1.

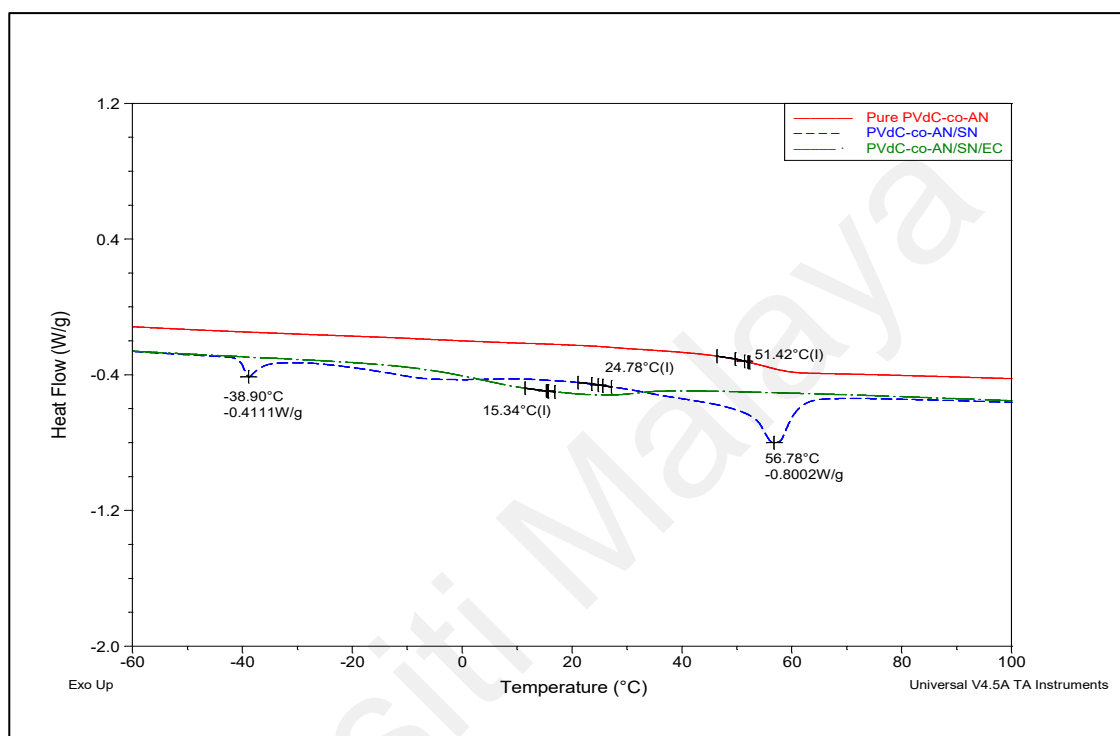


Figure 6.1: DSC curves of pure PVdC-co-AN, PVdC-co-AN/SN and PVdC-co-AN/SN/EC samples.

Table 6.1: Glass transition temperature and ionic conductivity of unsalted GPEs.

Sample	Glass Transition Temperature, T_g (°C)	Room Temperature Ionic Conductivity, σ (S cm ⁻¹)
Pure PVdC-co-AN	51.42	7.35×10^{-10}
PVdC-co-AN/SN	24.78	1.82×10^{-9}
PVdC-co-AN/SN/EC	15.34	6.67×10^{-9}

6.1.1 PVdC-co-AN/SN/MgTf₂ and PVdC-co-AN/SN/EC/MgTf₂

The DSC thermograms for PVdC-co-AN/SN and PVdC-co-AN/SN/EC containing 10 wt.%, 20 wt.% and 30 wt.% of MgTf₂ are as shown in Figure 6.2 and 6.3 respectively. For figure 6.2, the curves clearly shown that the characteristic peaks of SN i.e., T_{cp} and T_m in Figure 6.1 disappeared after the addition of MgTf₂ salt. This is relatively due to the strong interaction between SN and MgTf₂ that causes the deterioration of the crystalline structure. As a result, the rate of isomer transition of SN from gauche to trans enhanced that leads to the increase in the trans conformer concentration. This high defect density state phase will also facilitate the ionic mobility in the GPE system that will give increment in ionic conduction (Alarco et al., 2004a; Das et al., 2009; Zainuddin et al., 2016).

The T_g values of each GPE sample for both PVdC-co-AN/SN/MgTf₂ and PVdC-co-AN/SN/EC/MgTf₂ systems were tabulated in Table 6.2 with their respective ionic conductivity values. It can be observed that the T_g values of GPE samples for each system decreased throughout the system as the concentration of MgTf₂ increases with the lowest T_g value of 3.73 °C for PVdC-co-AN/SN/30 wt.% MgTf₂ and 2.01 °C for PVdC-co-AN/SN/EC/30 wt.% MgTf₂ respectively. The decrease of T_g with the addition of MgTf₂ suggests that the addition of MgTf₂ can increase the flexibility of polymer chain and an improved segmental motion may be expected (Karmakar & Ghosh, 2014). Since the conduction of ions in polymer electrolyte system depends partly on the flexibility of the polymer chains, a more flexible macromolecules produced in the system can allow faster ion migration than rigid polymers, thus, give higher ionic conductivities.

In addition, the reduction of T_g in both systems also shows that the interaction between magnesium salt and the polymer matrix affects the main chain dynamics of the polymer. The PVdC-co-AN is generally disturbed by MgTf₂ due to the coordination interactions

between the Mg^{2+} ions and nitrile group in the polymer (the presence of plasticizer is neglected in this explanation) which causes the increase in amorphous nature of the polymer electrolytes. Therefore, as the concentration of MgTf_2 increases, a better ionic diffusivity and higher ionic conductivity will be obtained.

However, as a whole, the T_g values of GPE samples in PVdC-co-AN/SN/EC/ MgTf_2 system are lower than samples in PVdC-co-AN/SN/ MgTf_2 system. This shows that the role of EC as organic plasticizer helps in improving the amorphousness of the samples by softening the polymer backbone compared with samples in GPE system without EC. These results are in accordance with the ionic conductivity values obtained.

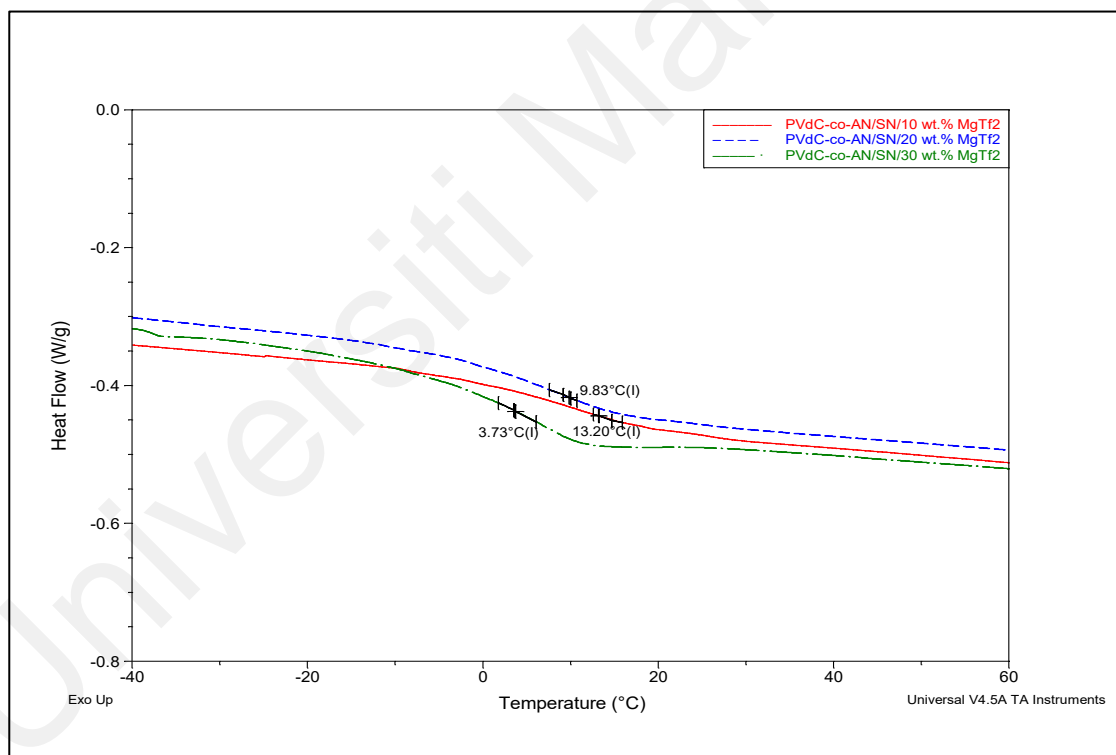


Figure 6.2: DSC curves of PVdC-co-AN/SN/10 wt.% MgTf_2 , PVdC-co-AN/SN/20 wt.% MgTf_2 and PVdC-co-AN/SN/30 wt.% MgTf_2 samples at a temperature range of -40 °C to 60 °C.

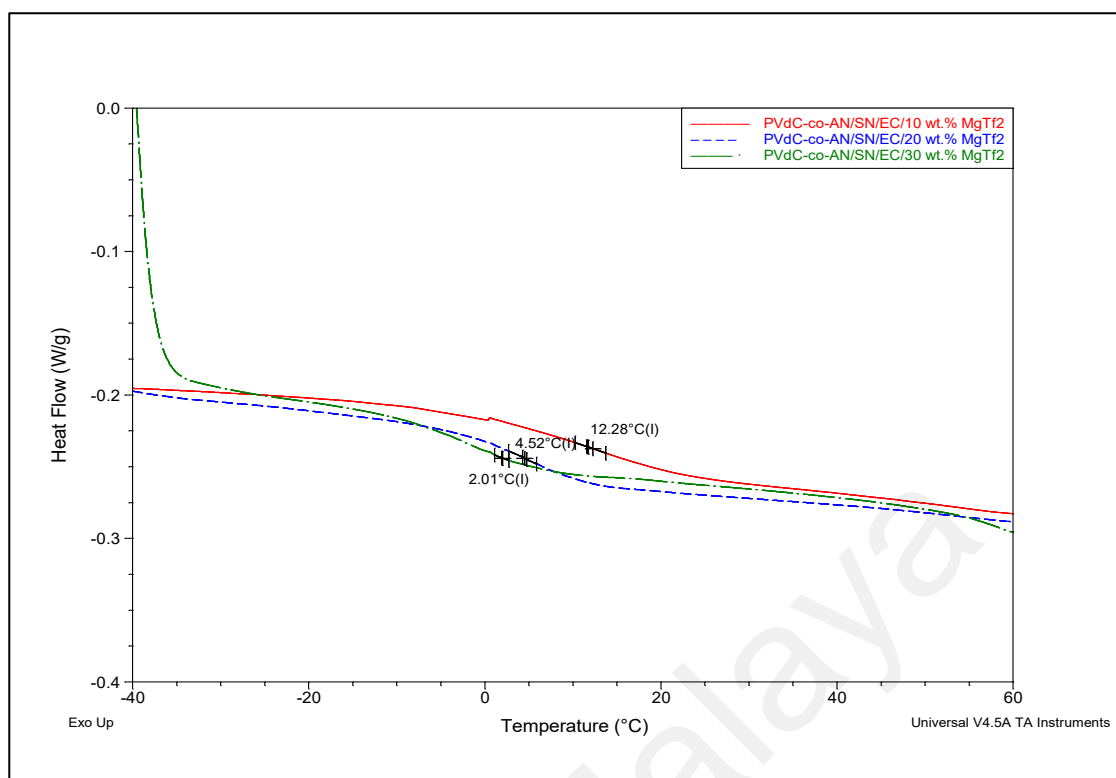


Figure 6.3: DSC curves of PVdC-co-AN/SN/EC/10 wt.% MgTf₂, PVdC-co-AN/SN/EC/20 wt.% MgTf₂ and PVdC-co-AN/SN/EC/30 wt.% MgTf₂ samples at a temperature range of -40 °C to 60 °C.

Table 6.2: T_g values for GPE samples in PVdC-co-AN/SN/MgTf₂ and PVdC-co-AN/SN/EC/MgTf₂ systems.

System	MgTf ₂ content (wt.%)	Glass transition temperature, T_g (°C)	Room temperature ionic conductivity, σ (S cm ⁻¹)
PVdC-co-AN/SN	10	13.20	2.34×10^{-8}
	20	9.83	3.81×10^{-8}
	30	3.73	2.26×10^{-7}
PVdC-co-AN/SN/EC	10	12.28	6.54×10^{-8}
	20	4.52	2.13×10^{-7}
	30	2.01	2.82×10^{-7}

6.1.2 PVdC-co-AN/SN/Mg(TFSI)₂ and PVdC-co-AN/SN/EC/Mg(TFSI)₂

Figure 6.4 shows the DSC profiles of PVdC-co-AN/SN system with 10 wt.%, 20 wt.% and 30 wt.% of Mg(TFSI)₂ at a temperature range of -40 °C to 60 °C. From the curves, it is clearly shown that no endothermic peaks due to plastic behavior of SN are detected for all GPE samples. It has been proposed that TFSI has a plasticization effect that can reduce both the crystallinity and the T_g of the polymer electrolytes (Lascaud et al., 1994) and might be the reason of the disappearance of the endothermic peaks of SN. This also proves the deterioration of crystallinity after the addition of Mg(TFSI)₂ salt to the PVdC-co-AN/SN system. As for PVdC-co-AN/SN/EC system, the DSC thermograms were plotted for the samples containing 10 wt.%, 15 wt.% and 30 wt.% of Mg(TFSI)₂ as shown in Figure 6.5.

The T_g values for GPE samples in PVdC-co-AN/SN/Mg(TFSI)₂ and PVdC-co-AN/SN/EC/Mg(TFSI)₂ systems were tabulated in Table 6.3 with their respective ionic conductivity values. From the table, the T_g values are observed to follow the pattern of ionic conductivity. For PVdC-co-AN/SN system, the highest conducting sample of PVdC-co-AN/SN/20 wt.% Mg(TFSI)₂ exhibits the lowest value of T_g which is 7.56 °C while the lowest conducting sample of PVdC-co-AN/SN/10 wt.% Mg(TFSI)₂ obtained the highest value of T_g which is 16.07 °C. Meanwhile, for PVdC-co-AN/SN/EC system, the lowest value of T_g is from the highest conducting sample of PVdC-co-AN/SN/EC/15 wt.% Mg(TFSI)₂ which is 4.51 °C while the highest value of T_g is from PVdC-co-AN/SN/EC/30 wt.% Mg(TFSI)₂ which is 11.85 °C. These results show that, the T_g values of the GPE of both systems decreased until maximum conductivity obtained and then decreased beyond that salt concentration. The decrease of T_g with the increase of Mg(TFSI)₂ concentrations can be explained by the increase of conformational mobility of the polymer backbone. As the Mg(TFSI)₂ concentration increases, it tends to exist in ion pairs or ion clusters between polymer matrix and thus lead to weaken the dipole-

dipole interactions, which again resulted in the softer polymer backbone and simultaneously increases ionic conductivity (Baskaran et al., 2007). With the increase in the segmental mobility, more empty space are formed which aid in the migration of Mg^{2+} cations when electric field is applied (Ramesh & Arof, 2001). However, beyond the minimum T_g , i.e. the maximum conductivity, the values of T_g increase upon the increasing of $\text{Mg}(\text{TFSI})_2$ concentration for both PVdC-co-AN/SN/ $\text{Mg}(\text{TFSI})_2$ and PVdC-co-AN/SN/EC/ $\text{Mg}(\text{TFSI})_2$ systems. A further increase in salt content may results in an increase in polymer rigidity caused by ionic crosslinking which hinder the segmental mobility and shift the T_g of the GPEs to higher temperatures.

Nevertheless, the values of T_g for both $\text{Mg}(\text{TFSI})_2$ systems are higher entirely compared to MgTf_2 systems. These higher T_g can be explained by a greater degree of dissociation of $\text{Mg}(\text{TFSI})_2$ salt because of its lower lattice energy than MgTf_2 salt. This higher degree of dissociation of $\text{Mg}(\text{TFSI})_2$ salt generates more cations that coordinate to the polymer and become the possible argument for the greater in values of T_g .

In summary, the GPE samples from PVdC-co-AN/SN/ MgTf_2 , PVdC-co-AN/SN/EC/ MgTf_2 , PVdC-co-AN/SN/ $\text{Mg}(\text{TFSI})_2$ and PVdC-co-AN/SN/EC/ $\text{Mg}(\text{TFSI})_2$ systems show no melting point, crystallization peaks and other endothermic peaks. Instead, they have a glass transition temperature, T_g which is a property of the polymer electrolyte in amorphous region. Thus, the GPE samples are confirmed to be amorphous in natures as proved by X-Ray diffraction analysis in Chapter 5.

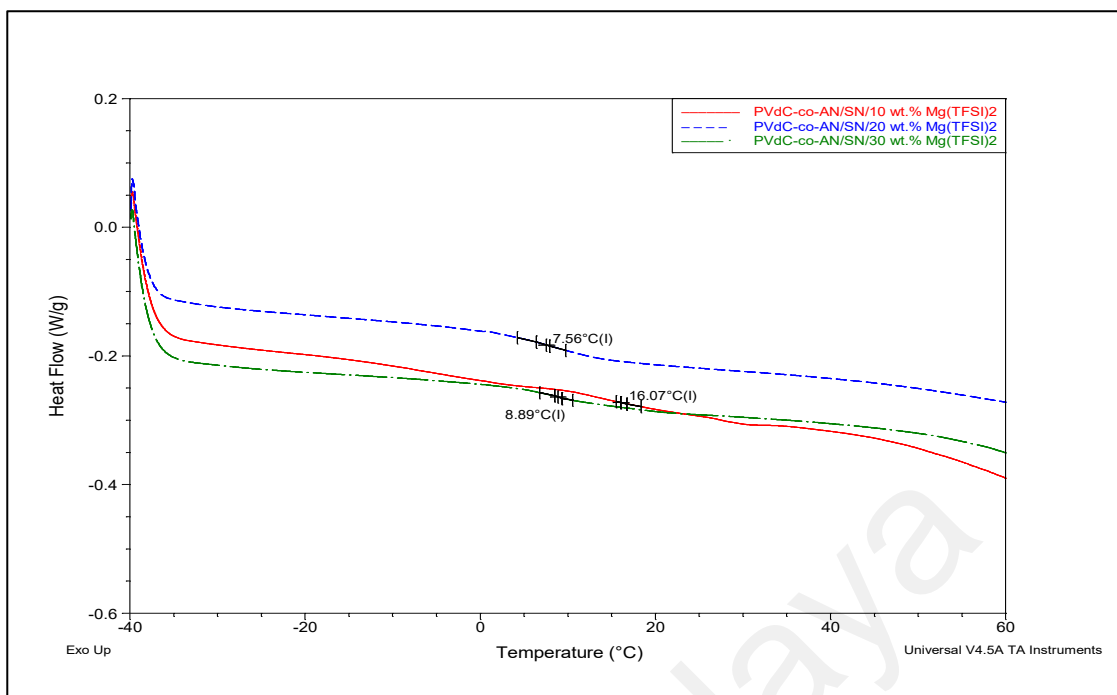


Figure 6.4: DSC curves of PVdC-co-AN/SN/10 wt.% Mg(TFSI)₂, PVdC-co-AN/SN/20 wt.% Mg(TFSI)₂ and PVdC-co-AN/SN/30 wt.% Mg(TFSI)₂ samples at a temperature range of -40 °C to 60 °C.

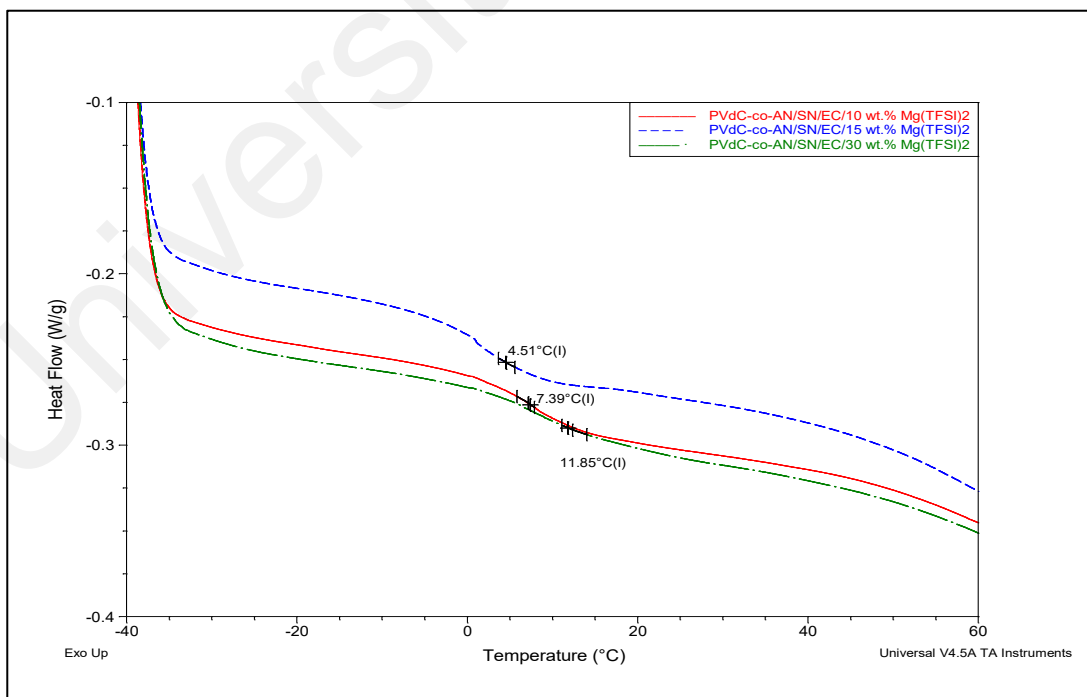


Figure 6.5: DSC curves of PVdC-co-AN/SN/EC/10 wt.% Mg(TFSI)₂, PVdC-co-AN/SN/EC/20 wt.% Mg(TFSI)₂ and PVdC-co-AN/SN/EC/30 wt.% Mg(TFSI)₂ samples at a temperature range of -40 °C to 60 °C.

Table 6.3: T_g values for GPE samples in PVdC-co-AN/SN/Mg(TFSI)₂ and PVdC-co-AN/SN/EC/Mg(TFSI)₂ systems.

System	Mg(TFSI)₂ content (wt.%)	Glass transition temperature, T_g (°C)	Room temperature ionic conductivity, σ (S cm⁻¹)
PVdC-co-AN/SN	10	16.07	2.12×10^{-7}
	20	7.56	1.61×10^{-6}
	30	8.89	4.57×10^{-7}
PVdC-co-AN/SN/EC	10	7.39	1.54×10^{-6}
	15	4.51	1.93×10^{-6}
	30	11.85	1.00×10^{-7}

Universiti Malaysia

CHAPTER 7: ELECTROCHEMICAL STUDIES AND BATTERY

FABRICATION

Electrochemical studies are essential in evaluating the performance of polymer electrolyte to be employed successfully in electrochemical devices. In this study, linear sweep voltammetry (LSV) and cyclic voltammetry (CV) were carried out for the highest conducting sample from each GPE system and the most electrochemically stable GPE from each system will be fabricated as magnesium rechargeable batteries.

7.1 Linear sweep voltammetry (LSV)

Linear sweep voltammetry is a facile method in determining the decomposition voltage of polymer electrolytes to ensure the charge-discharge stability in a battery. The sweep voltammogram measurements were performed with stainless steel as working electrode and magnesium as the reference/counter electrode SS/GPE/Mg cell (vs Mg/Mg²⁺) with a scan rate of 5 mV s⁻¹.

7.1.1 PVdC-co-AN/SN/MgTf₂ and PVdC-co-AN/SN/EC/MgTf₂

Figure 7.1 (a) and (b) show the linear sweep voltammograms of GPE samples of PVdC-co-AN/SN/30 wt.% MgTf₂ and PVdC-co-AN/SN/EC/30 wt.% MgTf₂ respectively. From both plots, it can be observed that there is a very low background current measured initially that might be attributed to the change of the surface of the stainless steel electrode (Zhou et al., 2008). The current then began to flow and increased rapidly upon reaching the cut-off voltage indicates that the electrolyte decomposition process has taken place (Saikia et al., 2011; Yang et al., 2006). The cut-off voltage; i.e. the onset decomposition voltage is observed at 3.0 V for PVdC-co-AN/SN/30 wt.%

MgTf₂ and 3.6 V for PVdC-co-AN/SN/EC/30 wt.% MgTf₂ which indicates that the electrolyte decomposition process has taken place at these voltage values (Saikia et al., 2011; Yang et al., 2006). The results indicate that the onset decomposition voltage is higher for PVdC-co-AN/SN/EC/30 wt.% MgTf₂ compared to PVdC-co-AN/SN/30 wt.% MgTf₂. This might be due to the introducing of the carbonate units from EC into the polymer backbone that can improve the oxidative stability of the polymer electrolyte (Jung et al., 2017). Thus, the double plasticized GPE is more electrochemically stable as its capability to withstand high voltages at the cathode interface (Lee et al., 2000) is higher than single plasticized GPE.

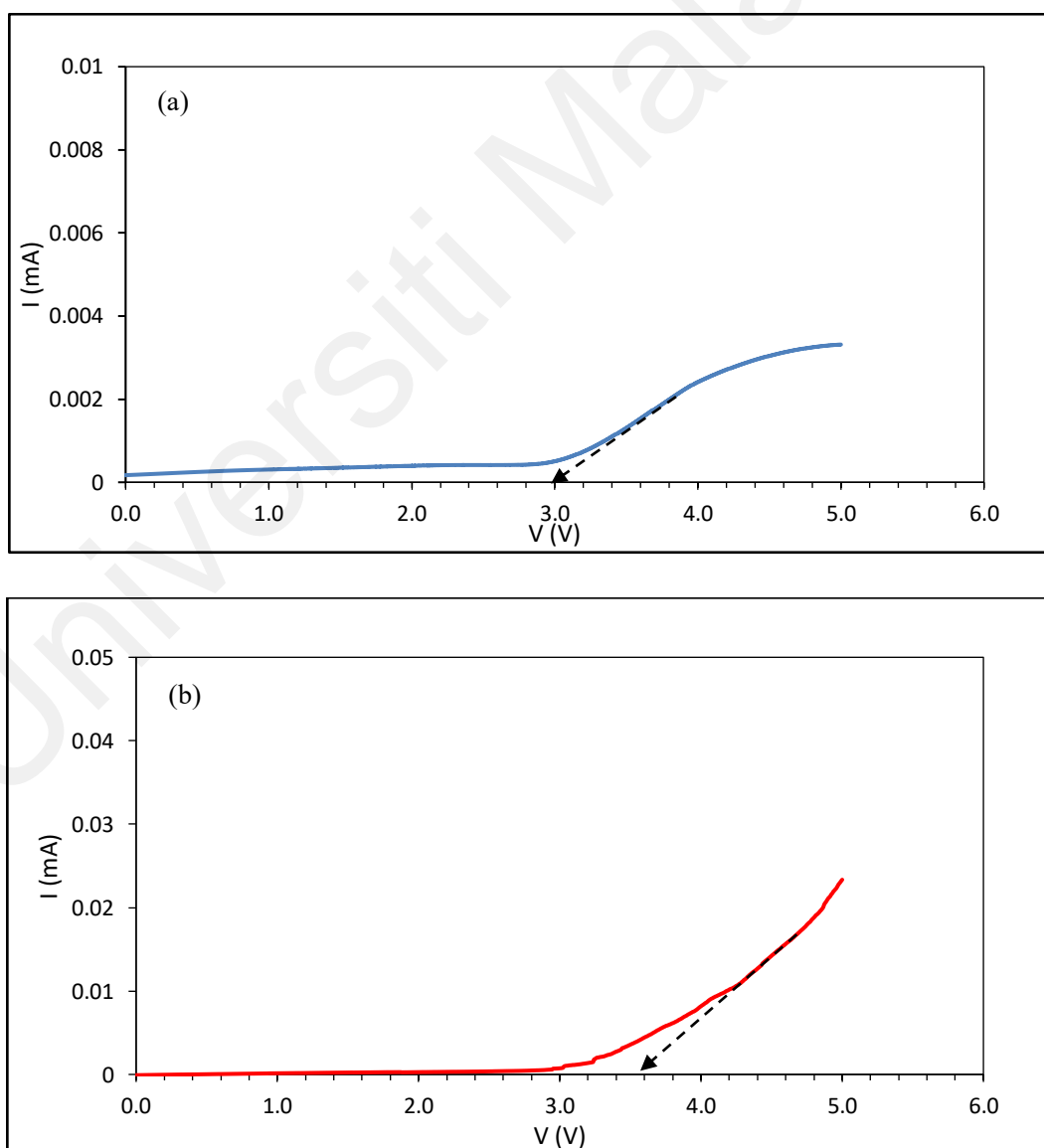


Figure 7.1: The linear voltammogram of (a) PVdC-co-AN/SN/30 wt.% MgTf₂ and (b) PVdC-co-AN/SN/EC/30 wt.% MgTf₂.

7.1.2 PVdC-co-AN/SN/Mg(TFSI)₂ and PVdC-co-AN/SN/EC/Mg(TFSI)₂

Figure 7.2 shows the linear sweep voltammograms of PVdC-co-AN/SN/20 wt.% Mg(TFSI)₂ and PVdC-co-AN/SN/EC/15 wt.% Mg(TFSI)₂.

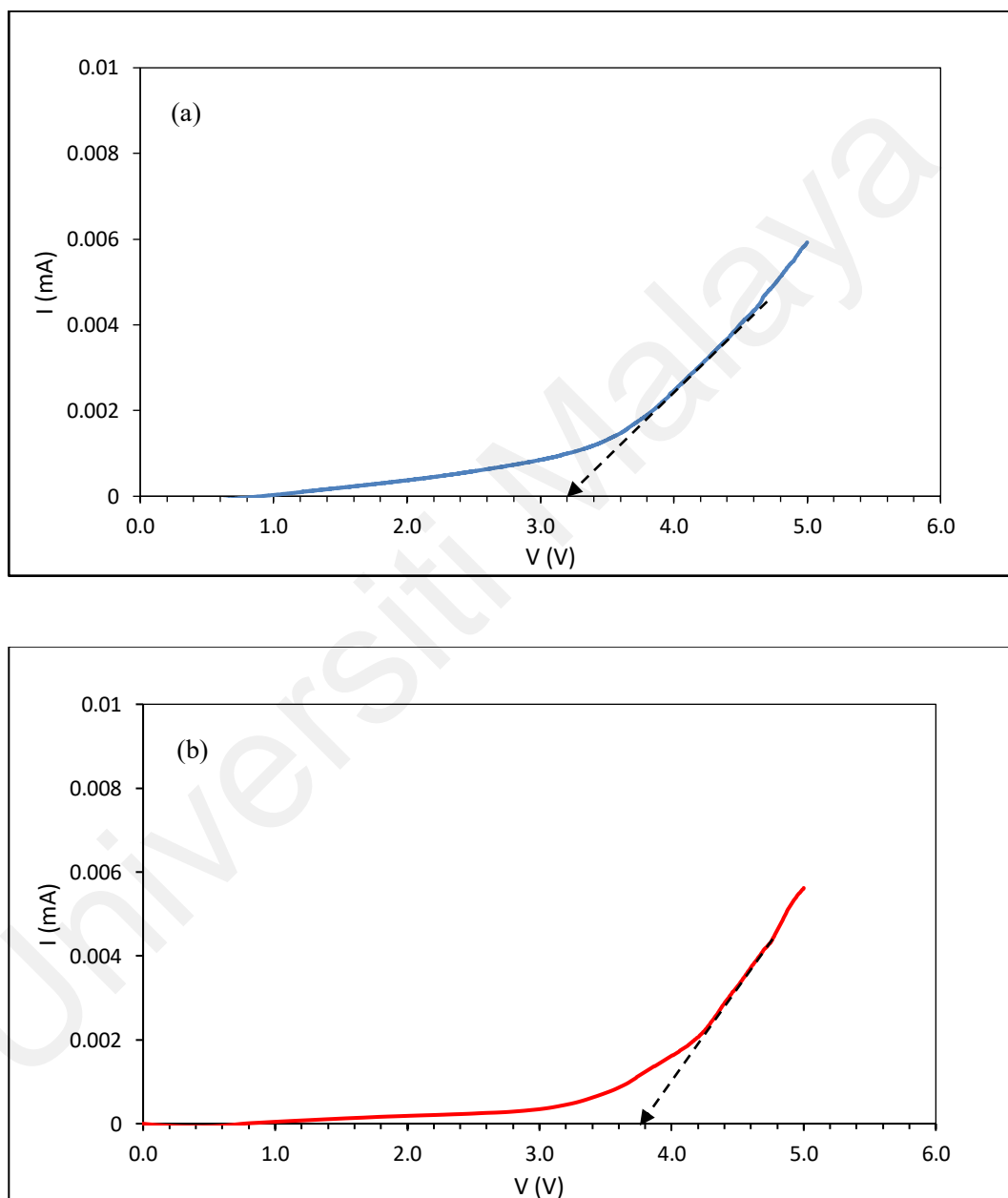


Figure 7.2: The linear voltammogram of (a) PVdC-co-AN/SN/20 wt.% Mg(TFSI)₂ and (b) PVdC-co-AN/SN/EC/15 wt.% Mg(TFSI)₂.

A voltage breakdown is observed at 3.2 V for single plasticized GPE and 3.8 V for double plasticized GPE which indicates that the electrolyte decomposition process has taken place at these voltage values (Saikia et al., 2011; Yang et al., 2006). The results imply that the onset decomposition voltage is higher for PVdC-co-AN/SN/EC/15 wt.% Mg(TFSI)₂ than PVdC-co-AN/SN/20 wt.% Mg(TFSI)₂ also due to the presence of carbonate unit from EC. In contrast, GPE samples containing Mg(TFSI)₂ exhibit higher in electrochemical stability window than GPE samples containing MgTf₂ for both single and double plasticized systems. Therefore, the GPEs containing Mg(TFSI)₂ salt are expected to perform better as rechargeable batteries compared to GPEs containing MgTf₂ salt.

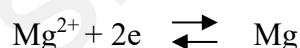
7.2 Cyclic voltammetry

Cyclic voltammetry (CV) is another electrochemical technique that commonly employed to investigate the reduction and oxidation processes occur between polymer electrolyte and electrodes. This technique is also an electroanalytical method for the purpose of analysis of GPE systems for battery development especially for identifying reversible reactions (desirable for rechargeable batteries). In this work, the cyclic voltammogram measurements were performed for symmetrical Cell I (SS/GPE/SS) and Cell II (Mg/GPE/Mg) for the highest conducting sample from each system with a voltage range of -5.0 V to 5.0 V (vs. Mg²⁺/Mg) and a scan rate of 5 mV s⁻¹.

7.2.1 PVdC-co-AN/SN/MgTf₂ and PVdC-co-AN/SN/EC/MgTf₂

Figure 7.3 (a) and (b) show the CV profiles for Cell-I and Cell-II respectively for the symmetrical cells containing PVdC-co-AN/SN/30 wt.% MgTf₂ sample while Figure 7.4

(a) and (b) are for the cells containing PVdC-co-AN/SN/EC/30 wt.% MgTf₂. In Cell-I, the GPE is in contact with the stainless steel which act as blocking electrodes, whereas in Cell-II, magnesium foils are used as reversible electrodes. From Cell-I for both samples, no distinct peaks are observed indicate no side reaction occurred between the electrolyte and SS electrodes (Balo et al., 2017). For Cell-II containing PVdC-co-AN/SN/30 wt.% MgTf₂ sample, an anodic peak is defined between 3.0 to 5.0 V which shows anodic oxidation at Mg electrode. Whereas, a poorly cathodic peak is detected in the potential range of -2.0 to -5.0 V due to the reduction of decomposition products (Silva et al., 2006). The poor peak also may be due to the strong participation of capacitive current (Silva et al., 2006; Subbu et al., 2015). For Cell-II containing PVdC-co-AN/SN/EC/30 wt.% MgTf₂, the anodic peak between 0 to 5.0 V and cathodic peak between 0 to -5.0 V are distinctly observed. This suggests that the cathodic deposition and anodic oxidation of Mg are facile at the Mg electrode and composite gel electrolyte interface due to the following reversible reaction (Pandey et al., 2011) :



Meanwhile, from the CV results also, it can be concluded that Cell-II shows higher in magnitude of currents for both samples compared to Cell-I. The higher in values of cathodic and anodic currents of Cell-II corresponds to the cathodic deposition and anodic oxidation of Mg at the electrode-electrolyte interfaces and the equilibrium attained by Mg²⁺ ions at the interfaces following the reversible redox reaction (Sharma & Hashmi, 2018). However, the cell-II containing PVdC-co-AN/SN/EC/30 wt.% MgTf₂ sample shows more distinct peaks for both anodic and cathodic with nearly equal in amplitudes of currents compared to the cell-II containing PVdC-co-AN/SN/30 wt.% MgTf₂ sample and thus implying a better in reversibility of magnesium ion insertion and extraction (Balo

et al., 2017). This also shows that double plasticized sample obtained better in CV performance and hence, will perform better as rechargeable magnesium battery.

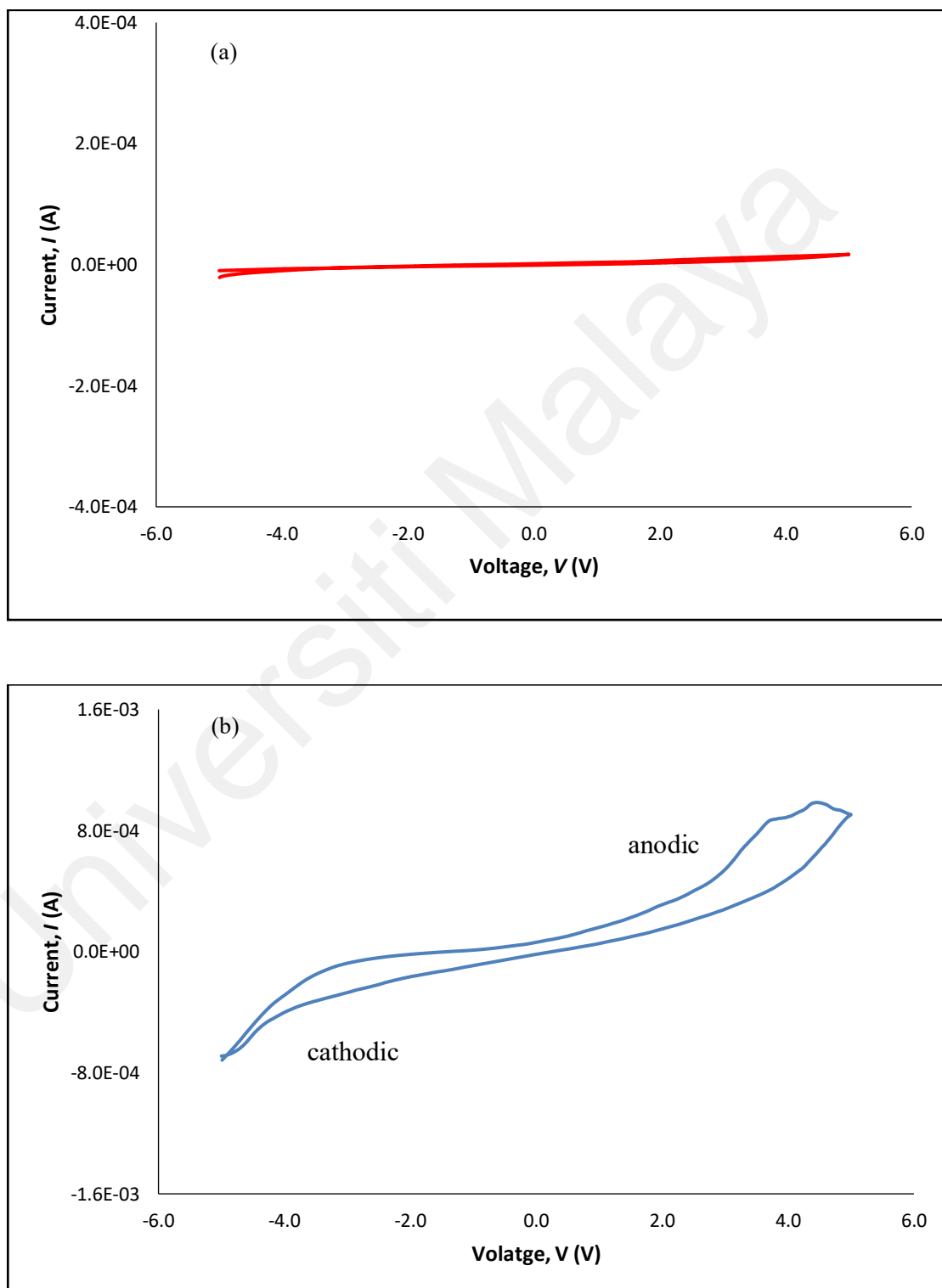


Figure 7.3: The cyclic voltammograms of (a) Cell-I: SS/GPE/SS and (b) Cell-II: Mg/GPE/Mg for PVdC-co-AN/SN/30 wt.% MgTf_2 sample.

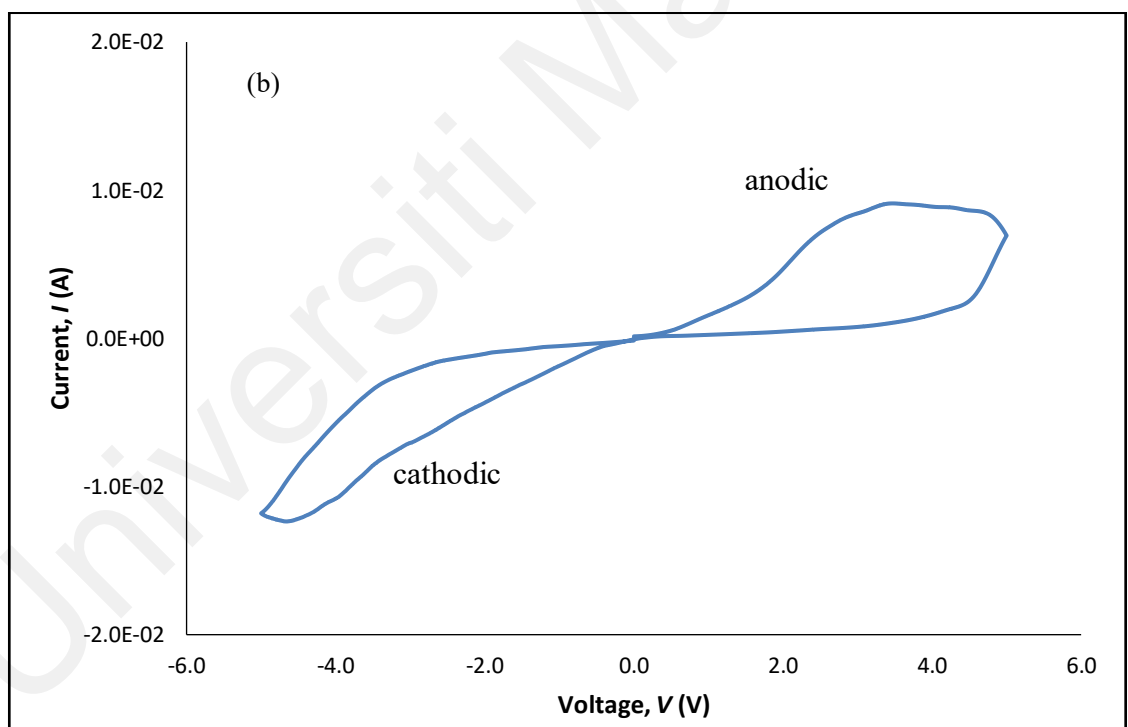
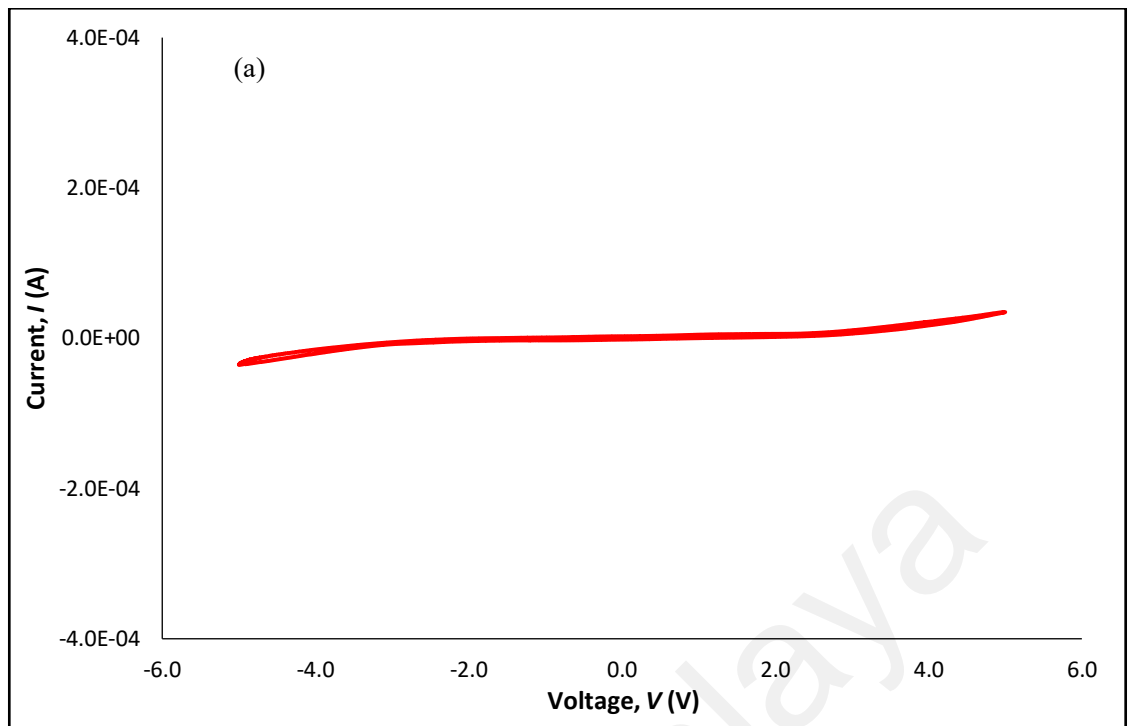


Figure 7.4: The cyclic voltammograms of (a) Cell-I: SS/GPE/SS and (b) Cell-II: Mg/GPE/Mg for PVdC-co-AN/SN/EC/30 wt.% MgTf₂ sample.

7.2.2 PVdC-co-AN/SN/Mg(TFSI)₂ and PVdC-co-AN/SN/EC/Mg(TFSI)₂

Figure 7.5 (a) and (b) show the CV profiles for Cell-I and Cell-II respectively for the symmetrical cells containing PVdC-co-AN/SN/20 wt.% Mg(TFSI)₂ sample while Figure 7.6 (a) and (b) are for the cells containing PVdC-co-AN/SN/EC/15 wt.% Mg(TFSI)₂. For these samples, also, no distinct peaks are observed from Cell-I indicates no side reaction occurred between the electrolyte and SS electrodes (Balo et al., 2017). Meanwhile, for Cell-II containing PVdC-co-AN/SN/20 wt.% Mg(TFSI)₂ sample, an anodic peak is clearly defined between 0 to 5.0 V and a cathodic peak detected in the potential range of 0 to -3.0 V due to anode oxidation and cathode deposition on the Mg electrodes respectively. For Cell-II containing PVdC-co-AN/SN/EC/15 wt.% Mg(TFSI)₂ sample, the anodic peak between 3.0 to 5.0 V and cathodic peak between -3.0 to -5.0 V are distinctly observe and proved the redox reaction has occurred in the cell. In comparison of the CV profiles for Cell-II of both samples, the cell containing PVdC-co-AN/SN/EC/15 wt.% Mg(TFSI)₂ sample exhibits higher in magnitude of anodic/cathodic currents and better in reversibility of magnesium ion insertion and extraction than the cell containing PVdC-co-AN/SN/20 wt.% Mg(TFSI)₂ sample. This suggests that the combination of two types of plasticizers helps in increasing the CV performance due to the high dielectric constant of SN and EC and thus easier in ion dissociation i.e., producing more Mg ions for reversible redox reaction. Again, the double plasticized sample obtained better in CV performance and hence, will perform better as rechargeable magnesium battery.

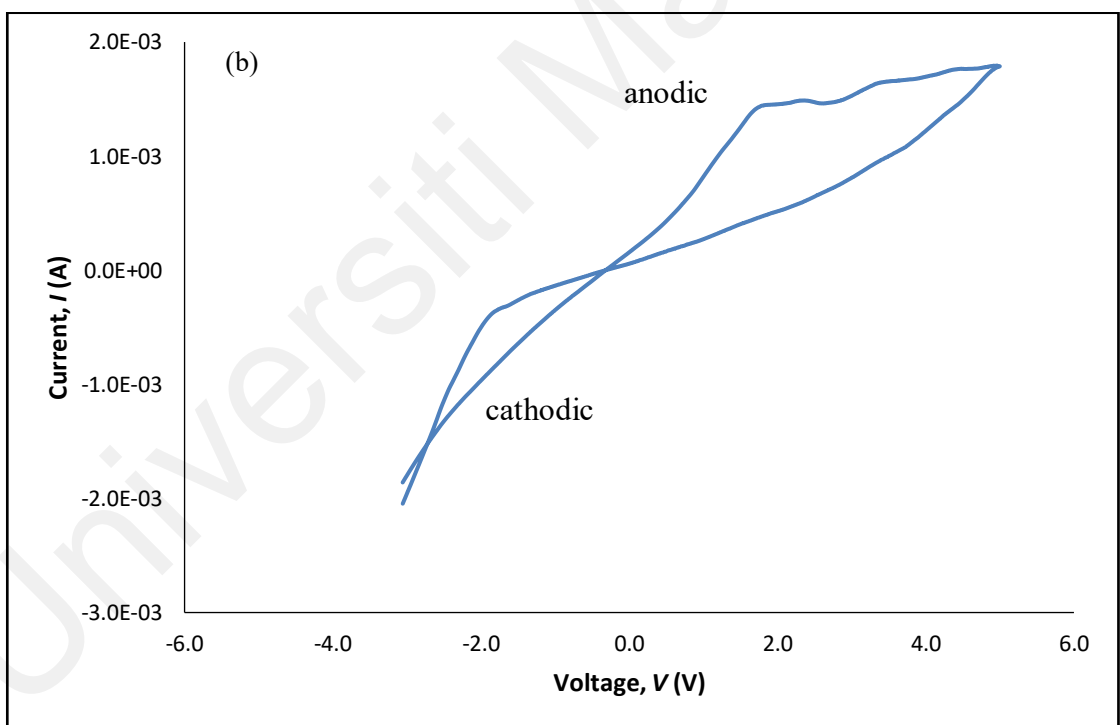
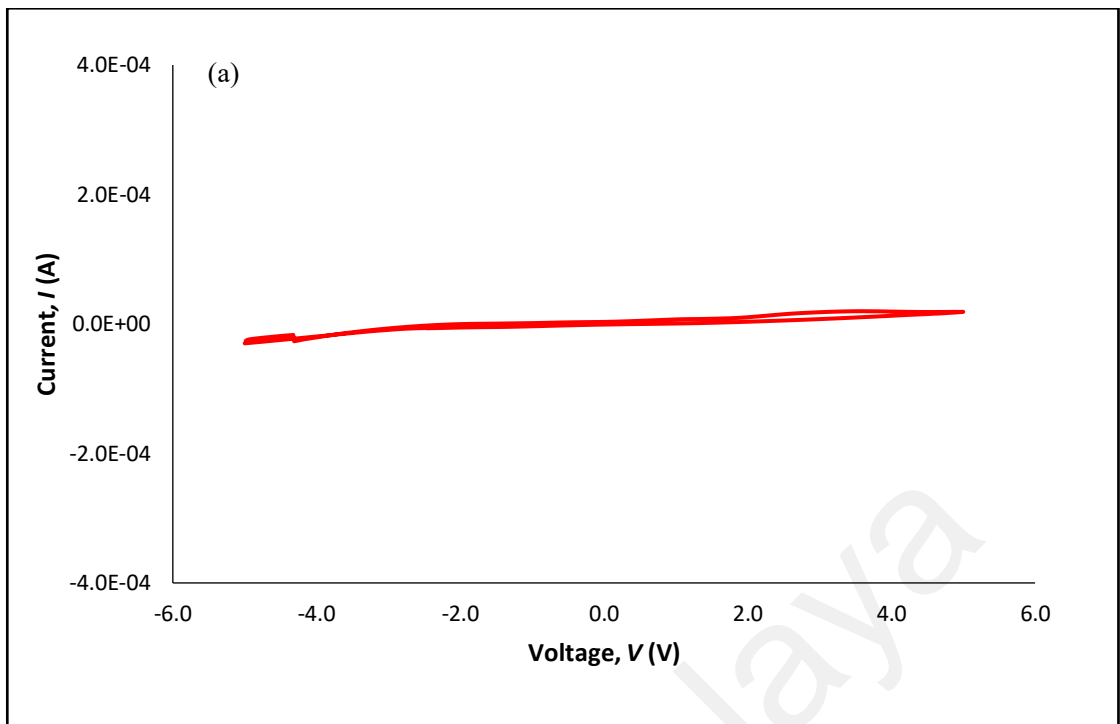


Figure 7.5: The cyclic voltammograms of (a) Cell I: SS/GPE/SS and (b) Cell II: Mg/GPE/Mg for PVdC-co-AN/SN/20 wt.% Mg(TFSI)₂ sample.

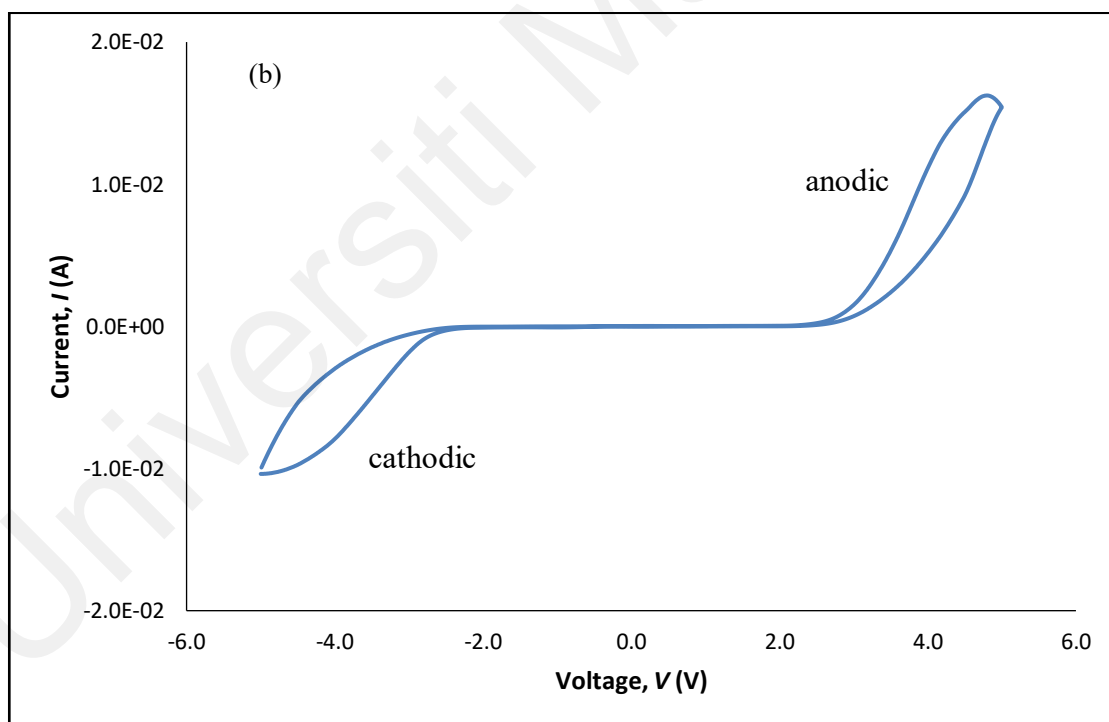
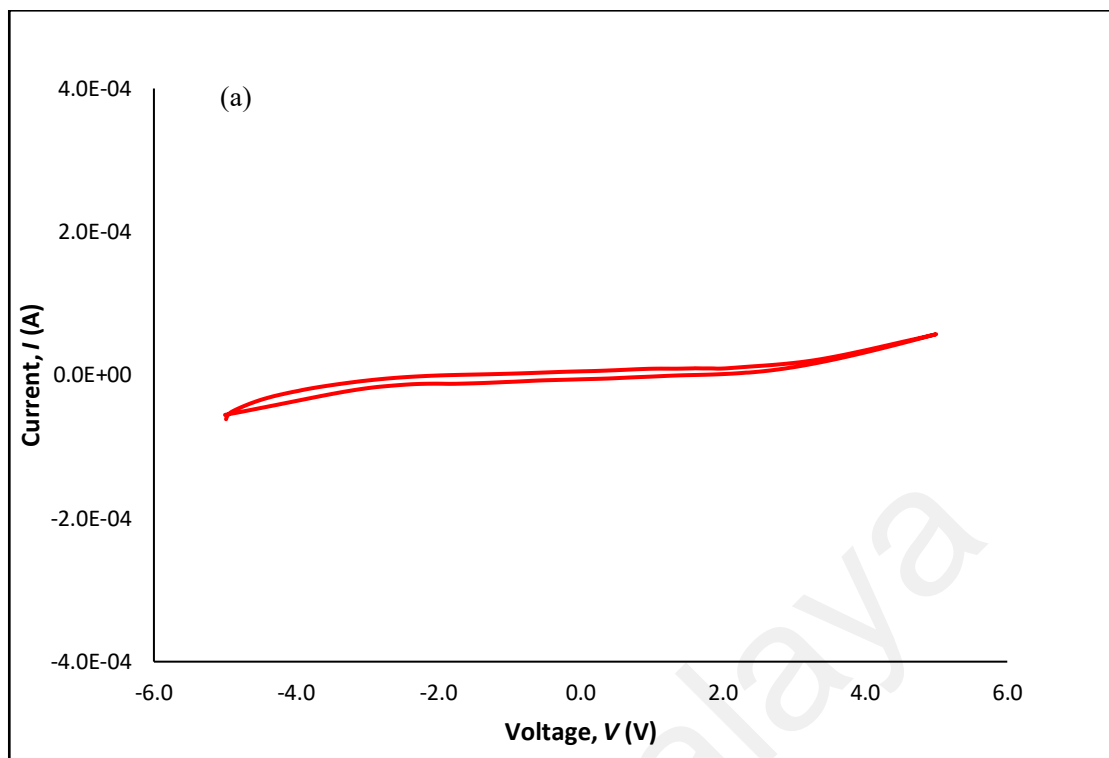


Figure 7.6: The cyclic voltammograms of (a) Cell I: SS/GPE/SS and (b) Cell II: Mg/GPE/Mg for PVdC-co-AN/SN/EC/15 wt.% Mg(TFSI)₂ sample.

7.3 Magnesium Rechargeable Batteries

The analysis and discussion of results revealed the most optimum GPEs which are PVdC-co-AN/SN/EC/30 wt.% MgTf₂ and PVdC-co-AN/SN/EC/15 wt.% Mg(TFSI)₂ samples. Therefore, these samples have been chosen to be used as electrolyte in rechargeable batteries. The batteries were assembled by sandwiching the GPE between the magnesium manganese oxide (MgMn₂O₄) cathode and Mg foil, and accordingly, the charge and discharge cycling tests of the magnesium-ion batteries were conducted over a voltage range of 1.5 to 3.0 V by using Neware battery tester.

7.3.1 Magnesium rechargeable battery containing PVdC-co-AN/SN/EC/30 wt.% MgTf₂ based GPE

After the fabrication of battery with battery configuration of MgMn₂O₄/GPE/Mg, an open circuit voltage (OCV) is observed at 1.4 V before charging up to 3.0 V. Figure 7.7 shows the discharge voltage against specific capacity of rechargeable battery containing PVdC-co-AN/SN/EC/30 wt.% MgTf₂ based GPE for ten cycles. The battery achieved the highest specific capacity of 67 mA h g⁻¹ at a discharge/charge rate of 0.2 C during the first cycle. The discharge capacity is then decreased gradually upon completing all the ten cycles. The decline of discharge capacity with cycling is attributed to the formation of Mg/GPE interface layer, where the passivation film grows in thickness during the repeating cycling (Kuo et al., 2002; Oh et al., 2004). As a consequent, the internal resistance increased and will block the charge transfer between the Mg anode and GPE resulting in the loss of discharge capacity during cycling. However, for this battery, the discharge capacity decreased mildly by each cycle and almost plateau that is from cycle 3 to 4, cycle 5 to 7 and cycle 8 to 10 as shown in Figure 7.8. This shows less capacity

fading of the battery and the consistency of the battery is quite high during discharging process.

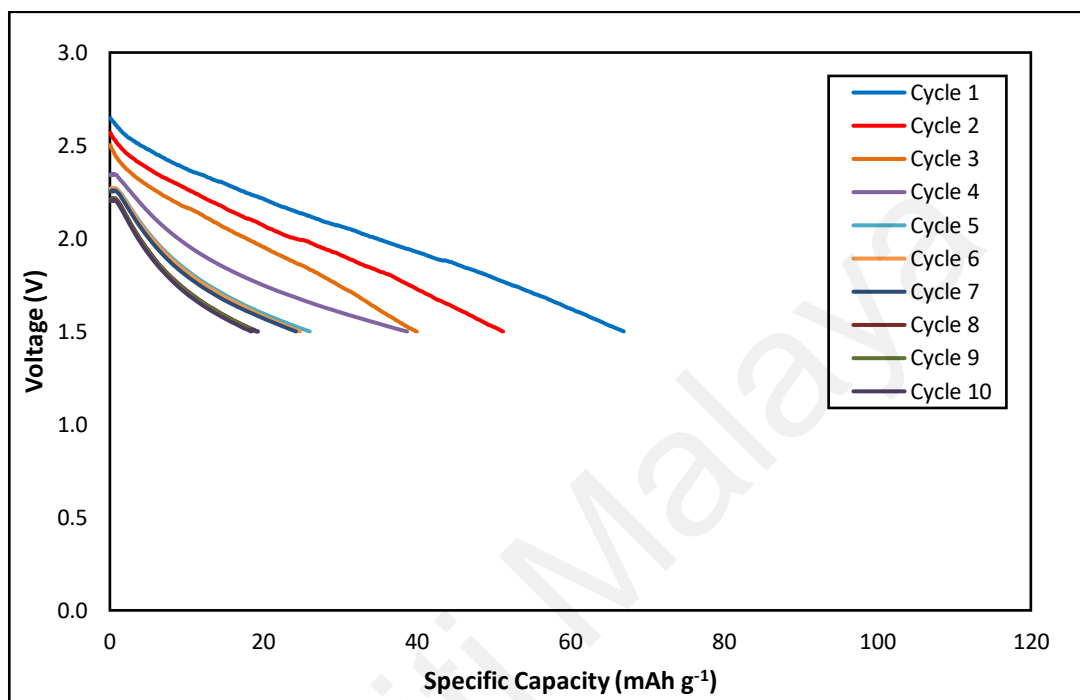


Figure 7.7: Discharge voltage against specific capacity for magnesium battery containing PVdC-co-AN/SN/EC/30 wt.% MgTf₂.

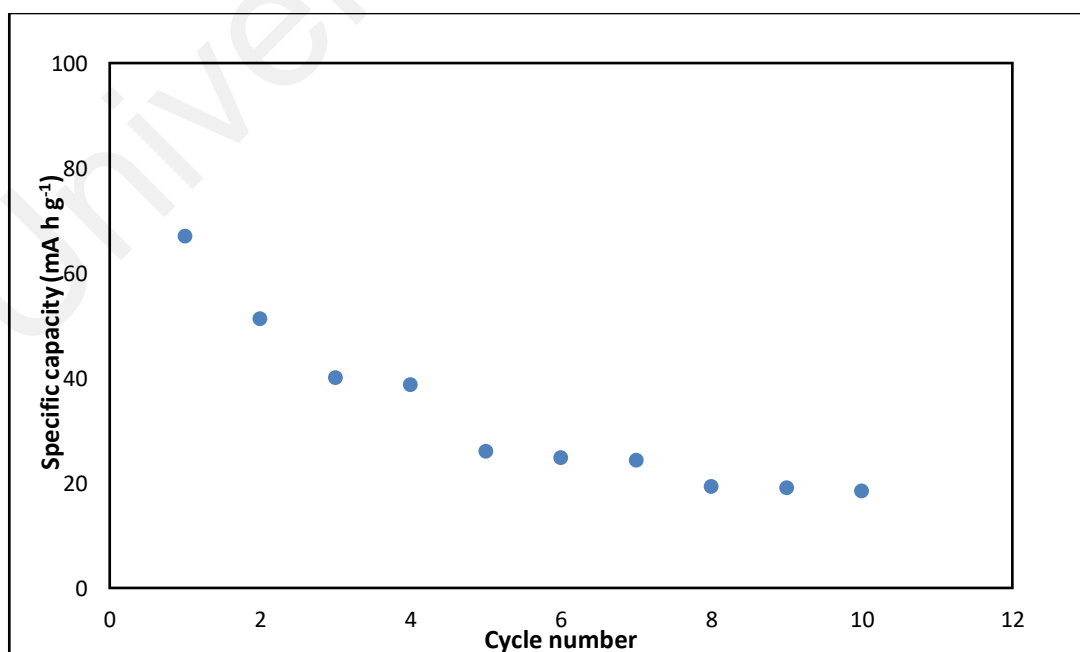


Figure 7.8: Specific capacity against cycle number for magnesium battery containing PVdC-co-AN/SN/EC/30 wt.% MgTf₂.

7.3.2 Magnesium rechargeable battery containing PVdC-co-AN/SN/EC/15 wt.% Mg(TFSI)₂ based GPE

For battery containing PVdC-co-AN/SN/EC/15 wt.% Mg(TFSI)₂ based GPE, an OCV is observed at 1.5 V before charging up to 3.0 V. Figure 7.9 shows the discharge voltage against specific capacity of rechargeable battery containing PVdC-co-AN/SN/EC/15 wt.% Mg(TFSI)₂ based GPE for ten cycles. During the first cycle, the battery achieved the highest capacity of 90 mA h g⁻¹ at a discharge/charge rate of 0.2 C. The discharge capacity is then decreased abruptly to 65 mA h g⁻¹ during the second cycle and continued to decrease until completed all the ten cycles. The decline in discharge capacity with cycling is also attributed to the Mg/GPE interface, where the passive layer grows in thickness during the repeated cycling. The passivating layer blocked the charge transfer reaction between Mg anode and gel polymer electrolyte, since the mobility of Mg²⁺ ions in the passivating layer is extremely low and hence, decrease the capacity of the battery (Oh et al., 2004). Meanwhile, graph of specific capacity against cycle number is then plotted in Figure 7.10 to observe the pattern of discharge capacity with cycle. It can be observed that the discharge capacity decreased drastically only during the second cycle and then decreased gradually until the tenth cycle. This shows a high capacity fading during the second cycle but lower in other cycles. In comparison with the battery containing PVdC-co-AN/SN/EC/30 wt.% MgTf₂ based GPE, the capacity fading is lower than the battery containing PVdC-co-AN/SN/EC/15 wt.% Mg(TFSI)₂ based GPE which both are affected due to the increase in the thickness of passivation layer. Further, the battery containing PVdC-co-AN/SN/EC/15 wt.% Mg(TFSI)₂ achieved higher in capacity during the first cycle which is 90 mA h g⁻¹ compared to the battery containing PVdC-co-AN/SN/EC/30 wt.% MgTf₂ which is 67 mA h g⁻¹. This reflects that a good properties of GPE assists in obtaining higher capacity which in this case, PVdC-co-AN/SN/EC/15 wt.% Mg(TFSI)₂ sample obtained higher in conductivity (more charge transfer) and

greater cationic transference number (reduce concentration polarization of electrolytes during charge–discharge steps) than that of PVdC-co-AN/SN/EC/30 wt.% MgTf₂ sample. Nevertheless, it can be concluded that further research on Mg/GPE interface should be conducted to improve the cycling performances as certain undesirable reactions are possible during cycling, which could block the ion exchange at the electrolyte/electrode interfaces resulting to high capacity fading and low in specific capacity.

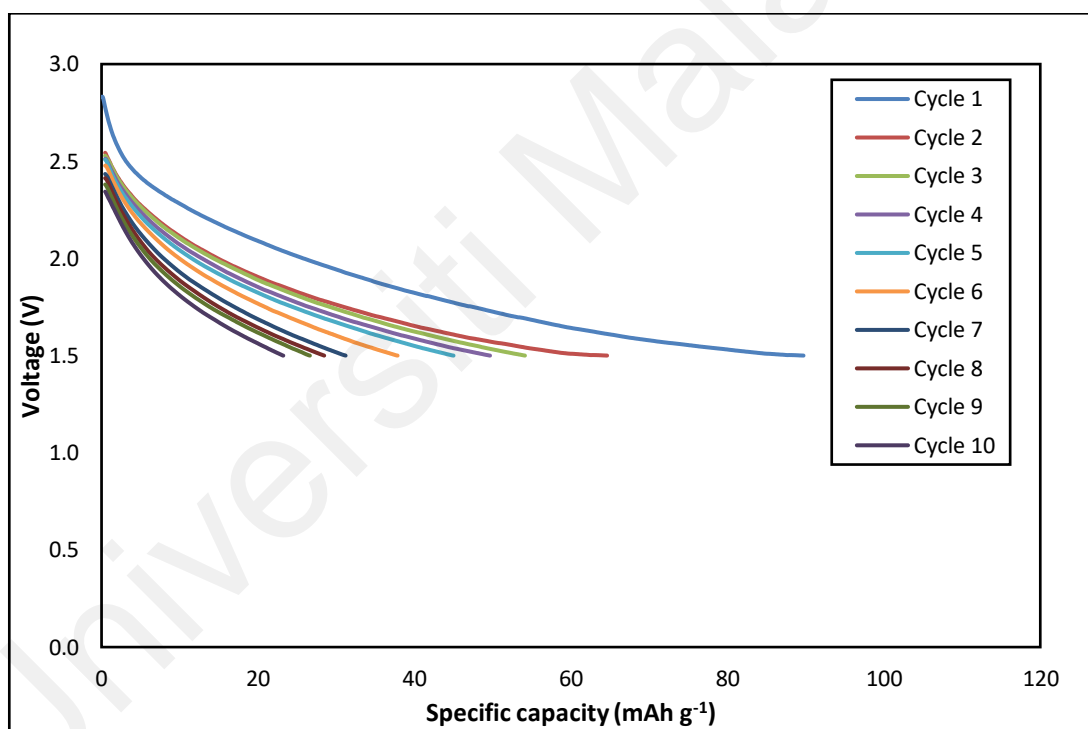


Figure 7.9: Discharge voltage against specific capacity for magnesium battery containing PVdC-co-AN/SN/EC/15 wt.% Mg(TFSI)₂.

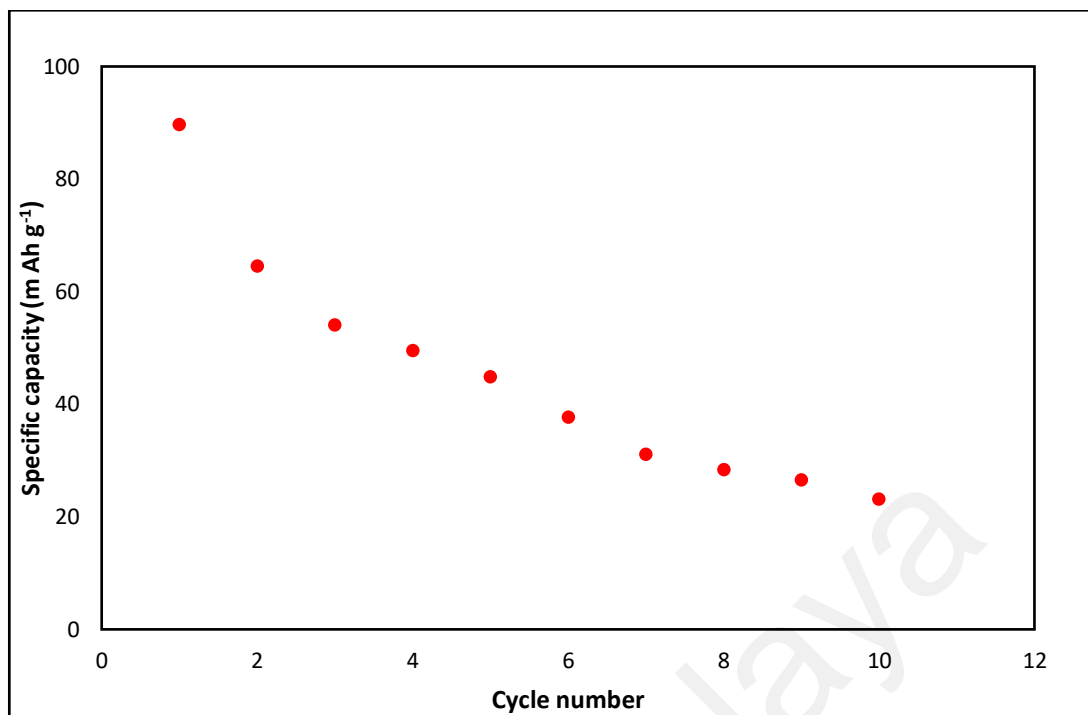


Figure 7.10: Specific capacity against cycle number for magnesium battery containing PVdC-co-AN/SN/EC/15 wt.% $\text{Mg}(\text{TFSI})_2$.

Universiti Malaysia

CHAPTER 8: CONCLUSIONS AND SUGGESTIONS FOR FUTURE WORK

8.1 Conclusions

In this work, four plastic crystal - gel polymer electrolyte (GPE) systems have been prepared consist of PVdC-co-AN as the polymer host which are single and double-plasticized-MgTf₂ and single and double plasticized-Mg(TFSI)₂ systems. The highest room temperature ionic conductivity obtained from MgTf₂ systems are $(2.26 \pm 0.13) \times 10^{-7} \text{ S cm}^{-1}$ and $(2.82 \pm 0.01) \times 10^{-7} \text{ S cm}^{-1}$ which comes from PVdC-co-AN/SN/30 wt.% MgTf₂ and PVdC-co-AN/SN/EC/30 wt.% MgTf₂ samples respectively. For Mg(TFSI)₂ systems, the maximum conductivity obtained is from PVdC-co-AN/SN/20 wt.% Mg(TFSI)₂ and PVdC-co-AN/SN/EC/15 wt.% Mg(TFSI)₂ samples which are $(1.61 \pm 0.03) \times 10^{-6} \text{ S cm}^{-1}$ and $(1.93 \pm 0.04) \times 10^{-6} \text{ S cm}^{-1}$ respectively. The ionic conductivity results show that GPEs from double plasticized system show higher in conductivity values than that of single plasticized system. This confirms that the presence of EC helps in improving the conductivity of polymer electrolytes as well as the effect of double plasticizers in the polymer electrolyte system by assisting in dissociating of ions. Whereas, GPE systems with Mg(TFSI)₂ exhibit higher in ionic conductivity than MgTf₂ due to a larger size of ionic radius of TFSI anion resulting in the easier of ionic dissociation of Mg(TFSI)₂ within the nitrile group of the polymer.

For all the GPE samples in all systems, the temperature dependence ionic conductivity studies obeyed the VTF behaviour which shows the ionic transport mechanism in the GPEs results from polymer segmental motion. The parameters B and A_0 were also calculated after the fitting of the plotted graphs into VTF equation. In transference number study, the ionic transference numbers obtained are greater than 0.9 which confirmed the charge carrier species exists in the GPEs are predominantly ions i.e.; the GPE samples are ionic conductors. Further, the highest value of Mg²⁺ ions transference number is 0.33

and 0.56 for single and double plasticized-MgTf₂ and 0.36 and 0.59 for single and double plasticized-Mg(TFSI)₂ respectively.

On the other hand, FTIR studies confirmed the interaction between the polymer, plasticizers and salts and complexation has occurred in the GPE systems. The influence of free ions, ion pairs and ion aggregates of the magnesium salts on ionic conductivity has also been proven by the deconvolution of FTIR spectra which the values of n , μ and D have also been determined. As for XRD analysis, all GPE samples are amorphous in nature which is essential for a polymer electrolyte. In FESEM analysis, smoother and clearer surface of GPEs are obtained from GPE samples containing EC compared to GPEs without EC.

In addition, DSC studies determined the value of T_g of pure PVdC-co-AN at 51.42 °C and the value of the T_g decreased after the complexation of pure polymer with SN, EC and magnesium salts. The decrease of T_g suggests that the addition of SN, EC, and magnesium salts can increase the flexibility of polymer chain and an improved segmental motion was expected.

In linear sweep voltammetry analysis, the highest electrochemical stability window were obtained from the highest conducting double plasticized-MgTf₂ and double plasticized-Mg(TFSI)₂ sample which is 3.6 V and 3.8 V respectively. Thus, these GPE samples are the most electrochemically stable as the capability to withstand high voltages at the cathode interface are the best. Their CV analysis on the other hand also confirmed the reversibility of the GPEs in the prepared cell and redox reaction has occurred between the GPEs and the magnesium electrodes. Therefore, by using these GPE samples which are PVdC-co-AN/SN/EC/30 wt.% MgTf₂ and PVdC-co-AN/SN/EC/15 wt.% Mg(TFSI)₂ samples, magnesium rechargeable batteries were fabricated with battery configuration of MgMn₂O₄/GPE/Mg. The analysis of the battery shows the maximum specific capacity

obtained for battery containing $\text{Mg}(\text{TFSI})_2$ based-GPE is higher which is 90 mAh g^{-1} than the battery containing MgTf_2 based-GPE which is 67 mAh g^{-1} .

From all the results and analysis of the prepared GPEs, double plasticized system of both MgTf_2 and $\text{Mg}(\text{TFSI})_2$ salts obtained higher in ionic conductivity, more Mg ions transference number, better in electrochemical stability and finally can perform as rechargeable batteries. Whereas, in comparison between MgTf_2 and $\text{Mg}(\text{TFSI})_2$ salts, $\text{Mg}(\text{TFSI})_2$ -based GPE is proved to be better than MgTf_2 -based GPE in obtaining preferable results of ionic conductivity and other characterization techniques.

8.2 Suggestions for Future Work

For future work, the ionic conductivity of the GPEs should be improved ($\sim 10^{-4}$ to $10^{-2} \text{ S cm}^{-1}$) for them to perform better in electrochemical devices. In order to achieve higher in ionic conductivity, blending of PVdC-co-AN with another polymer can be considered such as blending of PVdC-co-AN/PMMA, PVdC-co-AN/PAN and PVdC-co-AN/PVA. This blending method might be useful since more vacant site can be supplied for attachment of mobile ions as more functional group exists as well as the combination of the characteristics of both polymers could be beneficial.

Secondly, the use of ionic liquid can also increase the ionic conductivity of the GPEs. This ionic liquid can be used whether as a single dopant or with the combination of other salt, usually both with the same anion. The supplying of mobile ions is very important in GPEs as ionic conductivity is closely related to the number density of mobile ions and their mobility.

Finally, despite the conductivity, the compatibility of GPEs with electrodes in devices are also important in improving the performance of GPEs in devices. The use of

anode/cathode, specifically in rechargeable battery can be explored first before assembling the battery. This is because, for a battery to perform efficiently, all components in one complete cell which are the anode, cathode and polymer electrolyte played their own important roles. If all the components work perfectly, a great rechargeable battery can be produced and patented especially for magnesium ion rechargeable battery which is still under research and not commercialized elsewhere.

Universiti Malaya

REFERENCES

- Abraham, K. M., & Alamgir, M. (1989). Li⁺-Conductive solid polymer electrolytes with liquid-like conductivity. *Journal of The Electrochemical Society*, 3576, 1989–1990.
- Ahmad, S., Bohidar, H. B., Ahmad, S., & Agnihotry, S. A. (2006). Role of fumed silica on ion conduction and rheology in nanocomposite polymeric electrolytes. *Polymer*, 47, 3583–3590.
- Alamgir, M., & Abraham, K. M. (1993). Li ion conductive electrolytes based on poly(vinyl chloride). *Journal of The Electrochemical Society*, 140(2), 3–4.
- Alarco, P. J., Abu-Lebdeh, Y., Abouimrane, A., & Armand, M. (2004a). The plastic-crystalline phase of succinonitrile as a universal matrix for solid-state ionic conductors. *Nature Materials*, 3(7), 476–481.
- Alarco, P. J., Abu-Lebdeh, Y., Abouimrane, A., & Armand, M. (2004b). The plastic-crystalline phase of succinonitrile as a universal matrix for solid-state ionic conductors. *Nature Materials*, 3(7), 476–481.
- Ali, A. M. M., Yahya, M. Z. A., Bahron, H., Subban, R. H. Y., Harun, M. K., & Atan, I. (2007). Impedance studies on plasticized PMMA-LiX [X: CF₃SO₃⁻, N(CF₃SO₂)₂⁻] polymer electrolytes. *Materials Letters*, 61(10), 2026–2029.
- Andreev, Y. G., & Bruce, P. G. (2000). Polymer electrolyte structure and its implications. *Electrochimica Acta*, 45, 1417–1423.
- Angulakshmi, N., Nahm, K. S., Nair, J. R., Gerbaldi, C., Bongiovanni, R., Penazzi, N., & Stephan, A. M. (2013). Cycling profile of MgAl₂O₄-incorporated composite electrolytes composed of PEO and LiPF₆ for lithium polymer batteries. *Electrochimica Acta*, 90, 179–185.
- Aniskari, N. A. B., & Mohd Isa, M. I. N. (2017). The effect of ionic charge carriers in 2-hydroxyethyl cellulose solid biopolymer electrolytes doped glycolic acid via FTIR-deconvolution technique. *Journal of Sustainability Science and Management*, 2017(Special Issue 2), 71–79.
- Appetecchi, G. B., Croce, F., Persi, L., Ronci, F., & Scrosati, B. (2000). Transport and interfacial properties of composite polymer electrolytes. *Electrochimica Acta*, 45, 1481–1490.
- Armand, M. (1983). Polymer solid electrolytes - an overview. *Solid State Ionics*, 9–10, 745–754.
- Armand, M., Chabagno, J. M., & Duclot, M. (1979). *Fast ion transport in solids*. (P. Vahisha, J. N. Mundy, & G. K. Shenoy, Eds.). North Holland, New York: Elsevier.

- Arof, A. K., Amirudin, S., Yusof, S. Z., & Noor, I. M. (2014). A method based on impedance spectroscopy to determine transport properties of polymer electrolytes. *Physical Chemistry Chemical Physics*, *16*(5), 1856–1867.
- Arya, A., & Sharma, A. L. (2018). Structural, microstructural and electrochemical properties of dispersed-type polymer nanocomposite films. *Journal of Physics D: Applied Physics*, *51*(4), Article #045504.
- Asmara, S. N., Kufian, M. Z., Majid, S. R., & Arof, A. K. (2011). Preparation and characterization of magnesium ion gel polymer electrolytes for application in electrical double layer capacitors. *Electrochimica Acta*, *57*, 91–97.
- Aziz, N. A., Majid, S. R., & Arof, A. K. (2012). Synthesis and characterizations of phthaloyl chitosan-based polymer electrolytes. *Journal of Non-Crystalline Solids*, *358*(12–13), 1581–1590.
- Aziz, S. B. (2013). Li⁺ ion conduction mechanism in poly (ϵ -caprolactone)-based polymer electrolyte. *Iranian Polymer Journal (English Edition)*, *22*(12), 877–883.
- Aziz, S. B., Woo, T. J., Kadir, M. F. Z., & Ahmed, H. M. (2018). A conceptual review on polymer electrolytes and ion transport models. *Journal of Science: Advanced Materials and Devices*, *3*(1), 1–17.
- Balasubramanian, M., Sun, X., Yang, X. Q., & Mcbreen, J. (2001). In situ X-ray diffraction and X-ray absorption studies. *Journal of Power Sources*, *92*, 1–8.
- Balo, L., Shalu, Gupta, H., Kumar Singh, V., & Kumar Singh, R. (2017). Flexible gel polymer electrolyte based on ionic liquid EMIMTFSI for rechargeable battery application. *Electrochimica Acta*, *230*, 123–131.
- Bandara, L. R. A. K., Dissanayake, M. A. K. L., & Mellander, B. (1998). Ionic conductivity of plasticized (PEO)-LiCF₃SO₃ electrolytes. *Electrochimica Acta*, *43*, 1447–145114.
- Barsoukov, E., & Macdonald, J. R. (2005). *Impedance Spectroscopy. Impedance Spectroscopy: Theory, Experiment, and Applications* (2nd Editio). New Jersey: John Wiley & Sons, Inc.
- Baskaran, R., Selvasekarapandian, S., Kuwata, N., Kawamura, J., & Hattori, T. (2007). Structure, thermal and transport properties of PVAc-LiClO₄ solid polymer electrolytes. *Journal of Physics and Chemistry of Solids*, *68*(3), 407–412.
- Billah, A. (n.d.). Schematic-diagram-of-Field-Emission-Scanning-Electron-Microscope-FESEM. Retrieved on June 14, 2019, from https://www.researchgate.net/figure/Schematic-diagram-of-Field-Emission-Scanning-Electron-Microscope-FESEM_fig31_318487306
- Boaretto, N., Meabe, L., Martinez-Ibañez, M., Armand, M., & Zhang, H. (2020). Review—Polymer electrolytes for rechargeable batteries: From nanocomposite to

nanohybrid. *Journal of The Electrochemical Society*, 167(7), Article #070524.

- Bruce, P. G. (1995). Structure and electrochemistry electrolytes. *Electrochimica Acta*, 40(13), 2077–2085.
- Bruce, P. G., Campbell, S. A., Lightfoot, P., & Mehta, M. A. (1995). Polymer electrolytes: structure and electrode processes. *Solid State Ionics*, 78(3–4), 191–198.
- Bruce, P. G., Hardgrave, M. T., & Vincent, C. A. (1989). Steady state current flow in solid binary electrolyte cells Part 2. The effect of ion association. *Journal of Electroanalytical Chemistry*, 271, 27–34.
- Cao, J., Wang, L., Shang, Y., Fang, M., Deng, L., & Gao, J. (2013). Dispersibility of nano-TiO₂ on performance of composite polymer electrolytes for Li-ion batteries. *Electrochimica Acta*, 111, 674–679.
- Carquigny, S., Segut, O., Lakard, B., Lallemand, F., & Fievet, P. (2008). Effect of electrolyte solvent on the morphology of polypyrrole films: Application to the use of polypyrrole in pH sensors. *Synthetic Metals*, 158(11), 453–461.
- Chen, Z., Yang, H., Li, X., Li, F., Yi, T., & Huang, C. (2007). Thermostable succinonitrile-based gel electrolyte for efficient, long-life dye-sensitized solar cells. *Journal of Materials Chemistry*, 17(16), 1602–1607.
- Cheng, H., Zhu, C., Huang, B., Lu, M., & Yang, Y. (2007). Synthesis and electrochemical characterization of PEO-based polymer electrolytes with room temperature ionic liquids. *Electrochimica Acta*, 52(19), 5789–5794.
- Chintapalli, S., & Frech, R. (1996). Effect of plasticizers on high molecular weight PEO-LiCF₃SO₃ complexes. *Solid State Ionics*, 86–88, 341–346.
- Choe, H. S., Carroll, B. G., Pasquariello, D. M., & Abraham, K. M. (1997). Characterization of some polyacrylonitrile-based electrolytes. *Chemistry of Materials*, 9(1), 367–379.
- Chong, W. G., & Osman, Z. (2014). The effect of carbonate-phthalate plasticizers on structural, morphological and electrical properties of polyacrylonitrile-based solid polymer electrolytes. *Journal of Polymer Research*, 21(3), Article #381.
- Choudhary, S., & Sengwa, R. J. (2017). Effects of different inorganic nanoparticles on the structural, dielectric and ion transportation properties of polymers blend based nanocomposite solid polymer electrolytes. *Electrochimica Acta*, 247, 924–941.
- Communication, S., Chattaraj, A. P., & Basumallick, I. N. (1995). Fabrication and charge/discharge behaviour of some lithium solid polymer electrolyte cells. *Journal of Power Sources*, 55, 123–126.
- Das, S., & Bhattacharyya, A. J. (2010). Influence of water and thermal history on ion

transport in lithium salt-succinonitrile plastic crystalline electrolytes. *Solid State Ionics*, 181(39–40), 1732–1739.

Das, S., & Ghosh, A. (2015). Ionic conductivity and dielectric permittivity of PEO-LiClO₄ solid polymer electrolyte plasticized with propylene carbonate. *AIP Advances*, 5(2), Article #027125.

Das, S., Prathapa, S. J., Menezes, P. V, Row, T. N. G., & Bhattacharyya, A. J. (2009). Study of ion transport in lithium perchlorate-succinonitrile plastic crystalline electrolyte via ionic conductivity and in situ cryo-crystallography. *Journal of Physical Chemistry B*, 113, 5025–5031.

Deka, M., & Kumar, A. (2011). Electrical and electrochemical studies of poly(vinylidene fluoride)–clay nanocomposite gel polymer electrolytes for Li-ion batteries. *Journal of Power Sources*, 196(3), 1358–1364.

Echeverri, M., Kim, N., & Kyu, T. (2012). Ionic conductivity in relation to ternary phase diagram of poly(ethylene oxide), succinonitrile, and lithium bis(trifluoromethane)sulfonimide blends. *Macromolecules*, 45(15), 6068–6077.

Ericson, H., Svanberg, C., Brodin, A., Grillone, a M., & Panero, S. (2000). Poly(methyl methacrylate)-based protonic gel electrolytes: a spectroscopic study. *Electrochimica Acta*, 45, 1409–1414.

Evans, J., Vincent, C. A., & Bruce, P. G. (1987). Electrochemical measurement of transference numbers in polymer electrolytes. *Polymer*, 28(13), 2324–2328.

Fan, L., Wang, X., & Long, F. (2009). All-solid-state polymer electrolyte with plastic crystal materials for rechargeable lithium-ion battery. *Journal of Power Sources*, 189, 775–778.

Fan, L., Wang, X., Long, F., & Wang, X. (2008). Enhanced ionic conductivities in composite polymer electrolytes by using succinonitrile as a plasticizer. *Solid State Ionics*, 179, 1772–1775.

Fenton, D. E., Parker, J. M., & Wright, P. V. (1973). Complexes of alkali metal ions with poly(ethylene oxide). *Polymer*, 14(11), Article #589.

Fernández-Sánchez, C., McNeil, C. J., & Rawson, K. (2005). Electrochemical impedance spectroscopy studies of polymer degradation: Application to biosensor development. *TrAC - Trends in Analytical Chemistry*, 24(1), 37–48.

Flora, X. H., Ulaganathan, M., & Rajendran, S. (2013). Role of different plasticizers in li-ion conducting poly(acrylonitrile)- poly(methyl methacrylate) hybrid polymer electrolyte. *International Journal of Polymeric Materials and Polymeric Biomaterials*, 62(14), 737–742.

Frand, G., Rezrazi, M., Rousselot, C., & Truche, C. (1993). Fast ion transport in new lithium electrolytes gelled with PMMA . 1 . Influence of polymer concentration.

- Gibson, D. (n.d.). X-Ray Diffraction System. Retrieved on December 9, 2019, from <https://www.energy.gov/eere/amo/portable-parallel-beam-x-ray-diffraction-system>
- Gupta, R. K., & Rhee, H.-W. (2012). Effect of succinonitrile on electrical, structural, optical, and thermal properties of [poly(ethylene oxide)-succinonitrile]/LiI–I₂ redox-couple solid polymer electrolyte. *Electrochimica Acta*, 76, 159–164.
- Ha, S. Y., Lee, Y. W., Woo, S. W., Koo, B., Kim, J. S., Cho, J., ... Choi, N. S. (2014). Magnesium(II) bis(trifluoromethane sulfonyl) imide-based electrolytes with wide electrochemical windows for rechargeable magnesium batteries. *ACS Applied Materials and Interfaces*, 6(6), 4063–4073.
- Hallinan, D. T., & Balsara, N. P. (2013). Polymer Electrolytes. *Annual Review of Materials Research*, 43(1), 503–525.
- Hambali, D., Zainol, N. H., Isa, K. B. M., Osman, Z., & Othman, L. (2018). Magnesium ion-conducting gel polymer electrolytes based on poly(vinylidene chloride-co-acrylonitrile) (PVdC-co-AN): a comparative study between magnesium trifluoromethanesulfonate (MgTf₂) and magnesium bis(trifluoromethanesulfonimide) (Mg(TFSI)₂). *Ionics*, 25(3), 1187–1198.
- Hambali, D., Zainuddin, Z., & Osman, Z. (2016). Studies of plastic crystal gel polymer electrolytes based on poly(vinylidene chloride-co-acrylonitrile). *AIP Conference Proceedings*, 050004, 0–6.
- Hambali, D., Zainuddin, Z., & Osman, Z. (2017). Characteristics of novel plastic crystal gel polymer electrolytes based on PVdC-co-AN. *Ionics*, 23, 285–294.
- Hambali, D., Zainuddin, Z., Supa'at, I., & Osman, Z. (2016). Studies of ion transport and electrochemical properties of plasticized composite polymer electrolytes. *Sains Malaysiana*, 45(11), 1697–1705.
- He, D., Kim, D. W., Park, J. S., Cho, S. Y., & Kang, Y. (2013). Electrochemical properties of semi-interpenetrating polymer network solid polymer electrolytes based on multi-armed oligo(ethyleneoxy) phosphate. *Journal of Power Sources*, 244, 170–176.
- Hofmann, A., Schulz, M., & Hanemann, T. (2013). Gel electrolytes based on ionic liquids for advanced lithium polymer batteries. *Electrochimica Acta*, 89, 823–831.
- How an FTIR Spectrometer Operates. (n.d.). Retrieved on January 20, 2020, from [https://chem.libretexts.org/Bookshelves/Physical_and_Theoretical_Chemistry_Textbook_Maps/Supplemental_Modules_\(Physical_and_Theoretical_Chemistry\)/Spectroscopy/Vibrational_Spectroscopy/Infrared_Spectroscopy/How_an_FTIR_Spectrometer_Operates](https://chem.libretexts.org/Bookshelves/Physical_and_Theoretical_Chemistry_Textbook_Maps/Supplemental_Modules_(Physical_and_Theoretical_Chemistry)/Spectroscopy/Vibrational_Spectroscopy/Infrared_Spectroscopy/How_an_FTIR_Spectrometer_Operates)

- Huang, B. (1996). Lithium ion conduction in polymer electrolytes based on PAN. *Solid State Ionics*, 85(1–4), 79–84.
- Imperiya, M., Ahmad, A., Hanifah, S. A., Mohamed, N. S., & Rahman, M. Y. A. (2014). Investigation of plasticized UV-curable glycidyl methacrylate based solid polymer electrolyte for photoelectrochemical cell (PEC) application. *International Journal of Hydrogen Energy*, 39(6), 3018–3024.
- Isa, K. B. M., Osman, Z., Arof, A. K., Othman, L., Zainol, N. H., Samin, S. M., ... Kamarulzaman, N. (2014). Lithium ion conduction and ion-polymer interaction in PVdF-HFP based gel polymer electrolytes. *Solid State Ionics*, 268, 288–293.
- Jayaraman, R., Vickraman, P., Subramanian, N. M. V., & Justin, A. S. (2016). A.C impedance , XRD , DSC , FTIR studies on PbTiO₃ dispersoid pristine PVdF-co-HFP and PEMA blended PVdF-co-HFP microcomposite electrolytes. *Journal of Non-Crystalline Solids*, 435, 27–32.
- Jeong, S.-K., Jo, Y.-K., & Jo, N.-J. (2006). Decoupled ion conduction mechanism of poly(vinyl alcohol) based Mg-conducting solid polymer electrolyte. *Electrochimica Acta*, 52(4), 1549–1555.
- Johan, M. R., Shy, O. H., Ibrahim, S., Mohd Yassin, S. M., & Hui, T. Y. (2011). Effects of Al₂O₃ nanofiller and EC plasticizer on the ionic conductivity enhancement of solid PEO–LiCF₃SO₃ solid polymer electrolyte. *Solid State Ionics*, 196(1), 41–47.
- Jung, Y. C., Park, M. S., Kim, D. H., Ue, M., Eftekhari, A., & Kim, D. W. (2017). Room-temperature performance of poly(ethylene ether carbonate)-based solid polymer electrolytes for all-solid-state lithium batteries. *Scientific Reports*, 7(1), 1–11.
- Karmakar, A., & Ghosh, A. (2014). Structure and ionic conductivity of ionic liquid embedded PEO- LiCF₃SO₃ polymer electrolyte. *AIP Advances*, 4(8), Article #087112.
- Kauppinen, J. K., Moffatt, D. J., Mantsch, H. H., & Cameron, D. G. (1981). Fourier self-deconvolution: A method for resolving intrinsically overlapped bands. *Applied Spectroscopy*, 35(3), 271–276.
- Kim, C.-H., Park, J.-K., Moon, S.-I., & Yoon, M.-S. (1998). Study on ion conduction behavior of the plasticized polymer electrolytes based on poly(methylmethacrylate-co-alkali metal methacrylate) by FT-IR spectroscopy. *Electrochimica Acta*, 43(10–11), 1421–1427.
- Kim, D. W., Sun, Y. K., Cho, J. H., & Moon, S. I. (1999). Novel polymer electrolytes for rechargeable lithium-ion polymer batteries. *Electrochemical and Solid State Letters*, 2(6), 256–258.
- Kumar, D., & Hashmi, S. a. (2010). Ion transport and ion-filler-polymer interaction in poly(methyl methacrylate)-based, sodium ion conducting, gel polymer

- electrolytes dispersed with silica nanoparticles. *Journal of Power Sources*, 195(15), 5101–5108.
- Kumar, G. G., & Munichandraiah, N. (2000a). Effect of plasticizers on magnesium-poly (ethyleneoxide) polymer electrolyte. *Journal of Electroanalytical Chemistry*, 495, 42–50.
- Kumar, G. G., & Munichandraiah, N. (2000b). Solid-state Mg/MnO₂ cell employing a gel polymer electrolyte of magnesium triflate. *Journal of Power Sources*, 91, 157–160.
- Kumar, G. G., & Munichandraiah, N. (2002). Poly (methylmethacrylate) — magnesium triflate gel polymer electrolyte for solid state magnesium battery application. *Electrochimica Acta*, 47, 1013–1022.
- Kumar, M., & Sekhon, S. S. (2002). Role of plasticizer's dielectric constant on conductivity modification of PEO-NH₄F polymer electrolytes. *European Polymer Journal*, 38(7), 1297–1304.
- Kuo, H.-H., Chen, W.-C., Wen, T.-C., & Gopalan, A. (2002). A novel composite gel polymer electrolyte for rechargeable lithium batteries. *Journal of Power Sources*, 110(1), 27–33.
- Lascaud, S., Perrier, M., Vallee, A., Besner, S., Prud'homme, J., & Armand, M. (1994). Phase diagrams and conductivity behavior of poly(ethylene oxide)-molten salt rubbery electrolytes. *Macromolecules*, 27(25), 7469–7477.
- Lee, D. K., & Allcock, H. R. (2010). The effects of cations and anions on the ionic conductivity of poly[bis(2-(2-methoxyethoxy)ethoxy)phosphazene] doped with lithium and magnesium salts of trifluoromethanesulfonate and bis(trifluoromethanesulfonyl)imidate. *Solid State Ionics*, 181(39–40), 1721–1726.
- Lee, K.-H., Lee, Y.-G., Park, J.-K., & Seung, D.-Y. (2000). Effect of silica on the electrochemical characteristics of the plasticized polymer electrolytes based on the P(AN-co-MMA) copolymer. *Solid State Ionics*, 133(3–4), 257–263.
- Li, M., Yang, L., Fang, S., Dong, S., Hirano, S. I., & Tachibana, K. (2011). Polymer electrolytes containing guanidinium-based polymeric ionic liquids for rechargeable lithium batteries. *Journal of Power Sources*, 196(20), 8662–8668.
- Li, X., Zhang, Z., Li, S., Yang, L., & Hirano, S. (2016). Polymeric ionic liquid-plastic crystal composite electrolytes for lithium ion batteries. *Journal of Power Sources*, 307, 678–683.
- Liden, D., & Reddy, T. (2004). *Handbook of batteries. Cell*.
- Liu, K., Ding, F., Lu, Q., Liu, J., Zhang, Q., Liu, X., & Xu, Q. (2016). A novel plastic crystal composite polymer electrolyte with excellent mechanical bendability and electrochemical performance for flexible lithium-ion batteries. *Solid State Ionics*,

- Long, L., Wang, S., Xiao, M., & Meng, Y. (2016). Polymer electrolytes for lithium polymer batteries. *Journal of Materials Chemistry A*, 4(26), 10038–10039.
- Long, S., Macfarlane, D. R., & Forsyth, M. (2003). Fast ion conduction in molecular plastic crystals. *Solid State Ionics*, 161, 105–112.
- Long, S., MacFarlane, D. R., & Forsyth, M. (2004). Ionic conduction in doped succinonitrile. *Solid State Ionics*, 175, 733–738.
- Lu, Q., Fang, J., Yang, J., Yan, G., Liu, S., & Wang, J. (2013). A novel solid composite polymer electrolyte based on poly(ethylene oxide) segmented polysulfone copolymers for rechargeable lithium batteries. *Journal of Membrane Science*, 425–426, 105–112.
- Mahalakshmi, M., Selvanayagam, S., Selvasekarapandian, S., Chandra, M. V. L., Sangeetha, P., & Manjuladevi, R. (2020). Magnesium ion-conducting solid polymer electrolyte based on cellulose acetate with magnesium nitrate ($\text{Mg}(\text{NO}_3)_2 \cdot 6\text{H}_2\text{O}$) for electrochemical studies. *Ionics*, 26(9), 4553–4565.
- Marcinek, M., Syzdek, J., Marczewski, M., Piszcz, M., Niedzicki, L., Kalita, M., ... Wieczorek, W. (2015). Electrolytes for Li-ion transport - Review. *Solid State Ionics*, 276, 107–126.
- Marzantowicz, M., Dygas, J. R., Krok, F., Tomaszewska, A., Florjańczyk, Z., Zygadło-Monikowska, E., & Lapienis, G. (2009). Star-branched poly(ethylene oxide) $\text{LiN}(\text{CF}_3\text{SO}_2)_2$: A promising polymer electrolyte. *Journal of Power Sources*, 194(1), 51–57.
- Masoud, E. M., El-Bellihi, A. A., Bayoumy, W. A., & Mousa, M. A. (2013). Organic-inorganic composite polymer electrolyte based on PEO- LiClO_4 and nano- Al_2O_3 filler for lithium polymer batteries: Dielectric and transport properties. *Journal of Alloys and Compounds*, 575(October), 223–228.
- Mathew, C. M., Kesavan, K., & Rajendran, S. (2015). Structural and electrochemical analysis of PMMA based gel electrolyte membranes. *International Journal of Electrochemistry*, 2015, 1–7.
- Mohapatra, S. R. (2018). Role of succinonitrile in improving ionic conductivity of sodium-ion conductive polymer electrolyte. *AIP Conference Proceedings*, 1953(030171), 090081-1-090081–5.
- Morita, M., Yoshimoto, N., Yakushiji, S., & Ishikawa, M. (2001). Rechargeable magnesium batteries using a novel polymeric solid electrolyte. *Electrochemical and Solid-State Letters*, 4(11), Article #A177.
- Muldoon, J., Bucur, C. B., Oliver, A. G., Sugimoto, T., Matsui, M., Kim, H. S., ... Kotani, Y. (2012). Electrolyte roadblocks to a magnesium rechargeable battery. *Energy*

and Environmental Science, 5(3), 5941–5950.

- Muniyandi, N., Kalaiselvi, N., Periyasamy, P., Thirunakaran, R., Ramesh, B., Gopukumar, S., ... Raghavan, M. (2001). Optimisation of PVdF-based polymer electrolytes. *Journal of Power Sources*, 96, 14–19.
- Nguyen, D. T., & Song, S. W. (2017). Magnesium stannide as a high-capacity anode for magnesium-ion batteries. *Journal of Power Sources*, 368, 11–17.
- Oh, J., Ko, J., & Kim, D. (2004). Preparation and characterization of gel polymer electrolytes for solid state magnesium batteries. *Electrochimica Acta*, 50, 903–906.
- Osman, Z., Samin, S. M., Othman, L., & Isa, K. B. M. (2012). Ionic transport in PMMA-NaCF₃SO₃ gel polymer electrolyte. *Advanced Materials Research*, 545, 259–263.
- Osman, Z., Zainol, N. H., Samin, S. M., Chong, W. G., Isa, K. B. M., Othman, L., ... Sonsudin, F. (2014). Electrochemical impedance spectroscopy studies of magnesium-based polymethylmethacrylate gel polymer electrolytes. *Electrochimica Acta*, 131, 148–153.
- Othman, L., Chew, K. W., & Osman, Z. (2007). Impedance spectroscopy studies of poly (methyl methacrylate)-lithium salts polymer electrolyte systems. *Ionics*, 13(5), 337–342.
- Othman, L., Isa, K. B. M., Osman, Z., & Yahya, R. (2013). Ionic conductivity, morphology and transport number of lithium ions in PMMA based gel polymer electrolytes. *Defect and Diffusion Forum*, 334–335, 137–142.
- Othman, L., Isa, K. B. M., Osman, Z., & Yahya, R. (2017). Ionic transport studies of gel polymer electrolytes containing sodium Salt. *Materials Today: Proceedings*, 4(4), 5122–5129.
- Pandey, G. P., Agrawal, R. C., & Hashmi, S. A. (2009). Magnesium ion-conducting gel polymer electrolytes dispersed with nanosized magnesium oxide. *Journal of Power Sources*, 190(2), 563–572.
- Pandey, G. P., Agrawal, R. C., & Hashmi, S. A. (2011). Performance studies on composite gel polymer electrolytes for rechargeable magnesium battery application. *Journal of Physics and Chemistry of Solids*, 72(12), 1408–1413.
- Pandey, G. P., & Hashmi, S. A. (2009). Experimental investigations of an ionic-liquid-based, magnesium ion conducting, polymer gel electrolyte. *Journal of Power Sources*, 187(2), 627–634.
- Patel, M., Chandrappa, K. G., & Bhattacharyya, A. J. (2008). Increasing ionic conductivity and mechanical strength of a plastic electrolyte by inclusion of a polymer. *Electrochimica Acta*, 54(2), 209–215.

- Petrowsky, M., & Frech, R. (2008). Concentration dependence of ionic transport in dilute organic electrolyte solutions. *Journal of Physical Chemistry B*, 112(28), 8285–8290.
- Pistoia, G., Rossi, M. De, & Scrosati, B. (1970). Study of the behavior of ethylene carbonate as a nonaqueous battery solvent. *Journal of The Electrochemical Society*, 117(4), Article #500.
- Poly(vinylidene-chloride-co-acrylonitrile). (n.d.). Retrieved on May 15, 2019, from <https://www.sigmaaldrich.com/catalog/product/aldrich/496707?lang=en®ion=MY>
- Pradhan, D. K., Karan, N. K., Thomas, R., & Katiyar, R. S. (2014). Coupling of conductivity to the relaxation process in polymer electrolytes. *Materials Chemistry and Physics*, 147(3), 1016–1021.
- Pradhan, D. K., Samantaray, B. K., Choudhary, R. N. P., Karan, N. K., Thomas, R., & Katiyar, R. S. (2007). Effect of plasticizer on structural and electrical properties of nanocomposite solid polymer electrolytes. *International Journal of Electrochemical Science*, 2, 861–871.
- Pradhan, D. K., Samantaray, B. K., Choudhary, R. N. P., Karan, N. K., Thomas, R., & Katiyar, R. S. (2011). Effect of plasticizer on structural and electrical properties of nanocomposite solid polymer electrolytes. *Ionics*, 17(2), 127–134.
- Premila, R., Subbu, C., Rajendran, S., & Selva kumar, K. (2018). Experimental investigation of nano filler TiO₂ doped composite polymerelectrolytes for lithium ion batteries. *Applied Surface Science*, 449, 426–434.
- Rajendran, S., Mahendran, O., & Mahalingam, T. (2002). Thermal and ionic conductivity studies of plasticized PMMA/PVdF blend polymer electrolytes. *European Polymer Journal*, 38(1), 49–55.
- Rajendran, S., & Uma, T. (2000). Effect of ZrO₂ on conductivity of PVC – LiBF₄ – DBP polymer electrolytes. *Materials Letters*, 44, 208–214.
- Rajendran, S., Uma, T., & Mahalingam, T. (1999). Characterisation of plasticized PMMA based solid polymer electrolytes. *Ionics*, 5, 232–235.
- Ramesh, S., & Arof, A. K. (2001). Structural, thermal and electrochemical cell characteristics of poly(vinyl chloride)-based polymer electrolytes. *Journal of Power Sources*, 99(1–2), 41–47.
- Ramesh, S., & Lu, S. C. (2008). Effect of nanosized silica in poly(methyl methacrylate)-lithium bis(trifluoromethanesulfonyl)imide based polymer electrolytes. *Journal of Power Sources*, 185(2), 1439–1443.
- Ramesh, S., Lu, S. C., & Morris, E. (2012). Towards magnesium ion conducting poly(vinylidene fluoride-hexafluoropropylene)-based solid polymer electrolytes

with great prospects: Ionic conductivity and dielectric behaviours. *Journal of the Taiwan Institute of Chemical Engineers*, 43(5), 806–812.

- Ramesh, S., Yahaya, A. H., & Arof, A. K. (2002). Dielectric behaviour of PVC-based polymer electrolytes. *Solid State Ionics*, 152–1533, 291–294.
- Ratner, M. A., & Shriver, D. F. (1988). Ion transport in solvent-free polymers. *Chemical Reviews*, 88(1), 109–124.
- Reich, S., & Michaeli, I. (1975). Electrical conductivity of small ions in polyacrylonitrile in the glass-transition region. *Journal of Polymer Science, Polymer Physics Edition*, 13, 9–18.
- Saha, P., Kanchan, M., & Velikokhatnyi, O. I. (2014). Progress in materials science rechargeable magnesium battery : Current status and key challenges for the future. *Progress in Materials Science*, 66, 1–86.
- Saidi, M. A. A., W. A. Rahman, W. A., & Majid, R. A. (2014). Effect of different solvents on the thermal, IR spectroscopy and morphological properties of solution casted PLA/starch films. *Malaysian Journal of Fundamental and Applied Sciences*, 10(1), 33–36.
- Saikia, D., & Kumar, A. (2004). Ionic conduction in P(VDF-HFP)/PVDF-(PC + DEC)-LiClO₄polymer gel electrolytes. *Electrochimica Acta*, 49(16), 2581–2589.
- Saikia, D., Wu, H. Y., Pan, Y. C., Lin, C. P., Huang, K. P., Chen, K. N., ... Kao, H. M. (2011). Highly conductive and electrochemically stable plasticized blend polymer electrolytes based on PVdF-HFP and triblock copolymer PPG-PEG-PPG diamine for Li-ion batteries. *Journal of Power Sources*, 196(5), 2826–2834.
- Scott, A. J., & Penlidis, A. (2017). Copolymerization. *Reference Module in Chemistry, Molecular Sciences and Chemical Engineering*, 1–11.
- Shanthi, M., Mathew, C. M., Ulaganathan, M., & Rajendran, S. (2013a). FT-IR and DSC studies of poly(vinylidene chloride-co-acrylonitrile) complexed with LiBF₄. *Spectrochimica Acta - Part A: Molecular and Biomolecular Spectroscopy*, 109, 105–109.
- Shanthi, M., Mathew, C. M., Ulaganathan, M., & Rajendran, S. (2013b). Spectrochimica Acta Part A : Molecular and Biomolecular Spectroscopy FT-IR and DSC studies of poly (vinylidene chloride- co -acrylonitrile) complexed with LiBF₄. *Spectrochimica Acta Part A: Molecular and Biomolecular Spectroscopy*, 109, 105–109.
- Shanthi, M., Ramachandran, M., Rajendran, S., Subadevi, R., & Sivakumar, M. (2017). Effect of different salts on P(VdC-co-AN) gel polymer electrolytes for Li-rechargeable batteries. *International Research Journal of Engineering and Technology (IRJET)*, 4(9), 302–307.

- Shanthi, M., Subadevi, R., Ramachandran, M., & Sivakumar, M. (2017). Optimization of blend of polymethyl methacrylate (PMMA) with poly vinylidene chloride-co-acrylonitrile (PVdC-co-AN) composite electrolytes. *International Journal of Advance Engineering and Research*, 4(6), 1–6.
- Shao, Y., Rajput, N. N., Hu, J., Hu, M., Liu, T., Wei, Z., ... Liu, J. (2015). Nanocomposite polymer electrolyte for rechargeable magnesium batteries. *Nano Energy*, 12, 750–759.
- Sharma, J., & Hashmi, S. A. (2018). Plastic crystal-incorporated magnesium ion conducting gel polymer electrolyte for battery application. *Bulletin of Materials Science*, 41(147), 1–8.
- Shurvell, H. F., & Southby, M. C. (1997). Infrared and Raman spectra of tetrahydrofuran hydroperoxide. *Vibrational Spectroscopy*, 15(1), 137–146.
- Silva, M. M., Nunes, S. C., Barbosa, P. C., Evans, A., de Zea Bermudez, V., Smith, M. J., & Ostrovskii, D. (2006). Sol-gel preparation of a di-ureasil electrolyte doped with lithium perchlorate. *Electrochimica Acta*, 52(4), 1542–1548.
- Sim, L. N., Yahya, R., & Arof, A. K. (2016). Infrared studies of polyacrylonitrile-based polymer electrolytes incorporated with lithium bis(trifluoromethane)sulfonimide and urea as deep eutectic solvent. *Optical Materials*, 56, 140–144.
- Sing, D. (n.d.). Li-ion Batteries in the Hot Seat (A Primer on the Science of Exploding Smartphones) - Aptelligent. Retrieved on October 12, 2019, from <https://medium.com/aptelligent/li-ion-batteries-in-the-hot-seat-a-primer-on-the-science-of-exploding-smartphones-28ac0e2f6a95>
- Singh, M. K., Suleman, M., Kumar, Y., & Hashmi, S. A. (2015). A novel configuration of electrical double layer capacitor with plastic crystal based gel polymer electrolyte and graphene nano-platelets as electrodes: A high rate performance. *Energy*, 80, 465–473.
- Song, J. Y., Wang, Y. Y., & Wan, C. C. (1999). Review of gel-type polymer electrolytes for lithium-ion batteries. *Journal of Power Sources*, 77, 183–197.
- Song, J. Y., Wang, Y. Y., & Wan, C. C. (2000). Conductivity study of porous plasticized polymer electrolytes based on poly(vinylidene fluoride) A comparison with polypropylene separators. *Journal of The Electrochemical Society*, 147(9), 3219–3225.
- Stephan, A. M. (2006). Review on gel polymer electrolytes for lithium batteries. *European Polymer Journal*, 42, 21–42.
- Stephan, A. M., & Nahm, K. S. (2006). Review on composite polymer electrolytes for lithium batteries. *Polymer*, 47(16), 5952–5964.
- Stephan, A. M., Nahm, K. S., Anbu Kulandainathan, M., Ravi, G., & Wilson, J. (2006).

Electrochemical studies on nanofiller incorporated poly(vinylidene fluoride-hexafluoropropylene) (PVdF-HFP) composite electrolytes for lithium batteries. *Journal of Applied Electrochemistry*, 36(10), 1091–1097.

Subbu, C., Rajendran, S., Kesavan, K., & Mathew, C. M. (2015). Lithium ion conduction in PVdC-co-AN based polymer blend electrolytes doped with different lithium salts. *International Polymer Processing*, 30(4), 476–486.

Subbu, C., Rajendran, S., Kesavan, K., & Premila, R. (2016). The physical and electrochemical properties of poly(vinylidene chloride-co-acrylonitrile)-based polymer electrolytes prepared with different plasticizers. *Ionics*, 22(2), 229–240.

Succinonitrile. (n.d.). Retrieved on December 2, 2018, from <https://en.wikipedia.org/wiki/Succinonitrile>

Sumathipala, H. H., Hassoun, J., Panero, S., & Scrosati, B. (2007). High performance PEO-based polymer electrolytes and their application in rechargeable lithium polymer batteries. *Ionics*, 13(5), 281–286.

Taib, N. U., & Hayati, N. (2014). Plastic crystal – solid biopolymer electrolytes for rechargeable lithium batteries. *Journal of Membrane Science*, 468, 149–154.

Tang, X., Muchakayala, R., Song, S., Zhang, Z., & Reddy, A. (2016). A study of structural, electrical and electrochemical properties of PVdF-HFP gel polymer electrolyte films for magnesium ion battery applications. *Journal of Industrial and Engineering Chemistry*, 37, 67–74.

Tarascon, J. M., & Armand, M. (2001). Issues and challenges facing rechargeable lithium batteries. *Nature*, 414(6861), 359–367.

Three electrode system. (n.d.). Retrieved on August 2, 2019, from <http://www.customsensorsolutions.com/ap-pstat.html>

Tsuchida, E., & Ohno, H. (1983). Conduction of lithium ions in polyvinylidene fluoride and its derivatives-i. *Electrochimica Acta*, 28(5), 591–595.

Ulaganathan, M., Nithya, R., Rajendran, S., & Raghu, S. (2012). Li-ion conduction on nano filler incorporated PVdF-co-HFP based composite polymer blend electrolytes for flexible battery applications. *Solid State Ionics*, 218, 7–12.

Voigt, N., & Wüllen, L. Van. (2014). The effect of plastic-crystalline succinonitrile on the electrolyte system PEO : LiBF₄ : Insights from solid state NMR. *Solid State Ionics*, 260, 65–75.

Wagner, J. B., & Wagner, C. (1957). Electrical conductivity measurements on cuprous halides. *The Journal of Chemical Physics*, 26(6), 1597–1601.

Wang, J., Song, S., Gao, S., Ravi, M., Liu, R., & Ma, Q. (2017). Mg-ion conducting gel

- polymer electrolyte membranes containing biodegradable chitosan: Preparation, structural, electrical and electrochemical properties. *Polymer Testing*, 62, 278–286.
- Wang, P., Dai, Q., Zakeeruddin, S. M., Forsyth, M., MacFarlane, D. R., & Grätzel, M. (2004). Ambient temperature plastic crystal electrolyte for efficient, all-solid-state dye-sensitized solar cell. *Journal of the American Chemical Society*, 126(42), 13590–13591.
- Wang, Z., Huang, B., Huang, H., Xue, R., Chen, L., & Wang, F. (1996). The vibrational spectroscopic study of polyacrylonitrile-based electrolyte. *Spectrochimica Acta - Part A: Molecular and Biomolecular Spectroscopy*, 52(6), 691–703.
- Watanabe, M., Kanba, M. O. T., & Nagaoka, K. (1983). Ionic conductivity of hybrid films composed of polyacrylonitrile, ethylene carbonate, and LiClO₄. *Journal of Polymer Science: Polymer Physics Edition*, 21, 939–948.
- Yang, C.-M., Kim, H.-S., Na, B.-K., Kum, K.-S., & Cho, B. W. (2006). Gel-type polymer electrolytes with different types of ceramic fillers and lithium salts for lithium-ion polymer batteries. *Journal of Power Sources*, 156(2), 574–580.
- Yoshihara, T., Tadokoro, H., & Murahashi, S. (1964). Normal vibrations of the polymer molecules of helical conformation. IV. Polyethylene oxide and polyethylene-d₄ oxide. *The Journal of Chemical Physics*, 41(9), 2902–2911.
- Young, W. S., Kuan, W. F., & Epps, T. H. (2014). Block copolymer electrolytes for rechargeable lithium batteries. *Journal of Polymer Science, Part B: Polymer Physics*, 52(1), 1–16.
- Zainol, N. H., Samin, S. M., Othman, L., Isa, K. B. M., Chong, W. G., & Osman, Z. (2013). Magnesium ion-based gel polymer electrolytes: Ionic conduction and infrared spectroscopy studies. *International Journal of Electrochemical Science*, 8, 3602–3614.
- Zainuddin, Z., Hambali, D., Supa'at, I., & Osman, Z. (2016). Ionic conductivity, ionic transport and electrochemical characterizations of plastic crystal polymer electrolytes. *Ionics*, 23(2), 265–273.
- Zhou, D. Y., Wang, G. Z., Li, W. S., Li, G. L., Tan, C. L., Rao, M. M., & Liao, Y. H. (2008). Preparation and performances of porous polyacrylonitrile-methyl methacrylate membrane for lithium-ion batteries. *Journal of Power Sources*, 184(2), 477–480.
- Zugmann, S., Fleischmann, M., Amereller, M., Gschwind, R. M., Wiemhöfer, H. D., & Gores, H. J. (2011). Measurement of transference numbers for lithium ion electrolytes via four different methods, a comparative study. *Electrochimica Acta*, 56(11), 3926–3933.
- Zulkepeli, N. A. S. N., Winie, T., & Subban, R. H. Y. (2017). Infrared studies of PVC-

based electrolytes incorporated with lithium triflate and 1-butyl-3-methyl imidazolium trifluoromethanesulfonate as ionic liquid. *AIP Conference Proceedings*, 1877, 1–8.

Universiti Malaya